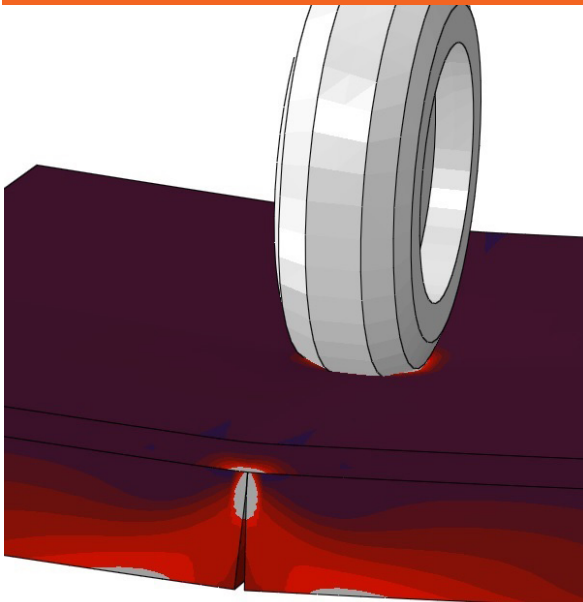


# Deterioration Models for Cement Bound Materials in Structural Design and Evaluation of Heavy Duty Pavements

A rational approach to pavement analysis



Asmus Skar

PhD Thesis

Department of Civil Engineering  
2017

DTU Civil Engineering Report R-364

# Deterioration Models for Cement Bound Materials in Structural Design and Evaluation of Heavy Duty Pavements

- A rational approach to pavement analysis

Asmus Skar

Ph.D. Thesis

Department of Civil Engineering  
Technical University of Denmark

2017

### Supervisors:

Associated Professor Peter Noe Poulsen, DTU Byg  
Associated Professor Varvara Zania, DTU Byg  
Specialist Mogens Løvendorf Holst, COWI A/S

### Assesment Committee:

Research Director Armelle Chabot, IFSTTAR Centre de Nantes, France  
Professor Lev Khazanovich, University of Pittsburgh, USA  
Associated Professor Eyal Levenberg, DTU Byg, Denmark

Deterioration Models for Cement Bound Materials in Structural  
Design and Evaluation of Heavy Duty Pavements  
-A rational approach to pavement analysis

Copyright © 2017 by Asmus Skar  
Printed by DTU-Tryk  
Department of Civil Engineering  
Technical University of Denmark  
ISBN: 9788778779991  
ISSN: 1601-2917

# Preface

This thesis is submitted as a partial fulfilment of the requirements for the Danish Ph.D. degree. The thesis is divided into two parts. The first part introduces the background and motivation for the study and concludes the major findings. Also a presentation of the work conducted is given here. The second part is a collection of three papers focused on the most important topics of the research that has been undertaken.

## **Preface to published version**

The thesis was defended at a public defense on Friday the 31st of March 2017. Official opponents were Associated Professor Eyal Levenberg, Technical University of Denmark, Research Director Armelle Chabot, IFSTTAR and Professor Lev Khazanovich, University of Pittsburgh. Compared to the the original submitted version of the thesis, several minor editorial corrections have been made and the status of some of the appended papers has been updated.

Kongens Lyngby, April 8, 2017

Asmus Skar



# Acknowledgements

This Ph.D. project was funded by COWI A/S, COWIfonden (grant no. C-123.03) and the Innovation Fund Denmark (grant no. 1355-00060).

The presented work would not have been achieved without the help and support of a range of people and I would like to take the opportunity to express my gratitude.

First of all, I would like to acknowledge the supervision of Associated Professor Peter Noe Poulsen. He has guided me all the way through and provided me with useful advices and feedback. I would also thank co-author John Forbes Olesen for his advices and significant contribution to the present work, as well as co-supervisors Varvara Zania and Mogens Løvendorf Holst for their support during the project.

Further, I will express my gratitude to COWI A/S for their belief in me and the support throughout the project. A special thanks to my closest leaders Thomas Mejer and Gregers Hildebrand for taking a strong ownership in the project, your support and encouragement.

Sincere thanks to my fellow Ph.D. colleagues at DTU Byg, Sebastian Andersen, Jesper Harrild Sørensen, Morten Andersen Herfelt and Anders Bau Hansen for creating a fantastic working environment and enjoyable atmosphere. Finally, I would like to thank my family and friends who encouraged me throughout the entire project.



# Abstract

Ports and industries require special types of pavements to resist the heavy static load from containers and continuous loads from operation vehicles. To reduce the risk of rutting and settlements over time concrete or composite pavement systems are typically applied. The structural design of such pavements are today based on Mechanistic-Empirical (M-E) methods. The M-E method is appropriate for many situations, in other situations it may lead to overdesign, or maybe worse, underdesign. The method has limited capabilities and cannot account for significant factors affecting the pavement response, such as geometry, realistic material behavior and arbitrary loading conditions in a unified manner.

In recent years we have seen significant growth in the capabilities of computer hardware and software that has allowed numerical modeling and analysis of structural problems for an increasing variety of applications. Such models allow use of constitutive models that have the potential to replicate a wide range of material behavior under arbitrary loading conditions. However, successful application of numerical models in engineering design is often prevented by complex implementation, unstable simulations and a large number of model parameters.

In order to move a step towards more generalised structural design methods for analysis of heavy duty pavements, this study aims at developing a mechanistic approach based on constitutive models. A simple framework for engineering application is sought; creating a rational link between laboratory tests, design and field applications.

First, a realistic 3-D cohesive finite element model for structural analysis of composite block pavement systems is developed. This model is used for verification and compared to experimental results. Secondly, a simplified two-dimensional engineering model is developed incorporating a cohesive hinge and a two-parameter foundation model into a beam element. This model includes the most significant parameters that influences the structural response, i.e. soil-structure interaction and cyclic damage of the cemented material.

It is found that both the conventional cohesive zone model and the cohesive hinge model is suitable for the description of the fracture behaviour of cemented materials in concrete and composite pavement systems. The engineering model is efficient, resulting in computationally fast and stable simulations, and a simple calibration method for estimating foundation model parameters is developed. The consistent format applied enables straightforward implementation of different unloading and reloading schemes. The presented damage model accounts for the material behavior in all the cracked phases, linking the development of the fracture process zone and damage of the existing fracture process zone to the monotonic material characteristics in a unified manner.

The obtained results show that the methodology is attractive and well-suited for further developments and practical use. The real-scale model can be used directly in design, whereas the engineering model can be used in special design cases, for sensitivity analysis and simple studies. The engineering model, can when extended to three-dimensional applications, replace many of the more complex real-scale cohesive zone models. The engineering model can then be used for structural analysis enabling a full mechanistic analysis of concrete and composite pavement structures, something which is not possible today.

# Resumé

Havne- og industriområder kræver specialbelægninger for at modstå tunge statiske containerlaster og kontinuerlige laster fra køretøjer. Typisk benyttes beton eller cementstabiliserede materialer i stive eller halvstive belægningstyper for at reducere sporkøring og sætningsskader over tid. Dimensionering af denne type belægninger er i dag baseret på analytisk-empiriske metoder. Metoden kan være passende i mange situationer, men i enkelte vil den medføre overdimensionerede, eller meget værre, underdimensionerede konstruktioner. Denne type metode har begrænset anvendelse og tager ikke højde for væsentlige faktorer der påvirker belægningens respons, som geometri, realistisk materiale opførsel og vilkårlige belastningsforhold på en konsistent måde.

De seneste års betydelige udvikling indenfor computerteknologi tillader nu numerisk modellering og strukturel analyse for en række forskellige applikationer. Denne teknologiske udvikling tillader brug af konstitutive modeller, der har potentiale til at realistisk afspejle en bred vifte af materialers opførsel under vilkårlige belastningsforhold. Dog er effektiv anvendelse i praksis ofte forhindret af modellernes kompleksitet, et højt antal af materiale parametre og numerisk instabilitet.

Formålet med dette forskningsprojekt er at udvikle nye og mere generelle nedbrydningsmodeller for havne- og industribelægninger. Velfunderede mekaniske principper og konstitutive modeller er inddraget for at skabe en rationel forbindelse mellem laboratorieforsøg, design og anvendelser i marken.

Først, er der udviklet en fuldskala model til analyse af halv-stive betonstensbelgninger. Denne model benyttes til verifikation og sammenligning med eksperimentelle resultater. Dernæst, er en forenklet ingeniørmodel udviklet på baggrund af en bjælkemodel hvori et plastisk hængsel og en to-parameter jordmodel er indarbejdet på konstitutivt niveau. Denne model beskriver de væsentligste parametre der påvirker den strukturelle opførsel, dvs. interaktion mellem konstruktion og jord samt udmattelse af det cementstabiliserede materiale.

Både en traditionel kohesiv model og hængsel-modellen er velegnet til beskrivelsen af revnernes opførsel i beton og cementstabiliserede materialer i

stive- og halvstive belægnings. Ingeniørmodellen er effektiv, hvilket resulterer i hurtige og stabile numeriske simulationer, og kalibrering af modellen er enkel og ligetil. Et generelt format muliggør simpel implementering af konstitutiv materialeopførsel. Udmattelsesmodellen præsenteret tager højde for materialets opførsel i alle faser af revneudviklingen. Dette sikrer et konsistent format der kan beskrive materialernes væsentligste karakteristika under vilkårlige lasttilfælde.

Resultaterne viser, at metoden udviklet er effektiv og anvendelig til videre udvikling og praktisk implementering. Fuldskala modellen kan benyttes direkte til dimensionering, hvorimod ingeniørmodellen kan benyttes til specielle design cases, forundersøgelser samt sensitivitets analyser. Ingeniørmodellen kan, når udvidet til 3-D, erstatte komplekse fuldskala modeller og dermed benyttes i en fuld mekanisk og rationel analyse, som ikke er mulig i dag.

# Contents

<b>I</b>	<b>Introduction and Summary</b>	<b>1</b>
<b>1</b>	<b>Introduction</b>	<b>3</b>
1.1	Background . . . . .	3
1.2	Behavior of cemented material . . . . .	10
1.3	Constitutive crack model . . . . .	14
1.4	Numerical methods for crack modeling . . . . .	17
1.5	Soil-structure interaction model . . . . .	22
1.6	Objectives of the thesis . . . . .	25
1.7	Outline of the thesis . . . . .	27
<b>2</b>	<b>3-D cohesive finite element model</b>	<b>29</b>
2.1	Introduction . . . . .	29
2.2	Modeling framework . . . . .	30
2.3	Concrete block pavement model . . . . .	35
2.4	Large-scale experiments . . . . .	38
2.5	Influence of load position . . . . .	41
2.6	Summary of sensitivity studies . . . . .	44
2.7	Concluding remarks . . . . .	45
<b>3</b>	<b>Cohesive cracked-hinge model</b>	<b>49</b>
3.1	Introduction . . . . .	49
3.2	The mechanics of the hinge model . . . . .	50
3.3	Implementation of hinge into beam element . . . . .	55
3.4	User-built finite element code . . . . .	59
3.5	Numerical analysis of beam fracture tests . . . . .	65
3.6	Implementation of hinge into plate element . . . . .	67
<b>4</b>	<b>Cracked-hinge beam on soil</b>	<b>71</b>
4.1	Introduction . . . . .	71
4.2	Soil-structure interaction models . . . . .	72
4.3	Two-parameter coupled spring model . . . . .	79

4.4	Numerical simulation of one-way slabs on grade . . . . .	86
4.5	Evaluation of methodology . . . . .	91
4.6	Non-linear behavior of soil . . . . .	95
<b>5</b>	<b>Cyclic fiber hinge model</b>	<b>99</b>
5.1	Introduction . . . . .	99
5.2	The mechanics of the fiber hinge model . . . . .	101
5.3	Tensile damage model . . . . .	105
5.4	Fatigue model . . . . .	109
5.5	Fiber hinge tangent stiffness matrix . . . . .	117
5.6	Numerical examples . . . . .	121
<b>6</b>	<b>Conclusions and Recommendations</b>	<b>129</b>
6.1	Conclusions . . . . .	130
6.2	Practical applications . . . . .	134
6.3	Recommendations for future research . . . . .	136
	<b>Bibliography</b>	<b>157</b>
<b>II</b>	<b>Appended Papers</b>	<b>159</b>

**Paper I**

*"3-D cohesive finite element model for application in structural analysis of heavy duty composite pavements",*

A. Skar & P.N. Poulsen.

Published in: *Construction & Building Materials, 2015* . . . . . 161

**Paper II**

*"Cohesive cracked-hinge model for simulation of fracture in one-way slabs on grade",*

A. Skar & P.N. Poulsen & J.F. Olesen.

Published in: *International Journal of Pavement Engineering, 2017* . . . 179

**Paper III**

*"General cracked-hinge model for simulation of low-cycle damage in cemented beams on soil",*

A. Skar & P.N. Poulsen & J.F. Olesen.

Published in: *Engineering Fracture Mechanics, 2017* . . . . . 197

**Additional work (not included in the thesis)**

1. *Modelling of composite concrete block pavement systems applying a cohesive zone model*

A. Skar & P.N. Poulsen

Paper presented at: *11<sup>th</sup> International Conference on Concrete Block Pavement*, Dresden, Germany, 2015



# Part I

## Introduction and Summary

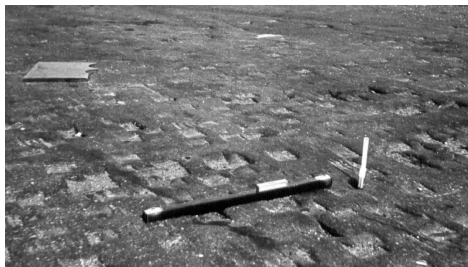


# Chapter 1

## Introduction

### 1.1 Background

With the phenomenal container trade growth in the 1970's many ports experienced catastrophic problems with paving systems. Existing port surface areas when used for container operations suffered severe failures (Meletiou and Knapton, 1987). Asphalt rutting and punching, and concrete slab cracking were among the primary damage types observed, see Figure 1.1.



(a)



(b)

**Figure 1.1:** *Pavement failure types reported in Barber (1980): (a) Asphalt punching from static loads. (b) Concrete cracking from differential settlements and overload.*

Similar problems were also observed in many newly constructed areas and soon such pavement systems were treated separately from conventional paving and construction. Research in this area started in the the late 1970's by detailed assessment of port pavement failures, see e.g. Barber (1980). Following a series of new and more consistent design guidelines (Knapton, 1984, 1986; Knapton and Meletiou, 1996; Silfwerbrand, 2005; Asphalt-Institute, 2006; Knapton, 2008; PIANC, 2015).

In order to resist the heavy static loads from containers and continuous loads from vehicles the pavement systems developed were thicker and stiffer compared to conventional highway pavements. To reduce the risk of surface damage, rutting and settlements over time, concrete and composite<sup>1</sup> concrete block pavement systems are typically preferred in design, see example in Figure 1.2.

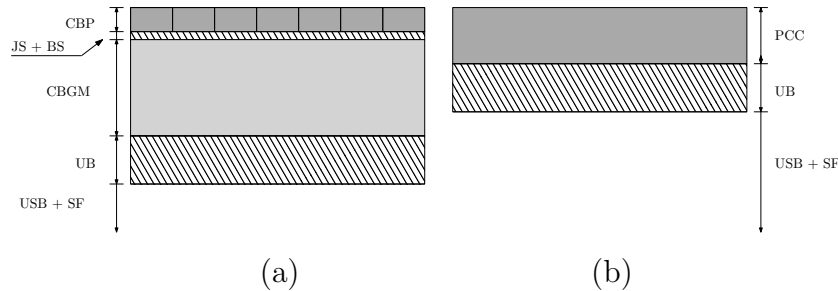


**Figure 1.2:** Sketch of typical pavement systems considered in the present study: (a) composite concrete block pavement and (b) concrete pavement. PCC: Portland Cement Concrete, CBP: Concrete Block Pavers, JS: Jointing Sand, BS: Bedding Sand, CBGM: Cement Bound Granular Mixture, UB: Unbound Base, USB: Unbound Sub Base, SF: Subgrade Foundation.

Although these special pavements are treated separately, the design method rely on the same principles as for conventional pavements. The structural design of such pavement systems is based on empirical formulas which converts the response analysis into a measure of performance, commonly referred to as the Mechanistic-Empirical (M-E) method, first introduced in pavement engineering by Kerkhoven and Dormon (1953). Figure 1.3 shows a schematic overview of the various design approaches used in pavement engineering. The pavement failure criterion is typically divided in two types:

- (i) Stress-based: Reduction in pavement condition index (combined measure of pavement performance), crack initiation, area of visible cracks.
- (ii) Strain-based: Reduction in E-modulus of the material (typically failure at 50% of initial modulus).

For controlled stress laboratory testing the specimen will clearly fail after a certain number of load repetition, but in controlled strain testing this is not always the case. In controlled strain testing the modulus of the material will

<sup>1</sup>The term 'composite pavement' is used in this thesis referring to a semi-rigid pavement type consisting of a relatively thin layer of concrete blocks or asphalt constructed over a cement bound granular mixture, providing the main bearing capacity of the structure.

initially decrease before reaching a relatively constant level. Thus, failure of the material is often defined as a decrease in modulus. For in-situ pavements, failure is mostly defined as a certain severity and extent of cracking.

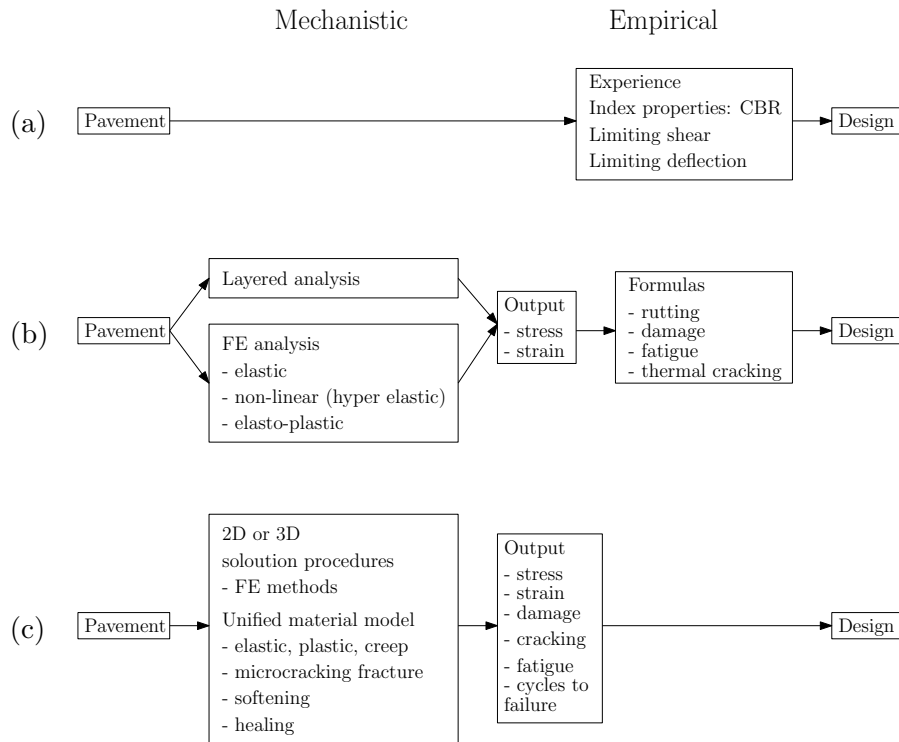


**Figure 1.3:** Schematic description of various approaches for design of pavements according to Desai (2007): (a) Empirical, (b) Mechanistic-Empirical (M-E), (c) Mechanistic.

The M-E method represent one step forward from empirical methods, see Figure 1.3 (a); the response model (mechanical part), is used to calculate critical stress or strain in each material layer. This measure is then used as input in an appropriate fatigue relationship (empirical part) to calculate the performance. Very often uni-axial quantities are used as response measure (Huang, 1993); for concrete and high-quality cement bound granular mixtures<sup>2</sup>, considered here, the horizontal tensile stress or strain at the bottom of the layer. The number of load repetitions to failure is then calculated based on one of these measures. The general empirical expression is formulated as

<sup>2</sup>The term 'cemented material' is used in this thesis referring to both concrete and high-quality cement bound granular mixtures.

a *Wöhler* type of fatigue relationship, or a so-called *S-N* curve, i.e.

$$N_\sigma = A \left[ \frac{\sigma_b}{\sigma_t} \right]^B \quad ; \quad N_\varepsilon = A \left[ \frac{\varepsilon_b}{\varepsilon_t} \right]^B \quad (1.1)$$

where  $\sigma_b$  and  $\varepsilon_b$  are the stress and strain at failure and  $\sigma_t$  and  $\varepsilon_t$  are the stress and strain applied (*S*), *N* is the number of load repetitions to failure, *A* and *B* are empirical constants, the latter often referred to as the load damage exponent. To account for changing loading characteristics, i.e. varying amplitude and number of cycles, the linear damage hypothesis by Palmgren (1924) and Miner (1945), here referred to as the 'PM-rule', is typically used.

The different parts in the M-E design procedure entails different types of weak links in the methodology. The M-E method can be divided into three main parts, shown in Figure 1.3 (b); the response model, monotonic model parameters and fatigue relationship.

### Response model

The response model applied has to reflect the actual response of the pavement structure. However, this is not always the case as models are often over-simplified. Typically layered linear elastic theory (Burmister, 1945) or the method of equivalent thickness (Odemark, 1949) is used to calculate the pavement response in flexible and composite pavements. In these methods the materials are idealised as semi-infinite homogeneous layers of material with linear elastic isotropic properties. Thus, non-linear material behavior and geometry is neglected. Moreover, layer interaction and contact is typically limited to unbonded or bonded behavior.

For design of rigid concrete pavements Westergaard's analytical solutions for interior, edge and corner loading of infinite or semi-infinite plates have traditionally been applied (Westergaard, 1926, 1948). Ioannides et al. (1985b) used the finite element (FE) method to re-evaluate Westergaard's solutions and establish their limitations using the special purpose computer program ILLI-SLAB (Tabatabaie and Barenberg, 1980). With the growth of computer capabilities the FE method has increased in popularity and several response analysis tools have been developed for the purpose of concrete pavement design, see e.g. (NCHRP, 2003). The FE method has also become a standard feature in FAARFIELD, used for airport pavement design (Kawa et al., 2007). These models can account for geometry and boundary conditions, soil-structure interaction to some extent, as well as linear and non-linear temperature distribution. However, their use do not involve calculation of pavement performance based on evolving stresses and strains.

### Monotonic model parameters

For composite pavements both stress-based models (Corté and Goux, 1996; NCHRP, 2004; Knapton, 2008) and strain-based models (Walker et al., 1977; Freeme et al., 1982; NAASRA, 1992; Jameson et al., 1992; Knapton and Meletiou, 1996; Thøgersen et al., 2004; Austroads, 2004) are used for structural design. For concrete pavements stress-based models are primarily used (Packard, 1984; NCHRP, 2004; FAA, 2009).

Development of methods for determining  $\varepsilon_b$  is a difficult task as experimental research show that the strain becomes uncontrollable at the sudden strain localisation at failure (Otte, 1978). Thus,  $\varepsilon_b$  is typically determined at a certain load level below the failure load (Litwinowicz and Brandon, 1994; Gonzalez et al., 2010; Alderson, 2013).

Standard methods for determining  $\sigma_b$ , or so-called modulus of rupture, have been developed based on beam tests, see e.g. ASTM (2015, 2016). However, experimental research (Roesler, 1998; Roesler et al., 2004a, 2005, 2012) has shown that concrete slabs under fatigue loading sustain greater stress ratios and higher cracking resistance than that predicted by concrete beam fatigue curves cast with the same material, see Figure 1.4.

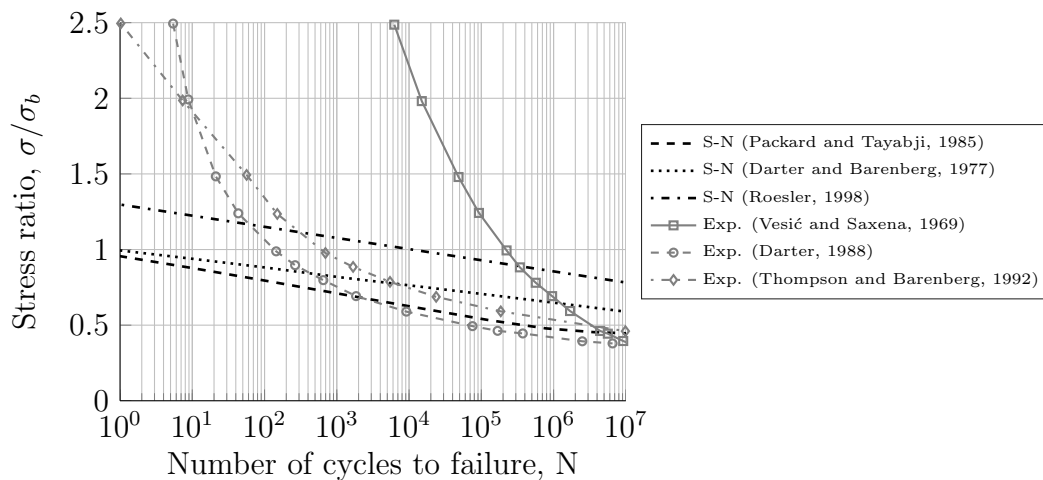


**Figure 1.4:** *S-N design fatigue curves based on beam tests (Packard, 1984; Darter and Barenberg, 1977) and slab tests (Roesler, 1998) compared to experimental slabs on grade (concrete slab resting on soil foundation) fatigue curves (Vesic and Saxena, 1969; Darter, 1988; Thompson and Barenberg, 1992).*

This phenomenon has also been observed in plain concrete slabs (Rao, 2005; Cervantes and Roesler, 2009), fiber-reinforced concrete slabs (Beckett,

1990; Roesler et al., 2004b), and full-scale continuously reinforced concrete pavement sections (Kohler and Roesler, 2006). To predict the fatigue life of the concrete slabs more accurately, Roesler and Barenberg (1999) proposed to use the static flexural strength of the slab instead of the beam flexural strength.

### **Fatigue relationship**

The fatigue relationship is the weakest component of the M-E method which generally requires an additional calibration function to match the observed field performance. The M-E method is heavily dependent on the empirical input from large-scale pavement tests and the failure criterion selected. To date only one official authority, the U.S Federal Administration of Aviation (FAA), has been able to establish a consistent test program and design method for pavement structures subjected to heavy duty loads. These data can be used to some extent for development of material models for other applications, although both load levels (lower) and load configurations (more distributed) as well as pavement systems differ slightly compared to typical port and industrial pavements.

Rodway and Wardle (1998) applied data from the FAA test facility for development of fatigue relationships based on the permanent deformation of the subgrade foundation and incorporated this in the design software HIPAVE (Wardle et al., 2006). However, other failure criteria applied to port and industrial pavement designs are either directly or indirectly related to fatigue in conventional pavements. Knapton (2008) suggested to use allowable stress levels found from linear elastic response analysis of catalogue highway pavements (BS, 2001). Thus, fatigue relationships presently available for design of heavy duty pavements are an inseparable part of their design method.

The methodology proposed introduces a range of further simplifications and may in some cases lead to inconsistent results. For example it can be shown, that for composite block pavement systems with cemented base thickness below 300 mm, the static load is more critical than the cyclic load for the same load magnitude, see Figure 1.5.

The M-E models currently used in design of heavy duty pavements rely mainly on the empirical part. This type of model does not distinguish between crack initiation and crack propagation or elastic and inelastic work, model parameters are simply regression constants without direct physical meaning. The PM-rule does not consider sequence effects, i.e. the order of the loading makes no difference. Moreover, damage accumulation is independent on stress level. The method assumes that each single cycle of load contributes to damage and the total fatigue failure is due to the linear ac-

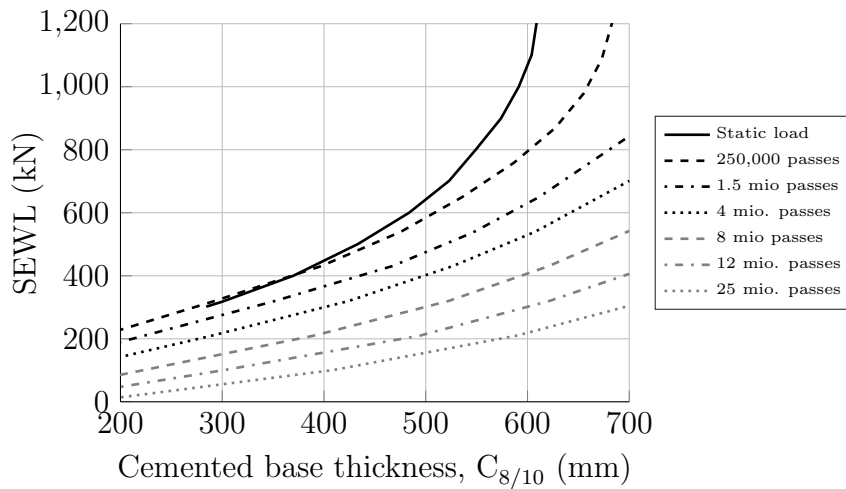


**Figure 1.5:** Design chart for heavy duty pavements ( $E_{soil}=50$  MPa) according to Knapton (2008): Cemented base thickness for different load levels given in Single Equivalent Wheel Load (SEWL).

cumulation. However, research shows that damage in cemented materials is not linear (Bache and Vinding, 1990; Ioannides, 1997; Roesler and Barenberg, 1999; Barenberg, 2005) as clearly indicated in Figure 1.4.

## Summary

The M-E method deals with a limited number of materials in a restricted range of design options; each fatigue relationship being restricted by its own design method. The method is practical and simple because it gives the user direct analytical expressions, however, such empirically based material models have only limited capabilities.

M-E models have difficulties in accurately predicting the complex interactions between the loads, cemented material properties, geometry, and soil-structure interaction, without significant calibration. This can, in some cases, lead to poor service life prediction, overly conservative designs, or the elimination of important parameters influencing the response. Data reported in the literature suggest that predictions of pavement fatigue life using the PM-rule can approximate reality at best within an order of magnitude and more commonly within two or even three orders of magnitude (Ioannides, 2005).

In order to improve current methods and move a step towards more generalised structural design methods for analysis of heavy duty pavements, this thesis aims at developing a mechanistic approach based on constitutive mod-

els, see Figure 1.3 (c). A simple framework for engineering application is sought; creating a rational link between laboratory tests, design and field applications. For such a methodology to be widely accepted and implemented in practice, a set of principles have been established for the present study inspired by Colasanti and Horvath (2010):

- (i) The methodology must be consistent, have a theoretical basis and include all the main parameters influencing the response in a unified manner.
- (ii) Implementation of models must be simple and straight forward applying appropriate computer packages or commercially available structural analysis software.
- (iii) There must be sound logic and science for evaluation of the material and model parameters in the laboratory and in the field. This should be achievable using standard test methods on a routine basis.

## 1.2 Behavior of cemented material

### Field observations

Assessment of failure in composite pavement is difficult as the cemented layer is placed below additional surface layers, in highway pavements typically asphalt surface, binder and base course. Geometry and construction methods also influence the mechanisms of failure. Since the 1990's pre-cracking techniques have typically been applied to allow for movement, e.g. from temperature and moisture changes as well as shrinkage, see e.g. (Colombier and Marchand, 1993; Shahid and Thom, 1996).

Shahid (1997) stated that once initial shrinkage cracking has developed, degradation of aggregate interlock joints through shear movement of the cracked edges finally causes the occurrence of longitudinal cracks in wheel paths due to the relatively higher flexural stresses. Thøgersen et al. (2004) found that shrinkage cracking can be completely avoided and Yeo (2008b) identified both transverse and longitudinal fatigue cracking in post-processing assessment of damaged composite pavements. Full-scale experiments of cement bound granular mixture slabs reported in Busch et al. (2006) show that empirically based models yield unrealistic results considering a loading regime and configuration different from typical truck wheel loads, e.g. ultimate loading condition.

Darter and Barenberg (1977) concluded that the highest tensile stresses in highway concrete pavement occurred at the longitudinal edge of the pavement midway between the transverse joints. The critical failure point in most highway slabs was at the longitudinal edge, as was seen in the AASHO road test (HRB, 1962), Bates road test (Older, 1924), and Michigan road test (Finney and Oehler, 1959). For thin slabs (less than 200 mm) the critical location was at the transverse joint (HRB, 1962). Condition surveys of pavements without dowels or tied shoulders have shown that longitudinal and corner cracking occur as frequently as transverse cracking (Mahoney et al., 1991; Harvey et al., 2000; Roesler et al., 2000). From full-scale experiments on airport concrete slabs on grade Roesler et al. (2005) found that concrete slab fatigue curves were not unique and depended on the specific boundary conditions and slab geometry tested. Moreover, it was concluded that for high stress ratios, the subgrade soil support condition changed progressively, which overshadowed the effect of stress range on concrete slab fatigue resistance.

### Material properties

In the present study normal plain concrete and high quality cement bound granular mixtures, i.e. a  $C_8/10$ -material (BS, 2013), commonly applied in port and industry concrete and composite pavements, are of primary interest. However, whereas concrete mixtures are dense, where aggregates are completely bonded by the cement paste, as shown in Figure 1.6 (a), cement bound granular mixtures are less dense and aggregates are bonded by weaker cement links, as shown in Figure 1.6 (b), resulting in a somewhat lower strength.

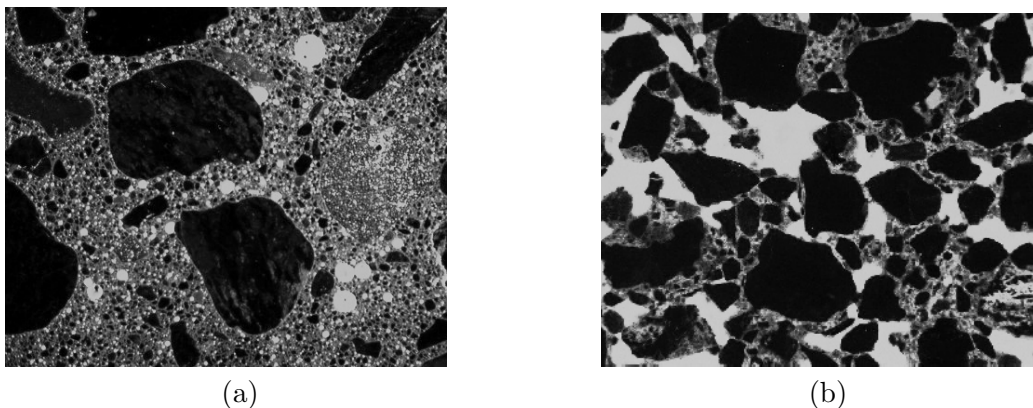


**Figure 1.6:** Thin section: (a) normal concrete and (b) cement bound granular mixture.

These materials are composed of the same constituents, as shown in Table 1.1 and Figure 1.7.

**Table 1.1:** Material mixture and mechanical properties for CBGM  $C_{8/10}$ -material and plain concrete. Typical values.

<i>Material properties</i>		CBGM	Concrete
Sand (0.1-4 mm)	(%)	45	70
Gravel (4-32 mm)	(%)	55	30
Maximum stone size, $D_{max}$	(mm)	16-32	8-32
Cement content	(%)	5.0	15.0
Water-Cement ratio	(-)	1.0	0.5
<i>Mechanical and fracture properties</i>			
Young's modulus, $E$	(GPa)	15	30
Poisson's ratio, $\nu$	(-)	0.20	0.15
Tensile strength, $f_t$	(MPa)	1.0	3.0
Compression strength, $f_c$	(MPa)	10	30
Fracture energy, $G_F$	(N/mm)	0.035*	0.150

\*Note: predicted based on Hilsdorf and Brameshuber (1991)

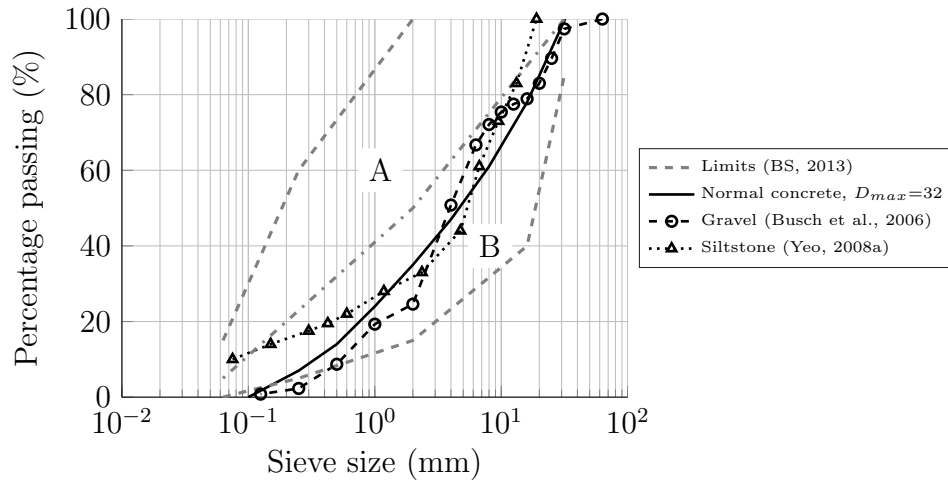


**Figure 1.7:** Grading curves for high quality (envelope 'B') CBGM-materials according to BS (2013) (gray) compared to CBGM materials and standard concrete considered in the present study.

The quasi-brittle nature of concrete (Kaplan, 1961; Shah and McGarry, 1971; Shah et al., 1995; Bažant, 2002) and cement bound granular mixtures (Otte, 1978; Balbo, 1997) have been recognised for many years and is usually characterised by having a tensile load-deformation response as illustrated in Figure 1.8 (a) with a long post-peak tensile softening response.

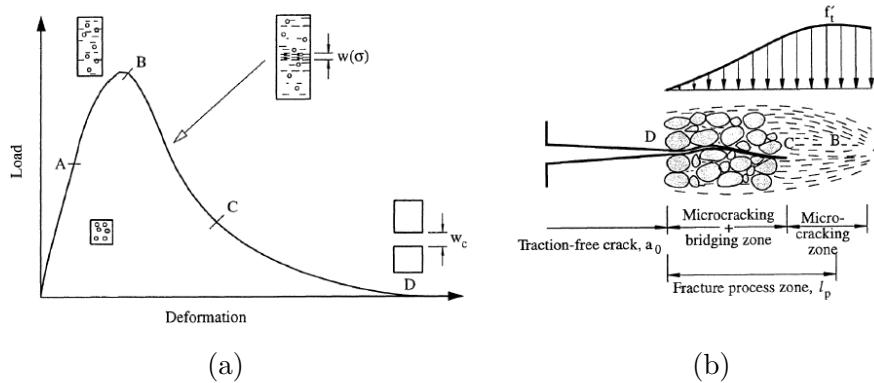


**Figure 1.8:** (a) Typical tensile load-deformation response for a concrete specimen; (b) illustration of the fracture process zone around the traction free crack. From Karihaloo (1995).

For an increasing tensile load the elastic behavior changes to a non-linear response (A) and the loading results in the formation of micro-cracks. At some point after the peak, during the tensile softening region (BC) the micro-cracks coalesce into the formation of a macro-crack. A continued opening will primarily open the now established macro-crack. For a single crack the crack evolution is shown in Figure 1.8 (b), relating the micro-cracking and bridging over the crack as a consequence of e.g. aggregate interlock to the different crack opening stages (A-D).

## Summary

- (i) Field observations and large-scale experiments of concrete and composite pavements indicate that the two primary controlling structural failure mechanisms are initiation and propagation of cracks due to bending and the shear interaction of aggregate interlocking joints.
- (ii) Both monotonic and fatigue load response curves are influenced by the non-linear fracture behavior and slab geometry.
- (iii) The structural response is highly influenced by soil-structure interaction, especially for high stress ratios, i.e. close to ultimate loading state

and at the end of fatigue life.

- (iv) Based on material composition and characteristics it is deemed reasonable to treat the differences between concrete and high quality cement bound granular mixtures as a difference in mechanical material properties applying the same constitutive model.

### 1.3 Constitutive crack model

Cohesive zone modeling (CZM) is one of the primary methods to handle discrete crack propagation in diverse types of materials. This concept was introduced by Barenblatt (1959) and Dugdale (1960) in order to address the stress singularity at crack tips. In these models, all non-linearities take place in a cohesive zone ahead of the main crack tip, which is associated with the physical fracture process zone  $l_p$  of the material, see Figure 1.8 (b).

The first non-linear fracture mechanics model for cemented quasi-brittle materials is named the fictitious crack model (FCM) developed by Hillerborg et al. (1976). The fictitious crack model relies upon the smooth crack closure eliminating the energy dissipation at the crack tip. The term fictitious is used to underline the fact that ahead of the real, stress free crack, an artificial crack is supposed to be present and to transfer certain stresses causing the smooth crack closure. The fictitious crack model was first introduced in design of concrete pavements by Bache and Vinding (1990).

Initiation and propagation of cracks is assumed to take place in pure opening (*Mode I*), perpendicular to the largest principal stress. In the fictitious crack model the tensile load-deformation response for concrete displayed in Figure 1.8 is divided into a linear elastic part and a tensile softening part, as shown in Figure 1.9.

The fictitious crack model assumes that the traction stress is purely a material property, independent of specimen geometry and size. The linear elastic part is characterised by the Young's Modulus,  $E_c$ , and the tensile strength  $f_t$ . The softening part is described through  $f_t$ , the fracture energy  $G_F$ , and the critical crack opening  $w_c$ .  $G_F$  is the area under the softening curve whereas  $w_c$  corresponds to the crack opening at the end of the fictitious crack where the crack becomes stress free (point D in Figure 1.8). The softening response is often described through a bi-linear, power or exponential relation where  $f_t$  and  $G_F$  are usually kept constant between the relations and  $w_c$  varies.

Several researchers have argued that the shape of the softening curve significantly affects structural response, particularly local failure behavior

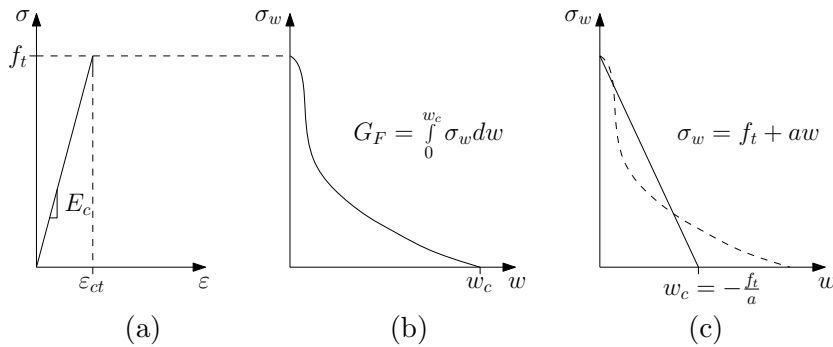


**Figure 1.9:** Splitting of the stress-deformation curve into (a) pre-peak elastic stress-strain relationship and (b) post-peak softening curve or stress-crack opening relationship. (c) defines a simplified linear softening as proposed by Hillerborg et al. (1976).  $G_F$  is the total fracture energy needed to produce a stress free crack.

(Pettersson, 1981; Gustafsson et al., 1985; Roelfstra and Wittmann, 1986; Alvarado and Torrent, 1987). Consequently, numerous different curve shapes have been proposed, see e.g. Shah et al. (1995). However, for the fracture analysis of slab on grade pavement structures, applying a simple linear softening curve does not influence the response significantly while significantly reducing the computation time (Gaedicke and Roesler, 2009; Aure and Ioannides, 2012).

The constitutive relation between crack opening and the normal stresses across the crack is well described through the fictitious crack model and related models. However, to get a complete and thorough description of the structural consequences of cracking in concrete structures, more advanced mixed-mode models have been proposed in the literature (Carol et al., 1997; Högberg, 2006; Nielsen et al., 2010; Jacobsen, 2012; Jacobsen et al., 2013). The mixed-mode models take into account the combination of crack-opening and crack-sliding (*Mode II*) after initiation of cracks. Thus, more complex cracking behavior, e.g. shear cracking, can be described with such a model.

Fatigue cracking is one of the major structural damage types and considered to be the primary mode of failure in pavements as described in Section 1.1. The cyclic behavior of cemented materials has mainly been studied subjected to fatigue loading in direct tensile, flexural or indirect tensile loading, see e.g. Cornelissen (1984). These types of experiments have typically been used to establish the before mentioned fatigue relationships and provide some information about the number of cycles to failure and the damage development. However, these tests do not distinguish between crack initiation and crack propagation period or elastic and inelastic work.

Slowik et al. (1996) stated that damage mainly occurs in the micro-cracked zone present at the tip of a crack. Moreover, the authors showed that peaks in the loading history enlarged the fracture process zone and accelerate fatigue crack propagation. This observation confirms the importance of studying cemented material behavior after crack initiation and damage that occurs in the fracture process zone, i.e. deterioration of the aggregate bridging stress during cyclic loading. Thus, experimental results from deformation controlled uni-axial testing are required in order to distinguish between the different phenomena and phases occurring during fatigue crack growth.

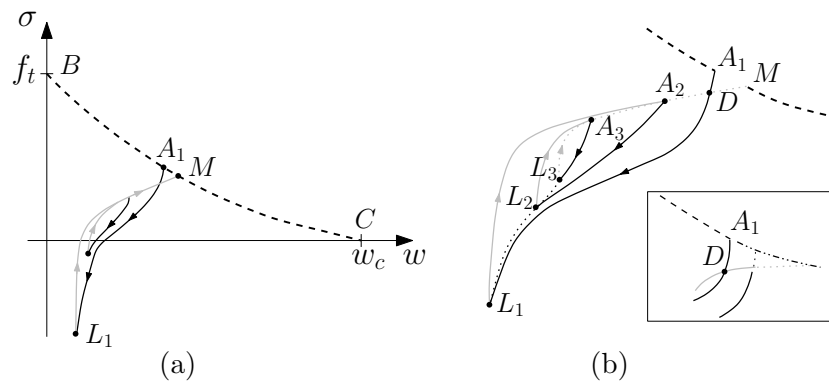


**Figure 1.10:** Cyclic behavior of concrete: (a) monotonic cohesive law (dashed black), unloading (gray solid) and reloading (black solid). (b) Unloading and reloading loops according to the continuous function model proposed by Hordijk (1991).

Deterioration of aggregate bridging stress on plain concrete under cyclic uni-axial tension was investigated experimentally by Gylltoft (1983), Gopalaratnam and Shah (1985), Reinhardt et al. (1986), Hordijk (1991), Plizzari et al. (1997) and Kessler-Kramer et al. (2001). Zhang et al. (1999, 2000) performed similar experiments on plain and fiber reinforced concrete. This work resulted in several analytical stress-based models for low-cyclic analysis (Yankelevsky and Reinhardt, 1987; Plizzari et al., 1997), including the continuous function model proposed by Hordijk (1991), shown in Figure 1.10. Zhang et al. (2001) developed an empirical fatigue law based on experiments reported in Hordijk (1992).

Elias and Le (2012) applied the cyclic cohesive zone model proposed by Nguyen et al. (2001) to simulate the tension regime in *Mode I* crack growth in quasi-brittle structures under compressive fatigue. In such cyclic cohesive models, irreversible damage accumulation is controlled by an explicit damage evolution equation where an endurance limit can be incorporated (Nguyen

et al., 2001; Yang et al., 2001; Roe and Siegmund, 2003; Xu and Yuan, 2009; Roth et al., 2014). While in monotonic cohesive zone models the damage state is uniquely defined by the maximum separation attained during the loading history, cyclic cohesive zone models need a more general damage variable. In the literature, stiffness-type (Nguyen et al., 2001), separation type (Yang et al., 2001) and micro-mechanical motivated damage variables (Roe and Siegmund, 2003) are suggested. For visualisation purpose, Ortiz and Pandolfi (1999) proposed an energy based conversion of a separation-type damage variable into the range between zero and one.

### Summary

- (i) Several constitutive crack models for concrete materials have been proposed in the literature, primarily focusing on the monotonic softening behavior of the material.
- (ii) For pavement slab on grade structures the softening curve does not influence the response significantly.
- (iii) Few unified mechanical cyclic crack models for cemented materials have been published in the literature; models typically suitable only to low-cyclic loading or are based on empirical methods with limited capabilities.
- (iv) There is a need for general models - linking the different crack behavior, i.e. monotonic, low-cycle and fatigue, enabling the possibility for analysis of complex arbitrary load cases.
- (v) An energy based approach for damage evolution in cyclic cohesive zone models seems promising for numerical analysis of fatigue crack growth phenomena.

## 1.4 Numerical methods for crack modeling

The establishment of a detailed computational model can be divided into a number of steps, as shown in Figure 1.11. First, there is the realisation of the need for a model, here triggered by the observations presented in Section 1.1 and 1.2. From the experimental knowledge the constitutive behavior may then be sought explained through a suitable theory as discussed in Section 1.3.

Dependent on the character of the problem to be modeled, a suitable numerical tool may be developed before the constitutive relation can be used

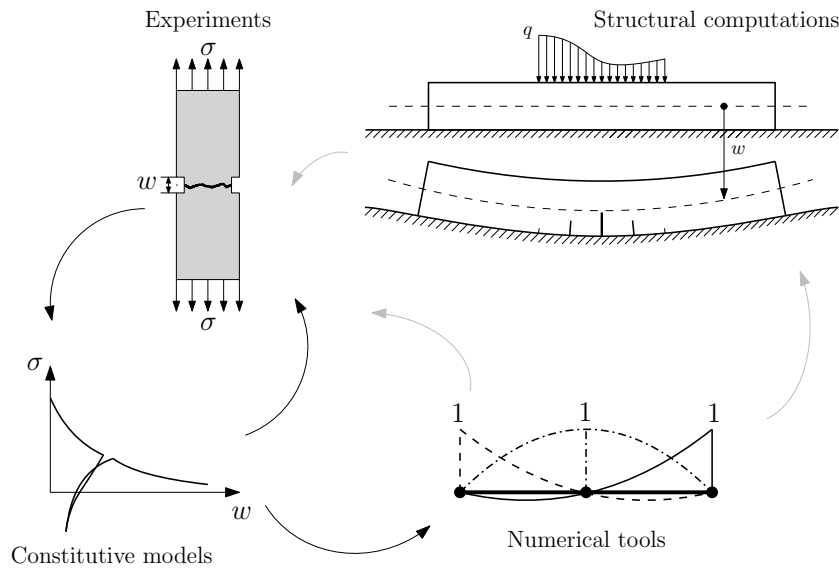


**Figure 1.11:** The process of developing a detailed computational model for structural analysis with relation to experiments, theoretical framework and numerical tools.

to model the structural behavior. On the other hand, the available numerical tools may also dictate the framework in which the constitutive model is formulated. Often the numerical tool is established in relation to the FE method, also selected for the present study, due to its capability of solving a wide variety of engineering problems and as it is currently one of few widely accepted numerical tools used by design engineers.

The heterogeneous nature of cemented material shown in Figure 1.8 can be modeled at the micro-scale, but in terms of computational resources a micro-scale model, modeling aggregates, mortar and interlayer, is very demanding with regard to computational power. In the modeling of real size structures, it is therefore advantageous to use a macro-scale model where the cemented material can be considered as homogeneous and for instance include the micro-cracking effects in the larger cracks through the constitutive description. Typically, at the structural scale, the cemented material is considered as a homogeneous material and the softening law depicted in Figure 1.9 (c) does not distinguish if the bridging stress originates from micro-cracking, in pure cement paste, aggregates debonding, crack branching or other effects; the softening law describes its averaged resulting actions on the current material scale only.

Not only will the heterogeneous nature of the cemented material exhibit softening behavior in tension locally, but also on a structural level concrete

and composite pavements will exhibit softening, or so-called snap-back type of load-displacement response. This type of localised fracture behaviour can be described numerically with different classes of constitutive models, e.g., those proposed by Jirásek (2001) as; (i) strong discontinuity models, (ii) weak discontinuity models, and (iii) continuum models. The first model considers a crack as a geometrical discontinuity, whereas the latter two approaches imagine a cracked solid to be a continuum.

### Discontinuity models

The discontinuity models, e.g. the fictitious crack model, embedded elements with strong discontinuities and the extended finite elements (XFEM), incorporate jumps in displacements across a discontinuity surface corresponding to the crack.

The cohesive zone models have typically been used with FE modeling in conjunction with interface elements (Needleman, 1987; Tvergaard and Hutchinson, 1992; Camacho and Ortiz, 1996). Here cohesive elements are defined at the edges (interface) in a pre-determined path between standard finite elements to initiate cracks and propagate them following the deformation process. Methods inserting interface elements once the bulk material reaches the cohesive strength of the material have, also been used in the literature (Camacho and Ortiz, 1996; Oliver, 1996). However, the computational cost and data structure management for these models have currently restricted their application to more simple problems.

Other methods have also been used to describe fracture growth without a pre-determined path such as the embedded formulations, see e.g. Jirásek (2000). With embedded crack models, strain or displacement discontinuities are embedded into standard finite elements. In the extended finite element method proposed by Belytschko and Black (1999) and Moës et al. (1999) an enrichment of the elemental basis functions allows the displacement field to be decomposed into a continuous and a discontinuous part. The discontinuous part can then represent a discontinuity like a crack in a discrete manner where the direction of the crack and the crack propagation are independent of the element mesh. With the use of the extended finite element method cohesive opening-mode cracking in concrete has been considered by e.g. Asferg et al. (2007) and mixed-mode cracking by Mougard et al. (2010). The extended finite element method seems to be an effective tool for modeling concrete structures, however, the elemental enrichment results in extremely complex and demanding data structure management. To overcome this problem Olesen and Poulsen (2013) proposed to use an alternative formulation of the embedded element with an discrete crack, taking advantage of the direct

formulations developed within XFEM.

For fracture analysis of concrete pavements cohesive interface elements have primarily been used with some very encouraging results, considering both plain concrete (Ioannides et al., 2006; Gaedicke and Roesler, 2009; Gaedicke et al., 2012; Aure and Ioannides, 2012; Evangelista et al., 2013; Aure and Ioannides, 2015b) and fiber reinforced concrete (Meda et al., 2004; Sorelli et al., 2006; Belletti et al., 2008). In these models the fracture process, built-in traction separation based cohesive elements was inserted along the anticipated fracture plane in the concrete slabs in the orthogonal directions as per Meda et al., see Figure 1.12.

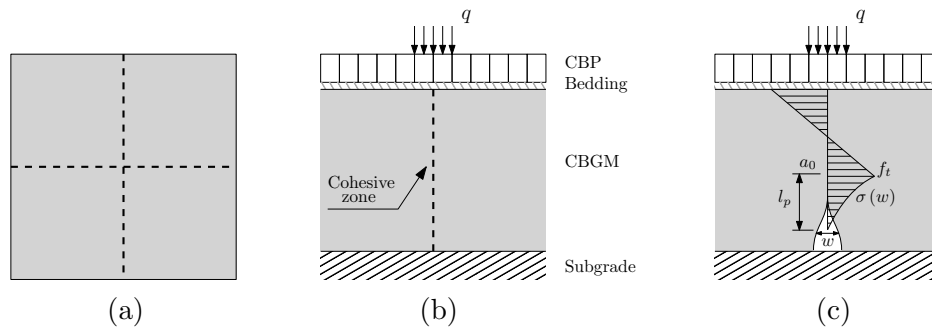


**Figure 1.12:** Sketch of cohesive zone model implemented in pavement structure: (a) plan overview of orthogonal fracture planes for interior and edge loading. (b) cross section of block pavement structure showing the cohesive zone. (c) the fictitious crack model, where  $a_0$  is the crack tip,  $l_p$  is the fracture process zone (FPZ),  $f_t$  is the tensile strength,  $w$ , is the stress free crack opening and  $\sigma(w)$  the cohesive softening law.

Moreover, cohesive zone modeling seems like an attractive method to describe the fracture behavior of cement bound granular mixtures, see e.g. Liu and Wang (2008); Zaman et al. (2009); Yeo et al. (2012).

## Continuum models

Models with localisation bands bounded by weak discontinuities can be considered as simple regularisations of models with strong discontinuities, e.g. the smeared crack model. In smeared crack models (Rashid, 1968; Bažant and Oh, 1983; De Borst and Nauta, 1985) the cracking in a given material point is the result of the micro-cracking and macro-cracking in a given volume surrounding the point. The smeared approach is often used in relation to the crack band model (Bažant and Oh, 1983). The smeared models tend to show some mesh dependencies and the smeared manner makes it difficult

to interpret the actual crack width and the exact location of a macro-crack in an element.

Instead of splitting the constitutive law into elastic and inelastic parts, one could use a law that directly links the stress to the total strain, which is the case for continuum models. Subsequently several models have been developed to describe the complicated fracture process in quasi-brittle materials, e.g. by coupling damage and plasticity (Mazars, 1986; Lubliner et al., 1989; Maekawa et al., 1993; Lee and Fenves, 1998; Nguyen, 2005; Grassl et al., 2013). However, these models suffer another drawback; as their implementation is complex, they often poses numerical challenges, are computationally expensive and generally require a large number of model parameters. Moreover, special laboratory tests are often needed to determine model parameters, making them less attractive for routine design purposes.

A simplified method combining the advantages of discontinuous approach, avoiding many numerical problems such as mesh dependency, combined with the continuum approach was proposed by Olesen and Poulsen (2012) using a cohesive hinge. In this method the underlying description is based on the formation of discrete cracks, i.e. according to Ulfkjær et al. (1995); Olesen (2001b), whereas the constitutive behavior of the hinge is smeared (smooth).

## Summary

- (i) Cemented materials exhibit softening behavior in tension on both the local and the structural level. No reinforcement is present to significantly increase the ductility and preventing a sudden collapse of pavement slabs, thus stable numerical methods are required.
- (ii) The discontinuous crack models have the advantage that they are relatively simple and numerically stable. However, to avoid heavy data structure management, their simplicity rely on the fact that interface elements are inserted in finite element models a-priori.
- (iii) Continuum models are able to capture the changes in stresses and stiffness during progressive cracking. However, their implementation is complex, they often poses numerical challenges, they are generally computationally expensive and require a large number of model parameters.
- (iv) Although unproven to analysis of pavement structures, or complex structures in general, the finite element hinge model seems like a promising method. This method combines some of the advantages of the discontinuous and the continuum approach.

## 1.5 Soil-structure interaction model

It is evident from the literature reviewed in Section 1.1 and 1.2, that the soil foundation properties are among one of the main parameters influencing the response of concrete and composite pavement systems. It is an important consideration to account for the ductility exhibited by concrete in rigid pavement design, but this property is not exclusively a material property, because it is affected considerably by the entire structural system as well (Bache and Vinding, 1990). Thus, the interaction between soil and structure should be evaluated as part of the process in the development of a mechanical model for engineering design purposes.

In geotechnical engineering a large proportion of research activity has been devoted to the development of stress-strain-time relationships for soils which exhibit non-linear and irreversible processes using continuum mechanics, see e.g. Puzrin (2012). These generalised constitutive models have been successfully applied to the examination of fundamental phenomena encountered under test conditions. However, such models are typically very complex and require a large number of model parameters. Further, taking into account the variety of soils and soil conditions encountered in engineering design, their applicability to soil-structure interaction problems represent difficulties (Selvadurai, 1979).

In order to reduce the complexity and size of numerical models, idealisation of the soil behavior is necessary, e.g. by employing the classical theories of elasticity and plasticity. For routine design purposes in pavement and geotechnical engineering Winkler's idealisation (Winkler, 1868) has been used almost exclusively (Horvath, 2002). However, care should be taken in application of such a model as it essentially suffers from a complete lack of continuity in the supporting medium, see Figure 1.13 (a).

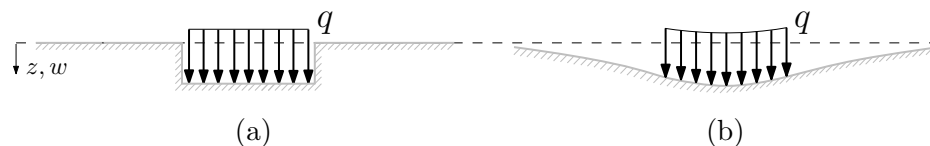


**Figure 1.13:** Response of (a) Winkler foundation model, consisting of independent springs, versus (b) elastic continuum model.

It is common experience, in the case of soil media, that surface deflections will occur not only immediately under the loaded region but also within certain limited zones outside the loaded region, see Figure 1.13 (b). In attempts to account for this continuous behavior, soil media have often been idealised as three-dimensional continuous elastic solids or elastic continua. The first continuum representation of soil media stems from the work of Boussinesq

(1885), who analysed the problem of a semi-infinite homogeneous isotropic linear elastic solid subjected to concentrated force which acts normal to the plane. The basic Boussinesq solution can be used to obtain the response function for the three dimensional elastic soil medium. Boussinesq solution can be simplified to the two-dimensional case by making use of Flamant's problem for a line load acting on the surface of a half-space, see e.g. Timoshenko et al. (1970). Such isotropic elastic continuum models can be employed effectively in the analytical treatment of soil-structure interaction problems.

The deficiency of the Winkler model in depicting the continuous behavior of real soil masses and the mathematical complexities of the elastic continuum has led to the development of many other simple soil response models. These models possess some of the characteristic features of continuous elastic solids, however, they represent the upper boundary of the soil-structure interface and are primarily intended for modeling of the response of soil media and not of the response of an element within the soil medium. This class of mathematical models has an additional constant parameter and hence, the models are called two-parameter foundation models.

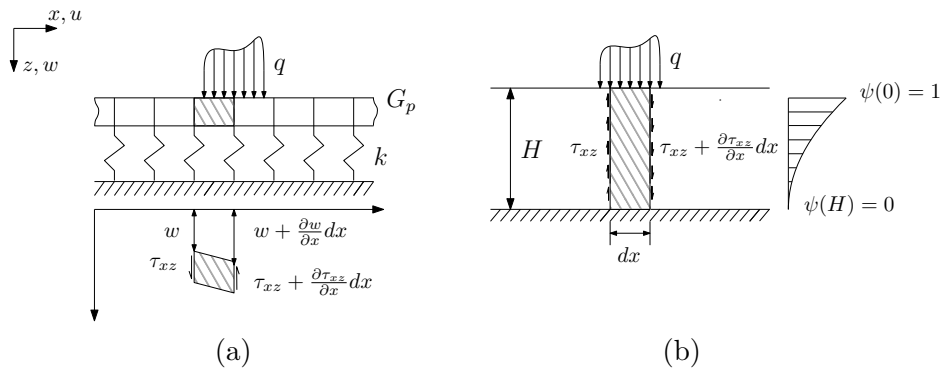


**Figure 1.14:** (a) Mechanical spring model with elastic layer capable of pure shear deformation proposed by Pasternak (1954). (b) Simplified elastic continuum model proposed by Vlasov and Leontev (1960).

The development of two-parameter models has been approached along two distinct lines. The first proceeds from the discontinuous Winkler model and eliminates its discontinuous behavior by providing mechanical interaction between the individual spring elements, see Figure 1.14 (a). The second approach starts from the elastic continuum model and introduces constraints or simplifying assumptions with respect to the distribution of displacements and stresses, see Figure 1.14 (b).

Two-parameter models for design of concrete pavement systems have been studied by Ioannides et al. (1985a) and Khazanovich and Ioannides

(1993), followed by implementation of such models in several special purpose FE-tools for rigid pavement design (NCHRP, 2003). Moreover, two-parameter models have been used to study complex phenomena occurring in rigid pavements, such as slab-curling (Khazanovich and Ioannides, 1994; Khazanovich, 2003; Zokaei-Ashtiani et al., 2015) and layer contact problems (Zokaei-Ashtiani et al., 2014). Lin and Folias (1975) studied the influence of the two foundation parameters on a finite surface crack and Jones (1978) developed expressions for incorporating the effect of the foundation properties on the transverse shear stresses of the cracked face. Ramsamooj (1993) extended these type of models to include the influence from moving vehicle loads, but only recently, effective numerical tools for stress fields in cracked layered elastic pavement systems have been developed, see Chabot et al. (2005) and Nasser and Chabot (2015). However, the influence of two-parameter models, or soil-idealisation techniques in general, for analysis of crack propagation and crack growth, has drawn little attention.

## Summary

- (i) Application of generalised continuum models to solve soil-structure interaction problems are difficult taking into account the variety of soils and soil conditions as well as complex material behaviour in an efficient manner.
- (ii) Mechanical two-parameter foundation models have been effectively employed in analysis of soil-structure interaction problems in pavement and foundation design.
- (iii) Two-parameter models represent the upper boundary of the soil-structure interface and are primarily intended for modeling of the response of soil media and not the response of an element within the soil medium.
- (iv) Although two-parameter models may be extended to account for non-linear behavior of the soil they are not capable of describing yielding which accompanies the formation of slip-lines.
- (v) The influence of using two-parameter models, or soil-idealisation techniques in general, for analysis of slab fracture, has drawn little attention.

## 1.6 Objectives of the thesis

As discussed in the introductory part of this Chapter, the use of M-E approaches for design of heavy duty pavements, and pavement structures in general, has limited capabilities. The M-E method cannot account for significant factors influencing the response, e.g. describing the interactions between loads, material properties, geometry and soil-structure interactions in a unified manner.

In order to move a step towards a more generalised structural design method for analysis of heavy duty pavements, this study aims at developing a mechanistic approach based on constitutive models. This allows for geometry, non-linear cemented material behavior and interactions with other material layers. Thus, the performance are evaluated as a part of the solution procedure using appropriate numerical methods.

### Objective 1

In the M-E method fatigue and monotonic behavior, i.e. ultimate loading state, is badly linked, making a complete structural analysis of heavy duty pavements a difficult task. Moreover, the influence from multi-dimensional geometry, soil-structure interaction and other boundary conditions are often neglected. Thus, the first objective of this thesis is to

- (i) develop a simple framework for numerical simulation of a cement bound granular base layer in composite block pavement systems subjected to monotonic loading.

This model is used to demonstrate the applicability of a cohesive zone model to describe the fracture behavior in cement bound granular materials in composite pavements.

### Objective 2

Numerical analysis of the fracture behavior in real-scale concrete and composite pavement systems is complex and does often possess numerical issues, such as instability problems and aborted simulations. Moreover, the soil-structure interaction models applied are often too complex or over-simplified. Thus, the second objective of this thesis is to

- (ii) introduce a simple methodology and numerical tool which significantly reduce the complexity in pavement analysis of cemented material fracture.

This model is used to evaluate and demonstrate the use of a cohesive cracked-hinge model for pavement applications, as well as study the influence from different mechanical soil-structure interaction models on the fracture behavior of cemented one-way slabs on grade.

### Objective 3

Whereas several constitutive models have been developed for low-cyclic damage of cemented materials, few published models create the required link between low-cyclic and high-cyclic damage. Moreover, the models developed are typically used to simulate one type of test or one simplified problem. Thus, all the different components in Figure 1.11 are seldom addressed in relation to each other. This often results in complex models with limited capabilities in context of design for engineering applications. Thus, the third and final objective of this thesis is to

- (iii) extend the framework developed to account for unloading of cracks, cyclic loading, and fatigue damage of the cemented material.

These models are used to evaluate standard fracture tests reported in the literature, e.g. simply supported beam tests and beams resting on soil.

## 1.7 Outline of the thesis

This thesis consists of two main parts; Introduction and Summary (Part I) and the Appended Papers (Part II). The different chapters in Part I and the papers in Part II overlap. Each chapter presents a brief overview of the work carried out with the main research findings detailed in the papers. The work is concluded in Chapter 6.

To give the reader an overview of where the different subjects are detailed, the organisation of the thesis is given in Table 1.2. The column to the right indicate which subjects are covered in which paper.

**Table 1.2:** *Organisation of thesis.*

<i>Chapter</i>	<i>Subject</i>	<i>Paper</i>
1	Introduction	
	Modeling framework	
2	Concrete block pavement model	
	Detailed analysis of the 3-D cohesive model	Paper I
	The cohesive cracked-hinge model	Paper II
3	User-built finite element code	
	3-D cracked-hinge model	
	Evaluation of soil-structure interaction models	
4	One-way slab resting on elastic continuum	Paper II
	Evaluation of methodology	
	Development of the fiber cracked-hinge model	Paper III
5	Low-cyclic tensile damage model	Paper III
	Energy based fatigue model	
6	Conclusion	
A	Appendices	



# Chapter 2

## 3-D cohesive finite element model

### 2.1 Introduction

Concrete block paving is in many regions the preferred surfacing material in container terminals because it combines the benefits of the durability of concrete with the flexibility of asphalt. Typically, the block pavers are applied over a stiff cemented base layer to resist the heavy static loads from containers, see Figure 2.1.

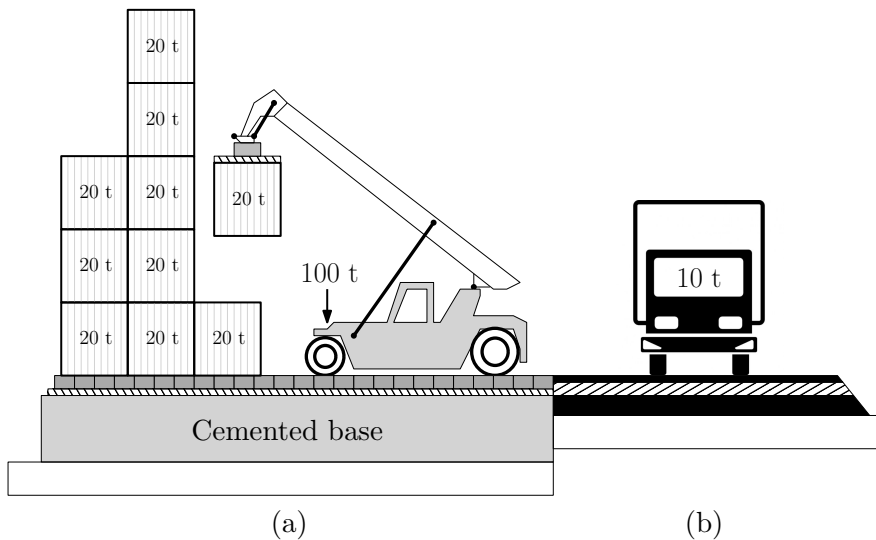


**Figure 2.1:** Sketch of pavement systems showing some typical axle loads and container loads ( $t = \text{ton}$ ): (a) Heavy duty composite concrete block pavement and (b) Typical highway asphalt pavement.

The inability of presently available design methods to realistically capture the monotonic behavior of pavement structures, i.e. ultimate loading state, makes a complete structural analysis of heavy duty pavements a difficult task. Moreover, the influence from geometry, soil-structure interaction and other boundary conditions are often neglected. To increase the versatility and improve existing methods, this chapter presents a 3-D cohesive finite element model for numerical analysis of the fracture behaviour of cement bound granular mixture in composite concrete block pavement systems.

## 2.2 Modeling framework

### Model idealisations

Analysis of a three-layered composite pavement structure is considered; concrete block pavers, cement bound granular mixture and subgrade soil, see Figure 2.2. In order to obtain models that are efficient for routine design purposes in a satisfying way, a certain amount of idealisation is applied in the FE model.

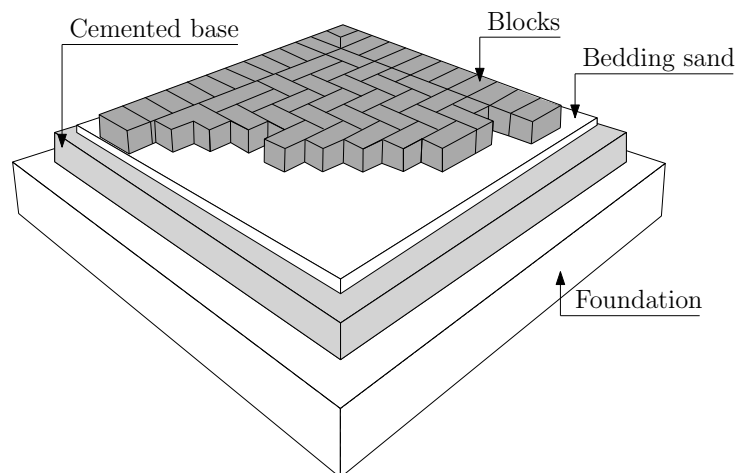


**Figure 2.2:** Sketch of simplified 3-D composite block pavement system considered in the present study.

The pavement structure is modeled as slabs on grade for evaluation of interior, edge and corner loading, assuming that the slabs are intact before monotonically loaded. Square slabs of  $2.5 \times 2.5 \text{ m}^2$  to  $4.5 \times 4.5 \text{ m}^2$ , dimensions commonly applied in port and industrial pavements, are considered. The interaction between the cemented slab and concrete block pavement surface

and soil is treated using different numerical strategies, e.g. FE sub-models and simplified mechanical models described in the subsequent sections.

A simple Winkler's idealisation for describing the soil-structure interaction is suggested. However, this method has limited capabilities, and to adequately capture the influence of the soil properties on experimental curves as demonstrated in Section 2.4, the FE model has been extended to account for the stress distribution in a linear elastic continuum using elastic solid elements. Moreover, the continuum model is extended to account for elastoplastic behavior applying a Mohr-Coulomb yield criterion, see e.g. Puzrin (2012). In the subsequent sections these three types of idealised soil-structure interaction models are referred to as the 'Winkler', 'Elastic' and 'Plastic' model, respectively.

## Cohesive zone modeling

### Failure mechanism

The limited capabilities of empirical and M-E methods has led to introduction of others, e.g. the yield-line theory, typically used for design of reinforced concrete slabs on grade (Johansen, 1955; Losberg, 1961, 1978; Baumann and Weisgerber, 1983) and steel fiber reinforced concrete slabs on grade (Silfwerbrand et al., 2000; Silfwerbrand, 2001; Meda, 2003). As load is applied to a concrete slab, certain sections experience bending moments equal to the plastic moment capacity of the section. Increasing the applied load results in plastifying more sections and eventually, through a number of yield lines, a collapse mechanism is formed. Plastic analysis by the yield-line considers large, plastic rotations occurring along lines where reinforcement has yielded.

The yield-line theory is applied for design evaluation of ultimate load capacity. Moreover, yield-line mechanisms can be used to predict the expected fracture pattern in slabs on grade and used in conjunction with discrete crack models within the FE method, i.e. cohesive zone modeling. Cohesive zone modeling has been extended to practical problems for concrete pavement structures or so-called slab on grade structures, applying cohesive interface elements, with some very encouraging results as mentioned in Section 1.4.

Meda (2003) compared a cohesive zone model with the yield-line theory and Westergaard's solution, for determining the ultimate loading-carrying capacity of concrete slabs on grade subjected to an interior point load, see Figure 2.3 (a).

From Figure 2.3 (a) it is observed that Westergaard's solution yields overly conservative designs, as it was reported that the cohesive zone model predicted the peak-loads of experimental curves with a 10% margin. It is

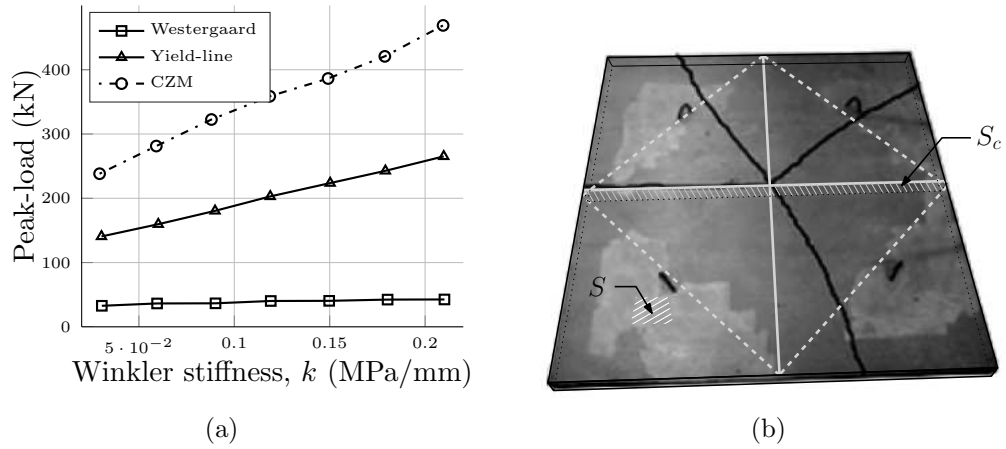


**Figure 2.3:** Slabs on grade under interior loading: (a) Comparison between different methods to determine ultimate load capacity of slab ( $4 \times 4 \times 0.2$  m<sup>3</sup>) for varying soil stiffness  $k$  (Meda, 2003). (b) experimental crack pattern (Sorelli et al., 2006) and fracture plane (solid gray) and axes of rotation (dashed gray) assumed in the yield-line method (Meda, 2003). Parameters  $S$  is the surface area (white tiled) and  $S_c$  is the cracked plane (gray tiled).

also noted that the increased stiffness of the structure from the support does not have any significant influence on the peak-load in Westergaard's solution. The difference between the yield-line method and the cohesive zone model is relatively constant around app. 1.5, indicating that the yield-line method gives a reasonable prediction of the ultimate load-carrying capacity, with a safe solution (Meda, 2003).

For the monotonic load case, considered here, the development of cracks is imagined to occur in a similar fashion as the yield-line mechanisms in the form of a straight separation band where the location is known in advance, i.e. considering *Mode I* fracture during crack propagation. For the fracture process, built-in traction separation based cohesive contact surfaces are inserted along the anticipated fracture plane in the cemented base layer (slab) in the orthogonal directions as, shown in Figure 2.3 (b). This is deemed a reasonable model at the edge and interior of the cemented base layer, since the fracture plane is anticipated in the direction of the maximum stress. This is also backed up by experimental results reported by Sorelli et al. (2006), see Figure 2.3 (b).

### Finite element description

For description of the fracture process the cohesive contact model, based on the fictitious crack model depicted in Figure 1.9 (c), in ABAQUS is selected

to save computational time; enabling the use of symmetry conditions and application of a coarser mesh for the cohesive zone. Moreover, as shown in Figure 2.4, the cohesive contact model is found to adequately describe the load-displacement response of slabs on grade reported by Aure and Ioannides (2012).

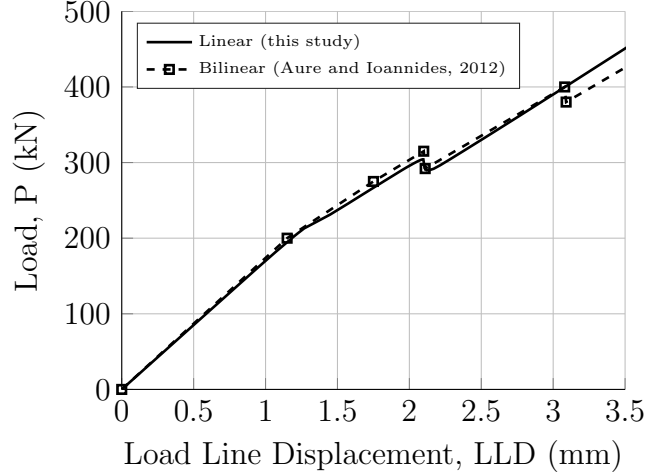


**Figure 2.4:** Comparison of load-displacement curves for interior loading of a rectangular concrete slab on grade ( $3 \times 6 \times 0.15 \text{ m}^3$ ), applying different modelling techniques in ABAQUS: cohesive contact (linear softening) and cohesive interface element (bi-linear softening) reported in Aure and Ioannides (2012), with element size of  $8 \times 15 \text{ mm}^2$  to  $8 \times 65 \text{ mm}^2$  and  $3.5 \times 3.5 \text{ mm}^2$  for the cohesive zone, respectively.

Based on the contribution to the variation in internal work,  $\delta\Omega$ , from the slab (elastic bulk material), the foundation, the cohesive zone and the potential work of external forces,  $\delta W$ , from point and surface loads, the principle of virtual work for the system in ABAQUS can be established

$$\int_V \delta \boldsymbol{\varepsilon}^T \boldsymbol{\sigma} + \delta \mathbf{u}^T k \mathbf{u} dV + \int_{S_c} \delta \mathbf{w}^T t dS_c = \int_S \delta \mathbf{u}^T \mathbf{f} dS + \sum_i \delta \mathbf{u}_i^T p_i \quad (2.1)$$

where  $V$  is the structural volume,  $S$  is the surface area,  $S_c$  is the cracked plane,  $\delta \boldsymbol{\varepsilon}$ ,  $\delta \mathbf{u}$ ,  $\delta \mathbf{w}$  is the strain, displacement and crack-opening displacement variations, respectively,  $k$  is the elastic stiffness of the foundation,  $\mathbf{f}$  is the surface traction vector,  $p_i$  is a concentrated (nodal) load and  $\delta \mathbf{u}_i$  is the associated (nodal) displacement variation.  $S$  and  $S_c$  is shown in Figure 2.3 (b).

The constitutive law for cohesive contact in ABAQUS (2013) is described in terms of contact stress and separation, i.e.  $t_n = F/A$  and  $w_n$  respectively, where  $F$  is the contact force and  $A$  is the current area at each contact point. Moreover, for cohesive surfaces the cohesive constraint is enforced at each slave node and not at material point. The traction stress vector,  $\mathbf{t}$ , consists of three components:  $t_n$ ,  $t_s$ , and  $t_t$ , which represent the normal and the two shear tractions respectively. The corresponding separations are denoted by:  $w_n$ ,  $w_s$ , and  $w_t$ . The elastic behavior can then be written as

$$\begin{bmatrix} t_n \\ t_s \\ t_t \end{bmatrix} = \begin{bmatrix} K_{nn} & K_{ns} & K_{nt} \\ K_{sn} & K_{ss} & K_{st} \\ K_{tn} & K_{ts} & K_{tt} \end{bmatrix} \begin{bmatrix} w_n \\ w_s \\ w_t \end{bmatrix} = \mathbf{K}\mathbf{w} \quad (2.2)$$

where  $\mathbf{K}$  is the nominal stiffness, also referred to as the penalty stiffness. In this study uncoupled traction is assumed, and thus the off-diagonal terms in the equation above are zero.

Following the onset of the crack and for as long as the strength of the cohesive zone exceeds that of the intact material, damage evolves based on the scalar stiffness degradation variable,  $\eta$ , defined as:

$$\eta = 1 - \frac{t(w)}{\bar{t}_n} \quad (2.3)$$

where  $t(w)$  is the contact stress for separation  $w$  along the softening curve,  $\bar{t}_n$  is the contact stress that would have corresponded to  $w$  had the pre-crack stiffness endured.

### Validation of the cohesive model

In order to verify the cohesive contact model, numerical analysis of a notched concrete beam under three point loading is carried out and compared to experimental and numerical results reported in Roesler et al. (2007) applying a bilinear softening law, see Figure 2.5 (a). Material and model parameters applied in the analysis is shown in Table 2.1.

Moreover, the model is tested to verify the functionality of the cohesive contact model to simulate the fracture behaviour of cement bound granular mixture beams under four point loading, see Figure 2.5 (b). Material and model parameters applied in the analysis is shown in Table 2.2.

From comparison of load-crack mouth opening displacement curves shown in Figure 2.5 (a), it can be observed that a good agreement with experimental

**Table 2.1:** Concrete beam geometry, average material properties and model parameters used in the numerical study of TPB tests carried out by Roesler et al. (2007)

	Roesler et al. (2007)	This study
Mesh size cohesive zone (mm)	2	2
Geometry (mm <sup>3</sup> )	700 × 150 × 80	700 × 150 × 80
Beam span (mm)	600	600
Element type(s)	CSP4 / UEL	CSP4
Young's modulus, $E$ (MPa)	32,040	32,040
Poisson's ratio, $\nu$ (-)	0.15	0.15
Penalty stiffness, $K_{nn}$ (MPa)	8,430,000	32,040
Tensile strength, $f_t$ (MPa)	4.15	4.15
Fracture energy, $G_F$ (N/mm)	0.164	0.164

**Table 2.2:** CBGM beam geometry, average material properties and model parameters used in the numerical study of FPB tests carried out by Yeo (2008a).

Geometry (mm <sup>3</sup> )	$E$ (MPa)	$\nu$ (-)	$f_t$ (MPa)	$f_c$ (MPa)	$D_{max}$ (mm)	$G_F$ (N/mm)
300 × 100 × 100	12,760	0.2	1.0	7.3	20	0.028

and numerical results reported in the literature can be obtained with the bi-linear contact softening law in ABAQUS. The difference in pre-peak behavior observed is related to the difference in penalty stiffness applied. Increasing penalty stiffness would reduce this difference. However, very high levels of penalty stiffness results in ill-conditioned stiffness matrix and thus slow convergence and aborted simulations with the contact model applied. It is also found from the load-displacement curves in Figure 2.5 (b), that adequately good fit is obtained between experimental and numerical results for cement bound granular mixture beams under four point loading.

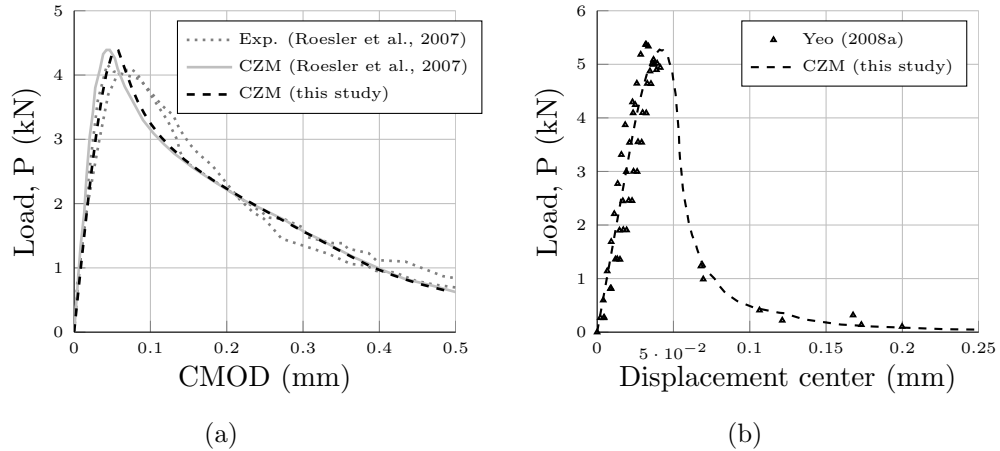


**Figure 2.5:** Comparison of results on simply supported beams: (a) Experimental and numerical study of plain concrete reported in Roesler et al. (2007) and the proposed cohesive contact model. (b) Experimental study of cement bound granular mixture material reported in Yeo (2008a) and the proposed cohesive contact model.

## 2.3 Concrete block pavement model

The FE method has an ability of treating discontinuities like cracks and joints in a rational way and has been employed for structural analysis of various types of pavements. For block pavements, several models have been proposed (Molenaar et al., 1984; Huben et al., 1984; Nishizawa et al., 1984; Nejad, 2003). Followed by a series of special purpose FE design tools for block pavement design (Huurman, 1994, 1996; Nishizawa, 2003; Moghadas Nejad and Shadravan, 2010; Gunatilake and Mamppearachchi, 2014). However, describing the geometry and interaction between concrete block pavers, jointing and bedding sand is demanding with regard to computational power. Moreover, the model geometry is complex resulting in time-consuming pre-processing of models. Thus, in the present study a simplified method is suggested for the description of concrete block pavers, placing unit displacements over an approximated area, i.e. the area of blocks in contact with the container corner casting (container footing), see Figure 2.6.

This is deemed to be a reasonable approach as the properties and thickness of the concrete block pavers do hardly influence the overall response and bearing capacity of the pavement structure (Huurman et al., 1992). Moreover, the loading from static loads, e.g. container corner castings, produce a close to rigid body movement of the stiff concrete block pavers over the soft layer of bedding sand, which is unable to absorb any significant bending

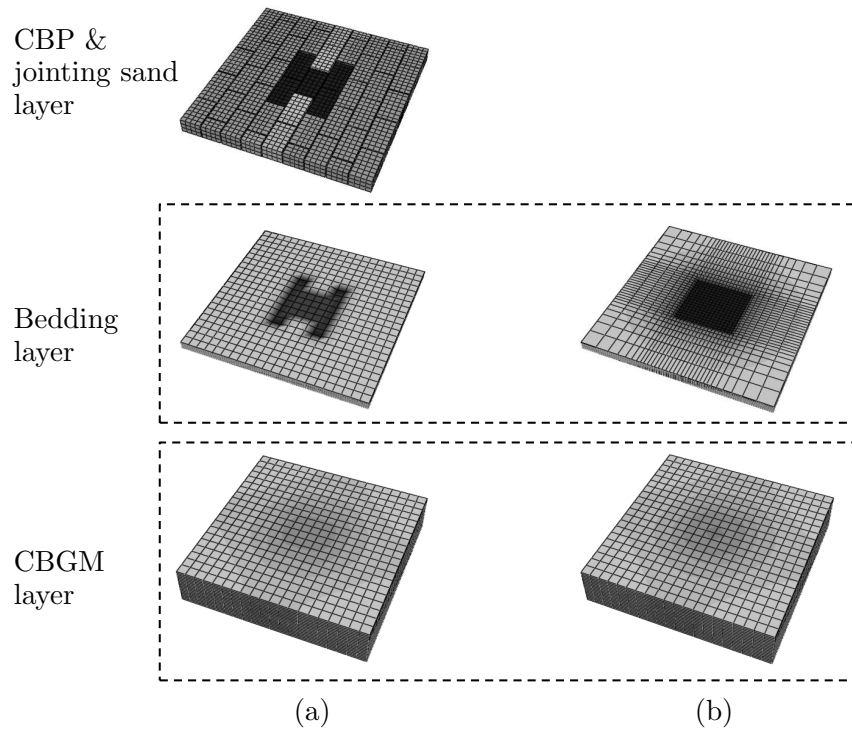


**Figure 2.6:** Surface displacements for the FE sub-model: (a) 'Complex' model considering both block, jointing- and bedding sand and (b) 'simplified' idealised model considering bedding layer only.

moments (Molenaar et al., 1984). The methodology proposed is validated creating two FE sub-models:

- (i) Figure 2.6 (a): 'Complex' FE sub-model representing the realistic pavement structure, considering concrete blocks, jointing- and bedding sand, including frictional contact between materials, subjected to a rigid load from container castings.
- (ii) Figure 2.6 (b): 'Simplified' FE sub-model, considering an equivalent distributed load, i.e. the area of blocks in contact with the container corner casting, on top of the bedding layer.

The complex FE sub-model is first validated against experimental and numerical results reported in Gunatilake and Mampearachchi (2014), applying the same material properties and geometry, to ensure satisfactory performance of the model. Then, this model is modified, exchanging the unbound granular base with a cemented bound granular mixture, for numerical evaluation of the different idealisation techniques (i) and (ii) above.

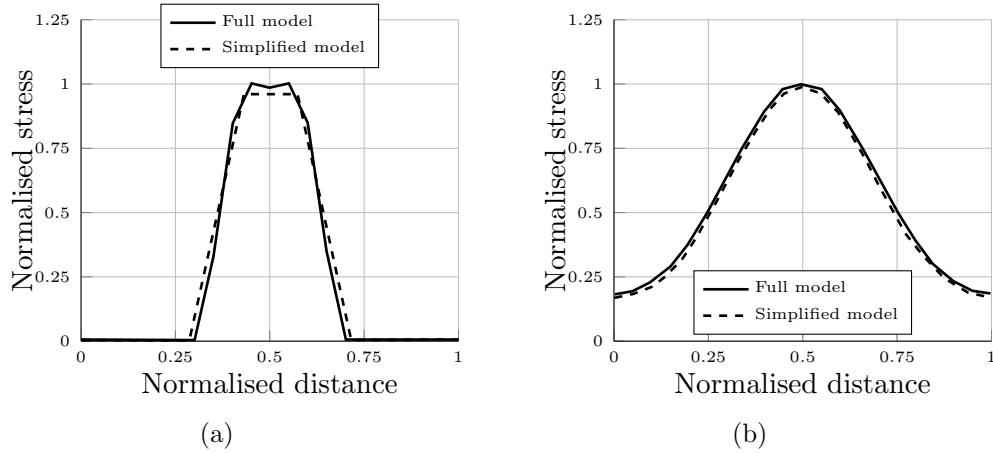


**Figure 2.7:** Comparative study evaluating the responses of a 'complex' and a 'simplified' CBP pavement: (a) normalised vertical stresses on top of the cemented base. (b) normalised maximum principal stress at the bottom of the cemented base. Normalised stress: normalised with regard to maximum value obtained in the 'complex' FE-sub model. Normalised distance: normalised with regard to the total width of the model.

It is observed from Figure 2.7 that adequately good results can be obtained with the simplified model for the response in the underlying cemented layer. Further simplification, omitting the bedding layer, is also possible. However, such simplification will affect the load-displacement response due to the relatively soft bedding layer compared to the cemented base.

## 2.4 Large-scale experiments

Numerical analysis of cement bound granular mixture slabs, shown in Figure 2.8, separated by aggregate interlock-or construction joints, on subgrade soil of 1.0 m clayey gravel material, is conducted in order to validate the methodology implemented, modeling the composite pavement as a slab on grade structure. The data was collected during the European Commission thematic network project ECO-serve (Busch et al., 2006) and was partly initiated in the attempt to evaluate the before mentioned M-E models. Detailed description of experimental data and the FE-model can be found in **Paper I**. Material parameters applied is shown in Table 2.3.

**Table 2.3:** Material properties used in numerical studies of large-scale experiments.

Material	$E$ (MPa)	$\nu$ (-)	$f_t$ (MPa)	$G_F$ (N/mm)	$k$ (MPa/mm)	$c_y$ (MPa)	$\varphi$ (°)
CBGM	12,300	0.2	0.96	0.037	-	-	-
'Winkler'	-	-	-	-	0.045	-	-
'Elastic'	350	0.35	-	-	-	-	-
'Plastic'	350	0.35	-	-	-	0.005	25-35

The success in the application of M-E models was modest at best, as no or little damage was recorded during each load cycle. To reduce the test time, the load was increased from typical equivalent standard axle load (ESAL) of 50-60 kN (per wheel) to 150 kN. However, to record damage development, the load was finally increased to 250 kN, which is likely to have caused excessive cracking in the cement bound granular mixture<sup>1</sup> and local yielding of the subgrade soil foundation below the plate load, correlating badly with the M-E models calibrated for highway pavement design.

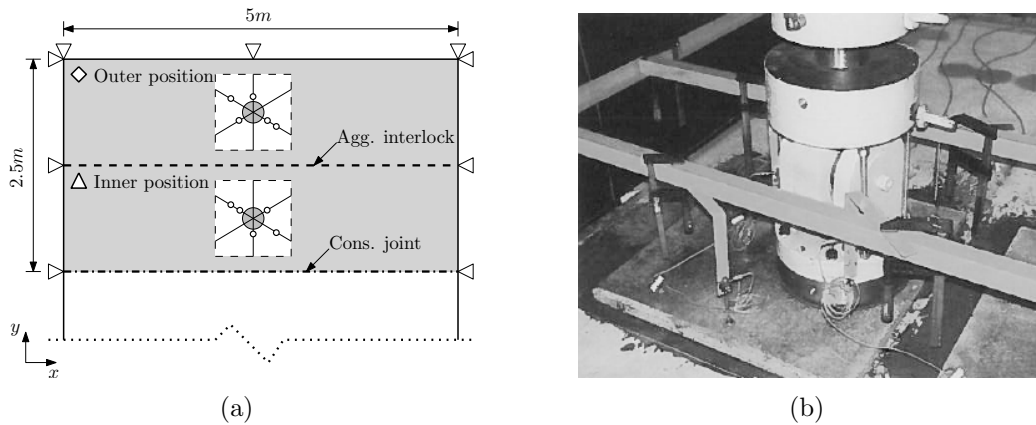


**Figure 2.8:** Layout of slabs, showing outer and inner loading position: (a) supports ( $x$ -axis:concrete wall,  $y$ -axis:steel wall) and the placing of displacement sensors. (b) picture of test set-up, showing the load configuration and the displacement sensors placed on top of a 35 mm thin asphalt plate.

From comparison between numerical and experimental load-displacement curves at a distance of 235 mm and 450 mm from the load centre, shown in

<sup>1</sup>Data recorded during and after tests were not adequate for evaluation of the fracture behavior of the cemented material.

Figure 2.9, it can be observed that a relatively good agreement is obtained between experimental and numerical results up to the peak-load for all three models. The peak-load is app. 157, 133 and 162 kN for the 'Elastic', 'Winkler' and 'Plastic' models, respectively. The experimental result shows a pronounced post-peak decrease in stiffness at a load level of app. 150 kN, probably due to local yielding of the subgrade soil. This behaviour can only be captured by the 'Plastic' model. Moreover, it is found that modeling the subgrade soil with elastic solid continuum elements results in a more realistic prediction of the peak-load compared to the 'Winkler' model. The influence of soil model type on local crack behaviour can be seen in Figure 2.10.

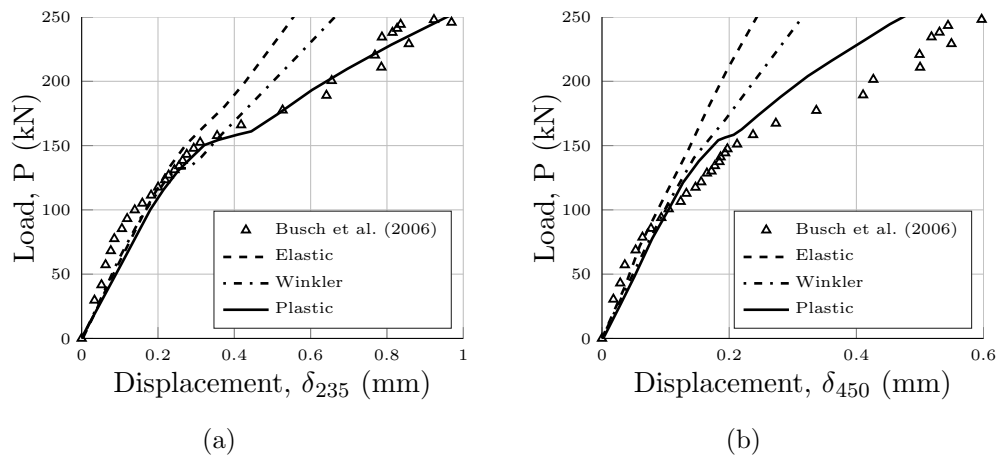


**Figure 2.9:** Comparison of experimental (five point average) load-displacement response obtained from data reported in Busch et al. (2006) and numerical results for the three selected soil models 'Winkler', 'Elastic' and 'Plastic' using a angle of internal friction of  $30^\circ$  for the latter model: (a) distance of 235 mm and (b) 450 mm from load centre, respectively.

From the load versus crack mouth opening displacement (CMOD) curve in Figure 2.10, it can be observed that cracks in both directions are initiated at load point 1. Damage of the cohesive crack then progresses towards the edges of the slab. At load level point 2, nodes at the bottom of the slab in length direction, i.e. along the y-axis in Figure 2.8 (a), has exceeded the final (zero stress) displacement. The cohesive zone then progress upwards until the 'snap' at load level point 3, resulting in the kink on the load-displacement curve in Figure 2.10. The crack in the width, i.e. along the x-axis in Figure 2.8 (a), remains stable in the width direction as shown in Figure 2.10 (b). Unloading on the load-displacement curve is prevented by the high stiffness of the subgrade soil and the geometry of the slab. At load level point 4, all

nodes in the length direction (y-axis) have exceeded the final displacement.

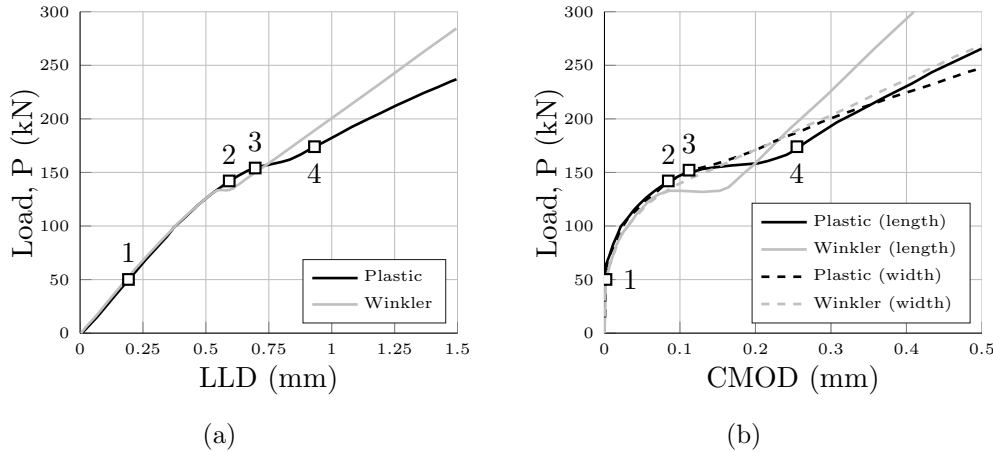


**Figure 2.10:** Presentation of numerical results for the 'Winkler' (gray) and 'Plastic' (black) soil model: (a) load line displacement (LLD). (b) load-CMOD curve for cohesive crack at the bottom of the slab under the load centre in the length and width direction.

The numerical results shown in Figure 2.10 can explain some of the observations made during the experimental investigations which couldn't be described by the M-E models. The most obvious observation is that the crack along the length (y-axis) has fully propagated at the applied load of app. 150 kN (load level point 3), indicating why no damage was recorded during experiments with repeated loads at this load level. Then, the response is controlled by further crack propagation along the width (x-axis) and the soil behavior. Moreover, it is observed that cracking is initiated at load level 1 of app. 50 kN, the same load magnitude as an equivalent standard axle load, although the pavement studied was designed to carry app. 10,000 passes of loads 2-3 times this magnitude. This also highlights one of the disadvantages of applying a strain-based fatigue model, as this model allows designs where the applied stress is much higher than the stress at failure.

## 2.5 Influence of load position

To evaluate the influences from interaction with adjacent slabs and the load position, numerical studies of two full slabs on grade structures is carried out. The influence of load position is evaluated at the interior and edge of the slab, see Figure 2.11 (a); assuming two orthogonal fracture planes.

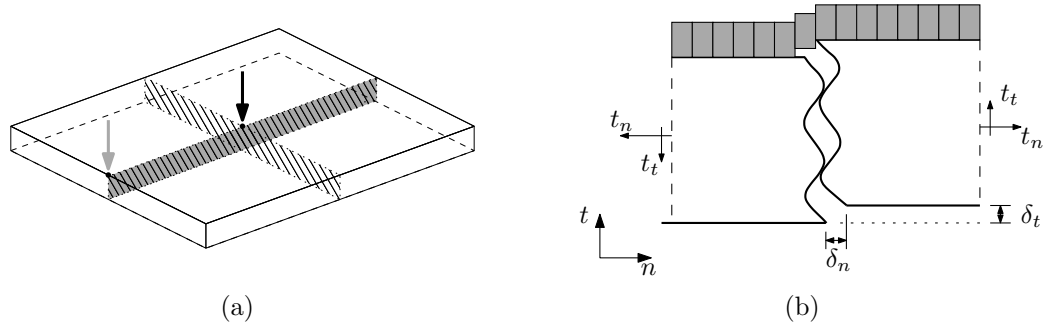


**Figure 2.11:** (a) Sketch of cemented slab with pre-determined cohesive zones for interior loading (black tiled) and edge loading (dark gray). (b) Sketch of the rough crack model (Bažant and Gambarova, 1980) within the composite pavement system.

The average strength properties for the cement bound granular mixture selected are shown in Table 2.4. The subgrade is idealised as linear elastic with a spring stiffness of 0.06 MPa/mm.

**Table 2.4:** CBGM slab geometry, average material properties and model parameters used in the numerical study.

Geometry (mm <sup>3</sup> )	$E$ (MPa)	$\nu$ (-)	$f_t$ (MPa)	$f_c$ (MPa)	$D_{max}$ (mm)	$G_F$ (N/mm)
$3000 \times 3000 \times 300$	15,000	0.2	0.80	8.0	32	0.0225

To allow for movement, i.e. from temperature and moisture changes as well as shrinkage, saw cutting or other techniques is used to induce a full crack between slabs. This also ensures a high load transfer efficiency ( $LTE_\delta$ ) between aggregate interlock joints. The mechanics of aggregate interlock between slabs, shown in Figure 2.11 (b), is a complex phenomenon that depends on several parameters, including aggregate size and distribution, compressive strength, friction between the aggregate particle and the cement paste, crack-opening, and crack-sliding. The influence of variation in normal and shear stiffness of joints is evaluated for an initial crack width,  $w$ , of 0.4 to 2.0 mm, simulated by application of idealised bilinear springs. Theory, model assumptions and material parameters for aggregate interlock behaviour used in numerical studies are described in **Paper I**.

As expected, Figure 2.12 (a) shows that the load supported by the slab is higher under interior than under edge loading, with peak loads of 156 and

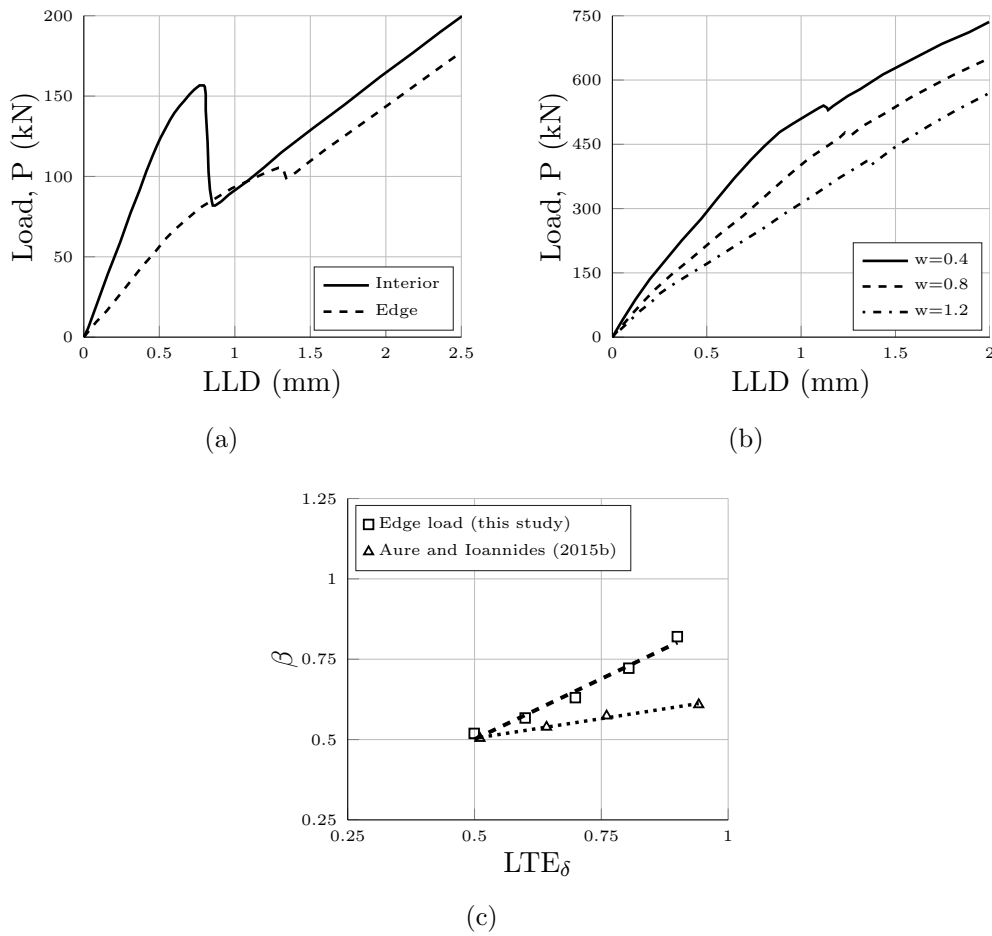


**Figure 2.12:** Evaluation of influence from load position and aggregate interlock joints: (a) load-displacement curve for the two load cases. (b) load-displacement curve with variation in initial joint opening for edge loading. (c) normalised peak-load ( $\beta$ ) versus  $LTE_\delta$ .

106, respectively, considering no load transfer between adjacent slabs. It is also found that the post-peak behaviour, in the case of interior and edge loading, is more or less similar.

The initial crack width has little influence on the peak-load and peak-load displacement for interior load whereas a pronounced increase in stiffness and peak-load can be found for edge loading, see Figure 2.12 (b). Plotting the normalised peak-load ( $\beta$ ) versus  $LTE_\delta$ , assuming a linear relationship between  $w$  and  $LTE_\delta$  (Davids and Mahoney, 1999), it can be found that  $\beta$  decrease linearly with increasing  $w$  as shown in Figure 2.12 (c). Similar trends have also been reported in numerical studies of slabs on grade reported

in Aure and Ioannides (2015b).

## 2.6 Summary of sensitivity studies

To investigate the influences of geometry and important material properties on the model response a sensitivity study is carried out for a single slab subjected to uniformly distributed load with radius of 150 mm. Symmetry conditions are applied, modelling one slab crack. Cohesive zones are inserted with a  $45^\circ$  angle between the symmetry-lines and in an arch close to the centre. The arch cohesive zone is inserted to avoid convergence problems at the boundary. Detailed description of the FE-model can be found in **Paper I**.

In linear elastic design of pavement structures, the layer thickness is increased for increasing load levels, to ensure a relatively constant stress level in the subgrade soil, avoiding any plastic deformation, as shown in Figure 1.5. This approach can be questioned based on the results presented herein; as it is observed in Figure 2.13 (a) that the allowable load levels in presently available guidelines is twice the magnitude compared to the peakloads found in the present study. The thickness of the cemented base layer has significant influence on the peak-load, but little influence on the post-peak response of the structure. After full crack propagation, the behavior of the system should be similar to a corner loading case. However, due to the relatively short slabs created by the cracks, the effect of bending is small. Thus, the influence of thickness is small.

The stiffness and peak-load of the structure increases with increasing thickness up to unloading on the load-displacement curve. Then the structural response is mainly affected by the slab dimension. Moreover, Figure 2.13 (b) shows that increasing subgrade soil stiffness results in higher peak-load, post-peak and pre-peak stiffness. The difference in peak-load is app. 20% for the variation in soil stiffness evaluated, assuming that slabs are constructed on a 150 mm thick high quality sub-base material over subgrade soil of varying quality (corresponding to a california bearing ratio (CBR) 5-20).

The two main material parameters influencing the fracture process of the quasi-brittle material is the tensile strength and the fracture energy. However, as shown in Figure 2.14 (a), the influence of tensile strength is small, both with regard to peak-load and pre- and post-peak response. This can be explained by the fact that cracking is initiated at a displacement of app. 0.2 mm. Then, the response is primarily controlled by the fracture energy, as shown in Figure 2.14 (b).

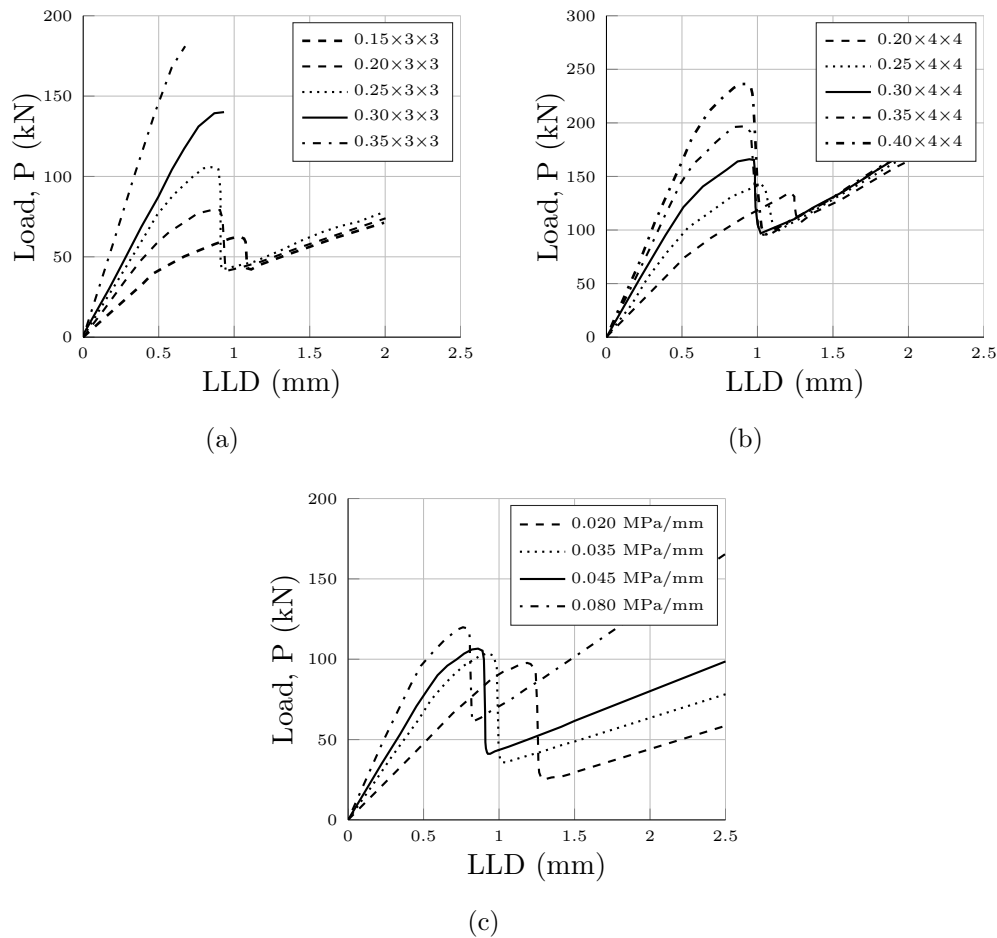


**Figure 2.13:** Load-displacement response: (a) Slab thickness varying from 150-350 mm keeping length/width constant for a  $3 \times 3$  m<sup>2</sup> slab. (b) Slab thickness varying from 200-400 mm keeping length/width constant for a  $4 \times 4$  m<sup>2</sup> slab. (c) Subgrade soil stiffness varying from 0.02 to 0.08 MPa/mm.

## 2.7 Concluding remarks

The presented FE model adequately describes the response of both simple fracture tests, as well as real-scale structures, indicating that the model is feasible for evaluation of composite block pavement systems in the ultimate loading state. Although encouraging results are obtained with the presented model, several aspects have been identified, which need further attention in order to develop the methodology for practical use:

- (i) A high degree of pre-processing is necessary for the development of 3-D models in commercial FE codes, describing material types, geometries

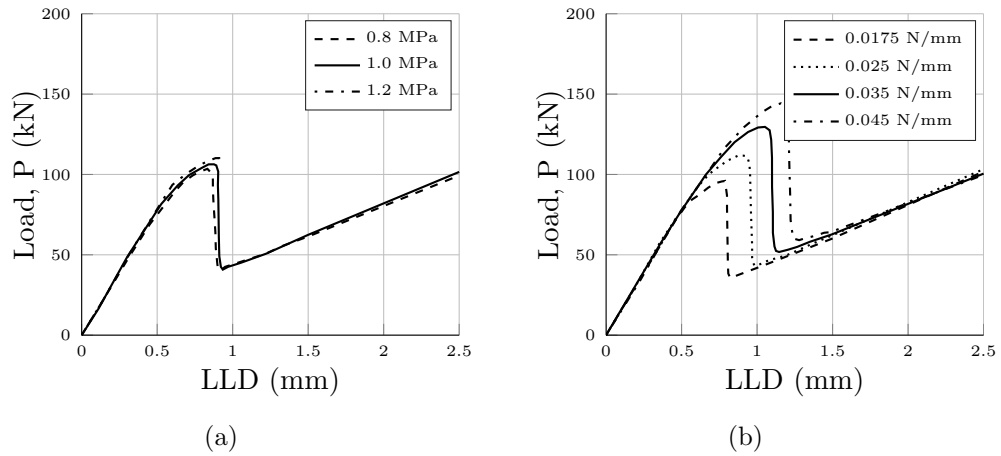


**Figure 2.14:** Load-displacement response: (a) Tensile strength varying from 0.8 to 1.2 MPa keeping fracture energy constant. (b) Fracture energy varying from 0.0175 to 0.045 N/mm keeping tensile strength constant.

and layer interactions. This part of the analysis is time-consuming and expensive.

- (ii) Although the model presented is significantly optimised compared to other models reported in the literature, the model is still demanding with regard to computational power when taking into consideration the relatively simple pavement systems studied. Moreover, it is well-known that numerical analysis of fracture in such large 3-D FE models often poses numerical issues, such as instability problems and aborted simulations, e.g due to a high penalty stiffness.
- (iii) From the results obtained, it can be shown that the soil properties highly influence the fracture behavior and the structural response of concrete and composite structures. This topic has received little attention in the literature and typically Winklers idealisation of the soil is applied without addressing the effect on the fracture behavior. Thus, further evaluation of soil-structure interaction models and model parameter estimation is necessary to develop realistic soil models applicable to analysis on a routine basis.
- (iv) The presented model can be used within the M-E method for evaluation of fatigue, i.e. determining the modulus of rupture of cemented slabs for input in fatigue relationships, as discussed in Section 1.1. This would result in an improvement of existing methods. However, to obtain a full mechanistic and consistent approach the cohesive model should be

extended, thus accounting for more complex constitutive behavior, e.g. considering cyclic crack behavior.

- (v) Experimental results for fracture testing of cement bound granular mixtures and composite pavements structures are limited. Thus, more testing is necessary to evaluate the fracture behaviour of cement bound granular mixtures.

This chapter show that 3-D cohesive zone modeling is an attractive method to handle fracture in composite pavements. However, further extension of the model to describe cyclic crack behavior of the cemented material would increase the complexity of the problem and the need for data storage capacity extensively. Considering the large size of the model compared to the relatively simple problem studied, extending this model will result in very demanding models with regard to computational power and time. Thus, this study will in the following chapters, focus on developing alternative numerical tools and methods, in order to create efficient mechanistic models for engineering design purposes.



# Chapter 3

## Cohesive cracked-hinge model

### 3.1 Introduction

Investigating crack propagation in beam and slab on grade structures subjected to mechanical loads is a highly complex matter. This type of analysis often requires large and computationally expensive models, which are applicable to relatively simple design problems as described in Chapter 2. To reduce the complexity of the models and to create a simple and robust modelling framework for engineering application this chapter presents a non-linear cracked-hinge model.

The cracked-hinge model is based on the fracture mechanics concepts of the fictitious crack model (Hillerborg et al., 1976). The hinge model for modelling the crack propagation due to pure bending in a concrete beam without reinforcement was first presented by Ulfkjær et al. (1995). This hinge was successfully applied in the modelling of pure concrete beams in three point bending considering the development of only one crack. Olesen (2001b) expanded the hinge model by applying a bi-linear softening curve to allow for the incorporation of the effects of fibers on concrete fracture. Furthermore, this modified hinge model allowed for the existence of a sectional normal force. This last feature is crucial for the ability of the hinge to model a number of situations such as the wedge splitting test (Walter et al., 2005) and the split cylinder test (Olesen et al., 2006).

The numerical hinge may be incorporated into a plane beam element for two-dimensional analysis, in a consistent and straightforward manner, as demonstrated by Olesen and Poulsen (2012). The effective stiffness concept is applied allowing for the formation of multiple cracks along the beam axis, which is an essential feature of both plain and reinforced concrete beams before exhibiting localised rotations. The effective stiffness which is a func-

tion of the state of deformation is treated as a constitutive relationship. This particular feature is practical and elegant as it requires no a-priori knowledge of the crack pattern.

## 3.2 The mechanics of the hinge model

The basic assumption of the hinge model is the fact, that the presence of a crack only affects the overall stress and strain field of a structure locally. The discontinuity created by the crack is expected to vanish outside a certain width. Under constant moment, e.g. the part of the beam between the loading points in Figure 3.1 (a), the beam sections at the midpoints between the cracks will, due to the periodicity of the cracks, remain plane during deformation of the beam. The width  $s$  between two such sections embracing one crack defines a hinge element. For the beam area outside the loaded points, the moment distribution is not constant. Such phenomena can be handled with appropriate numerical tools, i.e. the FE method, as exemplified in Figure 3.1 (b).

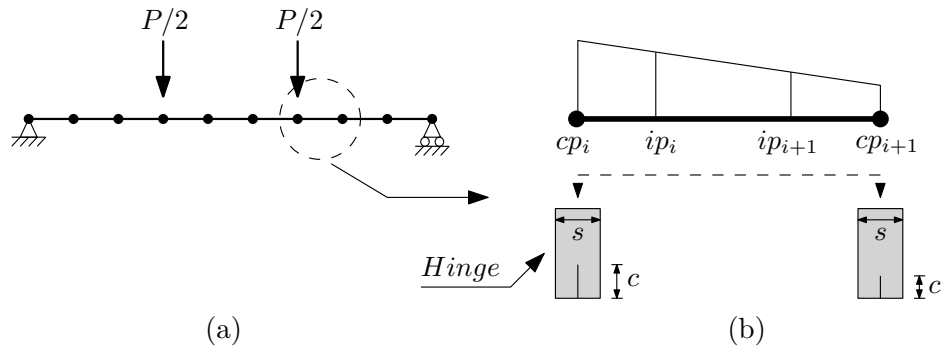


**Figure 3.1:** Sketch of hinge model implemented in a simply supported beam under four point loading: (a) overview of beam structure, (b) underlying discrete formulation of cracks at constitutive points,  $cp$ , and smeared constitutive behavior obtained from interpolation between constitutive points at integration points,  $ip$ .

The hinge width  $s$  is a fundamental calibration parameter of the model, and it was suggested in Ulfkjær et al. (1995) to use a hinge width half the height of the beam, also adopted in the present study. Thus, the flexural deformation of the beam is concentrated and the propagation of a crack can be modelled as a hinge whereas the rest of the beam can be treated as elastic bulk material.

The uni-axial tensile behaviour of the concrete is modeled according to the fictitious crack model. The linear elastic pre-crack state is described by the elastic modulus,  $E_c$ . The uni-axial tensile strength is denoted  $f_t$  and the corresponding strain  $\varepsilon_{ct}$ . The stress-crack opening relationship or so-called softening law is for simplicity here given as a linear curve

$$\sigma(w) = f_t + aw \quad \text{for } 0 \leq w \leq w_c \quad (3.1)$$

where  $a$  is the negative gradient on the softening curve,  $w$  is the crack opening and  $w_c$  is the final zero-stress crack opening. The fracture energy,  $G_F$ , is given by the area under the softening curve, resulting in  $w_c = -f_t/a$ .

The hinge model provides the relationship between the state of deformation of the hinge and the sectional forces ( $N, M$ ). The state of deformation is described by the mean normal strain of the beam axis and the mean curvature of the hinge,  $(\bar{\varepsilon}_0, \bar{\kappa})$ .

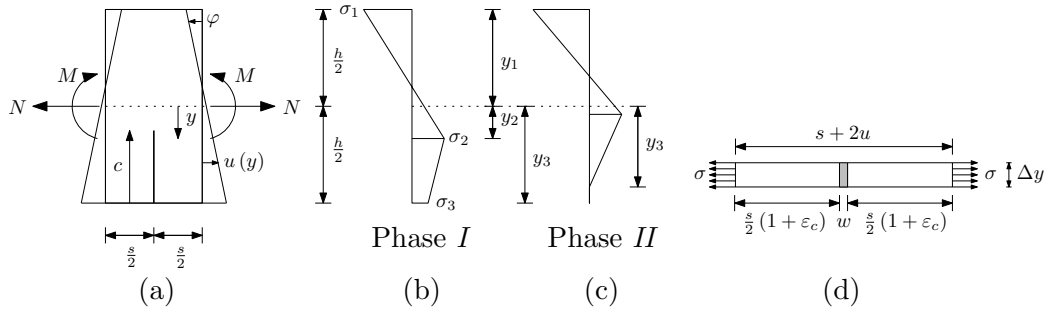


**Figure 3.2:** Hinge model: a) beam segment with constant sectional forces and deformation of cracked beam segment. b) and c) hinge stress distribution after initiation of cracking at the two different Phases I and II, respectively. (d) material strip in uni-axial tension: loaded state beyond peak-load showing crack deformations (Olesen and Poulsen, 2012).

The hinge solution is based on the assumption that the hinge may be seen as consisting of independent infinitesimal layers of cemented material. The tensile behaviour of this layer may be established by considering a strip of material in uni-axial tension as shown in Figure 3.2 (d). The elongation of the strip located at  $y$  can be expressed in terms of the mean normal strain

$$\bar{\varepsilon}(y) = \frac{2u(y)}{s} = \frac{2u_0(y)}{s} + \frac{2\varphi}{s}y \equiv \bar{\varepsilon}_0 + \bar{\kappa}y \quad (3.2)$$

where  $\bar{\varepsilon}_0$  is the mean normal strain at the beam axis, and  $\bar{\kappa}$  the mean curvature of the hinge. Utilising (3.2), the depth coordinates of characteristic

points of the stress distribution,  $y_i$ , with respect to the midsection of the hinge may be determined. Assuming that the hinge has been deformed to a state where a crack has formed and penetrated a distance  $c$  into the hinge. The position of the crack tip is denoted by  $y_2 = h/2 - c$ , and is given as follows

$$\sigma_2 = f_t \Rightarrow (\bar{\varepsilon}_0 + \bar{\kappa}y_2) E_c \Rightarrow y_2 = \frac{\varepsilon_{ct} - \bar{\varepsilon}_0}{\bar{\kappa}} \quad (3.3)$$

In the cracked state,  $0 < w \leq w_c$  (Phase *I*), the crack opening and the corresponding stress in the strip is given as

$$\left. \begin{aligned} \sigma_c = \sigma_w \Rightarrow \sigma_c = f_t + aw \\ s + 2u = s(1 + \varepsilon_c) + w \Rightarrow s\bar{\varepsilon}(y) = s\varepsilon_c + w \end{aligned} \right\} \Rightarrow \left\{ \begin{aligned} w^I &= s \frac{E_c \bar{\varepsilon}(y) - f_t}{E_c + as} \\ \sigma_3^I &= E_c \frac{f_t + as \bar{\varepsilon}(y)}{E_c + as} \end{aligned} \right. \quad (3.4)$$

It is noted that the denominator in (3.4) defines a critical length  $s_{crit}$  of the strip

$$0 < E_c + as \quad \Rightarrow \quad s < s_{crit} = -\frac{E_c}{a} = 2 \frac{E_c G_F}{f_t^2} \quad (3.5)$$

In the cracked state,  $w_c \leq w$  (Phase *II*), the crack is stress free, leading to the simple solution for the strip

$$\left. \begin{aligned} w &= s(1 + \bar{\varepsilon}(y)) - s \\ \sigma_c &= 0 \end{aligned} \right\} \Rightarrow \left\{ \begin{aligned} w^{II} &= s\bar{\varepsilon}(y) \\ \sigma_3^{II} &= 0 \end{aligned} \right. \quad (3.6)$$

From (3.4) and (3.6) the state of stress and crack opening in the cracked part of the hinge can be established. The cohesive stresses extend from  $y = y_2$  to  $y = y_3$ , depicted in Figure 3.2 (b) and (c);  $y_2$  is given by (3.3) and

$$y_3 = \min \left( \frac{h}{2}, -\frac{1}{\bar{\kappa}} \left( \frac{f_t}{as} + \varepsilon_0 \right) \right) \quad (3.7)$$

Here the transition between Phase *I* and *II* for  $y_3$  can be obtained by inserting the condition  $\sigma_3(y_3) = 0$  in (3.4).

Finally, the sectional forces with respect to  $y = 0$  may then be calculated from integration over the hinge height.

$$N(\bar{\varepsilon}_0, \bar{\kappa}) = t \int_{-h/2}^{h/2} \sigma_c dy \quad (3.8a)$$

$$M(\bar{\varepsilon}_0, \bar{\kappa}) = t \int_{-h/2}^{h/2} \sigma_c y dy \quad (3.8b)$$

Moment-curvature response, as well as normal strain,  $\varepsilon_0$ , crack-opening displacement,  $\delta_{COD}$ , and crack-length,  $c$ , can now be obtained for different hinge geometries and cemented material properties, applying the analytical hinge, as exemplified in Figure 3.3.

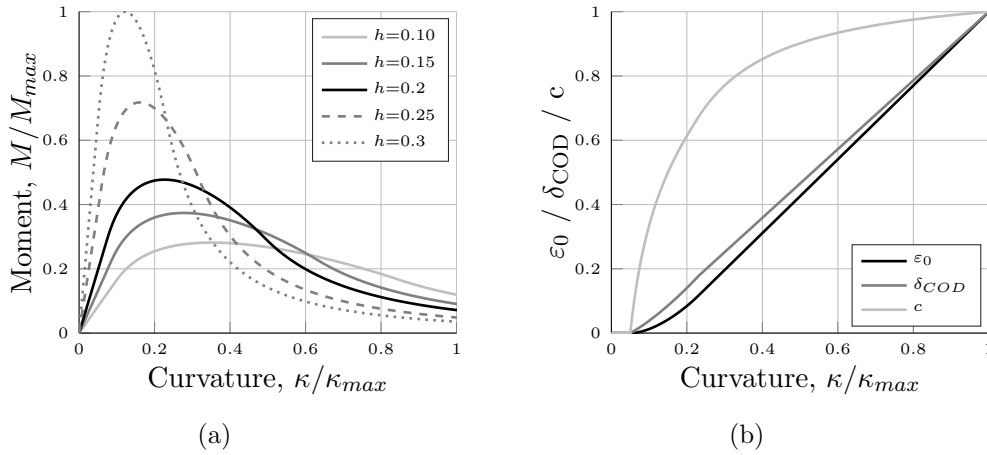


**Figure 3.3:** Analytical hinge model: (a) Normalised curvature-moment response for varying hinge heights  $h=0.1-0.3$  m. (b) normalised variation in normal strain, crack-opening displacement and crack-length for  $h=0.3$  m. Mechanical properties:  $E_c=30$  GPa,  $f_t=3.0$  MPa,  $G_F=150$  N/m (linear softening).

Here, the simplified computational scheme, shown in Algorithm 1, have been employed.

It is obvious from Algorithm 1 that increasing or decreasing hinge rotation is modeled by the same equilibrium path. Thus, the hinge model in the present chapter does not have a unique unloading branch that models the closure of a previously opened crack.

Further, the analytical hinge may be implemented in simply supported beam structures applying conventional beam-theory, as shown in Figure 3.4.

The displacement at midspan position of the beam is the sum of elastic deformation of the hinge and deformation due to the crack. The elastic

**Algorithm 1** Computational scheme for  $N$  and  $M$ : Hyperelastic

---

```

if  $\bar{\varepsilon} < \varepsilon_{ct}$ 
  Phase 0
else
  Phase I
  if  $\bar{\varepsilon} > -\frac{f_t}{a_s}$ 
    Phase II
  end
end
end

```

---

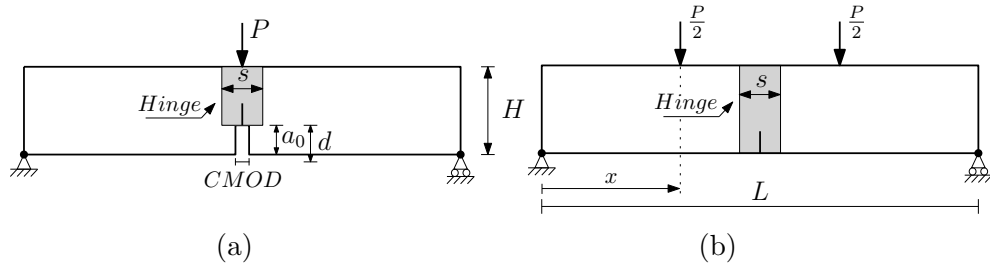


**Figure 3.4:** Analytical hinge implemented into elastic beam showing the definition of parameters: (a) Beam with a notch loaded in three-point bending. (b) Beam loaded in four-point bending.

displacement at midspan is given as

$$w_{3P}^{el} = \frac{PL^3}{48EI} \quad (3.9a)$$

$$w_{4P}^{el} = \frac{Px}{48EI} [3L^2 - 4x^2] \quad (3.9b)$$

where  $w_{3P}^{el}$  and  $w_{4P}^{el}$  is the elastic displacement for a beam under three and four point loading, respectively,  $L$  is the length of the beam and  $x$  is the position of the load in four point bending, i.e.  $x = L/3$  for a beam loaded at third point positions. Introducing the non-dimensional midspan displacement  $\delta = \frac{2w}{L} \frac{\theta}{\varphi}$ , moment  $\mu = \frac{6}{f_t h^2 t} M$  and rotation  $\theta = \frac{h E_c}{s f_t} \varphi$  the expressions can be rewritten as

$$\delta^{el} = f \frac{L}{s} \mu(\theta) \quad (3.10)$$

where  $f$  is a factor dependent on the loading configuration, i.e.  $f = 1/3$  and  $f = 23/54$  for the three and four point beam in (3.9a) and (3.9b), respectively.

The normalised deformation due to the crack only,  $\theta^{cr}$ , is found by subtracting the normalised elastic deformation,  $\theta^{el}$ , from the total rotation of the hinge,  $\theta$  (Olesen, 2001b). The normalised elastic rotation of the hinge is given by  $\theta^{el} = \mu(\theta)$ . Now, since the normalised displacement due to hinge rotation is equal to the normalised hinge rotation  $\theta$ , the normalised displacement due to the crack  $\delta^{cr}$  is given by

$$\delta^{cr} = \theta^{cr} = \theta - \mu(\theta) \quad (3.11)$$

The total midspan displacement can now be found from

$$\delta = \delta^{el} + \delta^{cr} = \theta + \left(f \frac{L}{s} - 1\right) \mu(\theta) \quad (3.12)$$

The load is related to the normalised moment through

$$P_{3P}(\theta) = \frac{2}{3} \frac{f_t h^2 t}{L} \mu(\theta) \quad (3.13a)$$

$$P_{4P}(\theta) = \frac{f_t h^2 t}{L} \mu(\theta) \quad (3.13b)$$

where  $P_{3P}$  and  $P_{4P}$  is the load for the three and four point beam shown in Figure 3.4 (a) and (b), respectively.

### 3.3 Implementation of hinge into beam element

The proposed numerical hinge is implemented following standard finite element beam theory and procedures for building elements with non-linear material behaviour, see e.g. Cook et al. (2007). The expressions for the element stiffness matrix and equivalent nodal loads are based on the cubic displacement function.

For the present study a plane three-node beam element is chosen as shown in Figure 3.5. This element is capable of modeling quadratic variations of the axial displacements and cubic variations of the transverse displacements. The choice of element ensures that both generalised strains are interpolated linearly as opposed to a typical two-node beam element where constant normal strain is assumed.

The vector of generalised displacements of the beam,  $\mathbf{u}$ , holds the axial displacements  $u_1(x_1)$  and the transverse displacements  $u_2(x_2)$ . The interpo-

### 3.3 Implementation of hinge into beam element Cohesive cracked-hinge model

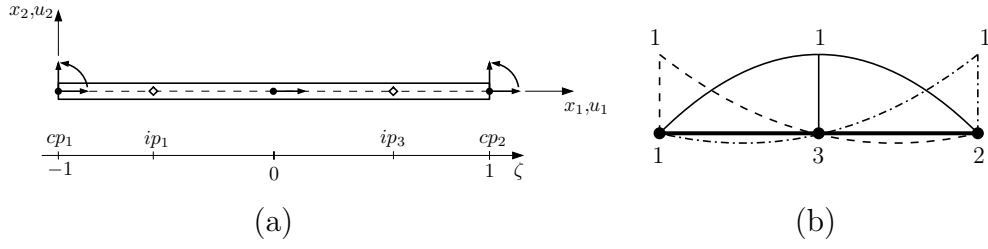


**Figure 3.5:** Plane beam element: (a) Constitutive points ( $cp_i$ ) are located at endpoints, integration points ( $ip_i$ ) at Gauss points. (b) Beam element axial shape functions and node numbers.

lation of  $\mathbf{u}$  in the element is given by

$$\mathbf{u} = \begin{bmatrix} u_1 \\ u_2 \end{bmatrix} = \mathbf{N}\mathbf{v} \quad (3.14)$$

where  $\mathbf{N}$  is the displacement interpolation matrix and  $\mathbf{v}$  is the element dof vector, i.e.

$$\mathbf{v} = [v_{1,1} \quad v_{2,1} \quad \varphi_{1,2} \quad v_{1,2} \quad v_{2,2} \quad \varphi_{2,2} \quad v_{1,3}]^T \quad (3.15)$$

where the latter subscript notation symbolises the element node number according to Figure 3.5 (b).

The interpolation functions are standard polynomial expressions. The vector of generalised strains,  $\boldsymbol{\varepsilon}$ , holds the linearised axial strain,  $\varepsilon_0$ , and the linearised curvature,  $\kappa$ . The interpolation of  $\boldsymbol{\varepsilon}$  in the element is given by

$$\boldsymbol{\varepsilon} = \begin{bmatrix} \varepsilon_0 \\ \kappa \end{bmatrix} = \begin{bmatrix} \frac{du_1}{dx} \\ \frac{d^2u_2}{dx^2} \end{bmatrix} = \mathbf{B}\mathbf{v} \quad (3.16)$$

where  $\mathbf{B}$  is the strain interpolation matrix. The vector of generalised stresses,  $\boldsymbol{\sigma}$ , holds the sectional normal force  $N$  and the sectional moment  $M$ . In the element,  $\boldsymbol{\sigma}$  may be established applying (3.8a) and (3.8b), and we may write

$$\boldsymbol{\sigma} = \boldsymbol{\sigma}(\boldsymbol{\varepsilon}) = \begin{bmatrix} N(\boldsymbol{\varepsilon}) \\ M(\boldsymbol{\varepsilon}) \end{bmatrix} \quad (3.17)$$

Based on the contribution to the variation in internal work  $\delta\Omega$ , from the beam and the potential work of external forces  $\delta W$  from point and surface loads, the principle of virtual work for the system can be established

$$\int_V \delta \boldsymbol{\varepsilon}^T \boldsymbol{\sigma} dV = \int_S \delta \mathbf{u}^T \mathbf{f} dS + \sum_i \delta \mathbf{u}_i^T p_i \quad (3.18)$$

where  $V$  is the structural volume,  $S$  is the surface area,  $\delta \boldsymbol{\varepsilon}$  and  $\delta \mathbf{u}$  is the strain and displacement variations, respectively,  $\mathbf{f}$  is the surface traction vector,  $p_i$  is a concentrated (nodal) load and  $\delta \mathbf{u}_i$  is the associated (nodal) displacement variation. The desired stiffness matrices can now be established from (3.18).

The displacement interpolation matrix is given as

$$\mathbf{N} = \begin{bmatrix} 2s^2 - 3s + 1 & 0 \\ 0 & 2s^3 - 3s^2 + 1 \\ 0 & (s^3 - 2s^2 + s)L_e \\ 2s^2 - s & 0 \\ 0 & -2s^3 + 3s^2 \\ 0 & (s^3 - s^2)L_e \\ -4s^2 + 4s & 0 \end{bmatrix}^T \quad (3.19)$$

where  $s = x/L_e$  is the normalised element length and  $L_e$  the actual element length.

The strain distribution matrix is given as

$$\mathbf{B} = \frac{1}{L_e^2} \begin{bmatrix} (4s - 3)L_e & 0 \\ 0 & 12s - 6 \\ 0 & (6s - 4)L_e \\ (4s - 1)L_e & 0 \\ 0 & -12s + 6 \\ 0 & (6s - 2)L_e \\ (-8s + 4)L_e & 0 \end{bmatrix}^T \quad (3.20)$$

The transformation matrix is given as

$$\mathbf{T} = \begin{bmatrix} e_1 & e_2 & 0 & 0 & 0 & 0 & 0 \\ -e_2 & e_1 & 0 & 0 & 0 & 0 & 0 \\ 0 & 0 & 1 & 0 & 0 & 0 & 0 \\ 0 & 0 & 0 & e_1 & e_2 & 0 & 0 \\ 0 & 0 & 0 & -e_2 & e_1 & 0 & 0 \\ 0 & 0 & 0 & 0 & 0 & 1 & 0 \\ 0 & 0 & 0 & 0 & 0 & 0 & 1 \end{bmatrix} \quad (3.21)$$

where  $e$  is the unit vector describing the direction of the beam in the 2-D space.

The internal nodal force,  $\mathbf{q}$ , is given by the expression

$$\mathbf{q} = \int_0^{L_e} \mathbf{B}^T \boldsymbol{\sigma} dx \quad (3.22)$$

The contribution from the beam-element to the tangential stiffness matrix,  $\mathbf{k}_t$ , is given by the expression

$$\mathbf{k}_t = \int_0^{L_e} \mathbf{B}^T \mathbf{D}_t \mathbf{B} dx \quad (3.23)$$

The hinge tangent stiffness matrix,  $\mathbf{D}_t$ , is defined through

$$\begin{bmatrix} dN \\ dM \end{bmatrix} = \mathbf{D}_t \begin{bmatrix} d\bar{\varepsilon}_0 \\ d\bar{\kappa} \end{bmatrix}, \text{ where } \mathbf{D}_t = \begin{bmatrix} \frac{\partial N}{\partial \bar{\varepsilon}_0} & \frac{\partial N}{\partial \bar{\kappa}} \\ \frac{\partial M}{\partial \bar{\varepsilon}_0} & \frac{\partial M}{\partial \bar{\kappa}} \end{bmatrix} \quad (3.24)$$

For the linear elastic phase, Phase 0, the hinge tangent stiffness matrix  $\mathbf{D}_t$  is given as

$$\mathbf{D}_t^0 = \begin{bmatrix} htE_c & 0 \\ 0 & \frac{1}{12}th^3E_c \end{bmatrix} \quad (3.25)$$

The constituents of (5.22) are obtained from the sectional forces  $N$  and  $M$  as given in (3.8a) and (3.8b), respectively, utilising the following relations for the relevant part of the integral corresponding to  $0 < w \leq w_c$

$$\frac{\partial \sigma_c}{\partial \bar{\varepsilon}_0} = E_c \frac{as}{E_c + as} \quad ; \quad \frac{\partial \sigma_c}{\partial \bar{\kappa}} = E_c \frac{as}{E_c + as} y \quad (3.26)$$

Here the parameters  $\alpha = \frac{as}{E_c + as}$  and  $E_{cc} = E_c \alpha$  is introduced, where the latter represents the reduced stiffness of the cracked part of the hinge. The full hinge tangent stiffness matrix for Phase *I* and *II* can then be established

$$\begin{aligned} dN &= t \int_{-h/2}^{h/2-c} E_c (d\bar{\varepsilon}_0 + d\bar{\kappa}y) dy + t \int_{h/2-c}^{h/2} E_{cc} (d\bar{\varepsilon}_0 + d\bar{\kappa}y) dy \\ &= D_t(1, 1) d\bar{\varepsilon}_0 + D_t(1, 2) d\bar{\kappa} \\ dM &= t \int_{-h/2}^{h/2-c} y E_c (d\bar{\varepsilon}_0 + d\bar{\kappa}y) dy + t \int_{h/2-c}^{h/2} y E_{cc} (d\bar{\varepsilon}_0 + d\bar{\kappa}y) dy \\ &= D_t(2, 1) d\bar{\varepsilon}_0 + D_t(2, 2) d\bar{\kappa} \end{aligned} \quad (3.27)$$

which by solving the differential equation yields

$$\begin{aligned} D_t(1, 1) &= E_c t ((y_2 - y_1) + (y_3 - y_2) \alpha) \\ D_t(1, 2) &= E_c t \left( \frac{1}{2} (y_2 - y_1) (y_1 + y_2) + \frac{1}{2} (y_3 - y_2) (y_2 + y_3) \alpha \right) \\ D_t(2, 1) &= D_t(1, 2) \\ D_t(2, 2) &= E_c t \left( \frac{1}{3} (y_2 - y_1) (y_1^2 + y_2^2 + y_1 y_2) \right. \\ &\quad \left. + \frac{1}{3} (y_3 - y_2) (y_2^2 + y_3^2 + y_2 y_3) \alpha \right) \\ \mathbf{D}_t^{I,II} &= \begin{bmatrix} D_t(1, 1) & D_t(1, 2) \\ D_t(2, 1) & D_t(2, 2) \end{bmatrix} \end{aligned} \quad (3.28)$$

### 3.4 User-built finite element code

The hinge model is implemented in a user-built FE code using the numerical computing package MATLAB. Basic elements and support functions is

provided by the 'BYG-FEM' software<sup>1</sup>. A simple schematic overview of the model code is shown in Figure 3.6.

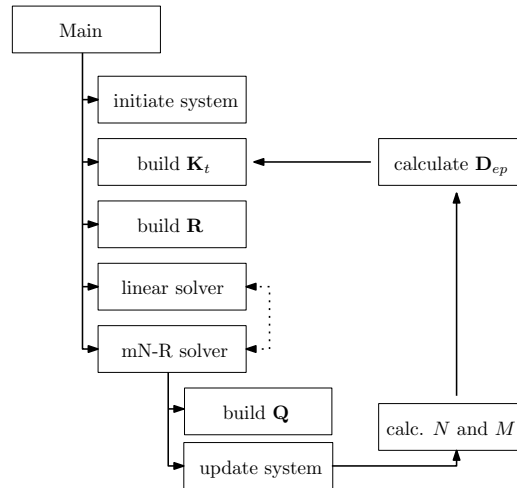


**Figure 3.6:** Schematic roadmap of user built FE code

The schematic in Figure 3.6 can be explained briefly as follows:

- (i) Geometry and material parameters are used as input in 'Main'. Then, necessary elements, storage matrices and parameters are initiated in 'initiate system'.
- (ii) The non-linear analysis then starts it's loop (going downwards) building the global tangent stiffness matrix in 'build  $\mathbf{K}$ ' by collecting all element contributions  $\mathbf{k}_t$  given in Equation (3.23). The global load vector in is then established in 'build  $\mathbf{R}$ '.
- (iii) These matrices is then used to calculate the first linear step, i.e. Equation (3.31), in the 'linear solver' after imposing boundary conditions.
- (iv) Then, via the non-linear 'mN-R solver', the load step  $\Delta \mathbf{f}$  is used to calculate the global internal force vector in 'build  $\mathbf{Q}$ ' collecting all element contributions  $\mathbf{q}$  given in Equation (3.22)
- (v) This requires an update of the system, calculating the updated sectional forces in 'calc.  $N$  and  $M$ ' given in Equation (3.8a) and (3.8b)

<sup>1</sup>The 'BYG-FEM' is a FE program developed at the Section for Structural Engineering at Technical University of Denmark.

- (vi) The material tangent stiffness matrix can be established from 'calculate  $\mathbf{D}_{ep}$ ' given in Equation (3.25) and (3.28), which in turn is used to calculate the updated global tangent stiffness matrix in 'build  $\mathbf{K}$ '

This section describes the governing finite element equations, whereas subsequent chapters mainly deal with the development of the constitutive material behavior, i.e. point (v) and (vi) in the list above. These constitutive models require additional computational schemes similar to Algorithm 1, which will be detailed in each chapter. Detailed coding of special purpose support functions and elements are not reported as part this thesis.

### Solution strategies

The step-size of the global load-adding loop can be controlled in several ways. Ideally, a solution method should be able to trace the entire pre and post-critical static load path of a structure, which may include both softening and stiffening behaviour, the presence of load and displacement limit points and the possible bifurcation of the path. However, in materials that exhibit snap-back type of load-displacement and particularly when a significant strain softening is introduced into the constitutive law tracing of the snap back may encounter numerous difficulties (Crisfield, 1983).

Due to the sudden snap-back or snap-through phenomena at failure a conventional Newton-Raphson (N-R) is selected to increase the efficiency of numerical simulations. In order to capture the softening behavior of the cemented material a solver with direct displacement control is implemented in addition to the standard load-controlled solver.

The global behavior of a structure or specimen can be obtained by solving the discretised equations of equilibrium that can be written as

$$\mathbf{q}(\mathbf{v}) = \mathbf{f} \quad (3.29)$$

where  $\mathbf{q}(\mathbf{v})$  is the internal force vector,  $\mathbf{v}$  is the vector collecting the nodal displacements of all nodes and  $\mathbf{f}$  is the external force vector collecting the load acting on the structure, assuming that the external force vector is independent on the nodal displacements. In the case of linear elasticity, the internal force vector can be directly expressed as

$$\mathbf{q}(\mathbf{v}) = \mathbf{K}\mathbf{v} \quad (3.30)$$

where  $\mathbf{K}$  is the global stiffness matrix of the model. Substituting (3.30) to (3.29) the global response of the model can be directly computed as

$$\mathbf{v} = \mathbf{K}^{-1} \mathbf{f} \quad (3.31)$$

For a non-linear material response, the internal force vector becomes a non-linear function of the nodal displacements,  $\mathbf{v}$ . Moreover, the global stiffness matrix,  $\mathbf{K}$ , becomes a function of the nodal displacements in (3.31) resulting in the following expression

$$\mathbf{v} = \mathbf{K}^{-1}(\mathbf{v}) \mathbf{f} \quad (3.32)$$

This type of non-linear equation cannot be solved directly and therefore the concept of linearisation is applied.

### Linearisation

Suppose that  $\mathbf{q}(\bar{\mathbf{v}})$  is the vector of internal forces generated by nodal displacements  $\bar{\mathbf{v}}$ . The internal forces in the vicinity of  $\bar{\mathbf{v}}$  can be expanded into Taylor series leading to

$$\mathbf{q}(\bar{\mathbf{v}} + \Delta\mathbf{v}) = \mathbf{q}(\bar{\mathbf{v}}) + \left. \frac{\partial \mathbf{q}}{\partial \mathbf{v}} \right|_{\mathbf{v}=\bar{\mathbf{v}}} \Delta\mathbf{v} + \dots \quad (3.33)$$

For small displacement increments,  $\Delta\mathbf{v}$ , the non-linear terms represented by dots can be neglected and we obtain a linear approximation of the internal forces.

$$\mathbf{q}(\bar{\mathbf{v}} + \Delta\mathbf{v}) \approx \mathbf{q}(\bar{\mathbf{v}}) + \mathbf{K}(\bar{\mathbf{v}}) \Delta\mathbf{v} \quad (3.34)$$

where  $\mathbf{K}(\bar{\mathbf{v}})$  is the global tangent stiffness matrix.

Having defined the linearised relationships, an incremental-iterative solution can be formulated to solve (3.32).

### Load control

Usually, the external load is applied in several incremental steps and in every step, the structural response is computed from the equilibrium equations in (3.29). In the Newton-Raphson method the stiffness from the current state

is used to calculate the deformation for the next load step,  $\mathbf{f}_n = \mathbf{f}_{n-1} + \Delta\mathbf{f}_n$ , by solving the linear system

$$\Delta\mathbf{f}_n = \mathbf{K}_{n-1}\Delta\mathbf{v}_n \quad (3.35)$$

where  $\mathbf{v}_n = \mathbf{v}_{n-1} + \Delta\mathbf{v}_n$ . The error is reduced by using the residual forces to calculate a new change in deformation by solving the linear system

$$\mathbf{r}_n = \mathbf{K}_{n-1}\Delta\mathbf{v}_n \quad (3.36)$$

where  $\mathbf{r}_n = \Delta\mathbf{f}_n - \Delta\mathbf{q}_n$ . Such iterative correction, shown in Algorithm 2, can be repeated until the equations of equilibrium is satisfied with a sufficient accuracy.

---

**Algorithm 2** N-R load control
 

---

Load steps  $n = 1, 2, \dots, n_{max}$

$$\mathbf{f}_n = \mathbf{f}_{n-1} + \Delta\mathbf{f}_n$$

$$\mathbf{v}_n = \mathbf{v}_{n-1}$$

Iterations  $i = 1, 2, \dots, i_{max}$

$$\mathbf{K}_n = \mathbf{K}(\mathbf{v}_n)$$

$$\mathbf{r}_n = \mathbf{f}_n - \mathbf{q}(\mathbf{v}_n)$$

$$\Delta\mathbf{v}_n = \mathbf{K}_{n-1}^{-1}\mathbf{r}_n$$

$$\mathbf{v}_n = \mathbf{v}_n + \Delta\mathbf{v}_n$$

Stop iteration when  $\frac{\delta E_1}{\Delta E_0} < \epsilon$

End of load steps

---

**Direct displacement control**

In direct displacement control the nodal displacements,  $\mathbf{v}$ , can be divided into two parts  $\mathbf{v} = [\mathbf{v}_k, \mathbf{v}_u]^T$ ;  $\mathbf{v}_u$  corresponds to the internal dof's which are unknown and  $\mathbf{v}_k$  collects dof's with prescribed values. Accordingly, the vector of internal and external forces can be divided into  $\mathbf{q} = [\mathbf{q}(\mathbf{v}_k), \mathbf{q}(\mathbf{v}_u)]^T$  and  $\mathbf{f} = [\mathbf{f}_u, \mathbf{f}_k]^T$ , respectively. The external forces,  $\mathbf{f}_k$ , are prescribed and external forces,  $\mathbf{f}_u$ , collect reactions at nodes with the prescribed nodal displacements,  $\mathbf{v}_k$ . The system is solved in incremental steps and can be written as

$$\begin{bmatrix} \mathbf{K}_{11} & \mathbf{K}_{12} \\ \mathbf{K}_{21} & \mathbf{K}_{22} \end{bmatrix} \begin{bmatrix} \Delta\mathbf{v}_k \\ \Delta\mathbf{v}_u \end{bmatrix} = \begin{bmatrix} \Delta\mathbf{f}_u \\ \Delta\mathbf{f}_k \end{bmatrix} \quad (3.37)$$

where  $\mathbf{K}_{ij}$  are blocks of the global tangent stiffness matrix

$$\mathbf{K} = \frac{\partial \mathbf{q}}{\partial \mathbf{v}} = \begin{bmatrix} \frac{\partial \mathbf{q}_1}{\partial \mathbf{v}_1} & \frac{\partial \mathbf{q}_1}{\partial \mathbf{v}_2} \\ \frac{\partial \mathbf{q}_2}{\partial \mathbf{v}_1} & \frac{\partial \mathbf{q}_2}{\partial \mathbf{v}_2} \end{bmatrix} \quad (3.38)$$

The unknown displacements  $\Delta \mathbf{v}_u$  can be found by solving

$$\Delta \mathbf{v}_u = \mathbf{K}_{22}^{-1} (\Delta \mathbf{f}_k - \mathbf{K}_{21} \Delta \mathbf{v}_k) \quad (3.39)$$

The external forces associated with the known displacements can then be calculated as

$$\Delta \mathbf{f}_u = \mathbf{K}_{11} \Delta \mathbf{v}_k + \mathbf{K}_{12} \Delta \mathbf{v}_u \quad (3.40)$$

Similarly to (3.36) the tangent stiffness matrix is updated and the residual force vector can be calculated. The iterative procedure is described in Algorithm 3.

---

**Algorithm 3** N-R displacement control

---

Calculate:  $\mathbf{K}$

Displacement steps  $n = 1, 2, \dots, n_{max}$

$\mathbf{v}_n = \mathbf{v}_{n-1}$  and  $\mathbf{f}_n = \mathbf{f}_{n-1}$

Iterations  $i = 1, 2, \dots, i_{max}$

$\Delta \mathbf{v}_u = \mathbf{K}_{22}^{-1} (\Delta \mathbf{f}_k - \mathbf{K}_{21} \Delta \mathbf{v}_k)$

$\Delta \mathbf{f}_u = \mathbf{K}_{11} \Delta \mathbf{v}_k + \mathbf{K}_{12} \Delta \mathbf{v}_u$

$\mathbf{K}_n = \mathbf{K}(\mathbf{v}_{n-1} + \Delta \mathbf{v}_n)$

$\mathbf{r}_n = \mathbf{K} \Delta \mathbf{v}_n - \Delta \mathbf{f}_n$

Stop iteration when  $\frac{\delta E_1}{\Delta E_0} < \epsilon$

$\mathbf{v}_n = \mathbf{v}_{n-1} + \Delta \mathbf{v}_n$  and  $\mathbf{f}_n = \mathbf{f}_{n-1} + \Delta \mathbf{f}_n$

End of displacement steps

---

In the present study the energy norm ratio  $\delta E_1 / \Delta E_0$  is applied as convergence criteria, i.e.

$$\frac{\delta E_1}{\Delta E_0} = \frac{\frac{1}{2} \Delta \mathbf{f} \Delta \mathbf{v}}{\frac{1}{2} \mathbf{r} \Delta \mathbf{v}} \quad (3.41)$$

The error tolerance,  $\epsilon$ , applied is  $10^{-4}$ .

### 3.5 Numerical analysis of beam fracture tests

A numerical analysis of a simply supported beam under three point loading is carried out to demonstrate the performance of the proposed element type. The load-displacement response of the cracked-hinge beam is plotted for a conventional two-node element, see e.g. (Cook et al., 2007), and the proposed three-node element, for different mesh densities,  $nel$ , and compared to the analytical hinge model described in Section 3.2.

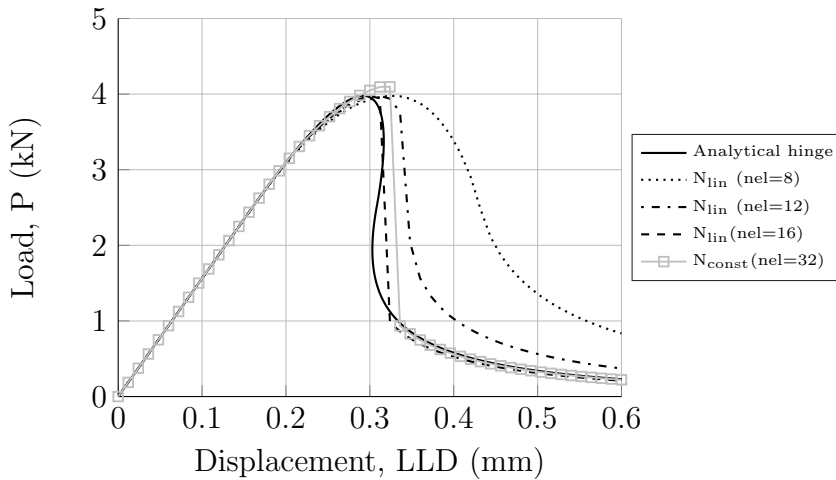


**Figure 3.7:** Convergence test and comparison between FE hinge and analytical model for a beam loaded in three-point bending. Beam dimensions ( $L/h/t$ ):  $0.8 \times 0.1 \times 0.1 \text{ m}^3$ . Hinge width:  $s = h/2$ . Mechanical properties:  $E_c=20 \text{ GPa}$ ,  $f_t=3.0 \text{ MPa}$ ,  $G_F=100 \text{ N/m}$  (linear softening).

It is observed from Figure 3.7 that satisfactory convergence for the specific fracture test is obtained with  $nel=16$  for the three-node element, whereas min.  $nel=32$  is required for the conventional two-node element. This difference in performance can be explained by the coupling in the diagonal of the stiffness matrix, i.e.  $D(1,2)$  and  $D(2,1)$  in (3.28). For the two-node element, these two parts will have different normal strain variation. This, further results in slow convergence and aborted simulations. Results for the analytical hinge is obtained by utilising (3.9)-(3.13). It is also found that the displacement controlled solver sufficiently describes both pre and post-peak behaviour, whereas the potential snap-back load-displacement response is ignored.

The functionality of the cracked-hinge beam model with a simple linear softening law can further be tested by comparing the proposed hinge model with experimental and numerical results for cement bound granular mixture

beam loaded in three-point bending presented in Chapter 2, shown in Figure 2.5 (b).

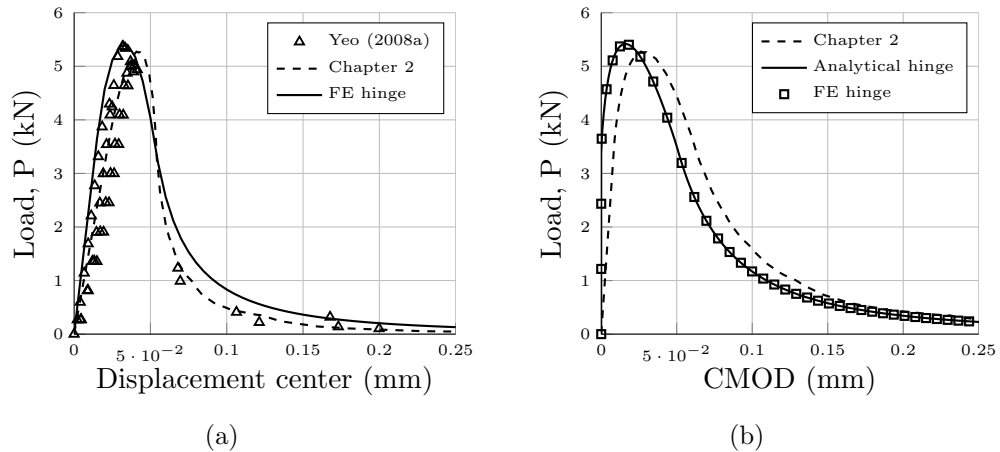


**Figure 3.8:** Comparison between the proposed hinge and experimental and numerical results reported in Chapter 2: (a) Load-displacement response (b) numerical Load-CMOD response. Beam geometry ( $L/h/t$ ):  $300 \times 100 \times 100 \text{ mm}^3$ . Element size  $9.375 \text{ mm}$ . Load positions:  $L/3, 2L/3$ . Mechanical properties:  $E_c=12.76 \text{ GPa}$ ,  $\nu=0.2$ ,  $f_t=1.0 \text{ MPa}$ ,  $G_F=28.0 \text{ N/m}$ .

It is observed from Figure 3.8 that there is good agreement between the proposed hinge model and experimental and numerical results reported in the literature. The difference between numerical models are mainly related to the pre-peak behavior; whereas the hinge model behaves perfectly elastic up to initiation of cracking (load level of app. 3.5 kN), the cohesive zone model incorporates a small error in crack-opening displacements related to the penalty stiffness, see (2.2). This error is best exemplified in Figure 3.8 (b), observing that the crack-opening in the cohesive zone model evolves from the beginning of the analysis and thus resulting in a more flexible behavior of the beam. Increasing penalty stiffness reduce this error, however, very high levels of penalty stiffness result in ill-conditioned stiffness matrix and thus slow convergence and aborted simulations. This problem is avoided applying the finite element hinge, resulting in a more robust model and stable simulations.

### 3.6 Implementation of hinge into plate element

In the subsequent chapters the development and use of the cracked-hinge model will be demonstrated considering two-dimensional problems. Two-dimensional models can be used in special design cases and simple studies. However, pavement fracture is a three-dimensional problem which is affected by geometry, as discussed in Chapter 2. Thus, this section outline a direction for further development of the proposed hinge model, i.e. including three-dimensional analysis, presenting a simplified method implementing the hinge model into a plate element.

The concept outlined here is based on the work by Jensen (2016) who used a numerical plate-hinge to investigate the fracture behavior of reinforced concrete slabs, shown in Figure 3.9, using the smeared crack stress-strain relationship proposed by Rots (1988).

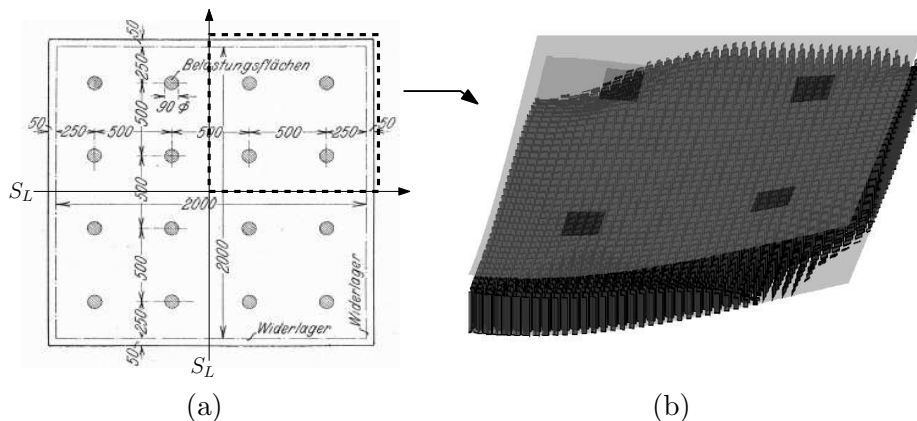


**Figure 3.9:** Simply supported reinforced concrete slab subjected to plate loads (circular gray areas) reported in Bach and Graf (1915). (b) 3-D visualisation of crack direction and height in the constitutive points for a quarter slab in deformed state (load level,  $P=320$  kN) applying the plate-hinge proposed by Jensen (2016).

In the methodology suggested by Jensen (2016), the following assumptions are introduced:

- (i) Plane stress conditions.
- (ii) When the first principal stress exceeds the tensile strength the first crack initiates.

- (iii) The crack is initiated in a direction perpendicular to the direction of the first principle stress.
- (iv) The crack direction is fixed after initiation.
- (v) If the second principle stress exceeds the tensile strength a second crack develop perpendicular to the first crack.
- (vi) Full and no shear stiffness during Phase I and Phase II, respectively.
- (vii) No coupling between crack-opening (*Mode I*) and crack sliding (*Mode II*).
- (viii) Reinforcement is assumed to only carry normal stresses.

In general three-dimensional problems, stresses can develop in any direction and thus the crack can develop in any direction, as shown for a layer  $dz$  in Figure 3.10.

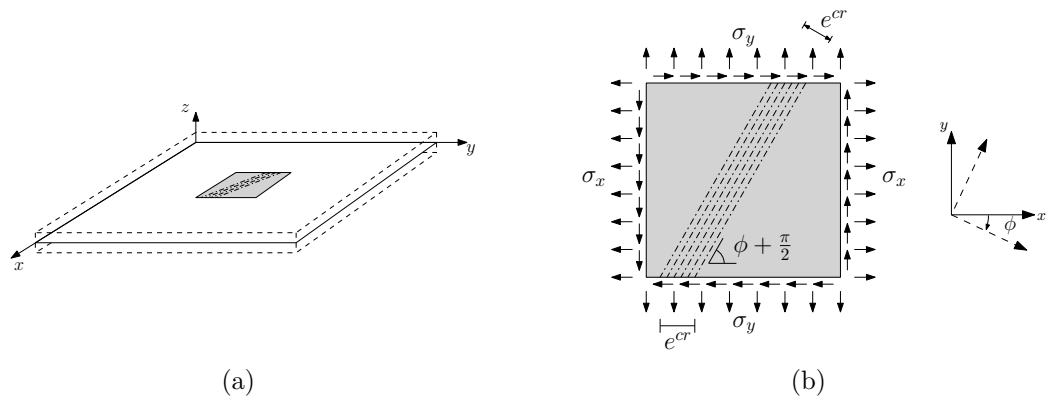


**Figure 3.10:** (a) Overview of three-dimensional plate. (b) Inelastic cracking strain in element layer  $dz$ .

The cemented material can behave as described in Section 3.2 in each direction. After initiation of a crack in the hinge layer  $dz$  in one direction, the direction of the second crack is fixed perpendicular to the first crack if the second principle stress exceeds the tensile strength. Then, the orthogonal cracks develop according to Figure 3.11. The hinge model was implemented in a triangular 'LDPNP' plate element with 6 nodes. In this element, the corner nodes have three degrees of freedom and the nodes along the sides have one degree of freedom, see Jensen (2016).

To validate the plate-hinge model a simply supported reinforced one-way concrete slab under four point loading is considered and compared to the

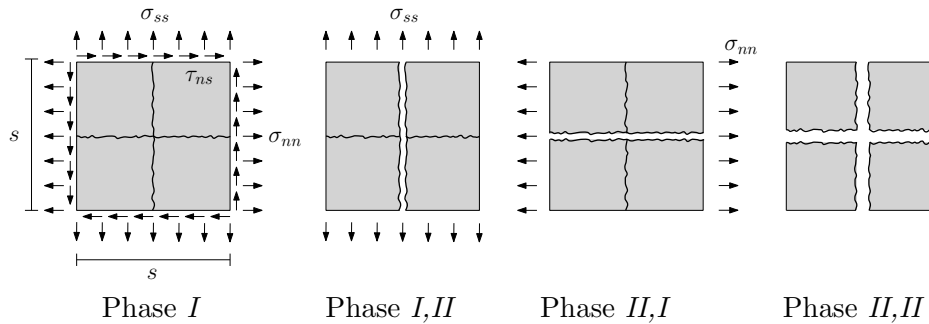


**Figure 3.11:** Cracked phases in hinge layer  $dz$  from initiation of two orthogonal cracks to two stress free-cracks.

beam-hinge model presented in Section 3.3 and experimental results reported in Bach and Graf (1915). The results are shown in Figure 3.12.

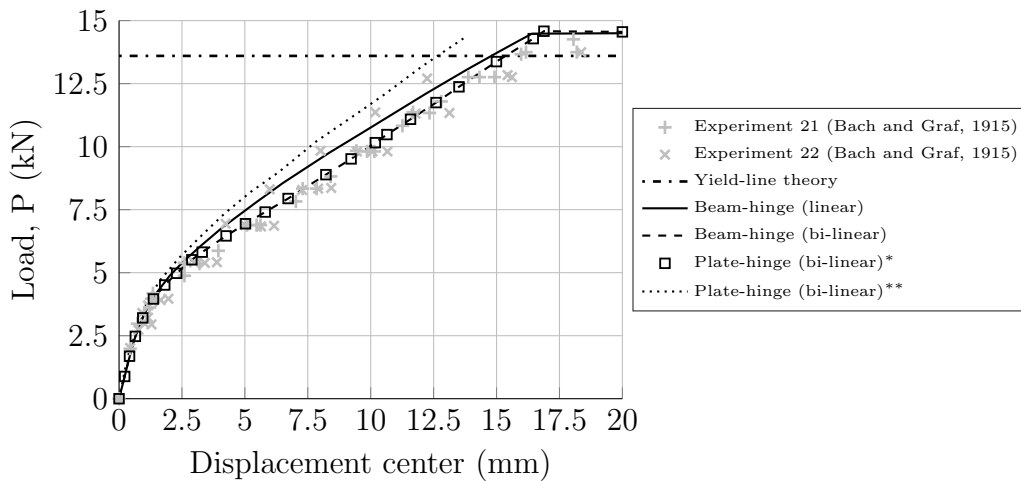


**Figure 3.12:** Load-displacement response of simply supported one-way slab subjected to four point loading: comparison between experimental results reported in Bach and Graf (1915), the proposed beam-hinge model and the plate-hinge model. In the latter model a beam stress-strain relation\* and the stress-strain relation proposed by Rots (1988)\*\* is shown.

It is observed from Figure 3.12 that adequately good fit is obtained between the numerical hinge models and experimental results. It is also observed that the peak-load comply well with the yield-line theory. The plate-hinge acts slightly stiffer compared to experimental results and the beam-hinge model. Jensen (2016) concluded that this effect could be due to the multi-axial effect on the stress-strain relation. However, this phenomena

was not investigated further. The plate-hinge model yields exactly the same results as the beam-hinge model if the same stress-strain relation is applied.

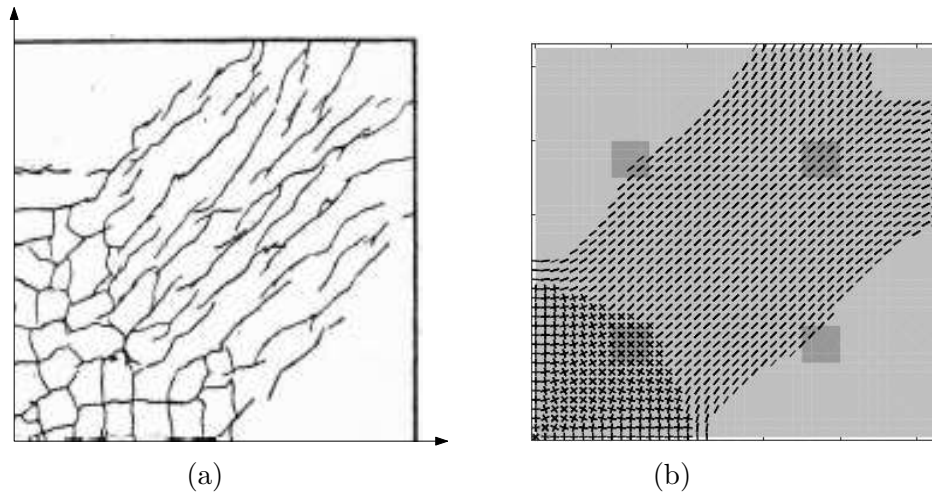


**Figure 3.13:** Simply supported reinforced concrete slab subjected to plate loads reported in Bach and Graf (1915): (a) Experimental crack-pattern (visual). (b) Predicted crack-pattern and crack-direction plate-hinge model (Jensen, 2016).

Furthermore, the plate-hinge model is used to simulate the fracture behavior of a simply supported reinforced two-way concrete slab and compared to experimental results reported in Bach and Graf (1915). Although the plate-hinge acts slightly stiffer compared to experimental results, shown in Figure 3.12, a realistic overall crack-pattern can be predicted with the plate-hinge model, as shown in Figure 3.13.

The study carried out by Jensen (2016) shows that the proposed hinge may be implemented into a plate element for three-dimensional analysis with some encouraging results. However, considering the importance of providing a realistic description of soil-structure interaction and cyclic crack behavior in pavement analysis, this study will focus these two latter topics in subsequent chapters. It is then envisaged that the models developed can be implemented into a plate element for analysis of more realistic pavement systems.

# Chapter 4

## Cracked-hinge beam on soil

### 4.1 Introduction

For analysis of fracture in slabs on grade, the interaction between structure and foundation are commonly idealised as independent linear elastic springs or so-called Winklers foundation. The Winkler model is simple and practical to solve many engineering problems, however, care should be taken in application of such a model, as it essentially suffers from a complete lack of continuity in the supporting medium. Moreover, another fundamental problem with the use of this model is to determine the stiffness of the elastic springs used to replace the soil. The problem becomes two-fold since the numerical value of the Winkler stiffness not only depends on the nature of the soil foundation, but also on the dimensions of the slab and the loaded area.

The deficiency of the Winkler model in depicting the continuous behavior of real soil masses has led to the development of many other simple soil response models. These models possess some of the characteristic features of continuous elastic solids (Kerr, 1964; Hetenyi, 1966). This class of mathematical models have an additional constant parameter and hence, they are called two-parameter foundation models.

This chapter presents a short review of two-parameter models reported in the literature and evaluate their applicability for FE implementation and use in engineering design. Moreover, this chapter presents a cohesive cracked-hinge beam resting on a two parameter foundation for analysis of fracture in one-way slabs on grade supported by an elastic medium, see Figure 4.1. The numerical hinge may be incorporated into a plane beam element in a consistent and straightforward manner as demonstrated in Chapter 3. The two-parameter spring foundation model is implemented in beam interpolation

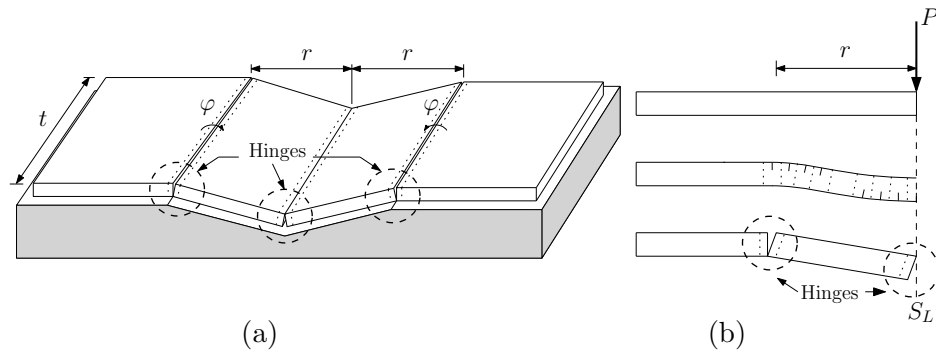


**Figure 4.1:** Hinge model implemented in one-way slab on grade structure: (a) sketch of slab and yield lines according to conventional yield-line theory (Baumann and Weisgerber, 1983), where  $t$  is the out of plane slab thickness,  $r$  is the minimum distance between potential yield-lines and  $\varphi$  is the angle of localised crack rotations and (b) deformation of unloaded, cracking and fully cracked slab showing cracks (solid line) and hinges (dotted line).

functions creating a consistent and simple tool for use in non-linear analysis of slab on grade structures.

## 4.2 Soil-structure interaction models

### The Winkler model

In the Winkler model, the soil foundation properties are idealised as independent springs on a rigid base neglecting the shear stiffness of the soil, as shown in Figure 1.13 (a). The Winkler model is simply a mathematical statement that the subgrade reaction,  $q_i$ , and normal displacement,  $w_i$ , at some arbitrary point  $i$  are linearly related according to the following simple relationship:

$$q_i = k_i w_i \quad (4.1)$$

where  $k_i$  is defined as the Winkler 'coefficient of subgrade reaction' at point  $i$ .  $k_i$  has the dimensions of force per length cubed although it is often more usefully visualised as force per length (dimensions of an axial-spring constant) per unit area supported by that imaginary spring.

## Two-parameter models

### Mechanical models

Mechanical two-parameter models have been proposed in the literature, where interaction between the spring elements is provided by either elastic membranes (Filonenko-Borodich, 1940), elastic layers capable of pure shear deformation (Pasternak, 1954; Kerr, 1965; Loof, 1965) or elastic beams (Hetényi, 1946). Basically, the models proposed by Filonenko-Borodich, Pasternak and Loof are mathematically equivalent and differ only in the definition of their parameters (Zhaohua and Cook, 1983). These two-parameters models define the surface displacement  $w(x, y)$  of the foundation in the vertical  $z$ -direction due to a pressure  $q(x, y)$  given as

$$q(x, y) = kw(x, y) - k_1 \nabla^2 w(x, y) \quad (4.2)$$

where

$$\nabla^2 = \frac{\partial^2}{\partial x^2} + \frac{\partial^2}{\partial y^2} \quad (4.3)$$

is the Laplace's differential operator in Cartesian coordinates,  $k$  is the Winkler stiffness and  $k_1$  is the second parameter. The Pasternak model is depicted in Figure 1.14 (a).

For two-dimensional problems (4.2) reduces to

$$q(x) = kw(x) - k_1 \frac{d^2}{dx^2} w(x) \quad (4.4)$$

It can also be shown that (4.4) is a possible mechanical model for the 'generalised foundation model'. In this formulation it is assumed, in addition to the Winkler model where at each point the pressure  $q$  is proportional to the deflection  $w$ , that also the moment is proportional to the angle of rotation  $\theta$  (Kerr, 1964; Zhaohua and Cook, 1983).

Hetényi (1946) proposed an elastic plate as interconnection, replacing the latter term in (4.2) with  $D\nabla^4 w(x, y)$ , where  $D$  is the flexural rigidity of the plate. Totsky (1981) suggested a multi-layered system consisting of a series of alternating plate elements and springs.

### Continuum approach

Vlasov and Leontev (1960) proposed a simplified continuum approach to the formulation of the soil model based on a variational method depicted in Figure 1.14 (b). By imposing certain restrictions upon the possible distribution of displacements in an elastic layer to an appropriate mode shape,  $\psi(z)$ , a soil response function of similar character to (4.2) can be obtained.

In the case of plane strain in the  $xz$ -plane, the state of strain in the foundation layer is assumed to be such that the displacement components are

$$u(x, z) = 0 \quad ; \quad w(x, z) = w(x)\psi(z) \quad (4.5)$$

where  $\psi(z)$  is a function describing the variation of displacement  $w$  in the  $z$ -direction. Both linear and exponential variations have been proposed

$$\psi(z) = 1 - \frac{z}{H} \quad ; \quad \psi(z) = \frac{\sinh[\gamma(H-z)/L]}{\sinh[\gamma H/L]} \quad (4.6)$$

where  $H$  is the depth of the foundation layer, and  $L$  and  $\gamma$  are constants. The details of the general variational method of analysis together with solutions to many practical problems are given in Vlasov (1966).

Applying the stress-strain relations for plane strain conditions and the principle of virtual work the response function is given as

$$q(x) = kw(x) - 2t \frac{d^2}{dx^2} w(x) \quad (4.7)$$

with the parameter  $k$  and  $2t$

$$k = \frac{E}{(1-\nu^2)} \int_0^H \left( \frac{d\psi}{dz} \right)^2 dz \quad ; \quad 2t = \frac{E}{2(1+\nu)} \int_0^H (\psi)^2 dz \quad (4.8)$$

where  $E = \frac{E_s}{(1-\nu_s^2)}$  is the Young's modulus, and  $\nu = \frac{\nu_s}{(1-\nu_s)}$  is the Poisson's ratio of the soil foundation for plain strain conditions.

Reissner (1958, 1967) pioneered a straightforward application of the simplified continuum concept assuming a foundation layer in which all in plane stresses are negligibly small;  $\sigma_x = \sigma_y = \tau_{xy} = 0$ , and the horizontal displacements at the top and bottom surfaces of the foundation are zero. The governing equation of the Reissner simplified continuum model for an isotropic, homogeneous linear-elastic continuum of finite thickness  $H$  is

$$q(x, y) - \frac{GH^2}{12E} \nabla^2 q(x, y) = \frac{E}{H} w(x, y) - \frac{GH}{H} \nabla^2 w(x, y) \quad (4.9)$$

where  $E$  is the Young's modulus,  $\nu$  is the Poisson's ratio and  $G$  is the shear modulus of the soil.

The model proposed by Reissner and the Modified Pasternak model proposed by Kerr (1965) are mathematically equivalent as approximations for an elastic continuum. The governing equation for the Modified Pasternak model for two-dimensional problems is given as

$$p(x) - \frac{G_p}{k_u + k_l} \frac{d^2}{dx^2} p(x) = \frac{k_u \cdot k_l}{k_u + k_l} w(x) - \frac{G_p \cdot k_u}{k_u + k_l} \frac{d^2}{dx^2} w(x) \quad (4.10)$$

where  $k_u = 4E/H$  is the upper spring stiffness,  $k_l = 4E/3H$  is the lower spring stiffness and  $G_p = 4GH/9$  is the stiffness of the shear layer. The equivalent stiffness  $k_{eq}$  of the two springs acting in series is equal to

$$k_{eq} = \frac{1}{\frac{1}{k_u} + \frac{1}{k_l}} = \frac{1}{\frac{H}{4E} + \frac{3H}{4E}} = \frac{1}{\frac{4H}{4E}} = \frac{E}{H} \quad (4.11)$$

### Interpretation of foundation model parameters

The disadvantage with the mechanical two-parameter models is that it is difficult to interpret exactly what soil material properties or characteristics are reflected in the various mechanical elements. This is especially true for the plate in the Hetényi model and the tensioned membrane in the Filonenko-Borodich model as there is no behavioral pattern of actual soil materials that can be related intuitively to either of these.

The Vlasov model is based upon a solid theoretical analysis and explicit formulations of the two parameters can be obtained from an approximation of elastic analysis. Assuming a simple linear variation of  $\psi(z)$  the model parameters from (4.8) are given as

$$k = \frac{E}{H(1 - \nu^2)} \quad ; \quad t = \frac{EH}{12(1 + \nu)} \quad (4.12)$$

For relatively deep soil media where the normal stresses are likely to vary with depth, it is possible to use a non-linear variation of  $\psi(z)$  including an additional parameter  $\gamma$ . However, experimental evidence for  $\gamma$  is almost nonexistent and thus another level analysis is needed to determine the model parameters.

Jones and Xenophontos (1977) established a relationship between the parameter  $\gamma$  and the displacement characteristics. Subsequently, Vallabhan and Das (1988) proposed a methodology to determine the parameter  $\gamma$  as a function of the characteristic of the beam and the foundation, using an

iterative procedure, referred to as the 'Modified Vlasov model'. Since  $\gamma$  is not known a-priori, the solution technique for parameters evaluation is an iterative process which depends upon the value of the parameter  $\gamma$ , see e.g. Vallabhan and Das (1988, 1991); Turhan (1992)

Due to the mode shape function introduced and the additional analysis steps the physical interpretation of the Vlasov model parameters becomes unclear. Another derivation is given by Ting (1973) considering the Pasternak model and (4.6), resulting in the following expressions

$$k = \int_0^H \frac{E}{(1 - \nu^2)} \left[ \frac{d\psi}{dz} \right]^2 dz \quad ; \quad G_p = \int_0^H \frac{E}{2(1 + \nu)} [\psi]^2 dz \quad (4.13)$$

These expressions for  $k$  and  $G_p$  are equivalent to (4.8). Moreover they are also valid of inhomogeneous elastic layers.

## Finite element implementation

There are reasons for the extensive use of the Winkler's idealisation in routine practice. The most significant, practical reason is that it allows the subgrade reaction,  $q$ , to be eliminated as a variable in the problem solution. This allows easy implementation in structural analysis software (Horvath, 2002).

Similarly, implementation of mechanical spring models given in (4.4) and (4.7) is straightforward. This can be visualised considering a simple beam element resting on four discrete springs, as shown in Figure 4.2 (a).

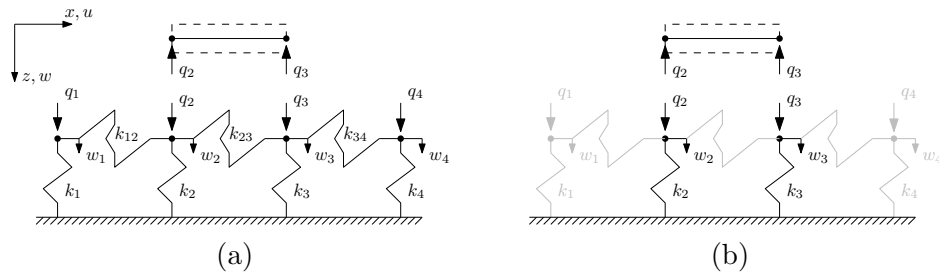


**Figure 4.2:** Principal 1-D spring foundation models: (a) two-parameter model showing four Winkler springs  $k_1 - k_4$  interconnected by shear springs  $k_{12} - k_{34}$  and subjected to external loading from a single beam element, representing the structure. (b) Winkler model showing four springs  $k_1 - k_4$ , whereof two are inactive (gray) as no load is applied at these points.

The springs are only affecting the structure in the vertical direction. Every spring is attached to two nodes, but since the lower nodes are fixed, those

nodes can be removed from the equations. The stiffness matrix for the simple 1-D spring model is given as

$$\begin{bmatrix} q_1 \\ q_2 \\ q_3 \\ q_4 \end{bmatrix} = \left( \begin{bmatrix} k_1 & 0 & 0 & 0 \\ 0 & k_2 & 0 & 0 \\ 0 & 0 & k_3 & 0 \\ 0 & 0 & 0 & k_4 \end{bmatrix} + \begin{bmatrix} k_{12} & -k_{12} & 0 & 0 \\ -k_{12} & k_{12} + k_{23} & -k_{23} & 0 \\ 0 & -k_{23} & k_{23} + k_{34} & -k_{34} \\ 0 & 0 & k_{34} & -k_{34} \end{bmatrix} \right) \begin{bmatrix} w_1 \\ w_2 \\ w_3 \\ w_4 \end{bmatrix} \quad (4.14)$$

As a special case the two-parameter model reduces to the Winkler model for  $k_{12} - k_{34} = 0$ . The stiffness matrix for the simple four node system then yields

$$\begin{bmatrix} q_1 \\ q_2 \\ q_3 \\ q_4 \end{bmatrix} = \begin{bmatrix} k_1 & 0 & 0 & 0 \\ 0 & k_2 & 0 & 0 \\ 0 & 0 & k_3 & 0 \\ 0 & 0 & 0 & k_4 \end{bmatrix} \begin{bmatrix} w_1 \\ w_2 \\ w_3 \\ w_4 \end{bmatrix} \quad (4.15)$$

where  $q_1$  and  $q_4$  and thus  $w_1$  and  $w_4$  are zero, as these points are outside the loaded region, i.e. no nodes 'outside' the beam geometry are added to the system of equations.

The Reissner model and the Modified Pasternak model given in (4.9) and (4.10), respectively, are less attractive with regard to FE implementation. This is because the incompressible shear layer cannot be modeled with standard finite elements. However, as mentioned in Section 4.2, the tensioned membrane is mechanically equivalent to an undeformed incompressible shear layer. Consequently, Horvath and Colasanti (2011) proposed the following formulation for implementation in FE software

- (i) Upper layer of linear springs of uniform stiffness  $4E/H$ .
- (ii) Plate element with zero flexural stiffness,  $D$ , to approximate a membrane under a constant tensile force per unit width,  $T = 4GH/9$ , around all of it's sides.
- (iii) Lower layer of linear springs of uniform stiffness  $4E/3H$ .

In addition, it is necessary to use a non-linear analysis to obtain the proper behavior of the membrane (plate) under tension. The model proposed by Horvath and Colasanti (2011) is also referred to as the 'hybrid foundation model'. A more direct approach for implementing this class of multi-layered spring systems was proposed by Khazanovich and Ioannides (1994) who implemented the Totsky-model in the commercial FE software ISLAB2000<sup>1</sup>.

## Summary

The mechanical and simplified continuum approach for idealisation of soil-structure interaction possesses both advantages as well as disadvantages:

- (i) Structural elements in the mechanical models are easy to implement in practice. However, interpretation of how soil foundation material properties and characteristics are reflected in the various elements in such models can be difficult.
- (ii) In the Vlasov model a mode shape function is used to define how vertical displacements vary as a function of depth. The model has a consistent format, however, calibration of the model requires additional parameters and analytical sophistication. This introduces another level of approximation and judgement into the solution process.
- (iii) In contrast to the mechanical approach the soil parameters are straightforward to specify for the Reissner elastic continuum model, but implementing such a model is problematic (Horvath and Colasanti, 2011). The format of this model is less intuitive compared to mechanical spring models. Moreover, complexity is added to the implementation procedure using 'pseudo-elements' and additional analysis steps.

Several recent efforts have been made to implement mechanical models that are more sound and logic than the Winkler model. However, no foundation model has yet replaced the Winkler model and achieved a reasonably widespread level of acceptance among design engineers (Horvath, 2002; Colasanti and Horvath, 2010). In this aspect, the Winkler foundation with shear interaction is mechanically a logical extension of the Winkler model and analytically the next higher approximation (Kerr, 1965). This model offers an attractive alternative to the elastic solid continuum by providing a degree of shear interaction between adjacent soil elements while it remains

---

<sup>1</sup>ISLAB 2000 - an extension and improvement of the ILLI-SLAB and ILSL2

relatively simple to analyse (Ioannides, 2006). Moreover, implementation of such a model in commercial FE codes is straightforward using discrete spring elements as shown in (4.14) and Figure 4.2 (a).

## 4.3 Two-parameter coupled spring model

### The mechanics of the two-parameter model

The coupling between two Winkler springs is modeled with a second spring transmitting a shear force  $T$  per unit width as shown in Figure 4.3. This force is associated with the difference in vertical displacements  $w$  between the elements. Only the two-dimensional problem is considered here.

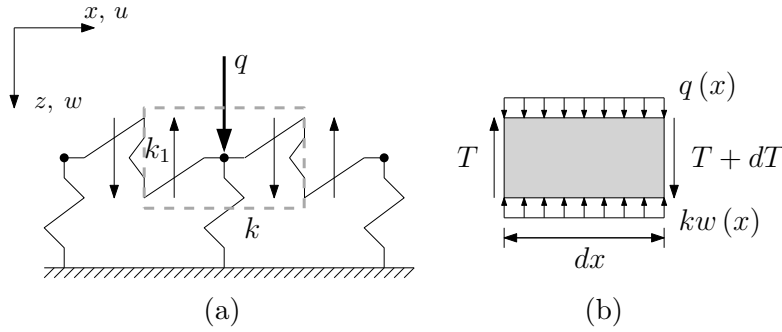


**Figure 4.3:** Mechanical model of two-parameter spring foundation, where  $k$  is the Winkler stiffness and  $k_1$  is the second parameter stiffness.

A simple assumption is, that the shear force is proportional to the difference in displacements between two consecutive elements and therefore to the first derivative of the displacement, where  $k_1$  is the second parameter. From the equilibrium of an element the differential equation governing the deflections of the soil surface is given in (4.4). Introducing the terms  $\alpha^2 = \frac{k_1}{k}$  and  $\beta = \frac{1}{\alpha}$ , the general solution yields

$$w = \frac{q}{k} + C_1 e^{-\beta x} + C_2 e^{\beta x} \quad (4.16)$$

First, investigating the case of a point load, the homogeneous equation reads

$$-w'' + \beta^2 w = 0 \quad (4.17)$$

with the general solution

$$w = C_1 e^{-\beta x} + C_2 e^{\beta x} \quad (4.18)$$

In the solution for large positive values of  $x$  the term with the coefficient  $C_1$  represents the decreasing displacement due to the influence of the load. The term with  $C_2$  does the same for large negative values of  $x$ . The solution for positive  $x$  can be found, inserting the boundary condition  $w \rightarrow 0$  for  $x \rightarrow \infty$  in (4.18), i.e.

$$w(x \rightarrow \infty) : C_1 e^{-\beta x} \rightarrow 0 \quad \wedge \quad C_2 e^{\beta x} \rightarrow \infty \Rightarrow C_2 = 0 \quad (4.19a)$$

For areas carrying no load the solution for positive  $x$  is

$$w = C_1 e^{-\beta x} \quad (4.20)$$

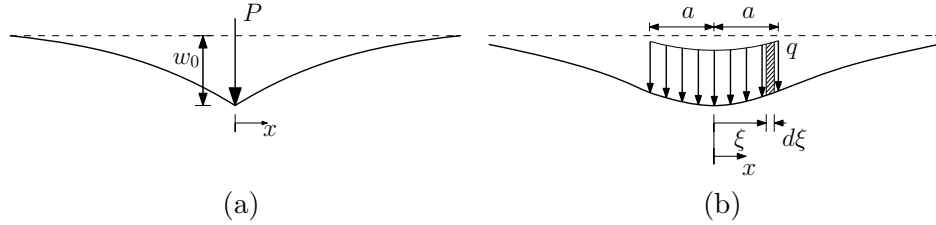


**Figure 4.4:** Sketch of elastic isotropic continuum foundation subjected to (a) a point load  $P$  and (b) a distributed load  $q$ .

In the case of a point load  $P$ , as shown in Figure 4.4 (a), the spring resistance under the load is an order of magnitude smaller than the load. All the bearing capacity must therefore be provided by the adjacent material. The difference in shear force to the right due to the point load in  $x = 0$  must therefore be equal to half the magnitude of the point load, giving the relations

$$\Delta T = -\frac{P}{2} \quad (4.21a)$$

$$\Delta T = k_1 \Delta w' = \Delta T = k_1 w'(0) \quad (4.21b)$$

$$w'(0) = -\beta C_1 e^{-\beta \cdot 0} = -\beta C_1 \quad (4.21c)$$

Combining (4.21a), (4.21b) and (4.21c) the coefficient  $C_1$  can be found

$$-\frac{P}{2} = -k_1 \beta C_1 \rightarrow C_1 = \frac{P}{2k_1 \beta} \quad (4.22)$$

Applying the term  $\alpha^2 = \frac{k_1}{k}$  (4.22) can be rewritten as

$$C_1 = \frac{P}{2\alpha^2 k \frac{1}{\alpha}} = \frac{P}{2\alpha k} \quad (4.23)$$

giving the full expression for the displacement for positive  $x$

$$w(x) = \frac{P}{2k\alpha} e^{-\beta x} \quad (4.24)$$

In the case of a uniform load over a strip  $l = 2a$ , as shown in Figure 4.4 (b), the solution can be obtained by integration of the point load over the loaded strip. Inserting  $\alpha = \frac{1}{\beta}$  the differential equation can be written as:

$$w = \frac{\beta q d \xi}{2k} e^{-\beta(l+x)} \text{ for } \xi \geq l \quad \text{and} \quad w = \frac{\beta q d \xi}{2k} e^{-\beta(l-x)} \text{ for } \xi \leq l \quad (4.25)$$

Integration over the loaded strip then gives

$$\begin{aligned} w_{\xi \leq l} &= \int_{\xi=-a}^{\xi=x} w(x-\xi) d\xi + \int_{\xi=x}^{\xi=a} w(\xi-x) d\xi \\ &= \frac{\beta q}{2k} \left[ \int_{-a}^x e^{-\beta(x-\xi)} d\xi + \int_x^a e^{-\beta(\xi-x)} d\xi \right] \\ &= \frac{\beta q}{2k} \left[ \left( -\frac{1}{\beta} e^{-\beta(x-\xi)} \right)_{-a}^x + \left( -\frac{1}{\beta} e^{-\beta(\xi-x)} \right)_x^a \right] \end{aligned} \quad (4.26a)$$

$$\begin{aligned} w_{\xi \geq l} &= \int_{\xi=-a}^{\xi=a} w(x-\xi) d\xi \\ &= \frac{\beta q}{2k} \left[ \int_{-a}^a e^{-\beta(x-\xi)} d\xi \right] \\ &= \frac{\beta q}{2k} \left[ \left( -\frac{1}{\beta} e^{-\beta(x-\xi)} \right)_{-a}^a \right] \end{aligned} \quad (4.26b)$$

which yields the expressions

$$w(x) = \frac{q}{2k} [2 - e^{-\beta(x+a)} - e^{-\beta(a-x)}] \quad \text{for } x \leq |a| \quad (4.27a)$$

$$w(x) = -\frac{q}{2k} [e^{-\beta(x+a)} - e^{-\beta(a-x)}] \quad \text{for } x \geq |a| \quad (4.27b)$$

the condition  $x \leq |a|$  and  $x \geq |a|$  symbolises if the displacement is calculated inside or outside the loaded area, respectively.

Expressions for points of interest can then be established, i.e. the displacement at the center, the displacement at the edge and the curvature at the centre of the loaded area

$$w(0) = \frac{q}{k} [1 - e^{-\beta a}] \quad (4.28a)$$

$$w(a) = \frac{q}{2k} [1 - e^{-2\beta a}] \quad (4.28b)$$

$$w''(0) = \frac{\beta^2 q}{k} [e^{-\beta a}] \quad (4.28c)$$

## Foundation model parameters

In order to obtain the necessary foundation model parameters, this study presents a simple methodology, combining the two-parameter model presented in the section above and the elastic continuum theory. The problem of the elastic stress field within a semi-infinite medium loaded by an infinitely long edge perpendicular to the plane delimiting the loaded medium has been solved by Flamant (1892) using Boussinesq's solution (Timoshenko et al., 1970). The surface displacement in the vertical direction can be written as

$$w_x = \frac{2P}{\pi E} \ln \left( \frac{d}{|x|} \right) - \frac{(1-\nu)P}{\pi E} \quad (4.29)$$

where  $P$  is the point load,  $E = \frac{E_s}{(1-\nu_s^2)}$  is the Young's modulus, and  $\nu = \frac{\nu_s}{(1-\nu_s)}$  is the Poisson's ratio of the soil foundation,  $|x|$  is the numerical value of  $x$  (distance from the loaded point) and  $d$  is a rigid body constant found from assuming zero vertical displacements at a distance  $x = d$ .

Using the superposition technique (4.29) can be integrated to obtain expressions for the surface displacements for a uniformly distributed load given as

$$w(x) = -\frac{2q}{\pi E} \left[ (x-a) \ln \left( \frac{d}{|a-x|} \right) + (-a-x) \ln \left( \frac{d}{|x+a|} \right) + a(\nu-1) \right] \text{ for } x \leq |a| \quad (4.30a)$$

$$w(x) = -\frac{2q}{\pi E} \left[ (x-a) \ln \left( -\frac{d}{a-x} \right) + (-a-x) \ln \left( \frac{d}{|x+a|} \right) + a(\nu-1) \right] \text{ for } x \geq |a| \quad (4.30b)$$

Expressions for points of interest can then be established, i.e. the displacement at the center, the displacement at the edge and the curvature at the centre of the loaded area

$$w_0 = \frac{2qa}{\pi E} \left[ 2 \ln \left( \frac{d}{|a|} \right) + (1-\nu) \right] \quad (4.31a)$$

$$w_a = \frac{2qa}{\pi E} \left[ 2 \ln \left( \frac{d}{|2a|} \right) + (1-\nu) \right] \quad (4.31b)$$

$$w_0'' = -\frac{4q}{\pi E a} \quad (4.31c)$$

In the present study, the response of the slab and the influence of model parameters on crack initiation and propagation are of primary interest. In this aspect the vertical displacements and the curvature of the foundation are important features due to localisation of cracks and the increasing soil stresses near the crack front during progressive cracking. Thus, combining these measures for calibration at different positions below the slab is found to give the most accurate prediction of the model parameters.

Based on the equations above the two-parameter model can now be calibrated analytically; first, the theoretical displacements and curvature at the centre and displacements at the edge of the distributed load can be found from (4.31a)-(4.31c) and inserted in the relevant simplified expressions, i.e. (4.28a)-(4.28c). A simple procedure is adopted here keeping one parameter constant, e.g.  $k_1 \rightarrow k_1^{w_0} = k_1^{w_0''}$ . The equation is then solved iteratively for  $k$  until  $k^{w_0} = k^{w_0''}$ .

In order to evaluate the influence of the different calibration methods a uniformly distributed load  $q$  with load strip length  $a$  of 1.0 m, is applied

**Table 4.1:** Calibrated foundation model parameters  $k$  and  $k_1$  showing the coefficient of determination,  $R^2$ , comparing the three two-parameter models to the analytical model.

Method	Criteria	$k$ (N/mm <sup>2</sup> )	$k_1$ (N)	$R^2$ ( $x \leq 10$ m)	$R^2$ ( $x \leq 1.0$ m)
1.	$w_0$ & $w_0''$	0.0076	$6.33 \cdot 10^7$	0.976	0.999
2.	$w_0$ & $w_a$	0.0104	$3.95 \cdot 10^7$	0.928	1.000
3.	$w_0''$ & $w_a$	0.0086	$6.18 \cdot 10^7$	0.978	0.992
Vlasov	-	0.0064	$1.54 \cdot 10^8$	0.941	0.996
Reissner	-	0.0046	$4.12 \cdot 10^8$	-	-

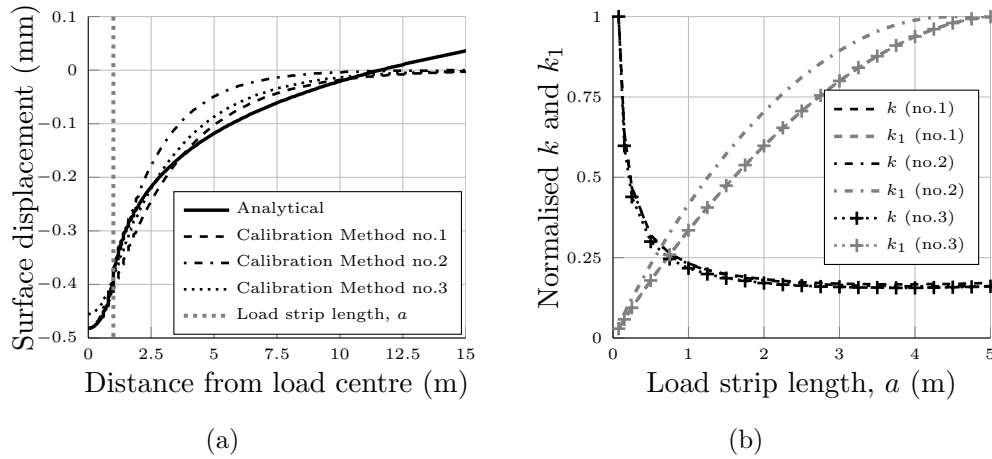


**Figure 4.5:** (a) Comparison of analytical and two-parameter foundation model for the three different calibration techniques (b) influence of load strip length  $a$  on model parameters  $k$  and  $k_1$  for a distributed load (normalised with respect to maximum value obtained in interval 0-5 m). Uniformly distributed load:  $q=25,000$  N/m. Soil properties:  $E_s=100$  MPa,  $\nu_s=0.35$ ,  $t=1$  m and  $d=25$  m.

directly on the soil surface. The resulting calibrated foundation model parameters can be found in Table 4.1.

Comparing the vertical surface displacements for the three different two-parameter models to the analytical model, shown in Figure 4.5 (a) and Table 4.1, it is observed that Calibration Method no. 1 gives a good overall fit. Method no. 2 gives the closest prediction of the surface displacements in the loaded region, i.e.  $x \leq 1.0$  m, whereas method no. 3 yields realistic results far from the loaded region. It is also observed from in Figure 4.5 (b) that increasing the load strip length results in a decreased  $k$ , stabilising at app.

$a=1-2$  m. Whereas  $k_1$  increases with increasing load strip length, stabilising at app.  $a=4-5$  m.

## Implementation of two-parameter model

The hinge model presented in Chapter 3 is extended to pavement applications by implementing the proposed two-parameter foundation model into a beam element for analysis of one way slabs on grade. Based on the contribution to the variation in internal work  $\delta\Omega$  from the beam and the two-parameter foundation, and the potential work of external forces  $\delta W$  from point and surface loads, the principle of virtual work for the system can be established

$$\int_V \delta \boldsymbol{\varepsilon}^T \boldsymbol{\sigma} + \delta \mathbf{u}^T k \mathbf{u} + \delta \boldsymbol{\theta}^T k_1 \boldsymbol{\theta} dV = \int_S \delta \mathbf{u}^T \mathbf{f} dS + \sum_i \delta \mathbf{u}_i^T p_i \quad (4.32)$$

where  $V$  is the structural volume,  $S$  is the surface area,  $\delta \mathbf{u}$  and  $\delta \boldsymbol{\theta}$  are the displacement and rotational variations, respectively,  $\mathbf{f}$  is the surface traction vector,  $p_i$  is a concentrated (nodal) load and  $\delta \mathbf{u}_i$  is the associated (nodal) displacement variation. The contribution from the second parameter spring is here given on a general form considering  $k_1$  as a rotational stiffness.

The beam element and two-parameter foundation contribution to the internal nodal force,  $\mathbf{q}$ , is then given by the expression

$$\mathbf{q} = \int_0^{L_e} \mathbf{B}^T \boldsymbol{\sigma} dx + \int_0^{L_e} \mathbf{N}^T k \mathbf{I} \mathbf{N} dx \mathbf{v}_e + \int_0^{L_e} \mathbf{G}^T k_1 \mathbf{G} dx \mathbf{v}_e \quad (4.33)$$

where  $L_e$  is the length of the element and  $\mathbf{v}_e$  is the global degrees of freedom (dof) element displacements. The displacement interpolation matrix and the strain distribution matrix  $\mathbf{N}$  and  $\mathbf{B}$  are given in (3.19) and (3.20), respectively.

The matrix  $\mathbf{I} = \begin{bmatrix} 0 & 0 \\ 0 & 1 \end{bmatrix}$  is used to omit axial terms in  $\mathbf{N}$ . Including axial terms in (4.33) would be equivalent to introducing a frictional contact in the system, the constitutive behavior of which should be controlled by another parameter, e.g. describing the frictional behavior, see Section 4.6.

The second-parameter matrix,  $\mathbf{G} = \mathbf{N}^T \mathbf{I}$  is given as

$$\mathbf{G} = \begin{bmatrix} 0 & 0 \\ 0 & (-6s + 6s^2)/L_e \\ 0 & 1 - 4s + 3s^2 \\ 0 & 0 \\ 0 & (6s - 6s^2)/L_e \\ 0 & -2s + 3s^2 \\ 0 & 0 \end{bmatrix}^T \quad (4.34)$$

where  $s = x/L_e$  is the normalised element length,  $L_e$

The beam-element and two-parameter foundation contribution to the tangential stiffness matrix,  $\mathbf{k}_t$ , is given by the expression

$$\mathbf{k}_t = \int_0^{L_e} \mathbf{B}^T \mathbf{D}_t \mathbf{B} dx + \int_0^{L_e} \mathbf{N}^T k \mathbf{I} \mathbf{N} dx + \int_0^{L_e} \mathbf{G}^T k_1 \mathbf{G} dx \quad (4.35)$$

## 4.4 Numerical simulation of one-way slabs on grade

### Single finite slab

In order to evaluate the hinge slab model and to investigate the influence of different modeling techniques for soil-structure interactions in concrete and composite pavement systems a model representing the full continuum model is developed, hereafter referred to as the 'CZM slab' model. FE models and mechanical properties used in analysis is described in **Paper II**. Consider a single slab of cement bound granular mixture with standard dimensions ( $L/h$ ) of  $4 \times 0.4 \text{ m}^2$ , resting on a soil foundation and loaded by a concentrated force at midspan position. The numerical models are shown in Figure 4.6.

The fracture behavior of the slab is evaluated by plotting the load-crack mouth opening and load-crack length curve for the different model types, shown in Figure 4.7 and 4.8, respectively. To visualise the influence of the second parameter and to compare the two modeling techniques, the response for both the hinge slab and CZM slab resting on a Winkler foundation is

#### 4.4 Numerical simulation of one-way slabs on grade Cracked-hinge beam on soil

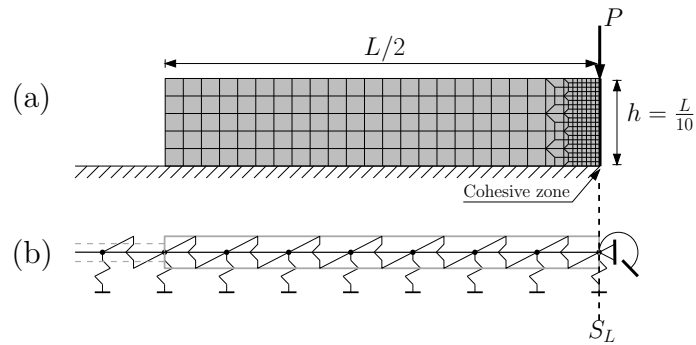


**Figure 4.6:** Sketch of FE models: (a) CZM slab model and (b) hinge slab model.

shown for reference. Moreover, an empirically calibrated Winkler model, used in design of airfield concrete pavements (FAA, 2009), is shown. Standard mechanical properties are given in **Paper II**.

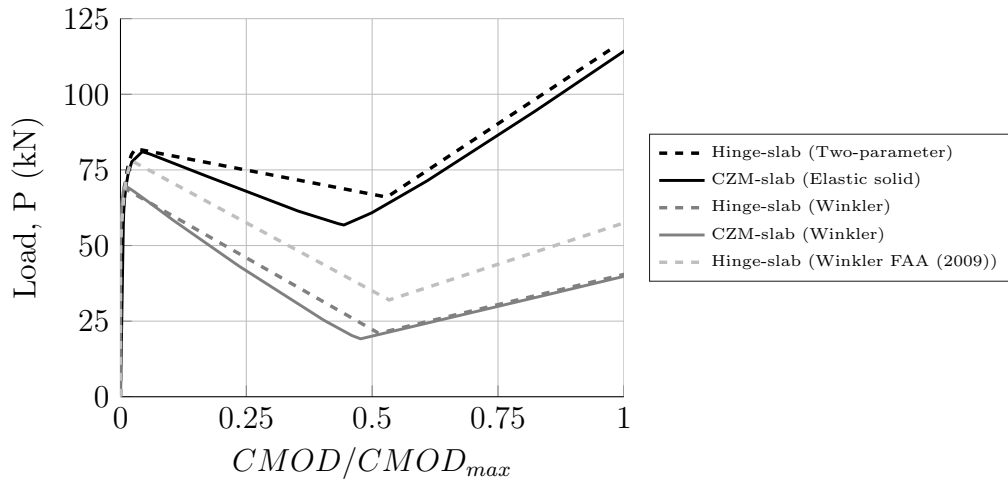


**Figure 4.7:** Comparing the structural response and fracture behaviour of the hinge slab versus the CZM slab model: load-CMOD curve (normalised with respect to maximum CMOD obtained for the CZM slab model).

It can be observed from Figure 4.7 and 4.8 that a reasonably good agreement between the hinge and CZM slab model can be obtained. Both models reflect the influence of the continuity in the soil comparing the two foundation types. By applying an empirical transfer function for converting the elastic soil properties to an equivalent 'apparent' Winkler stiffness a closer prediction of the first peak-load can be obtained. However, the post-peak

response resembles that of the analytical Winkler foundation type due to the lack of continuity between springs.

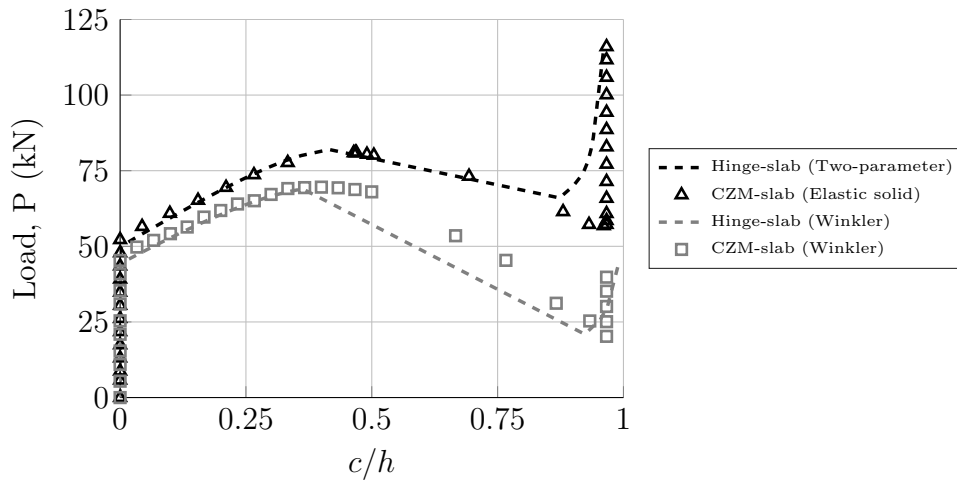


**Figure 4.8:** Comparing the structural response and fracture behaviour of the hinge slab versus the CZM slab model: load-crack length curve (normalised with respect to slab height). Where the crack length in the CZM slab model is taken as the progressive depth of damage initiation in the cohesive zone.

The difference in first peak-load and peak-load displacement is app.  $\pm 1\%$  for the two model types. The two-parameter slab hinge model slightly overestimates the post-peak residual stiffness compared to the CZM slab model. Close to perfect fit is obtained between the two modeling techniques applying only a Winkler foundation as the supporting medium. It is also observed that the load level at unloading is higher for the hinge slab model compared to the CZM slab model. This tendency is observed for both foundation model types, and can partly be regarded as an effect of the difference in modeling technique. However, this difference is also related to the foundation type and contact behavior applied.

## Infinite slab

In order to demonstrate the applicability of the numerical hinge to predict a realistic crack pattern an infinite slab ( $h=0.4$  m) resting on Winkler's foundation ( $k=0.0233$  MPa/mm) and loaded by a concentrated force at midspan position is considered. Slab displacements and internal forces decline relatively fast to zero as the distance from the load increases. Accordingly, a finite slab of 10 m ( $nel=100$ ) may replace the infinite beam. Standard material properties for the cemented material can be found in **Paper II**.

The numerical results are compared to the yield-line theory following the methodology proposed by Baumann and Weisgerber (1983) depicted on Figure 4.1 (a). The deformation of the slab during loading, i.e. before first peak, before second peak and after the second peak, is shown in Figure 4.9 (a). Load-displacement curves for the three models are plotted in Figure 4.9 (b).

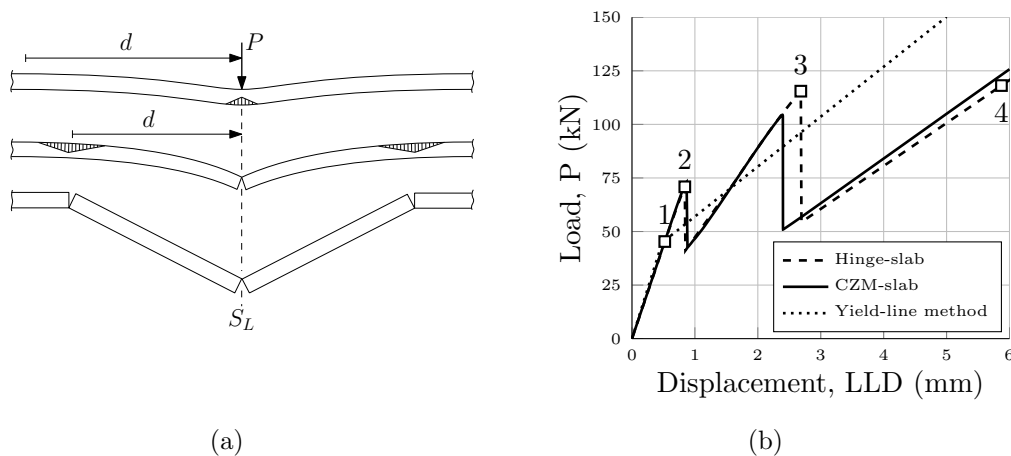


**Figure 4.9:** Comparison between modeling techniques for infinite slab: (a) Deformation of the slab during loading: before first peak, after first peak and after second peak. (b) CZM slab (solid line), hinge slab model (dashed line) and the yield-line method (dotted line) reported in Baumann and Weisgerber (1983).

It is observed from Figure 4.9 (b) that the first peak in the CZM slab model and the hinge slab model is app. 73 and 71 kN, respectively. Moreover, it is observed that the kink point on the yield-line curve is app. 45 kN, complying well with the results reported by Meda (2003), see Figure 2.3 (a). Moreover, it is found that the distance between yield-lines  $r=2.534$  m in the yield line method is approximately equal to the distance,  $d$ , from the negative peak moments to the crack at midspan in the hinge slab model at

crack-initiation (load level 1), shown in Figure 4.10 (a). Then, according to the CZM slab and hinge slab model the load continues to increase as the crack propagates before reaching the ultimate moment capacity of app. 33.3 kNm (load level 2), shown in Figure 4.10 (b).

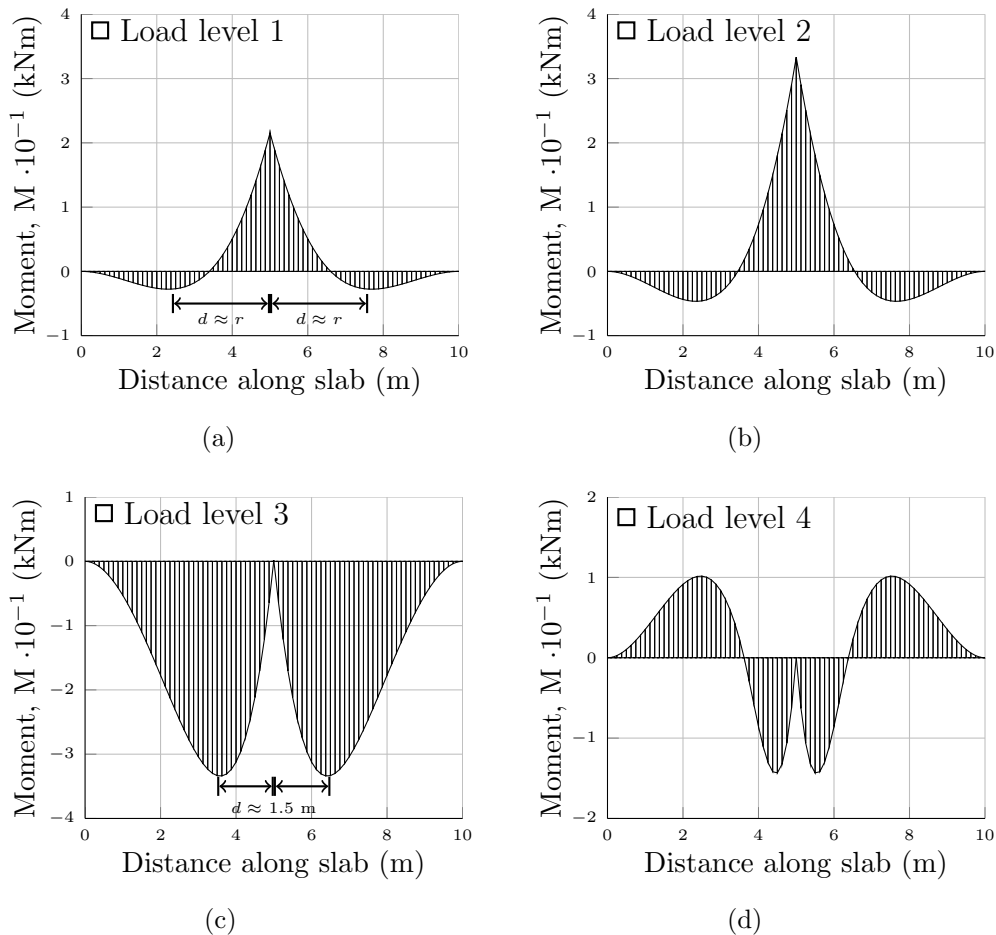


**Figure 4.10:** Predicting distance between cracks showing the moment in the hinge slab model at four different phases: (a) crack initiation, (b) first peak, (c) second peak and (d) after full crack propagation of top-down cracks, also visualising the distance between cracks equivalent to  $r$  in the yield line method.

The crack at midspan then unloads, before the load continues to increase, resulting in two top-down cracks initiating app.  $\pm 1.5$  m from the midspan position. Then, these cracks grow rapidly to the negative ultimate moment capacity of app. -33.3 kNm (load level 3), shown in Figure 4.10 (c), resulting in the second peak on the load-displacement curve. Finally, the post-peak

residual stiffness of the structure is reached (load level 4) with the moment distribution shown in Figure 4.10 (d).

The distance between cohesive zones in the CZM slab model is set to 1.5 m based on simulations with the hinge slab model. This results in a good fit between the two methods as shown in 4.9 (b). The response of the two methods is identical up to the second peak of the CZM slab model. Then, the load in the hinge slab model continues to increase due to the stiffness and stress redistribution in the hinge slab. The second peak in the two models is app. 105 and 115 kN, respectively. This difference in modeling technique is not as dominant under the concentrated load as cracks localise to one crack below the loaded point, whereas top-down cracks at a distance  $d$  is smeared over a larger area.

The present example highlights the practical use of the proposed model; as the hinge slab is able to predict the stress redistribution and stiffness during crack development. This results in a precise prediction of the crack-opening and the distance between cracks that finally localise and propagate through the thickness of the slab.

## 4.5 Evaluation of methodology

The two-parameter model possess some of the characteristic features of continuous elastic solids, as it is a simplification which cannot capture all complexities. Special care should be taken when selecting a representative load strip length  $a$  for the calibration of model parameters.

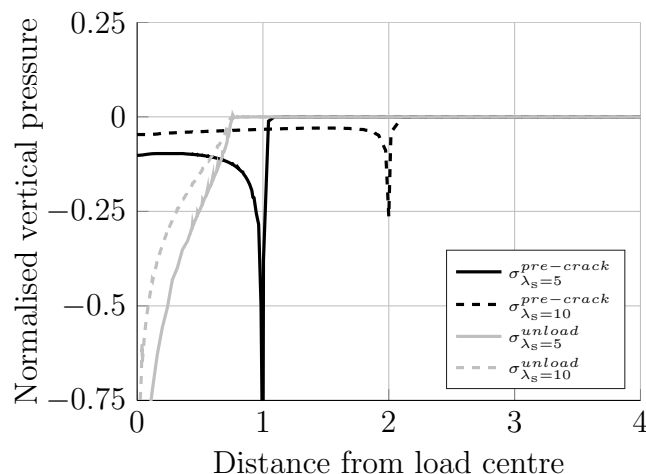


**Figure 4.11:** Vertical soil pressure of elastic solid under cemented slabs with slenderness ratio  $\lambda_s=5$  and 10 before and after unloading.

This is exemplified by plotting the vertical soil pressure below cemented slabs with different slenderness ratios (length/thickness ratio), as shown in Figure 4.11. It is observed from Figure 4.11 that the pressure will initially be distributed over the total slab length. As cracking is initiated and cracks propagate, there will only be minor changes in the overall vertical pressure profile, ignoring minor stress intensities below cracks. However, after unloading, the vertical soil pressure changes significantly and stresses will localise around the open cracks, in this case at the midspan position. Moreover, a variation in vertical pressure, and especially the vertical reaction pressure along slab edges, is expected when comparing different slab sizes. The soil pressure under short thick slabs will resemble the stress distribution under a stiff plate, whereas the vertical reaction pressure along slab edges for larger size and slender slabs will be small.

In order to capture both pre- and post-peak vertical pressure distributions in the two-parameter model considering typical slab lengths and thickness's of app. 2.0-5.0 m and 0.15-0.45 m, respectively, a fixed load strip length  $a$  of 1.0 m for calibration of foundation model parameters is applied for the present problem.

## Comparison of calibration methods

The three calibration methods proposed is evaluated in the view of load displacement behavior, as shown in the example in Figure 4.12. It is seen that all three methods adequately describe the overall structural behavior. Plotting the difference in peak-load and peak-load displacement between the hinge slab and the CZM slab, as shown in Figure 4.13, it is found that the method no. 1 and 3 fits well with a difference of app.  $\pm 2\%$  compared to the CZM slab model for  $\lambda_s \geq 10$ . Adequately good fit is also obtained for  $\lambda_s = 7.5$  (app. 5-10%). However, less consistent results are obtained for method no. 2. Moreover, for  $\lambda_s \leq 10$ , an increasing difference between models is observed for decreasing  $\lambda_s$  (maximum 26 %).

For slabs with  $\lambda_s < 10$ , the slab partially acts as a stiff plate and the influence from the adjacent soil increases. Thus, the effect of the second parameter becomes more significant resulting in increasing differences between method no. 2 compared to the other two methods, as this method only considers compatibility of vertical displacements in the two points.

From Figure 4.5 (b) it is evident that the second parameter is sensitive to the vertical pressure below the slab for the standard slab sizes studied, and that the second parameter cannot be predicted to the same level of accuracy as the Winkler stiffness. It is found that this effect results in a difference in vertical pressure along slab edges between the two model types, which

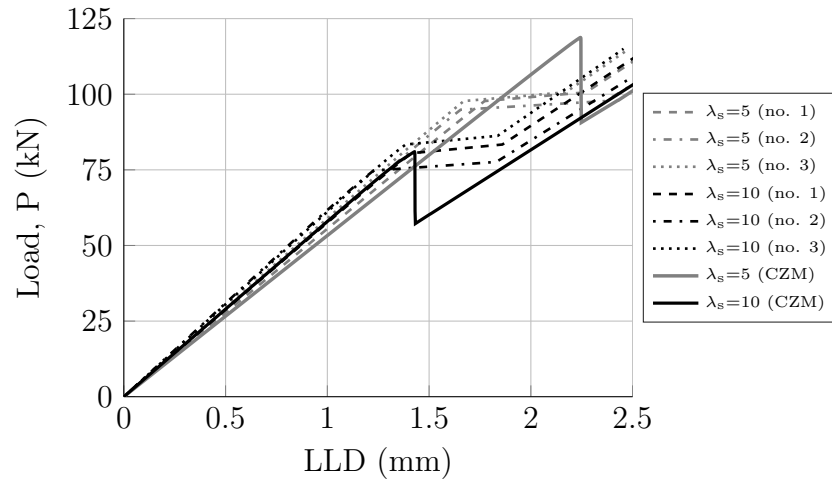


**Figure 4.12:** Evaluating calibration methods and comparing load-displacement responses for a hinge slab resting on a two-parameter foundation and a CZM slab resting on elastic solid foundation: load-displacement curves for  $\lambda_s=5$  and  $\lambda_s=10$ .

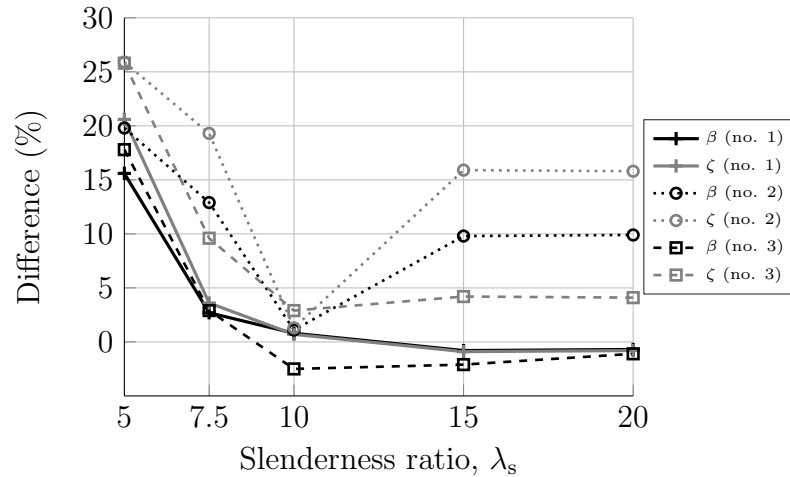


**Figure 4.13:** Evaluating calibration method and comparing load-displacement response of a hinge slab resting on a two-parameter foundation and a CZM slab resting on elastic solid foundation: difference in normalised peak-load,  $\beta$ , and peak-load displacement,  $\zeta$ , between the hinge slab and CZM slab model.

again results in a premature collapse for short stiff slabs ( $\lambda=5$ ) observed in Figure 4.12. Moreover, a somewhat higher residual stiffness after unloading is observed.

## Vlasov model parameters

The methodology for estimating model parameters as proposed in Section 4.3 does not give a direct physical interpretation of how soil foundation material properties and characteristics are reflected in the various elements. However, as mentioned in Section 4.2, the two parameters can be obtained from an approximation of elastic analysis using the Vlasov model, i.e. (4.8).

In order for this format to be simple and straightforward linear variation of  $\psi(z)$  is considered, eliminating the parameter  $\gamma$ . Thus, model parameters can be evaluated in similar fashion to the proposed methodology, e.g. by comparing the vertical surface displacements to the analytical continuum model.

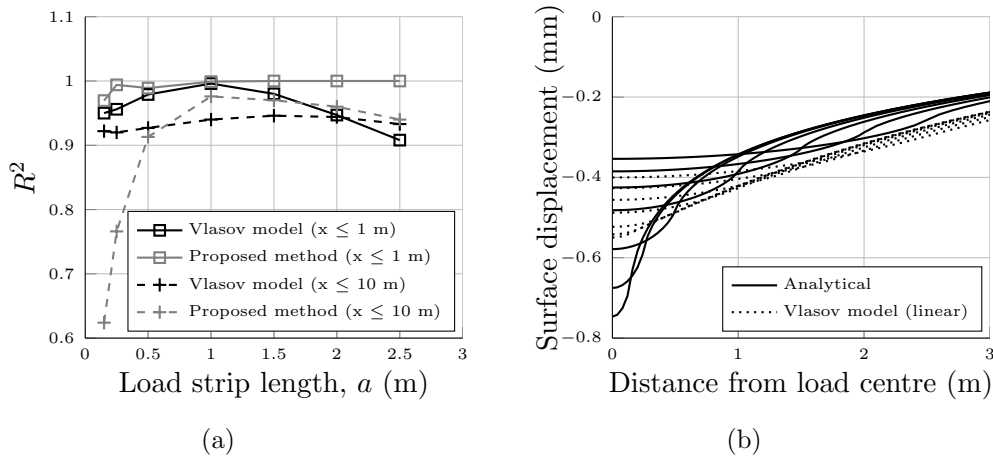


**Figure 4.14:** Evaluation of the Vlasov model: (a) Coefficient of determination  $R^2$  for the Vlasov model and the proposed method compared to the analytical model. (b) vertical surface displacements for the Vlasov model (dotted) and the analytical model (solid) for varying strip length  $a$  between 0.15 and 2.5 m.

It is observed from Figure 4.14 (a) that the Vlasov model results in a good overall fit compared to the analytical model. However, by plotting the vertical displacement profile for different load strip lengths, relatively large differences is observed in the peak region, see Figure 4.14 (b). Best fit is obtained for a load strip length of app. 1.0 m, giving  $k=0.0064$  N/mm<sup>2</sup> and  $k_1=1.54 \cdot 10^7$  N. These parameters are selected for further analysis.

The influence of using the Vlasov model compared to the proposed methodology in structural analysis is visualised in Figure 4.15.

It is observed from Figure 4.15 that the Vlasov model overestimates the stiffness of the soil by applying a linear mode shape function. Although

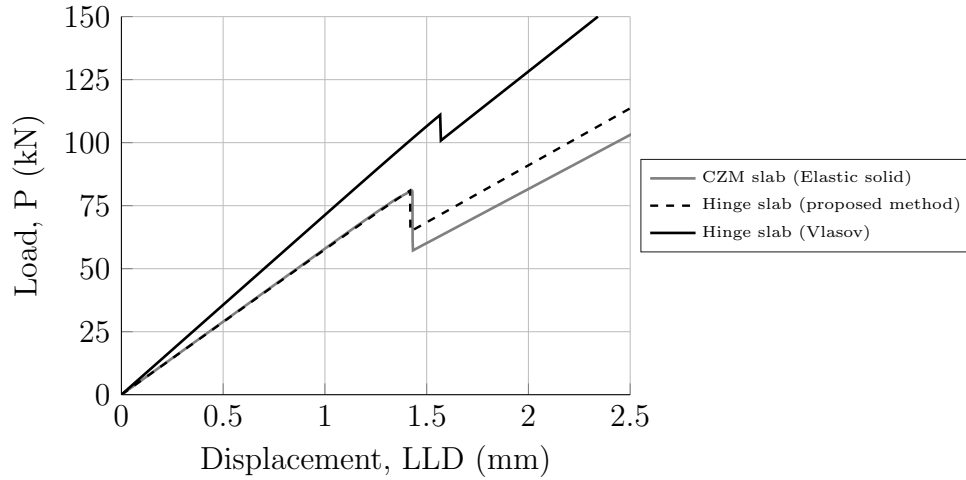


**Figure 4.15:** Comparing the structural response of the hinge slab versus the CZM slab model using the proposed calibration method and the Vlasov model with a linear mode shape function.

vertical displacements can be predicted within a 1% difference compared to the continuum model, the difference in curvature at midspan position, i.e. below the crack front, is app. 50% for the specific case. This highlights the influence of the soil response near the crack front and the need for analytical calibration techniques in order for two-parameter models to perform adequately well.

## 4.6 Non-linear behavior of soil

In the proposed engineering model the non-linear soil behavior is restricted to a simple Winkler spring model. This model was suggested by Gaedicke and Roesler (2009) and is used to simulate experimental results for beams resting on soil, as described in **Paper III**. A schematic overview of the constitutive spring behavior is shown in Figure 4.16.

This idealised spring foundation model consists of independent vertical springs with a spring stiffness coefficient,  $k_n$ , similar to a conventional Winkler model. The constitutive behavior of the vertical spring is modified to allow for separation between the beam and soil, i.e. for positive vertical displacements (tensionless spring). Moreover, the horizontal spring is implemented in the model, representing the frictional contact between soil and beam structure. The horizontal spring is modeled with a stiffness of  $k_t = k_n/10$  and a constant slip limit of  $u_t=0.5$  mm.

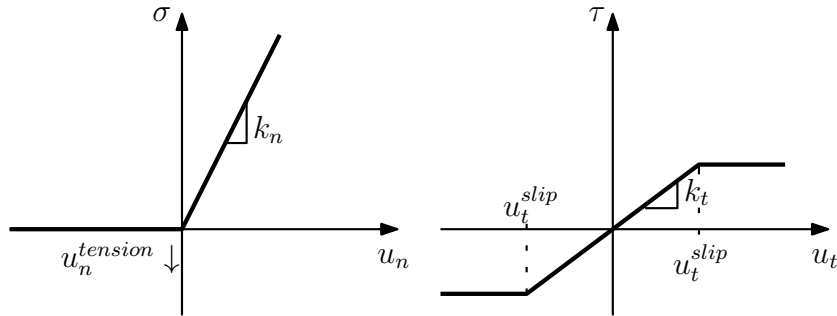


**Figure 4.16:** Constitutive behavior of Winkler spring foundation applied in Gaedicke and Roesler (2009).

The constitutive behavior shown in Figure 4.16 can be implemented including an update of the system during equilibrium iterations as shown in the modified Algorithm 4.

---

**Algorithm 4** N-R displacement control (modified)

---

Calculate:  $\mathbf{K}$

Displacement steps  $n = 1, 2, \dots, n_{max}$

$\mathbf{v}_n = \mathbf{v}_{n-1}$  and  $\mathbf{f}_n = \mathbf{f}_{n-1}$

Iterations  $i = 1, 2, \dots, i_{max}$

$\Delta \mathbf{v}_u = \mathbf{K}_{22}^{-1} (\Delta \mathbf{f}_k - \mathbf{K}_{21} \Delta \mathbf{v}_k)$

$\Delta \mathbf{f}_u = \mathbf{K}_{11} \Delta \mathbf{v}_k + \mathbf{K}_{12} \Delta \mathbf{v}_u$

**if** slip or slab rising

Update  $\Delta \mathbf{f}_k$

**end**

$\mathbf{K}_n = \mathbf{K} (\mathbf{v}_{n-1} + \Delta \mathbf{v}_n)$

$\mathbf{r}_n = \mathbf{K} \Delta \mathbf{v}_n - \Delta \mathbf{f}_n$

Stop iteration when  $\frac{\delta E_1}{\Delta E_0} < \epsilon$

$\mathbf{v}_n = \mathbf{v}_{n-1} + \Delta \mathbf{v}_n$  and  $\mathbf{f}_n = \mathbf{f}_{n-1} + \Delta \mathbf{f}_n$

End of displacement steps

---

The internal nodal force and the tangential stiffness matrix is then given

by

$$\mathbf{q} = \int_0^{L_e} \mathbf{B}^T \boldsymbol{\sigma} dx + \int_0^{L_e} \mathbf{N}^T \begin{bmatrix} k_n & 0 \\ 0 & k_t \end{bmatrix} \mathbf{N} dx \mathbf{v}_e \quad (4.36a)$$

$$\mathbf{k}_t = \int_0^{L_e} \mathbf{B}^T \mathbf{D}_t \mathbf{B} dx + \int_0^{L_e} \mathbf{N}^T \begin{bmatrix} k_n & 0 \\ 0 & k_t \end{bmatrix} \mathbf{N} dx \quad (4.36b)$$

In **Paper I** both an elasto-plastic Mohr-Coulomb model and a Coulomb friction model was used to describe the complex soil-structure interaction observed in the experiments. The latter model can be implemented following the methodology above. However, implementation of elasto-plastic soil behavior for slab fracture using mechanical two-parameter models is a topic that requires a great deal more study.

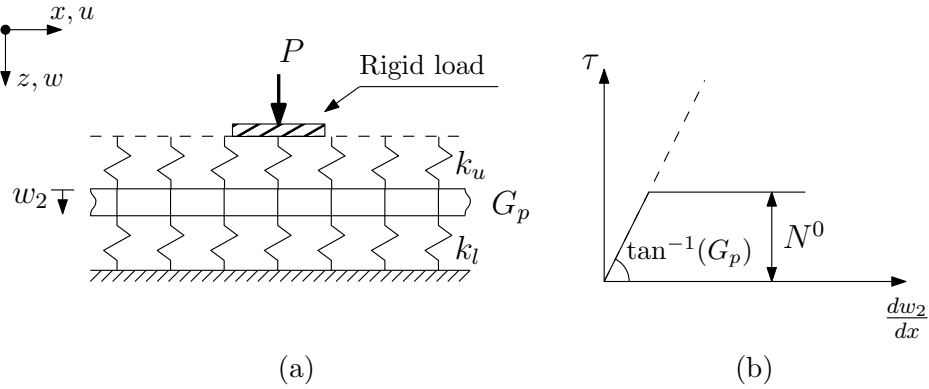


**Figure 4.17:** (a) Modified Pasternak model. (b) Elastic-perfectly plastic response of shear layer ( $N$  = shear force,  $N^0$  = yield limit of  $N$ ,  $dw_2/dx$  = shear strain).

Rhines (1969) proposed a Pasternak type of model, see Figure 4.17 (a), where the interconnecting shear layer is capable of sustaining finite shearing stress applying a elasto-plastic shear stress-strain relationship, shown in Figure 4.17 (b). Using this particular model, Rhines investigated the distribution of contact stresses below a rigid foundation structure which is subjected to symmetric load. The results indicate that including such yielding characteristics, can capture the change in the magnitude and the distribution of contact stresses, that are developed at the soil-structure interface.

The model proposed by Rhines describes a relatively simple case. Including the slab as well as the slab fracture into this model would significantly

increase the complexity of the problem, as both elastic properties and yielding characteristics of the foundation change during progressive cracking. Inspiration for further development of more advanced mechanical soil-interaction models could be found in methods for calculating bearing capacity of soils for design of shallow foundations, see e.g. Terzaghi (1943); Meyerhof (1963); Hansen (1970). Such failure types may be applicable to the present for predicting the yield limit of the soil as long as the slab behaves elastically. However, after onset of cracking the problem becomes more complex. Thus, methodologies should be extended to capture relevant failure types. Moreover, adaptive two-parameter models must be developed in order capture changing support characteristics.



# Chapter 5

## Cyclic fiber hinge model

### 5.1 Introduction

Concrete and composite pavement systems are subjected to cyclic loading from moving vehicles. This type of loading results in initiation of bending cracks in the quasi-brittle cemented material. Subsequently, these cracks propagate leading to failure of the pavement structure, see Figure 5.1.

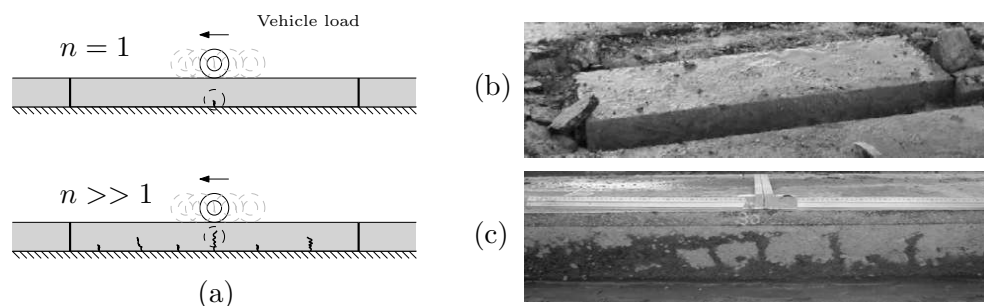


**Figure 5.1:** (a) Sketch of fatigue crack development in a simple concrete pavement system. (b) Intact block of cement bound granular mixture cut from field before trafficking (Thøgersen et al., 2004). (c) Cracks in cement bound granular mixture after app. 300,000 passes (Yeo, 2008b).

Constitutive models have been developed for low-cyclic damage of cemented materials. However, the developed models are typically used to simulate one type of test or one simplified problem. Thus, all the different components in Figure 1.11 are seldom addressed in relation to each other. This often results in complex models with limited capabilities. Moreover, only few published models, create the required link between low-cyclic and

high-cyclic fatigue damage, i.e. relate the development of new fracture process zone to damage in the existing fracture process zone, see Figure 5.2 (a) and (b), respectively.

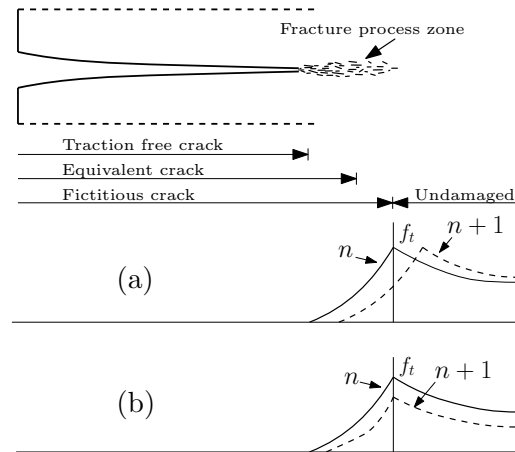


**Figure 5.2:** Stress distribution under cyclic loading according to Slowik et al. (1996): (a) development of new fracture process zone and (b) fatigue damage in existing fracture process zone.

In order to create a simple and robust modeling framework for engineering application, this chapter presents a multilayer hinge model, hereafter referred to as the 'fiber hinge' model. At the lowest level, a fiber of cemented material including a crack is considered and a stress-mean strain relationship is established. At the intermediate level a hinge element, which is a finite part of the beam, consisting of layered strips of cemented material is considered and a relationship between the generalised sectional forces and strains established. At the highest level the hinge model is applied as a constitutive model in a non-linear beam element as presented in Chapter 3. This particular format enables a straightforward implementation of different types of stress-crack opening relationships and unloading and reloading schemes.

Further, the fiber hinge is extended to account for the cyclic crack behavior of inner loops below the monotonic curve, i.e. fatigue crack growth after crack initiation. Deterioration during cyclic loading is incorporated in the model applying an energy based approach. The presented model accounts for the material behavior in all the cracked phases, linking the development of the fracture process zone and damage of the existing fracture process zone to the monotonic material characteristics in a rational manner.

## 5.2 The mechanics of the fiber hinge model

The uni-axial tensile behaviour of the concrete is modeled according to the fictitious crack model. To make the proposed model as versatile as possible, a multi-linear softening law is selected

$$\sigma(w) = b_i - a_i w \begin{cases} b_1 - a_1 w & \text{for } 0 \leq w \leq w_1 \\ b_2 - a_2 w & \text{for } w_1 \leq w \leq w_2 \\ b_3 - a_3 w & \text{for } w_2 \leq w \leq w_3 \\ \dots & \dots \\ 0 & \text{for } w_i > w_c \end{cases} \quad (5.1)$$

where  $w$  is the crack opening,  $w_c$  is the final zero-stress displacement,  $a_i$  is the slope and  $b_i$  the intersection of the tangent line segment and the abscissa for a given point on the softening curve as shown in Figure 5.3.

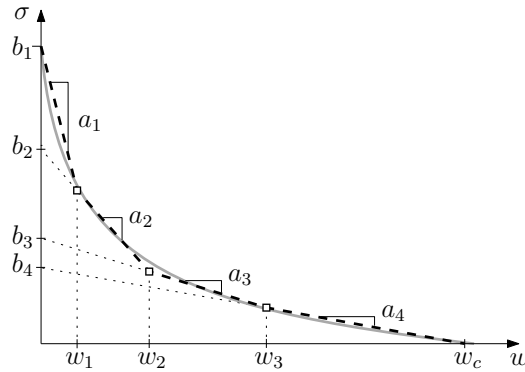


**Figure 5.3:** Definition of parameters  $a_i$ ,  $b_i$  and  $w_i$  for the softening law selected: multi-linear idealisation (black dashed) of exponential softening curve (gray solid) using four linear line segments.

The total fracture energy  $G_F$  given by the area under the softening curve is

$$G_F = \int_0^{w_c} \sigma(w) dw = \frac{1}{2} \sum_{i=1}^n [(2b_i - a_i(w_{i-1} + w_i))(w_i - w_{i-1})] \quad (5.2)$$

where  $n$  is the number of lines on the softening curve.

For semi-analytical hinge models published in the literature, see e.g. Olsen (2001a,b); Zhang et al. (2001); Iyengar et al. (2002); Brake and Chatti (2013), sectional forces are calculated over the full beam-hinge segment (integration in blocks) for a given stress crack-opening relationship. A similar approach was used in the finite element implementation of the cracked-hinge in Chapter 3. This type of model is simple and numerically robust, however, if one wishes to study unloading and reloading of cracks as well as more complex material behaviour, e.g. damage and fatigue, this particular formulation becomes cumbersome. Following the basic idea of the 'multilayer model' by Hordijk (1991), this study presents a general hinge model consisting of fibers of cemented material, as shown in Figure 5.4.

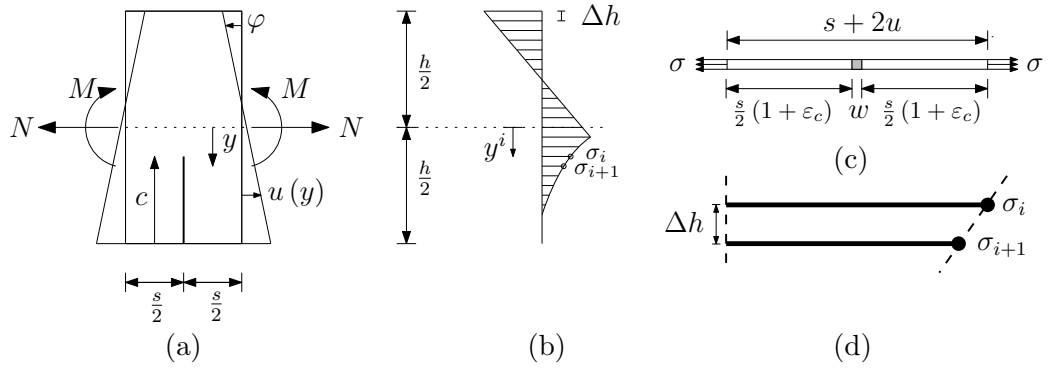


**Figure 5.4:** Fiber hinge model: (a) Beam segment with constant sectional forces and deformation of cracked beam segment. (b) Hinge stress distribution after initiation of cracking showing the individual fibers ( $n=24$ , whereof 4 are stress free). (c) Material fiber in uni-axial tension: loaded state beyond peak-load showing crack deformations. (d) Geometrical definition of one hinge strip (interpolation of stresses between two fibers).

The tensile behaviour of the hinge may be established by considering a fiber of material in uni-axial tension similarly to (3.2). The expression for crack opening and the corresponding stress in the fiber is modified to account for the multi-linear softening response, exchanging  $f_t$  with  $b_i$  in (3.4), i.e.

$$\left. \begin{aligned} \sigma_c = \sigma_w \Rightarrow \sigma_c = b_i + a_i w \\ s + 2u = s(1 + \varepsilon_c) + w \Rightarrow s\bar{\varepsilon}(y_i) = s\varepsilon_c + w \end{aligned} \right\} \Rightarrow \begin{cases} w_i = s \frac{E_c \bar{\varepsilon}(y_i) - b_i}{E_c - a_i s} \\ \sigma_i = E_c \frac{b_i - a_i s \bar{\varepsilon}(y_i)}{E_c - a_i s} \end{cases} \quad (5.3)$$

where the notation  $i$  is used for a discretised fiber.

In the cracked state,  $w_c \leq w$ , the crack is stress free, leading to the simple

solution for the fiber

$$\left. \begin{array}{l} w = s(1 + \bar{\varepsilon}(y_i)) - s \\ \sigma_c = 0 \end{array} \right\} \Rightarrow \left\{ \begin{array}{l} w_i = s\bar{\varepsilon}(y_i) \\ \sigma_i = 0 \end{array} \right. \quad (5.4)$$

The hinge is divided in  $n + 1$  number of fibers with the strip height  $\Delta h$  between fibers, shown in Figure 5.4 (b). The position (top-down) of each fiber with respect to  $y = 0$  can be calculated as  $y_i = -h/2 + \Delta h \cdot (i - 1)$ . The normal force contribution from each strip between two fibers is given by

$$N_i = \frac{1}{2} (\sigma_i + \sigma_{i+1}) \Delta h t \quad (5.5)$$

The eccentricity of the normal force for each strip is found from trapezoidal calculation and is given by

$$e_i = \frac{1}{3} \frac{\sigma_i + 2\sigma_{i+1}}{\sigma_i + \sigma_{i+1}} \Delta h + y_i \quad (5.6)$$

The moment contribution for each strip then yields

$$M_i = N_i \cdot e_i \quad (5.7)$$

The sectional forces with respect to  $y = 0$  is then a sum of the contribution from all,  $n$ , strips and may be calculated from

$$N(\bar{\varepsilon}_0, \bar{\kappa}) = t \int_{-h/2}^{h/2} \sigma_c dy = \sum_{i=1}^n N_i \quad (5.8a)$$

$$M(\bar{\varepsilon}_0, \bar{\kappa}) = t \int_{-h/2}^{h/2} \sigma_c y dy = \sum_{i=1}^n M_i \quad (5.8b)$$

Convergence of the hinge is evaluated plotting the normalised error in moment  $\beta$  between the original hinge model (Ulfkjær et al., 1995) and the proposed hinge considering a simple linear softening law for different hinge

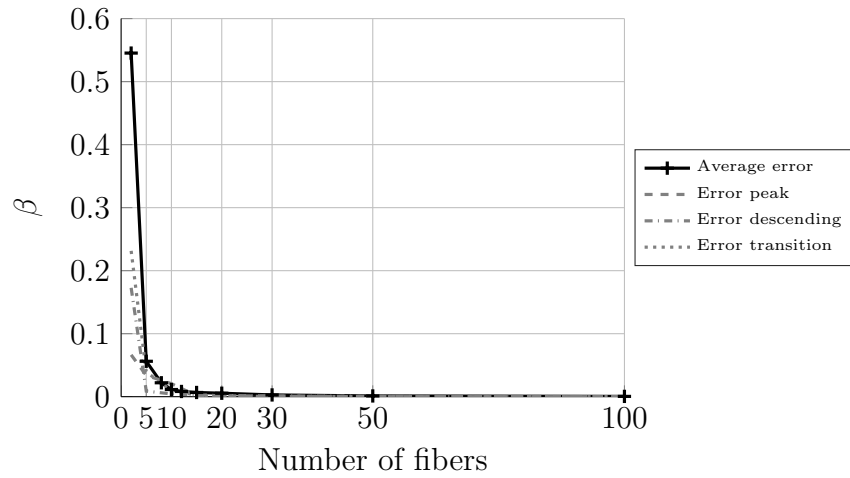


**Figure 5.5:** Number of hinge fibers,  $n$ : 2-100 (element size,  $elsz$ : 0.01-0.002 m) versus the average normalised difference in moment  $\beta$ .

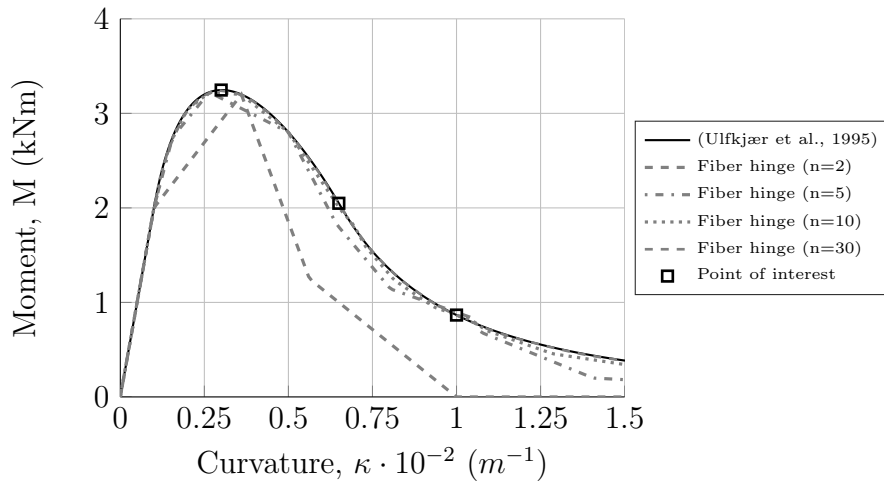


**Figure 5.6:** Typical moment-curvature response. Hinge dimensions ( $h/t$ ):  $0.20 \times 0.10 \text{ m}^2$ . Material properties:  $E_c=30 \text{ GPa}$ ,  $f_t=3.5 \text{ MPa}$ ,  $G_F=150 \text{ N/m}$  and  $w_c=0.1 \text{ mm}$  (linear softening).

mesh densities,  $n$ : 2-100, shown in Figure 5.5 (a). It is observed that sufficient accuracy can be obtained with 30 fibers, however, little is gained by increasing the number of fibers from 10 to 30.

In the analysis presented in Figure 5.5 the error in normalised moment is taken as the average difference in moment between the analytical hinge model in Ulfkjær et al. (1995) and the proposed fiber hinge at peak ( $\kappa=0.003 \text{ m}^{-1}$ ), at the transition point between softening and stress free hinge ( $\kappa=0.0066$

m<sup>-1</sup>) and at the lower part of the descending branch ( $\kappa=0.01$  m<sup>-1</sup>). This is exemplified in the typical moment-curvature obtained shown in Figure 5.6.

### 5.3 Tensile damage model

In order to realistically capture the influence from unloading of a previously open crack, as well as the stiffness reduction for structures subjected to repeated loads, a low-cyclic damage plasticity model for the fiber in tension is implemented. A simple format is proposed, defining a fixed negative intersecting point  $\sigma_u^k$  on the abscissa towards which unloading takes place after initiation of cracking. The geometrical meaning of strain components for the damage-plasticity model is shown in Figure 5.7.

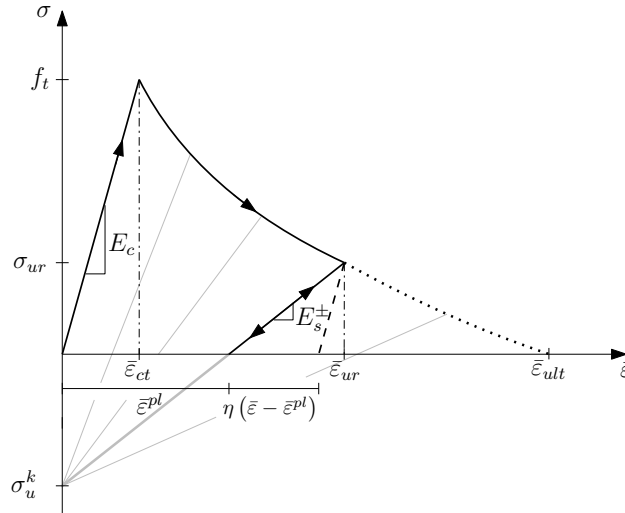


**Figure 5.7:** Geometrical meaning of strain components for the damage-plasticity model. The inelastic cracking strain  $\bar{\varepsilon}^{cr}$  is composed of the reversible  $\eta(\bar{\varepsilon} - \bar{\varepsilon}^{pl})$  and irreversible  $\bar{\varepsilon}^{pl}$  parts. The dashed line represent elastic unloading with the initial stiffness whereas grey lines represent the reduced stiffness and unloading towards point  $\sigma_u^k$ .

From Figure 5.7 it is evident that the unloading stiffness and plastic strain component can be defined as

$$E_s^\pm = \frac{\sigma_{ur} - \sigma_u^k}{\bar{\varepsilon}_{ur}} \quad (5.9a)$$

$$\bar{\varepsilon}^{pl} = -\frac{\sigma_u^k}{E_s^\pm} \quad (5.9b)$$

where  $E_s^\pm$  is the unloading- and reloading stiffness and  $\sigma_{ur}$  and  $\bar{\varepsilon}_{ur}$  is the maximum cracking stress and strain upon unloading and reloading, respectively. The format above is found to comply well with experimental data for concrete materials as well as more advanced concrete damage plasticity model formats, see e.g. Maekawa et al. (1993); Lee and Fenves (1998); Grassl et al. (2013). Accordingly, a conventional 1-D damage-plastic stress strain law can be formulated

$$\sigma = (1 - \eta) E_c (\bar{\varepsilon} - \bar{\varepsilon}^{pl}) \quad (5.10)$$

where the damage parameter is given as

$$\eta = 1 - \frac{E_s^\pm}{E_c} \quad (5.11)$$

The crack width  $w$  can be found from

$$w = \begin{cases} s\bar{\varepsilon} - s\frac{\sigma_{ur}}{E_c} & 0 < w \leq w_c \\ s\bar{\varepsilon} & w_c < w \end{cases} \quad (5.12)$$

A modified computational scheme is developed in order to determine the fiber hinge sectional forces  $N$  and  $M$ , accounting for the unloading and reloading response described by the damage-plasticity model, see Algorithm 5

---

**Algorithm 5** Computational scheme for  $N$  and  $M$ : Damage
 

---

State parameters:  $\bar{\varepsilon}$ ,  $\bar{\varepsilon}_{ur}$

**if**  $\bar{\varepsilon} < \varepsilon_{ct}$  (*Monotonic loading*)  
 Phase  $0$ :  $\eta=0$  and  $\bar{\varepsilon}^{pl}=0$   
**else**  
 Phase  $I$ :  $\eta$  and  $\bar{\varepsilon}^{pl}$  from (5.11) and (5.9b), respectively  
**if**  $\bar{\varepsilon} > -\frac{f_t}{\sigma_{as}}$   
 Phase  $II$ :  $\eta=1$  and  $\bar{\varepsilon}^{pl}=\bar{\varepsilon}$   
**end**  
**end**  
 $\sigma$  from (5.10)  
**if**  $\bar{\varepsilon} > 0$  &  $\bar{\varepsilon} < \bar{\varepsilon}_{ur}$  (*Unloading & Reloading*)  
**if**  $\varepsilon_{ur} < \varepsilon_{ct}$  (*Unloading & Reloading*)  
 Phase  $0$ :  $\eta=0$  and  $\bar{\varepsilon}^{pl}=0$   
**else**  
 Phase  $I$ :  $\eta$  and  $\bar{\varepsilon}^{pl}$  from (5.11) and (5.9b), respectively  
**if**  $\bar{\varepsilon}_{ur} > -\frac{f_t}{\sigma_{as}}$   
 Phase  $II$ :  $\eta=1$  and  $\bar{\varepsilon}^{pl}=\bar{\varepsilon}$   
**end**  
**end**  
 $\sigma$  from (5.10)  
**end**

---

From Algorithm 5 it is observed that the maximum strain  $\bar{\varepsilon}_{ur}$  experienced during cyclic loading and the current strain  $\bar{\varepsilon}$  are the only parameters needed to determine whether a fiber is monotonically loaded, unloading or reloading. Thus, if the current strain is larger than the maximum strain from the previous load cycle, the current maximum strain is updated, i.e. if  $\bar{\varepsilon}^j > \bar{\varepsilon}_{ur}^{1-j} \rightarrow \bar{\varepsilon}_{ur}^j = \bar{\varepsilon}^j$ .

Numerical analysis of a plain concrete beam under four point loading with a shallow notch is carried out to verify the functionality of the proposed damage model. The beam hinge load-displacement response is plotted and compared to experimental and numerical results reported in Hordijk (1991), shown in Figure 5.8. The displacement at midspan position of the beam-hinge is obtained by utilising (3.9)-(3.13).

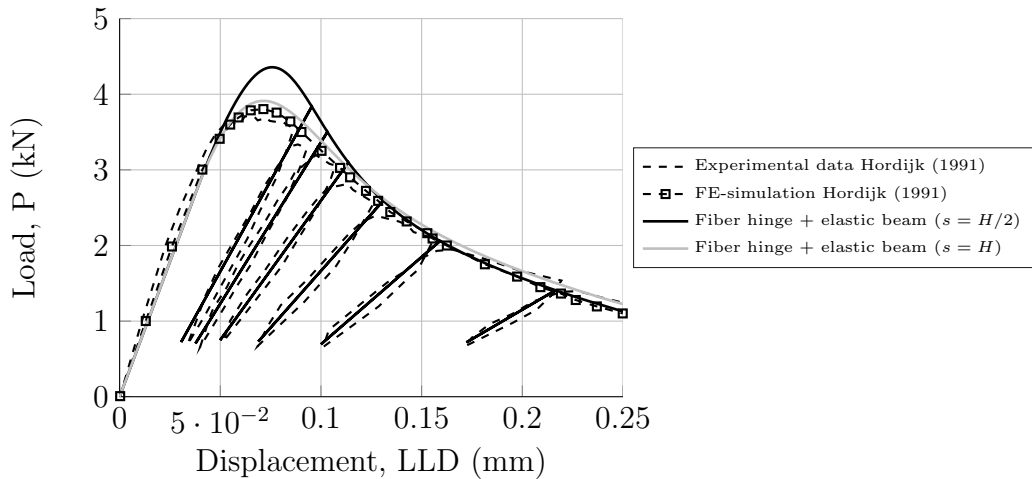


**Figure 5.8:** Load-displacement response of four point bending beam subjected to cyclic loading Hordijk (1991); Beam geometry ( $L/h/t$ ):  $450 \times 100 \times 50 \text{ mm}^3$ , notch depth,  $a_0=10 \text{ mm}$  and  $s=50 \text{ mm}$ . Relevant model parameters are:  $E_c=38 \text{ GPa}$ ,  $f_t=3.0 \text{ MPa}$ ,  $G_F=125 \text{ N/m}$ ,  $c_1=3.00$ ,  $c_2=6.93$  and  $w_c=5.14 \cdot G_F/f_t$  and  $\sigma_u^k = -0.4f_t$  (exponential softening).

It is observed from the load-displacement curve in Figure 5.8 that there is good agreement between the proposed fiber hinge model and the experimental results. It is also found that the monotonic behavior of the hinge comply well with finite element simulations reported in Hordijk (1991) using a discrete crack model and the commercial computer package DIANA. The peak-load is somewhat higher compared to results reported in Hordijk (1991). One explanation for this difference could be the influence from the notch, which is not being captured by the hinge model when using a constant  $s = H/2$ . It is also found that increasing the hinge width results in decreasing peak-loads, as shown in the calibrated curve (solid gray) in Figure 5.8.

The low-cyclic damage model presented in this section accounts for damage from the development of the fracture process zone, see Figure 5.2 (a). However, for pavement structures the loading is typically significantly lower than the flexural bearing capacity of the structure. This means that a large

proportion of the cemented material deterioration is caused by damage of the existing fracture process zone, i.e. fatigue crack growth, see Figure 5.2 (b). In order to capture this type of material deterioration an extension of the model is required.

## 5.4 Fatigue model

### Theoretical framework

The fatigue crack growth process in cemented materials can be divided in different phases. In the present study a simple and general format is sought with regard to the fatigue life prediction after crack initiation. This means that at some point the maximum load  $P_{max}$  is larger or at some point has been larger than the first crack load  $P_{ct}$ , where a crack in the cemented material was initiated.

Cyclic cohesive zone models provide the capability to simulate fatigue crack growth as discussed in Section 1.4. Ortiz and Pandolfi (1999) proposed an energy based approach for damage of the cyclic cohesive model. In this model, damage is defined as the ratio between the cohesive potential evaluated for the maximum attained separation and the fracture energy. However, this damage is not limited to the damage locus but rather distributed in the whole softening region, including the reversible branch (Roth et al., 2014).

In the present study the damage state after arbitrary loading is associated with a monotonic loading process that leads to the same damage state. A simple unloading and reloading scheme is applied, ensuring a consistent format where the fiber response is uniquely linked to the monotonic failure envelope and monotonic damage. Deterioration of the fracture energy is controlled by the accumulated inelastic work carried out during fatigue loading. The total fatigue loading process is visualised in Figure 5.9.

The initial residual fracture energy at the point where a cracked fiber enters the fatigue phase is given as, see Figure 5.9 (a).

$$G_{fat}^{init} = G_F - E_{mon}^{dis} = E^{rev} + E^{res} \quad (5.13)$$

where  $E_{mon}^{dis}$  is the dissipated energy from monotonic loading, and  $E^{rev}$  and  $E^{res}$  are the reversible and residual energy upon the first fatigue load cycle, respectively. Assuming a linear softening law and secant unloading (towards

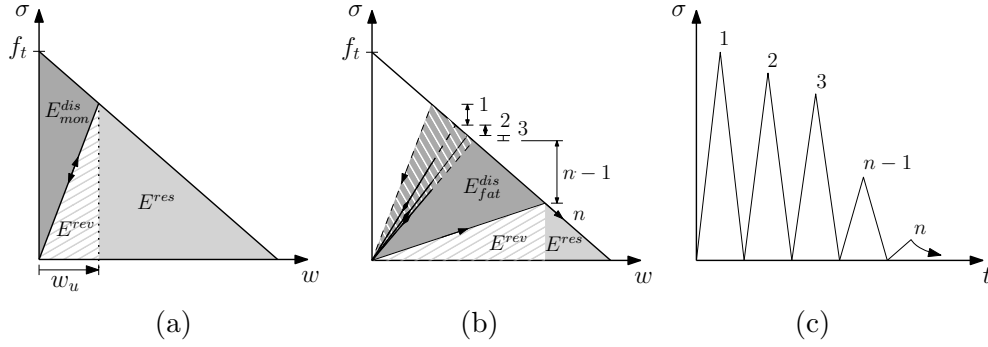


**Figure 5.9:** Energy considerations used for description of fatigue behavior of hinge fibers: (a) Monotonic damage at start of fatigue analysis. (b) Fatigue damage during cyclic loading. (c) Schematic overview of fatigue loading scheme under displacement control.

origin) these measures can be found from the following simple expressions

$$E^{rev} = \frac{1}{2} \sigma_u w_u \quad (5.14a)$$

$$E_{mon}^{dis} = \int_0^{w_u} \sigma(w) dw - E^{rev} = \frac{1}{2} f_t w_u \quad (5.14b)$$

$$E^{res} = \int_{w_u}^{w_c} \sigma(w) dw = \frac{1}{2} \sigma_u (w_c - w_u) \quad (5.14c)$$

where  $w_u$  is the crack-opening upon unloading,  $\sigma_u$  is the stress upon unloading and  $w_c$  is the final zero-stress displacement.

The damage evolution is then given by the initial residual fracture energy  $G_{fat}^{init}$  upon fatigue loading and the accumulated inelastic work  $\sum W^{cr}$ . A simple linear and exponential relationship are proposed, i.e.

$$G_F^{res} = G_{fat}^{init} - k_{fat} \sum W^{cr} \quad , \quad G_F^{res} = G_{fat}^{init} \cdot e^{-k_{fat} \sum W^{cr}} \quad (5.15)$$

where  $k_{fat}$  is the fatigue damage parameter.

In order to determine the the fatigue damage an arbitrary load case is considered, see Figure 5.10. After unloading from point  $M$  on the monotonic curve, the fiber enters fatigue loading. Considering a fiber in point  $C$ , the inelastic work  $W^{cr}$  from the loading process  $A-B-C$  is added to the accumulated work upon reloading.

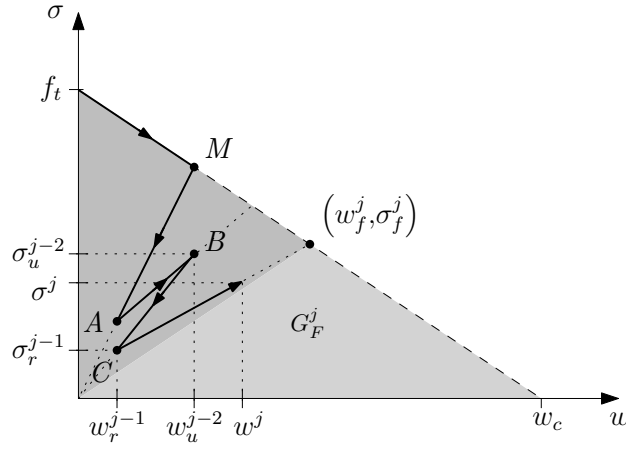


**Figure 5.10:** Sketch of arbitrary load case: unloading with constant damage (towards origin) and reloading with damage evolution (towards  $\sigma_f$ ).

The inelastic work for a load increment  $j$  is found from trapezoidal calculation

$$W_j^{cr} = (w_j - w_{j-1}) \left[ \frac{\sigma_j + \sigma_{j-1}}{2} \right] \quad (5.16)$$

Reloading from point  $C$  then takes place towards a fixed point on the monotonic failure envelope  $(w_f, \sigma_f)$ , for a linear softening law, given as

$$\sigma_f^j = \frac{2G_F^j}{w_c} \quad (5.17a)$$

$$w_f^j = \frac{\sigma_f^j - f_t}{a_i} \quad (5.17b)$$

where  $a_i$  is the slope of the softening curve at the point where the fatigue reloading curve and the monotonic curve intersects. The monotonic damage parameter  $\eta^j$  can be established from

$$\eta^j = 1 - \frac{\sigma_f^j}{E_c \bar{\varepsilon}_f^j}, \quad \text{where} \quad \bar{\varepsilon}_f^j = \frac{\bar{\varepsilon}^j}{E_c} + \frac{w_f^j}{s} \quad (5.18)$$

where  $\bar{\varepsilon}_f$  is the strain at the failure envelope.

The formulation proposed in (5.17a) ensures that damage is restricted to the monotonic failure envelope. For a fiber that fails in fatigue this means

that the evolving damage contribution from the final reloading cycle is neglected. However, in general this error will be small as typically several load cycles, each with a low damage contribution, are considered in fatigue.

The incremental stiffness during fatigue loading is determined depending on whether the cohesive surface opens or closes, i.e.

$$\dot{\sigma} = \begin{cases} E_s^- \dot{\bar{\epsilon}} & \text{for } \dot{\bar{\epsilon}} < 0 \\ E_s^+ \dot{\bar{\epsilon}} & \text{for } \dot{\bar{\epsilon}} > 0 \end{cases} \quad (5.19)$$

where  $E_s^-$  and  $E_s^+$  are the unloading and reloading stiffnesses, respectively, given by

$$E_s^- = \frac{\sigma_u}{\bar{\epsilon}_u} \quad (5.20a)$$

$$E_s^+ = \frac{\sigma_f - \sigma_r}{\bar{\epsilon}_f - \bar{\epsilon}_r} \quad (5.20b)$$

where  $\sigma_u$  and  $\sigma_r$  are the stress upon unloading and reloading, respectively, and  $\bar{\epsilon}_u$  and  $\bar{\epsilon}_r$  is the strain upon unloading and reloading, respectively.

The stress during during unloading and reloading is then given as

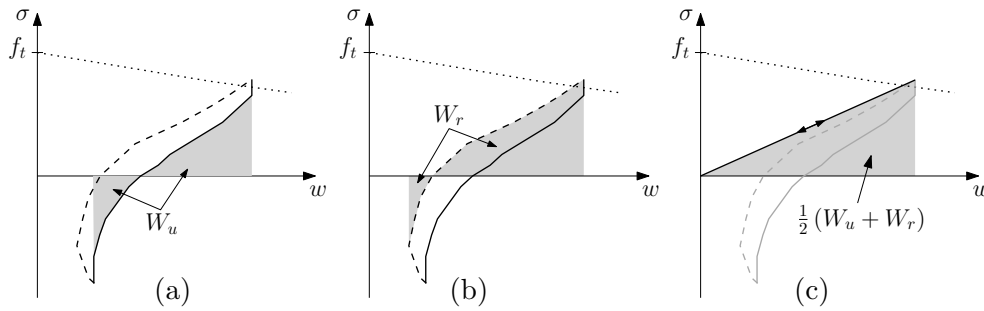
$$\sigma = \begin{cases} E_s^- \bar{\epsilon} & \text{for } \dot{\bar{\epsilon}} < 0 \\ E_s^+ (\bar{\epsilon} - \bar{\epsilon}_r) + \sigma_r & \text{for } \dot{\bar{\epsilon}} > 0 \end{cases} \quad (5.21)$$

## Uni-axial fiber response

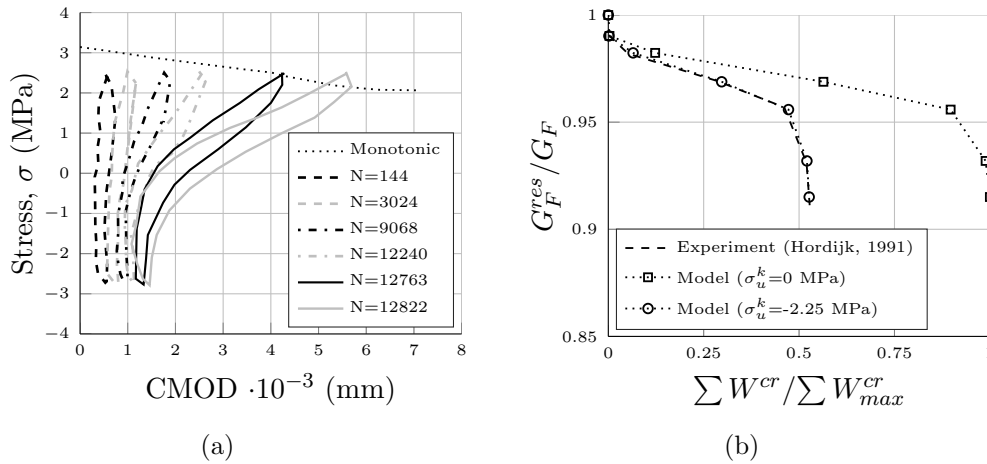
The proposed methodology is tested and compared to uni-axial fatigue test results of plain concrete, reported in Hordijk (1991). The inelastic work in each cycle of the experiment is calculated as the sum of the area under the unloading and reloading curve, as shown in Figure 5.11 (a) and (b), respectively. Whereas the proposed model simplifies to Figure 5.11 (c).

Figure 5.12 (a) shows an overview of the fatigue hysteresis loops  $n=[144, 3024, 9068, 12240, 12763, 12822]$ . The resulting inelastic work calculated with the two different methods is presented in Figure 5.12 (b).

From Figure 5.12 (b) it is observed that the proposed model resembles the trend of the experiments, however, the model overestimates the inelastic work. A good fit can be obtained using a more realistic unloading and reloading scheme, i.e. unloading towards a negative point on the abscissa as proposed in Section 5.3. For simplicity only unloading towards origin ( $\sigma_u^k=0$ )



**Figure 5.11:** Calculating inelastic work (gray solid area): (a) Work under unloading path (black solid) and (b) work under reloading path (black dashed). (c) Idealisation applied in the fiber hinge model.



**Figure 5.12:** (a) Fatigue cracking hysteresis loops reported in Hordijk (1991) (elastic deformation subtracted). (b) Accumulated inelastic work versus residual fracture energy. Specimen geometry ( $L/h/t$ ):  $150 \times 50 \times 50$  mm<sup>3</sup>, notch depth,  $a_0=0$  mm and  $s=35$  mm. Mechanical properties:  $E_c=38$  GPa,  $f_t=3.0$  MPa,  $G_F=125$  N/m,  $w_c=5.14 \cdot G_F/f_t$ .

is considered here. However, the implemented model is general which makes it suitable to consider more complex unloading and reloading schemes, as well as bi-linear or multi-linear softening curves.

From Figure 5.12 (a) it is observed that during the first app. 3000 load cycles, the inelastic response is small as the applied stress is below the tensile strength. Moreover, the reported tests includes a compression phase with closing of the cracks, which may influence the fatigue behavior. Plizzari et al. (1997) investigated the behavior of cracked plain concrete cylinders in

direct tension. In these tests only the cracked phase was considered and they are therefore suitable for comparison with the proposed fatigue model, see example in Figure 5.13.

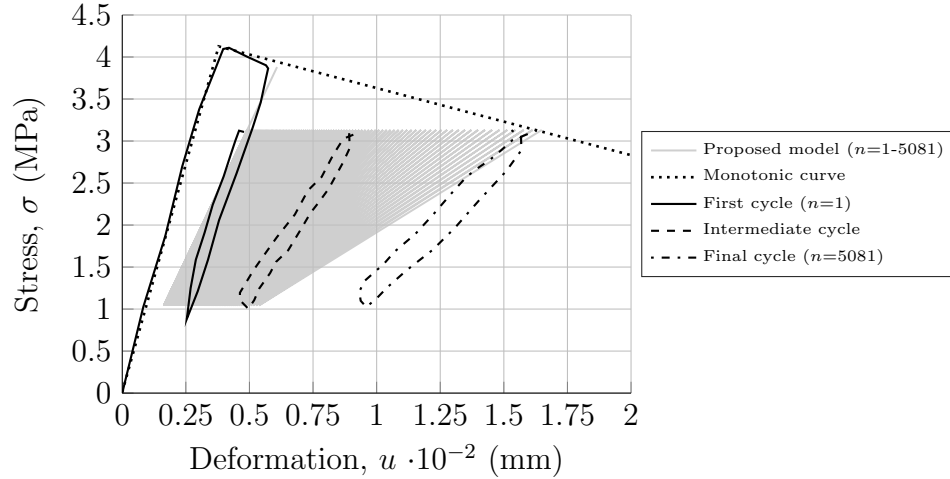


**Figure 5.13:** The proposed fatigue model (gray) for 1-5081 cycles compared to fatigue cracking hysteresis loops at the start ( $n=1$ ), intermediate and end of fatigue analysis ( $n=5081$ ) reported in Plizzari et al. (1997).  $k_{fat}=0.3 \cdot 10^{-3}$  (linear damage). Specimen geometry ( $L/d$ ):  $210 \times 80 \times 50$  mm<sup>3</sup>, notch depth,  $a_0=4$  mm and  $s=35$  mm. Mechanical properties:  $f_c=42.1$  MPa,  $f_t=4.25$  MPa,  $G_F=151$  N/m,  $w_c=0.341$  mm.

From Figure 5.13 it is observed that adequately good fit is obtained describing the deterioration of a single hinge fiber. In the three experiments evaluated the fatigue damage parameter  $k_{fat}$  is predicted to  $4.10 \cdot 10^{-3}$ ,  $1.75 \cdot 10^{-3}$  and  $0.3 \cdot 10^{-3}$  for failure after 344, 645 and 5081 load cycles, respectively.

## Analytical hinge response

In order to implement the fatigue model a number of modifications of Algorithm 5 is required, as the crack behavior is dependent on whether a crack opens or closes. The modified computational scheme for the fiber hinge sectional forces  $N$  and  $M$  is shown in Algorithm 6.

**Algorithm 6** Computational scheme for  $N$  and  $M$ : Fatigue

---

State parameters:  $\sum W^{cr}, G_{fat}^{init}, G_F^{res}, \sigma_u, \sigma_r, \sigma_f, \bar{\varepsilon}_u, \bar{\varepsilon}_r, \bar{\varepsilon}_f, \dot{\varepsilon}$

**if**  $\bar{\varepsilon} < \varepsilon_{ct}$  (*Monotonic loading*)  
  Phase 0

**else**  
  Phase I  
  **if**  $\bar{\varepsilon} > -\frac{f_t}{as}$   
    Phase II  
  **end**

**end**

**if**  $\bar{\varepsilon} > 0 \ \& \ \dot{\varepsilon} < 0 \ \& \ \bar{\varepsilon} < \bar{\varepsilon}_u$  (*Unloading*)  
  **if**  $\varepsilon_u < \varepsilon_{ct}$   
    Phase 0  
  **else**  
    Phase I:  $E_s^-$  from (5.20a) and  $\sigma$  from (5.21)  
    **if**  $\bar{\varepsilon} > -\frac{f_t}{as}$   
      Phase II  
    **end**  
  **end**

**end**

**if**  $\bar{\varepsilon} > 0 \ \& \ \dot{\varepsilon} > 0 \ \& \ \bar{\varepsilon} < \bar{\varepsilon}_f$  (*Reloading*)  
  **if**  $\varepsilon_f < \varepsilon_{ct}$   
    Phase 0  
  **else**  
    Phase I:  $E_s^+$  from (5.20b) and  $\sigma$  from (5.21)  
    **if**  $\bar{\varepsilon}_f > -\frac{f_t}{as}$   
      Phase II  
    **end**  
  **end**

**end**

**if**  $\sigma_u < 0$  or  $\sigma_f < 0$   
   $\sigma = 0$

**end**

---

From Algorithm 6 it is observed that several state parameters are needed to determine the fiber behavior. These parameters are mainly used to control whether a fiber has entered fatigue loading, is unloading, reloading or have failed in fatigue and then enters fatigue loading again, requiring a new initial fracture energy  $G_{fat}^{init}$ .

The functionality of the proposed fatigue model is tested on a single hinge subjected to 25 cycles ( $n=25$ ) with hinge rotations between  $\varphi=0.004$ - $0.001$  ( $m^{-1}$ ), as shown in Figure 5.14 (a) and (b) for a linear and exponential damage relationship, respectively.

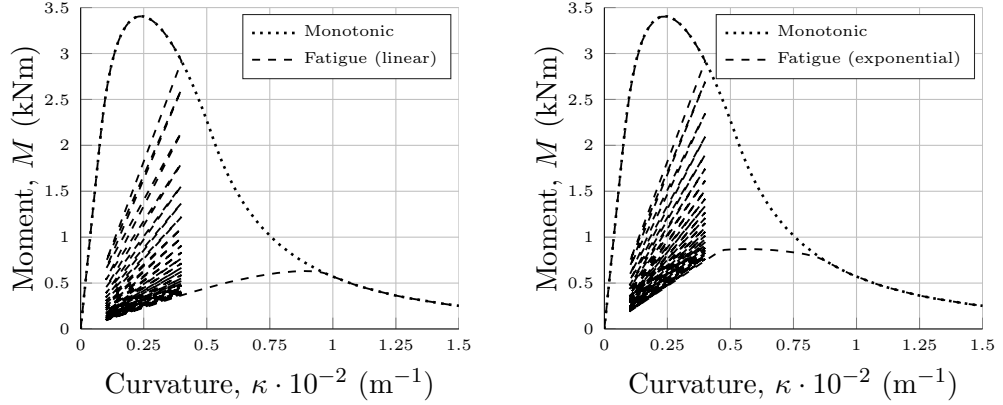


**Figure 5.14:** Fatigue behavior of hinge: (a) Linear damage relationship ( $k_{fat}=0.25$ ). (b) Exponential damage relationship ( $k_{fat}=0.0025$ ). Hinge dimensions ( $h/t$ ):  $0.20 \times 0.10$   $m^2$ . Material properties:  $E_c=30$  GPa,  $f_t=3.5$  MPa,  $G_F=150$  N/m and  $w_c=0.1$  mm (linear softening).

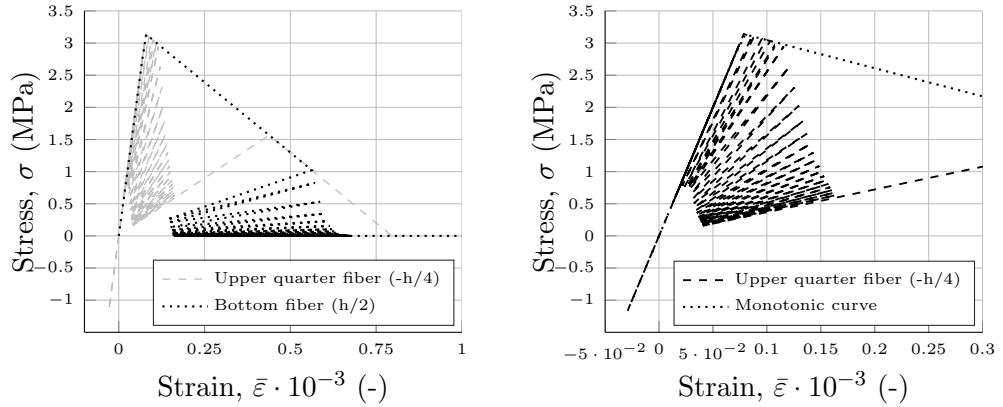


**Figure 5.15:** Behavior of hinge fibers during fatigue (linear damage): (a) Bottom fiber (black) and upper quarter fiber (gray). (b) Close-up of upper quarter fiber going through different phases during fatigue loading of hinge.

From Figure 5.15 (a) it is observed that the bottom fiber enters the fatigue phase after the first monotonic load step. As fibers on the lower part of the hinge deteriorate, new fibers in the upper part of the hinge are activated, see

Figure 5.15 (b). The hinge fiber on the upper quarter of the hinge is first in compression, then in linear elastic tension, before entering a short stage of low-cyclic damage and finally fatigue loading. This behavior highlights the importance of a consistent fatigue damage format for numerical simulations, accounting for all the different cracked phases in a unified manner.

## 5.5 Fiber hinge tangent stiffness matrix

The fiber hinge is implemented as described in Section 3.3. The hinge model presented here first determines the constitutive state and stiffness of each individual fiber. Integration over the strip height between fibers is then performed and the sum of all contributions is included in the tangent stiffness matrix. The hinge tangent stiffness matrix,  $\mathbf{D}_t$  is defined through

$$\begin{bmatrix} dN \\ dM \end{bmatrix} = \mathbf{D}_t \begin{bmatrix} d\bar{\varepsilon}_0 \\ d\bar{\kappa} \end{bmatrix}, \quad \mathbf{D}_t = \sum_{i=1}^n \begin{bmatrix} \frac{\partial N_i}{\partial \bar{\varepsilon}_0} & \frac{\partial N_i}{\partial \bar{\kappa}} \\ \frac{\partial M_i}{\partial \bar{\varepsilon}_0} & \frac{\partial M_i}{\partial \bar{\kappa}} \end{bmatrix} \quad (5.22)$$

Monotonic loading of the hinge results in constant positive stiffness of fibers in the linear elastic state. Fibers in the cracked state and cracked stress-free state result in negative and zero stiffness contributions, respectively. The constituents of (5.22) are obtained from (5.8a) and (5.8b) utilising the following relations for the relevant part of the integral corresponding to  $0 < w \leq w_c$

$$\frac{\partial \sigma_c}{\partial \bar{\varepsilon}_0} = E_c \frac{a_i s}{E_c + a_i s}, \quad \frac{\partial \sigma_c}{\partial \bar{\kappa}} = E_c \frac{a_i s}{E_c + a_i s} y_i \quad (5.23)$$

Here the parameters  $\alpha_i = \frac{a_i s}{E_c + a_i s}$  and  $E_{cc}^i = E_c \alpha_i$  are introduced, where the first is the monotonic damage parameter and the latter symbolises the reduced stiffness of the cracked fiber. The parameter  $a_i$  is the slope at a given point on the softening curve, see Figure 5.3. The stiffness contribution from one fiber in the three different phases; elastic, softening and stress-free

is given by (5.24a), (5.24b) and (5.24c), respectively

$$\mathbf{d}_t^{el} = \begin{bmatrix} E_{ct} & E_{ct}y \\ E_{ct}y & E_{ct}y^2 \end{bmatrix} \quad \bar{\varepsilon} \leq \bar{\varepsilon}_{ect} \quad (5.24a)$$

$$\mathbf{d}_t^{cr} = \begin{bmatrix} E_{cct} & E_{cct}y \\ E_{cct}y & E_{cct}y^2 \end{bmatrix} \quad \bar{\varepsilon}_{ect} < \bar{\varepsilon} \leq \bar{\varepsilon}_{ult} \quad (5.24b)$$

$$\mathbf{d}_t^0 = \begin{bmatrix} 0 & 0 \\ 0 & 0 \end{bmatrix} \quad \bar{\varepsilon} > \bar{\varepsilon}_{ult} \quad (5.24c)$$

The stiffness contribution from a fiber in the linear elastic state will not change whereas a fiber in the softening state changes from a negative to a positive stiffness. For a fiber during unloading and reloading tensile damage of the fiber is introduced

$$\mathbf{d}_t^{ur} = (1 - \eta) \mathbf{d}_t^{el} \quad \text{for } \bar{\varepsilon}_{ct} < \bar{\varepsilon} < \bar{\varepsilon}_f \quad (5.25)$$

where  $\eta$  is dependent on whether the crack opens or closes, i.e.

$$\eta = \begin{cases} 1 - \frac{E_s^-}{E_c} & \text{for } \dot{\varepsilon} < 0 \\ 1 - \frac{E_s^+}{E_c} & \text{for } \dot{\varepsilon} > 0 \end{cases} \quad (5.26)$$

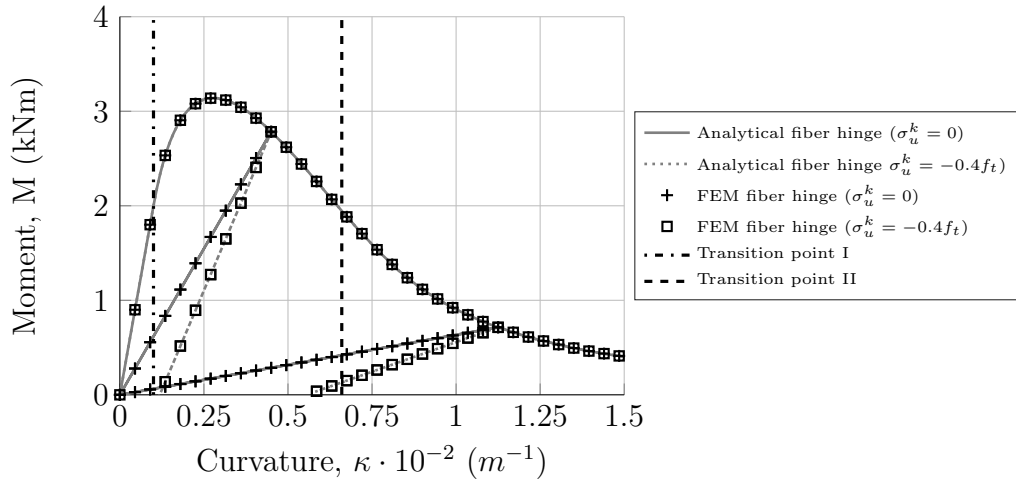
The full tangent stiffness matrix for loading, unloading and reloading can now be established by interpolation between each fiber and integration over the strip height, fiber and integration over the strip height, i.e.  $\mathbf{D}_t = \int_{-h/2}^{h/2} \mathbf{d}_t dy$ , as shown below

$$\begin{aligned}
dN_i &= \left( \int_{y_i}^{y_{i+1}} \frac{1}{2} (d_{11}^i + d_{12}^{i+1}) dy \right) d\bar{\varepsilon}_0 + \left( \int_{y_i}^{y_{i+1}} \frac{1}{2} (d_{12}^i + d_{12}^{i+1}) dy \right) d\bar{\kappa} \\
&= \left( \frac{1}{2} (d_{11}^i + d_{11}^{i+1}) (y_{i+1} - y_i) \right) d\bar{\varepsilon}_0 \\
&\quad + \left( \frac{1}{2} (d_{12}^i + d_{12}^{i+1}) (y_{i+1} - y_i) \frac{1}{2} (y_i + y_{i+1}) \right) d\bar{\kappa} \\
&= d_{11}^i d\bar{\varepsilon}_0 + d_{12}^i d\bar{\kappa} \\
&= \frac{\partial N_i}{\partial \bar{\varepsilon}_0} d\bar{\varepsilon}_0 + \frac{\partial N_i}{\partial \bar{\kappa}} d\bar{\kappa}
\end{aligned} \tag{5.27a}$$

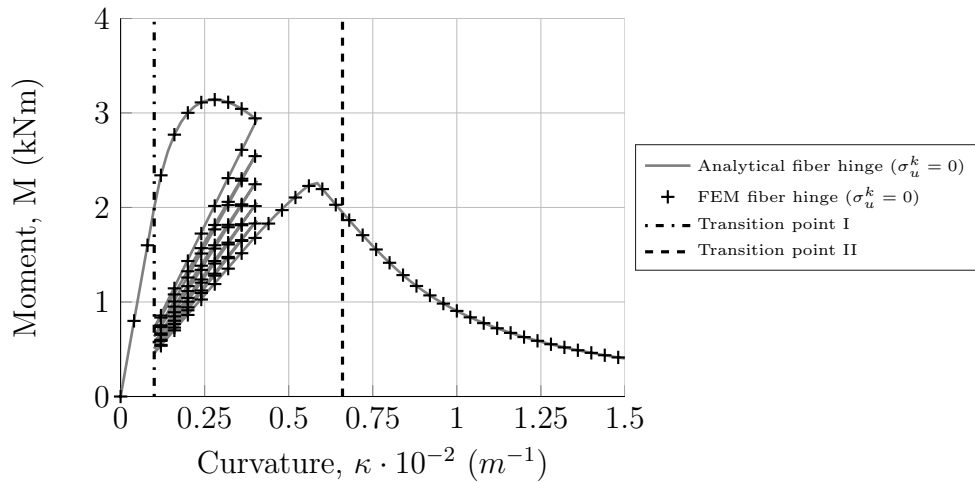
$$\begin{aligned}
dM_i &= \left( \int_{y_i}^{y_{i+1}} \frac{1}{2} (d_{21}^i + d_{21}^{i+1}) dy \right) d\bar{\varepsilon}_0 + \left( \int_{y_i}^{y_{i+1}} \frac{1}{2} (d_{22}^i + d_{22}^{i+1}) dy \right) d\bar{\kappa} \\
&= \left( \frac{1}{2} (d_{21}^i + d_{21}^{i+1}) (y_{i+1} - y_i) \frac{1}{2} (y_i + y_{i+1}) \right) d\bar{\varepsilon}_0 \\
&\quad + \left( \frac{1}{2} (d_{22}^i + d_{22}^{i+1}) (y_{i+1} - y_i) \frac{1}{3} (y_i^2 + y_{i+1}^2 + y_i y_{i+1}) \right) d\bar{\kappa} \\
&= d_{21}^i d\bar{\varepsilon}_0 + d_{22}^i d\bar{\kappa} \\
&= \frac{\partial M_i}{\partial \bar{\varepsilon}_0} d\bar{\varepsilon}_0 + \frac{\partial M_i}{\partial \bar{\kappa}} d\bar{\kappa}
\end{aligned} \tag{5.27b}$$

where  $y_i$  and  $y_{i+1}$  are the position of each fiber depicted on Figure 5.4 and  $d_{11}$ ,  $d_{12}$ ,  $d_{21}$  and  $d_{22}$  is defined in (5.24) as  $\mathbf{d}_t = \begin{bmatrix} d_{11} & y d_{12} \\ y d_{21} & y^2 d_{22} \end{bmatrix}$ .

The implemented hinge is validated by plotting the moment-curvature behavior for a single FEM fiber hinge versus the analytical fiber hinge for low-cyclic loading and fatigue loading, shown in Figure 5.16 (a) and (b), respectively.



(a)



(b)

**Figure 5.16:** Implementation of hinge into beam element: comparison between analytical and finite element hinge model: (a) low-cyclic loading and (b) fatigue loading. Hinge dimensions ( $h/t$ ):  $0.20 \times 0.10 \text{ m}^2$ . Material properties:  $E_c=30 \text{ GPa}$ ,  $f_t=3.5 \text{ MPa}$ ,  $G_F=150 \text{ N/m}$  and  $w_c=0.1 \text{ mm}$  (linear softening),  $k_{fat}=0.25$  (linear).

It is observed from Figure 5.16 (a) that exact fit is obtained between

the fiber hinge and the analytical model considering two types of unloading schemes. Exact fit is also observed for fatigue loading in Figure 5.16 (b). The two transition points between the phases; elastic-softening (crack initiation) and softening-stress free (bottom fiber stress free) are shown for reference.

## 5.6 Numerical examples

### Low-cyclic damage of simply supported beam

The functionality of the proposed FEM fiber hinge to simulate the low-cycle fracture behavior of a three point bending beam is demonstrated by plotting the load-crack mouth opening displacement versus experimental and numerical results reported in Gaedicke and Roesler (2009) shown in Figure 5.17. Model geometry and material properties are given in **Paper III**.

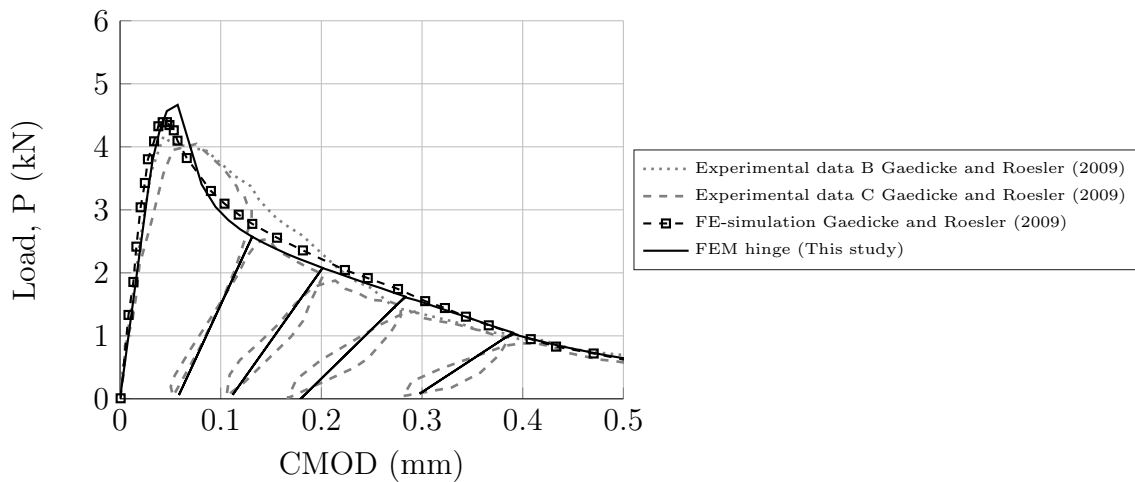


**Figure 5.17:** Load-crack mouth opening displacement response of three point beam: FEM hinge versus experimental and numerical results reported in Gaedicke and Roesler (2009).

It is observed from the load-CMOD curve in Figure 5.17 (a) that there is good agreement between the FEM hinge model and experimental results. The model simulates both pre-peak, softening and unloading reloading response adequately well. The difference in peak-load and peak-load displacement is app. 10% and 5% respectively, which is within the expected scatter. It is also found, that the monotonic behavior of the proposed hinge complies well with finite element simulations using a discrete cohesive zone model and the commercial computer package ABAQUS, as reported in Gaedicke and Roesler (2009).

## Low-cyclic damage of beam on soil

The functionality of the proposed FEM fiber hinge to simulate the low-cyclic fracture behavior of a beam resting on soil is demonstrated, applying the Winkler soil foundation model suggested in Section 4.6. The numerical hinge is compared to experimental and numerical results, reported in Gaedicke and Roesler (2009), by plotting the load-crack mouth opening displacement shown in Figure 5.18. Model geometry and material properties are given in **Paper III**.

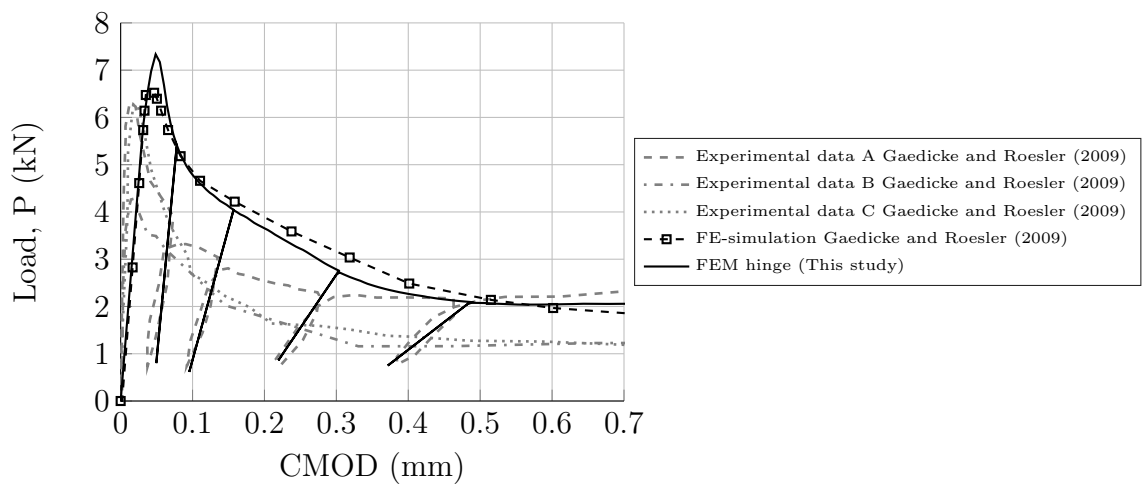


**Figure 5.18:** Load-crack mouth opening displacement response of beam on soil: FEM hinge versus experimental and numerical results reported in Gaedicke and Roesler (2009).

It is observed from the load-CMOD curve in Figure 5.18 that the FEM hinge model captures the overall characteristic response of the beam on soil on the descending branch. However, the peak-load and load level in general, as well as the peak-displacement are overestimated. The difference in peak-load varies between 15-50% compared to the experimental curves. A similar trend is also found in the numerical analysis reported in Gaedicke and Roesler (2009). Thus, the FEM hinge comply well with the numerical results from applying a discrete cohesive zone model.

The difference between experimental and numerical results indicate, that the soil model applied in simulations, does not reflect the stress distribution below the beam and/or other boundary conditions in the test set-up very well. The stiff pre-peak response and lower peak load in experiments indicate, that the continuity and shear stiffness of the soil influences the response significantly. For cohesive soils, considered in this experiment, this

influence will theoretically result in a large vertical reaction pressure along beam edges. Moreover, it is observed that the unloading and reloading stiffness in the FEM hinge deteriorates faster than the experimental curves. This effect, is not observed in analysis of the simply supported beam, see Figure 5.17, and further indicates an influence from the continuity in soil, which is not reflected in the numerical models presented. In order to obtain a more realistic response of the soil the use of a two-parameter spring model is discussed in **Paper III**.

### Fatigue damage of simply supported beam

The fatigue model is validated with the results of three point bending beam fatigue tests of plain concrete notched beams, as reported in Toumi et al. (1998); Toumi and Bascoul (2002). Static tests were carried out to obtain an average peak-load,  $P_u$ , of  $860 \pm 60$  N. Fatigue tests were then carried out with a maximum load  $P_{max}$  cycled between  $0.7P_u$  and  $0.98P_u$  with a constant lower load limit,  $P_{min}$ , of  $0.23P_u$ . Beam geometry, material properties and model parameters used are given in Table 5.1.

**Table 5.1:** Geometry and mechanical properties for beams used in experimental studies Toumi and Bascoul (2002).

<i>Geometry</i>	Unit	Toumi and Bascoul
Length, $L$	(m)	0.32
Height, $H$	(m)	0.08
Thickness, $t$	(m)	0.05
Notch depth, $a_0$	(m)	0.04
<i>Mechanical- and fracture properties</i>		
Young's modulus, $E$	(GPa)	31.6
Tensile strength, $f_t$	(MPa)	5.2
Fracture energy, $G_F$	(N/m)	34.2
<i>Hinge model and damage parameters</i>		
Number of fibers, $n$	(-)	200
Hinge width, $s = H/2$	(m)	0.04
Number of elements, $nel$	(-)	6
Fatigue damage parameter, $k_{fat}$	(-)	$4.6 \cdot 10^{-3}$

In lack of experimental data, the fatigue damage parameter  $k_{fat}$  is calibrated to obtain failure at  $n=140$  load cycles, found from experiments for a

load level of  $0.98P_u$ . This value is then used for fatigue simulations of the beam subjected to load levels of  $0.97P_u$  and  $0.93P_u$  without further calibration.

Convergence of the model is evaluated in view of load-displacement behavior of the beam, plotting the peak-load displacement for different beam mesh densities,  $nel$ : 2-12, shown in Figure 5.19 (a). It is observed, that sufficient accuracy, can be obtained with 6 elements, resulting in an element size of 0.0533 m, chosen in the following analysis. Typical load-displacement behavior is plotted in Figure 5.19 (b).

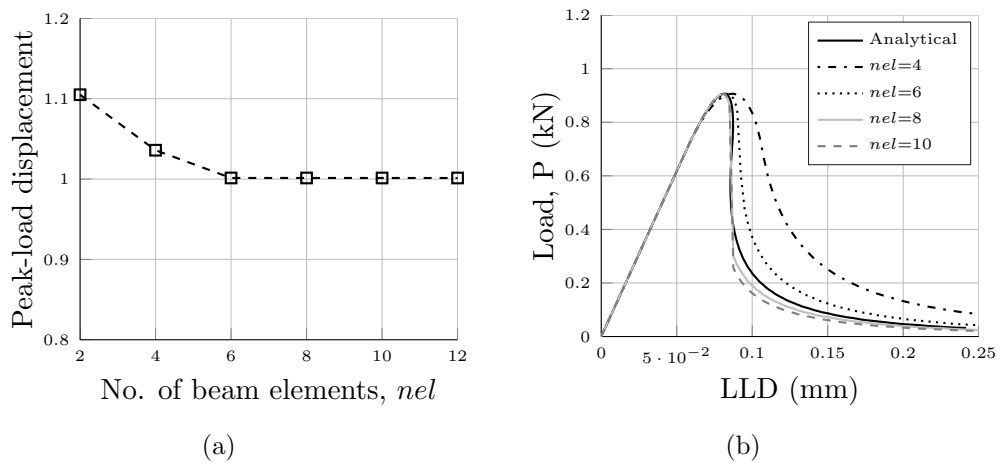


**Figure 5.19:** Convergence test: (a) Number of beam elements,  $nel$ :2-10 (element size,  $elsz$ : 0.032-0.16 m) versus peak-load displacement (normalised with regard to the analytical hinge solution) (b) Load-displacement behavior for different mesh densities compared to the analytical hinge solution.

From Figure 5.19 (b) it is observed that the peak-load  $P_u$  predicted with the hinge model is app. 900 N. This agrees reasonably well with the average peak load of  $860 \pm 60$  N that was obtained by Toumi et al. (1998). The functionality of the proposed numerical hinge for simulation the fatigue fracture behavior of a three point beam is demonstrated by plotting crack length versus the number of load cycles with the experimental results, as shown in Figure 5.20.

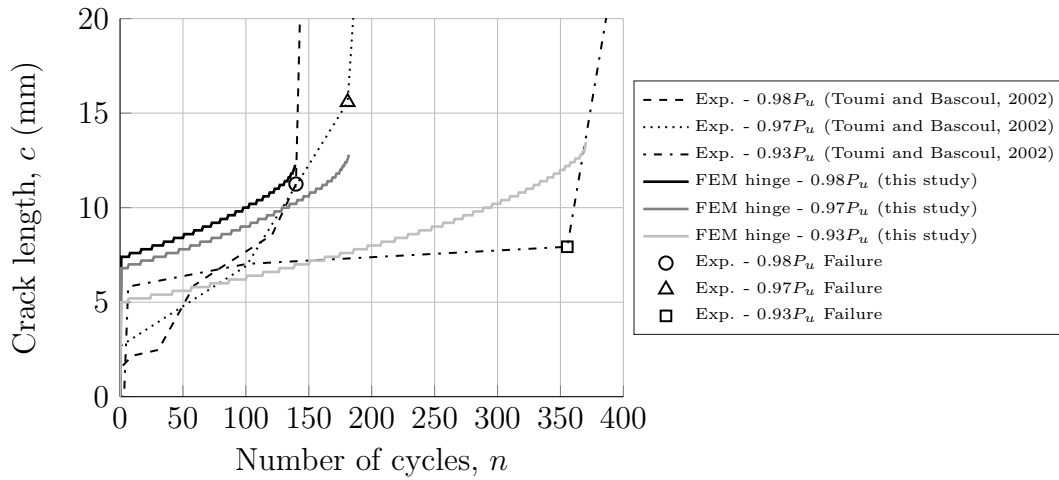


**Figure 5.20:** FEM hinge versus experimental and model curves reported in Toumi and Bascoul (2002): Crack length versus number of load cycles.

It is observed from Figure 5.20 (a) that the FEM hinge model is able to capture the crack growth development during fatigue loading. Moreover, some characteristic features of the model are shown, i.e.:

- (i) The initial crack length increase with increasing  $P_{max}$ .
- (ii) The crack growth rate increase with increasing  $P_{max}$ .
- (iii) The fatigue life increase for decreasing  $P_{max}$ .

It is also observed that the numerical crack growth curves for  $0.93P_u$  resemble the experimental, and that all three models are able to give a close prediction of the number of load repetitions to failure, without further calibration, as shown in Figure 5.21 (a).

From the load-crack mouth opening displacement curve in Figure 5.21 (b) it is observed, that the FEM hinge performs satisfactory, as the point of crack initiation, unloading and failure comply with the analytical monotonic curve.

In the analysis presented above, the fatigue damage parameter  $k_{fat}$  is calibrated to comply with one of the fatigue tests of experimental beams. An overview of the calibrated  $k_{fat}$  based on the experiments reported in Toumi and Bascoul (2002) and Plizzari et al. (1997), compared to the mechanical properties of the concrete is shown in Table 5.2.

From Table 5.2 it is observed, that the damage parameter is predicted within approximately one order of magnitude for the different experiments considered. It is also observed, that both maximum aggregate size  $D_{max}$  and

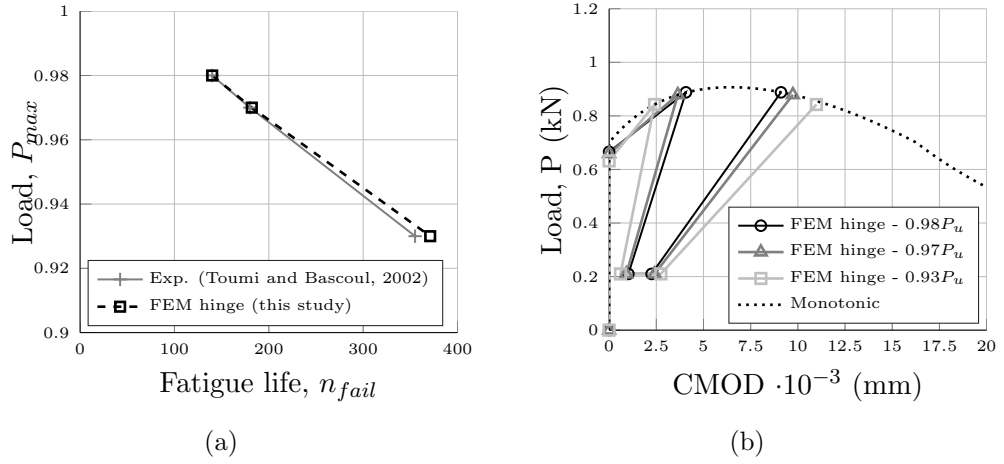


**Figure 5.21:** (a) FEM hinge versus experimental and model curves reported in Toumi and Bascoul (2002): Crack length versus number of load cycles comparing numerical. (b) Close-up of load-crack mouth opening displacement curve for the FEM hinge model plotting the first and last load cycle during fatigue loading versus the monotonic response.

**Table 5.2:** Comparison of fracture properties and fatigue damage parameter predicted in the present study. NC: Normal concrete. MC: Micro-concrete.

Test	Material	$k_{fat}$ ( $10^{-3}$ )	$D_{max}$ (mm)	$f_c$ (MPa)	$f_t$ (MPa)	$G_F$ (N/m)	$E_c$ (GPa)
Uni-axial	NC	0.3-4.1	15.0	42.1	2.41-4.25	151.0	-
Beam	MC	4.6	2.5	56.9	4.20	34.2	31.6

fracture energy  $G_F$  are lower for the micro-concrete mixture compared to the normal concrete, resulting in an increased damage parameter. This indicates that the proposed framework has the ability to capture main mechanical properties without further calibration.

The results obtained in this section give rise to further parametric studies. However, experimental validation of the fatigue damage parameter  $k_{fat}$  is difficult. The experimental data presented in this section are some of very few studies reported in the literature suitable for evaluation of cyclic cemented material behavior at constitutive level. In order to further evaluate the proposed method, or fatigue crack growth phenomena in general, more extensive fracture testing are required. These experiments should be carried out with a controlled test set-up, making it possible to distinguish between the different

cracked phases. Such tests could then be used to determine the influence from material properties, mechanical properties, test set-up (e.g. load-amplitude and frequency), geometry (e.g. size dependence and notch depth), as well as model parameters (e.g. hinge width). Moreover, the proposed model should be implemented in more realistic pavement structures to evaluate the influence of structural components on the fatigue crack response, i.e soil-structure interaction, load configuration and aggregate interlock behavior.



# Chapter 6

## Conclusions and Recommendations

This thesis presents a rational approach to pavement analysis based on mechanical models. A simple framework for engineering application is sought; creating a rational link between laboratory tests, design and field applications. The models developed and the results obtained are related to different aspects in structural design of heavy duty pavements; from a directly applicable real-scale pavement model to a local crack model that can account for crack propagation during cyclic loading. The objectives of the thesis were the following:

- (i) Develop a simple framework for numerical simulation of a cement bound granular base layer in composite block pavement systems subjected to monotonic loading.
- (ii) Introduce a simple methodology and numerical tool which significantly reduce the complexity in pavement analysis of cemented material fracture.
- (iii) Extend the framework and methodology developed to account for unloading of cracks, cyclic loading, and fatigue damage of the cemented material.

This chapter summarises the main research findings and conclusions. The conclusions are subdivided in three categories, i.e. **Real-scale model**, **Engineering model** and **Cyclic crack model**, linking the results obtained to the objectives (i), (ii) and (iii), respectively. Finally, the research outlined in this study provides a basis for recommendations applicable either to designers today or for improvement of future research.

## 6.1 Conclusions

### Real-scale model

Presently available design methods for heavy duty pavements have problems linking fatigue and monotonic behavior. Moreover, the influence from multi-dimensional geometry, soil-structure interaction and other boundary conditions are often neglected. In order to improve the current methods and move towards more generalised structural design methods for heavy duty pavements a cohesive zone model is proposed as presented in Chapter 2 and **Paper I**.

To evaluate the applicability of the cohesive zone model for the description of fracture in composite block pavement systems, a real-scale 3-D finite element model was developed assuming that the development of cracks occur in a similar fashion as the yield line mechanisms, i.e. considering *Mode I* fracture during crack propagation. Numerical analysis of four point bending beam tests and a large-scale experiment of a cement bound granular mixture slab on grade show that the cohesive zone model adequately describe the structural response. Numerical analysis of slabs revealed the importance of incorporating realistic subgrade soil behaviour in mechanical models. Most important are the shear stiffness of the soil and the plastic yield limit, as these two parameters have significantly influence on the prediction of peak-load and post-peak response, respectively. The friction between layers was found to have little influence on the overall structural response and pre-crack behavior, but significant influence on local soil response after the onset of yielding during progressive cracking.

The influence of slab thickness and dimensions proved to be important parameters. The peak-load is highly influenced by the thickness, whereas the slab dimensions proved to be a main controlling parameter of the post-peak response of the structure. Moreover, it can be concluded that the fracture process is more affected by the fracture energy than the tensile strength. The peak-loads found in the sensitivity study are significantly lower than the allowable load levels given in available guidelines for composite block pavements. This indicates that fracture cannot be avoided in this type of pavement system. Thus, accounting for the non-linear behavior of the cemented material is an overriding consideration in pavement design of concrete and composite pavements structures.

Studying the influence of loading the slab at different positions, the model showed that cracking is initiated at an early stage, and that the structural response is affected by aggregate interlock behaviour. This effect is primarily important to the response of structures subjected to edge loading. Moreover,

it is found that the peak-load decrease linearly with an increase in initial crack width.

In the real-scale model presented, the capabilities within ABAQUS are utilised using the cohesive contact model to save computational time; enabling the use of symmetry conditions and application of a coarser mesh for the cohesive zone. However, considering the large size of the model compared to the relatively simple problem studied, an extension of this model will result in very demanding models with regard to computational power and time. Moreover, the cohesive zone model incorporates a small error in crack-opening displacements related to the penalty stiffness. Increasing penalty stiffness reduce this error, however, very high levels of penalty stiffness result in ill-conditioned stiffness matrix and thus convergence issues. Thus, a more simple and robust framework, using alternative numerical tools and methods, are preferred for engineering design purpose.

## Engineering model

In order to develop a simplified and general concept for non-linear analysis of slab on grade structures, a cohesive cracked-hinge model aimed at the analysis of bending fracture of the cemented material was developed as presented in Chapter 3, 4 and **Paper II**.

The hinge model was evaluated by comparing numerical and experimental results for a four point bending beam showing good performance. Moreover, it was found that the hinge response comply well with the results obtained applying a cohesive zone model as described in the real-scale model. However, whereas the hinge model behaves perfectly elastic up to initiation of cracking, the cohesive zone model incorporates a small error in crack-opening displacements related to the penalty stiffness. This problem is avoided applying the finite element hinge, resulting in a more robust model and stable simulations.

The cracked-hinge model was extended to pavement applications, implementing a two-parameter foundation model into a beam element, making the model applicable to simulate fracture in one-way slabs supported by a semi-infinite elastic medium. Moreover, a simple method for estimating foundation model parameters was proposed. This part is important because it describes a simplified methodology for simulating fracture in slab on grade structures linking all necessary analysis steps in a rational and consistent manner.

The engineering model proposed showed that good agreement can be obtained, not only for simply supported beams, but also for structural and fracture behavior of slab on grade structures when comparing the hinge model

with the more conventional cohesive zone model. The two-parameter foundation model and the calibration methodology proposed is an efficient tool which realistically captures the response of the elastic medium below the slab. The calibration methodology is consistent and model parameters are determined on a rational basis. The methodology for estimating model parameters proposed do not give a direct physical interpretation of how soil foundation material properties and characteristics are reflected in the various elements. However, considering fracture of the slab, the proposed methodology performs significantly better than alternative methods, where model parameters are obtained from an approximation of elastic analysis.

The adaptive hinge proved to adequately predict the distance between cracks at ultimate load capacity, when compared to the yield-line theory. Moreover, peak-loads and structural responses complied well with other results reported in the literature. The beam-hinge model is able to predict the stress redistribution and stiffness during crack development. This results in a precise prediction of the crack-opening and the distance between cracks that localise and propagate through the beam depth.

A sensitivity analysis showed that the engineering model produce the same trends as the real-scale model. The slab thickness and soil stiffness again proved to be important parameters. The peak-load is highly influenced by the thickness of the slab, whereas the soil stiffness proved to be a main controlling parameter of both pre- and post-peak response of the structure. Furthermore, it can be concluded that the fracture process is more affected by the fracture energy than by the tensile strength.

In the engineering model used to study the soil-structure interaction models, increasing or decreasing the hinge rotation is modeled by the same equilibrium path. In case of a single one-way slab resting on a soil foundation and loaded by a concentrated force at midspan position the cracks developing outside midspan position are small ( $<1\%$ ) and do not influence the solution in the monotonic load case. However, as a general concept this hinge is not especially attractive, considering heavy duty pavements subjected to cyclic arbitrary loading conditions, where different phases of cracking occur at different positions in the structure simultaneously. Thus, development of a unified constitutive model that can account for these type of phenomena is preferred.

## Cyclic crack model

In order to develop a general and mechanistic modeling framework for non-linear analysis of low-cycle and fatigue damage phenomena in cemented materials, the cracked-hinge model is extended to account for unloading of a

previously open crack and evolving damage of the hinge when subjected to cyclic loading as presented in Chapter 5 and **Paper III**.

Implementation of the hinge into a beam element is relatively straightforward and the contribution to the tangent stiffness matrix from each fiber can be established following a general format, creating a versatile tool, allowing for different types of softening laws and damage formats considering both low-cyclic and high-cyclic loading. The implemented FE model was verified against the analytical model showing good performance. The implemented damage-plasticity format sufficiently captured the response of experimental cyclic uni-axial tensile tests of plain concrete. The developed analytical hinge model showed satisfying performance compared to integration over the full hinge segment. A good fit was obtained using a relatively coarse discretisation of 10 to 30 fibers. Further, this model was successfully used in conjunction with elastic beam theory, describing the structural behavior of experimental beams under four point loading.

A simple energy based approach for damage evolution during fatigue loading was proposed, requiring only a single model parameter additional to the monotonic parameters. The selected format is general and consistent and ensures that damage during fatigue loading is restricted to the monotonic failure envelope, i.e. the damage state after arbitrary loading is associated with a monotonic loading process that leads to the same damage state. When comparing the proposed model format with experimental results of plain concrete subjected to uni-axial tension fatigue loading, a good fit is obtained describing the deterioration of the single hinge fibers. However, experimental validation of the fatigue damage parameter  $k_{fat}$  is difficult due to the lack of sufficient experimental data.

The proposed FEM hinge model adequately describe the cyclic response of a plain concrete beam under three point loading. It was also found that the proposed hinge model comply well with other numerical results published in the literature using the same model parameters in a cohesive zone model. Simulation of a beam resting on soil foundation show that the hinge model captures the main structural response. The hinge model resting on a Winkler foundation does not describe the pre-peak behavior observed in experiments adequately well, and therefore indicates that the soil model and the boundary conditions applied does not comply with the test set-up. To overcome the deficiency of the Winkler model, a two-parameter model was applied, showing good performance in the pre-peak phase.

The FEM hinge adequately describe the fatigue crack growth of plain concrete beams under three point loading. Main characteristic features, such as initial crack length and fatigue crack growth rate, can be simulated with the FEM hinge model. Moreover, it was found that the energy based methodol-

ogy applied is able to capture the influence of varying load amplitude, as a close prediction of the number of cycles to failure could be obtained.

## 6.2 Practical applications

The models developed in this study provide some practical recommendations for pavement designers to either increase the reliability built into the design concept or reduce construction cost from optimised designs. The most important recommendations are summarised below:

- (i) In linear elastic analysis of heavy duty composite pavement structures, the layer thickness is normally increased for increasing load levels, to ensure a relatively constant stress level in the subgrade soil, avoiding any plastic deformation. This approach can be questioned as the allowable load levels in presently available guidelines are twice the magnitude compared to the peak-loads of the slabs found in the present study. The full slab model shows that cracking is initiated at an early stage, and that the structural response in addition to the non-linear response of the cemented material is affected by the subgrade soil stiffness, aggregate interlock behavior, and loading condition. These effects should be addressed in design of heavy duty concrete and composite pavements subjected to static loading by application of appropriate methods, e.g. cohesive zone modeling or the yield-line method. For concrete pavements it will also be relevant to evaluate climatic effects, e.g. by including the influence from slab-curling as proposed by Aure and Ioannides (2015a).
- (ii) Gaedicke et al. (2012) proposed to use a 3-D cohesive zone model to calculate the static flexural strength of concrete slabs on grade for input in M-E models. Similarly, the 3-D cohesive zone model presented in this study could be used in conjunction with appropriate stress-based fatigue laws for cement bound granular mixture materials, defining the stress ratio as the quotient between the applied tensile stress in the cemented layer and its monotonic strength, as proposed by Roesler and Barenberg (1999). This will result in a more consistent and rational approach within the M-E method, however, the influence on the evolving performance and structural response for cyclic loading will remain hidden in the empirical fatigue relationship. Moreover, such modification of existing fatigue relationships cannot be done without large-scale experimental validation.

- (iii) From the results obtained in this study it is evident that the soil stiffness significantly influences the response and it should therefore be considered in the design evaluation. This is not always the case as a conservatively low Young's modulus of the soil foundation often is applied in heavy duty pavement design. Moreover, localisation of cracks results in increasing soil stresses near the crack front during progressive cracking. Thus, a failure criterion for the supporting layers and soil foundation should be included in the analysis in order to make a complete rational design analysis. In the present study an idealised elasto-plastic Mohr-Coulomb model was successfully applied in numerical analysis of slabs from experiments.
- (iv) The FE method has the capability of solving a wide variety of engineering problems and it is currently the most widespread numerical tool used for routine design. However, there is a tendency in the industry that increasing software and hardware capabilities result in increasingly more complex and detailed models. Thus, models developed are often overcomplicated and oversized compared to the problem at hand. Engineering judgement should be used when selecting analysis tool. Element types and solver techniques should be carefully chosen and relevant model idealisation applied in order to reduce the computational time and increase the stability of the simulations. In the real-scale model the capabilities within a commercial software is utilised. However, to significantly boost this process new element types and methods are needed as exemplified in the engineering model.
- (v) Application of mechanical models for numerical analysis require material parameters based on tests of actual physical properties in the laboratory or from tests where relevant mechanical parameters can be extracted. Based on the results presented in this study it is obvious that for concrete and composite pavements testing of the cemented material fracture properties in the tensile regime is of primary interest. However, this is not the case today as concrete and cement bound granular mixtures used in paving and construction are typically classified based on their compression strength. The compressions strength is a relevant material property, however, classification of cemented materials cannot be based solely on this measure to describe their tensile behavior. Thus, in view of the present study, it is recommended to incorporate material properties in design standards and specifications which are relevant to the loading regime they are exposed to in the field.

## 6.3 Recommendations for future research

The research outlined in this study constitutes the initial development of a mechanistic based structural analysis procedure. However, there are many aspects of future research that can be built upon the work done. A few recommendations of this research are addressed as follows:

- (i) Novel use of alternative numerical methods and tools was demonstrated in the present study extending the hinge model proposed by Olesen and Poulsen (2012) to pavement applications. Future research should focus on developing optimised numerical tools for application in design. This should include aggregate interlock and soil-structure interaction models capable of describing the non-linear phenomena highlighted in the present study, also considering their cyclic behavior.
- (ii) The elastic two-parameter model presented does, by definition, not take into account any elastic-plastic or irreversible behavior of the soil medium. Such behavior may be incorporated in two-parameter models by introducing a yield limit for the springs. Including the slab as well as slab fracture into such model will significantly increase the complexity of the problem as both elastic properties and yielding characteristics of the foundation change during progressive cracking. New methodologies should be extended to capture relevant failure types, e.g. by incorporating adaptive methods in two-parameter models.
- (iii) The engineering model presented is applicable to two-dimensional problems, which can be used in special design cases, for sensitivity analysis, and simple studies. In order to make the proposed methodology applicable to three-dimensional analysis the cyclic hinge and mechanical soil-structure interaction models presented in this study can be incorporated into a plate element. This will further require a reformulation of the two-parameter foundation model to the axisymmetric case, see e.g. Loof (1965). The foundation model parameters can then be calibrated applying Boussinesq's solution following the methodology proposed in the present study.
- (iv) The development of new constitutive models such as the cyclic crack model proposed in this study, give rise to new parametric studies and sensitivity analysis. Experimental validation of the parameter  $k_{fat}$  is difficult at the present time due to lack of adequate data. Assuming that the proposed damage format is sufficient, extended parametric studies of experiments published in the literature can be used to obtain

realistic values for  $k_{fat}$ . Further, evaluation of the model parameter  $s$  (hinge width) should be conducted accounting for the influence from soil-structure interaction.

- (v) In the present study only deterioration of the cemented material subjected to mechanical loads was considered. However, also environmental effects, e.g. moisture and temperature, has significant influence on the stress condition in rigid pavements. Extending the methodology to incorporate these effects is possible, as a first step e.g. by including the strain contribution from linear temperature expansion. Further, cracking, warping and curling of slabs may lead to de-bonding of layers. For this purpose new elements, e.g. spring elements could be developed.
- (vi) The cyclic cracked-hinge model presented in this study is appropriate for further development and practical use. However, experimental data available in the literature are in most cases not adequate to describe the cyclic behaviour of materials at a constitutive level. In order to develop a complete mechanistic approach for design of heavy duty pavements, extensive experimental programs are needed, making it possible to verify and refine constitutive models. For cement bound granular mixture materials and other relevant cement stabilised materials, one must start with simple mechanical tests such as uni-axial tensile tests (or tensile split tests) and fracture energy tests. Then, the cyclic behavior of cemented materials should be addressed, e.g. uni-axial and beam fracture fatigue tests using a controlled test set-up, making it possible to distinguish between the different crack phases. Further, these methodologies should be transferred to the field and full-scale testing making it possible to link model, lab and field results.
- (vii) Finally, for such a methodology to be implemented in practice a safety format for design should be developed. Within the pavement engineering field, standards typically reflect local experience and tradition, often without any specific requirements to model parameters used in the structural design. Model codes form the basis of standards and guidelines within structural engineering and a more rational approach to pavement analysis would increase the motivation to implement such harmonised and consistent formats.



# Bibliography

- ABAQUS (2013). *Analysis users manual, Version 6.13-1*. Dassault Systems, Providence, R.I.
- Alderson, A. (2013). Prediction of flexural strength and breaking strain of cemented materials - laboratory study. Technical report, Ausroads.
- Alvaredo, A. and Torrent, R. (1987). The effect of the shape of the strain-softening diagram on the bearing capacity of concrete beams. *Materials and Structures*, 20(6):448–454.
- Asferg, J. L., Poulsen, P. N., and Nielsen, L. O. (2007). A consistent partly cracked xfm element for cohesive crack growth. *International Journal for Numerical Methods in Engineering*, 72(4):464–485.
- Asphalt-Institute (2006). *Thickness Design - Asphalt Pavements for Heavy Wheel Loads*. The Asphalt Institute, USA, 2 edition.
- ASTM (2015). Astm c293c293m15: Standard test method for flexural strength of concrete (using simple beam with center-point loading). *ASTM International, West Conshohocken, PA, 2015*.
- ASTM (2016). Astm c78c78m15b: Standard test method for flexural strength of concrete (using simple beam with third-point loading). *ASTM International, West Conshohocken, PA, 2016*.
- Aure, T. W. and Ioannides, A. M. (2012). Numerical analysis of fracture process in pavement slabs. *Canadian Journal of Civil Engineering*, 39(5):506–514.
- Aure, T. W. and Ioannides, A. M. (2015a). Curling effects on concrete slab-on-grade fracture. *Materials and Structures/materiaux Et Constructions*, 49(8):2991–3004.

- Aure, T. W. and Ioannides, A. M. (2015b). Fracture analysis of aggregate interlock jointed slabs-on-grade. *Construction and Building Materials*, 77(0):340 – 348.
- Austroroads (2004). *Pavement design: A guide to the structural design of road pavements*. Austroroads.
- Bach, C. and Graf, O. (1915). *Versuche mit allseitig aufliegenden, quadratischen und rechteckigen Eisenbetonplatten: ausgeführt in der Materialprüfungsanstalt der Königlichen Technischen Hochschule zu Stuttgart in den Jahren 1911 bis 1914; Bericht mit 34 Zusammenstellungen*. Wilhelm Ernst & Sohn.
- Bache, H. and Vinding, I. (1990). Fracture mechanics in design of concrete pavements. In *Second International Workshop on the Design and Evaluation of Concrete Pavements, Siguenza. Information and Technology Center for Transport and Infrastructure/Permanent International Association of Road Congresses-World Road Association, Spain*, pages 139–165.
- Balbo, J. T. (1997). High quality cement treated crushed stones for concrete pavement bases. In *Proceedings of the Sixth International Purdue Conference on Concrete Pavement November*, pages 18–21.
- Barber, S. D. (1980). *Pavement design for port areas*. PhD thesis, Newcastle University, United Kingdom.
- Barenberg, E. (2005). Factors affecting fatigue failure of concrete. In *Proceedings of workshop on fracture mechanics for concrete pavements: theory to practice. Colorado, USA*.
- Barenblatt, G. (1959). The formation of equilibrium cracks during brittle fracture. general ideas and hypotheses. axially-symmetric cracks. *Journal of Applied Mathematics and Mechanics*, 23(3):622–636.
- Baumann, R. A. and Weisgerber, F. E. (1983). Yield-line analysis of slabs-on-grade. *Journal of Structural Engineering*, 109(7):1553–1568.
- Bažant, Z. P. (2002). Concrete fracture models: testing and practice. *Engineering Fracture Mechanics*, 69(2):165–205.
- Bažant, Z. P. and Gambarova, P. (1980). Rough cracks in reinforced concrete. *ASCE J Struct Div*, 106(4):819–842.
- Bažant, Z. P. and Oh, B. H. (1983). Crack band theory for fracture of concrete. *Matériaux et construction*, 16(3):155–177.

- Beckett, D. (1990). Comparative tests on plain, fabric reinforced and steel fibre reinforced concrete ground slabs. *Concrete*, 24(3):43–45.
- Belletti, B., Cerioni, R., Meda, A., and Plizzari, G. (2008). Design aspects on steel fiber-reinforced concrete pavements. *Journal of Materials in Civil Engineering*, 20(9):599–607.
- Belytschko, T. and Black, T. (1999). Elastic crack growth in finite elements with minimal remeshing. *International journal for numerical methods in engineering*, 45(5):601–620.
- Boussinesq, J. (1885). *Application des potentiels a l'équilibre et du mouvement des solides élastiques...*, volume 4. Gauthier-Villars.
- Brake, N. A. and Chatti, K. (2013). Prediction of size effect and non-linear crack growth in plain concrete under fatigue loading. *Engineering Fracture Mechanics*, 109:169–185.
- BS (2001). Pavements constructed with clay, natural stone or concrete pavers. part 1: Guide for the structural design of heavy duty pavements constructed of clay pavers or precast concrete paving blocks. *BS 7533-1:2001*.
- BS (2013). British standards institution - hydraulically bound mixtures. specifications. cement bound granular mixtures. *BS EN 14227-1:2013*.
- Burmister, D. M. (1945). The general theory of stresses and displacements in layered systems. i. *Journal of applied physics*, 16(2):89–94.
- Busch, C., Wysokowski, A., Cwiakala, M., Adesiyun, A., Zurawicka, A., Duszynski, A., Korusiewicz, L., Kaszub, P., and Nowak, A. (2006). Large scale test of semi rigid pavements at test stand in zmigrod. *IBDiM, COWI A/S and ECO-SERVE Thematic Network European Construction in Service of Society*, Report no. TW 65406/G1RT-CT-2002-05085(2006).
- Camacho, G. T. and Ortiz, M. (1996). Computational modelling of impact damage in brittle materials. *International Journal of solids and structures*, 33(20):2899–2938.
- Carol, I., Prat, P. C., and López, C. M. (1997). Normal/shear cracking model: application to discrete crack analysis. *Journal of engineering mechanics*, 123(8):765–773.
- Cervantes, V. and Roesler, J. (2009). Performance of concrete pavements with optimized slab geometry. *Urbana*, 51:61801.

- Chabot, A., Tran, Q. D., and Ehrlicher, A. (2005). A simplified modeling for cracked pavements. *Bulletin des Laboratoires des Ponts et chaussées*, 258-259:105–120.
- Colasanti, R. J. and Horvath, J. S. (2010). Practical subgrade model for improved soil-structure interaction analysis: software implementation. *Practice Periodical on Structural Design and Construction*, 15(4):278–286.
- Colombier, G. and Marchand, J. (1993). The precracking of pavement underlays incorporating hydraulic binders. reflective cracking in pavements. In *Proceedings of the 2nd International RILEM Conference, Liege, Belgium*. Spon, London.
- Cook, R. D. et al. (2007). *Concepts and applications of finite element analysis*. John Wiley & Sons.
- Cornelissen, H. (1984). Fatigue failure of concrete in tension. *HERON*, 29(4), 1984.
- Corté, J.-F. and Goux, M.-T. (1996). Design of pavement structures: the french technical guide. *Transportation Research Record: Journal of the Transportation Research Board*, 1539(1):116–124.
- Crisfield, M. (1983). An arc-length method including line searches and accelerations. *International journal for numerical methods in engineering*, 19(9):1269–1289.
- Darter, M. I. (1988). A comparison between corps of engineers and eres consultants, inc. rigid pavement design procedures. Technical report, Technical Report Prepared for the United States Air Force SAC Command. Savoy, IL.
- Darter, M. I. and Barenberg, E. J. (1977). Design of a zero-maintenance plain jointed concrete pavement, volume one-development of design procedures. (FHWA-RD-77-III).
- Davids, W. G. and Mahoney, J. P. (1999). Experimental verification of rigid pavement joint load transfer modeling with everfe. *Transportation Research Record: Journal of the Transportation Research Board*, 1684(1):81–89.
- De Borst, R. and Nauta, P. (1985). Non-orthogonal cracks in a smeared finite element model. *Engineering Computations*, 2(1):35–46.

- Desai, C. S. (2007). Unified dsc constitutive model for pavement materials with numerical implementation. *International Journal of Geomechanics*, 7(2):83–101.
- Dugdale, D. (1960). Yielding of steel sheets containing slits. *Journal of the Mechanics and Physics of Solids*, 8(2):100–104.
- Elias, J. and Le, J.-L. (2012). Modeling of mode-i fatigue crack growth in quasibrittle structures under cyclic compression. *Engineering Fracture Mechanics*, 96:26–36.
- Evangelista, Francisco, J., Roesler, J. R., and Proena, S. P. (2013). Three-dimensional cohesive zone model for fracture of cementitious materials based on the thermodynamics of irreversible processes. *Engineering Fracture Mechanics*, 97:261–280.
- FAA (2009). *Advisory Circular (AC) 150/5320-6E*. Airport Pavement Design and Evaluation, Federal Aviation Administration, US Department of Transportation, Washington, DC.
- Filonenko-Borodich, M. (1940). Some approximate theories of the elastic foundation. *Uchenyie Zapiski Moskovskogo Gosudarstvennogo Universiteta Mekhanika*, 46:3–18.
- Finney, E. A. and Oehler, L. T. (1959). Final report on design project, michigan test road. In *Highway Research Board Proceedings*, volume 38.
- Flamant, A. (1892). *Compt. rend.* 114. (114):1465.
- Freeme, C., Maree, J., and Viljoen, A. (1982). *Mechanistic design of asphalt pavements and verification using the heavy vehicle simulator*. National Institute for Transport and Road Research.
- Gaedicke, C. and Roesler, J. (2009). Fracture-based method to determine the flexural load capacity of concrete slabs. *FAA COE Rep*, (31).
- Gaedicke, C., Roesler, J., and Evangelista, F. (2012). Three-dimensional cohesive crack model prediction of the flexural capacity of concrete slabs on soil. *Engineering Fracture Mechanics*, 94:1–12.
- Gonzalez, A., Howard, A., and de Carteret, R. (2010). Cost effective structural treatments for rural highways: cemented materials. Technical report, Ausroads.

- Gopalaratnam, V. S. and Shah, S. P. (1985). Softening response of plain concrete in direct tension. *Journal of the American Concrete Institute, J Am Conc I, J Am Concrete I, J Amer Concr Inst*, 82(3):310–323.
- Grassl, P., Xenos, D., Nyström, U., Rempling, R., and Gylltoft, K. (2013). Cdp2: A damage-plasticity approach to modelling the failure of concrete. *International Journal of Solids and Structures*, 50(24):3805–3816.
- Gunatilake, M. M. D. V. and Mampearachchi, W. K. (2014). Development of a finite element model for concrete block paving. *Journal of Society for Transportation and Traffic Studies*, 5(2):46–56.
- Gustafsson, P., i Lund. Avdelingen fr Byggnadsmateriallra., T. H., and LTH. (1985). *Fracture mechanics studies of non-yielding materials like concrete : Modelling of tensile fracture and applied strength analyses*.
- Gylltoft, K. (1983). *Fracture mechanics models for fatigue in concrete structures*. Luleå Institute of Technology, Division of Structural Engineering.
- Hansen, J. B. (1970). A revised and extended formula for bearing capacity. *The Danish Geotechnical Institute, Bulletin no. 28*.
- Harvey, J., Roesler, J., Farver, J., and Liang, L. (2000). Preliminary evaluation of proposed llprs rigid pavement structures and design inputs. *Final Report, FHWA/CA/OR-2000/02, University of California-Berkeley, Pavement Research Center, Richmond, California*.
- Hetényi, M. (1946). *Beams on elastic foundation: theory with applications in the fields of civil and mechanical engineering*. University of Michigan.
- Hetenyi, M. (1966). Beams and plates on elastic foundations and related problems. *Appl. Mech. Rev*, 19(2):95–102.
- Hillerborg, A., Modéer, M., and Petersson, P.-E. (1976). Analysis of crack formation and crack growth in concrete by means of fracture mechanics and finite elements. *Cement and concrete research*, 6(6):773–781.
- Hilsdorf and Brameshuber (1991). Code-type formulation of fracture mechanics concepts for concrete. *International Journal of Fracture*, 51(1):61–72.
- Högberg, J. L. (2006). Mixed mode cohesive law. *International Journal of Fracture*, 141(3-4):549–559.
- Hordijk, D. (1992). Tensile and tensile fatigue behaviour of concrete; experiments, modelling and analyses. *Heron*, 37(1):1–79.

- Hordijk, D. A. (1991). *Local Approach to fatigue of Concrete*. PhD thesis, Technische Universiteit Delft.
- Horvath, J. (2002). Soil-structure interaction research project: Basic ssi concepts and applications overview. *Manhattan College School of Engineering, Bronx, New York, USA*.
- Horvath, J. S. and Colasanti, R. J. (2011). New hybrid subgrade model for soil-structure interaction analysis: foundation and geosynthetics applications. *Proceedings of the Geo-Frontiers: Advances in Geotechnical Engineering*, pages 4359–4368.
- HRB (1962). The aasho road test, report 5: Pavement research. Technical Report in Special Report 61, HRB, National Research Council, Washington, D.C.
- Huang, Y. H. (1993). *Pavement analysis and design*. Prentice-Hall, Inc., Upper Saddle River, NJ.
- Huben, L., Molenaar, A., Fuchs, G., and Moll, H. (1984). Analysis and design of concrete block pavements. In *Proceedings, 2nd International Conference on Concrete Block Paving, Delft*, pages 86–99.
- Huurman, M. (1994). Development of the non-linear finite element program nolip for concrete block pavements. In *Proceedings Second International Workshop on Concrete Block Paving, Oslo, Norway*, pages 157–166.
- Huurman, M. (1996). Development of traffic induced permanent strain in concrete block pavements. *HERON*, 41 (1), 1996.
- Huurman, M., Houben, L. J. M., and Kok, A. W. M. (1992). Development of a three-dimensional finite element model for concrete block pavements. In *Proceedings Fourth International Conference on Concrete Block Paving*, pages 89–98.
- Ioannides, A., Thompson, M., and Barenberg, E. (1985a). Finite element analysis of slabs-on-grade using a variety of support models. In *Third International Conference on Concrete Pavement Design and Rehabilitation*, number 1 Volume.
- Ioannides, A., Thompson, M. R., and Barenberg, E. J. (1985b). Westergaard solutions reconsidered. *Transportation research record*, 1043:13–23.
- Ioannides, A. M. (1997). Fracture mechanics in pavement engineering: The specimen-size effect. *Transportation Research Record*, (1568):10.

- Ioannides, A. M. (2005). Stress prediction for cracking of jointed plain concrete pavements, 1925-2000: An overview. *Transportation Research Record: Journal of the Transportation Research Board*, (1919):47–53.
- Ioannides, A. M. (2006). Concrete pavement analysis: the first eighty years. *International Journal of Pavement Engineering*, 7(4):233–249.
- Ioannides, A. M., Peng, J., and Swindler Jr, J. R. (2006). Abaqus model for pcc slab cracking. *International Journal of Pavement Engineering*, 7(4):311–321.
- Iyengar, K. S. R., Raviraj, S., and Jayaram, T. (2002). Analysis of crack propagation in strain-softening beams. *Engineering Fracture Mechanics*, 69(6):761–778.
- Jacobsen, J., Poulsen, P., Olesen, J., and Krabbenhoft, K. (2013). Constitutive mixed mode model for cracks in concrete. *Engineering Fracture Mechanics*, 99:30–47.
- Jacobsen, J. S. (2012). *Constitutive Mixed Mode Behavior of Cracks in Concrete - Experimental Investigations of Material Modeling*. PhD thesis, Technical University of Denmark.
- Jameson, G., Sharp, K. G., and Yeo, R. (1992). *Cement-treated Crushed Rock Pavement Fatigue Under Accelerated Loading: The Mulgrave (Victoria) ALF Trial, 1989/1991*. Number ARR229.
- Jensen, T. W. (2016). Numerical analysis of existing concrete bridges in ultimate and serviceability limit state.
- Jirásek, M. (2000). Comparative study on finite elements with embedded discontinuities. *Computer methods in applied mechanics and engineering*, 188(1):307–330.
- Jirásek, M. (2001). Modeling of localized damage and fracture in quasibrittle materials. In *Continuous and Discontinuous Modelling of Cohesive-Frictional Materials*, pages 17–29. Springer.
- Johansen, K. W. (1955). Slabs on soil. *Research Laboratory of Building Technique, Technical University of Denmark*, (4).
- Jones, R. (1978). Consistent approach to the fracture of pavements. *ACTA MECHANICA*, 31(1-2):137–146.

- Jones, R. and Xenophontos, J. (1977). The vlasov foundation model. *International Journal of Mechanical Sciences*, 19(6):317–323.
- Kaplan, M. (1961). Crack propagation and the fracture of concrete. In *Journal Proceedings*, volume 58, pages 591–610.
- Kawa, I., Brill, D., and Hayhoe, G. F. (2007). Faarfield-new faa airport thickness design software. In *Proceedings of the 2007 FAA Worldwide Airport Technology Transfer Conference, Atlantic City, New Jersey*.
- Kerkhoven, R. and Dormon, G. M. (1953). *Some considerations on the California bearing ratio method for the design of flexible pavements*. Shell Petroleum Company.
- Kerr, A. D. (1964). Elastic and viscoelastic foundation models. *Journal of Applied Mechanics*, 31(3):491–498.
- Kerr, A. D. (1965). A study of a new foundation model. *Acta Mechanica*, 1(2):135–147.
- Kessler-Kramer, C., Mechtcherine, V., and Müller, H. (2001). Fatigue behaviour of concrete in tension. *Fracture Mechanics of Concrete Structures, de Borst et al.(eds), Sweets & Zeitlinger, Lisse*, pages 573–578.
- Khazanovich, L. (2003). Finite element analysis of curling of slabs on paster-nak foundation. In *16th ASCE Engineering Mechanics Conference, July*, pages 16–18.
- Khazanovich, L. and Ioannides, A. M. (1993). Finite element analysis of slabs-on-grade using higher order subgrade soil models. In *Airport Pavement Innovations Theory to Practice. Proceedings of conference held sept 8-10, 1993, Vicksburg, Mississippi, USA*.
- Khazanovich, L. and Ioannides, A. M. (1994). Structural analysis of unbonded concrete overlays under wheel and environmental loads. *Transportation Research Record*, (1449).
- Knapton, J. (1984). *The Structural Design of Heavy Duty Pavements for Ports and Other Industries*. British Ports Association, London, England, 1 edition.
- Knapton, J. (1986). *The Structural Design of Heavy Duty Pavements for Ports and Other Industries*. British Ports Federation, London, England, 2 edition.

- Knapton, J. (2008). *The Structural Design of Heavy Duty Pavements for Ports and Other Industries*. Interpave, 4 edition.
- Knapton, J. and Meletiou, M. (1996). *The Structural Design of Heavy Duty Pavements for Ports and Other Industries*. British Precast Concrete Federation, Leicester, England, 3 edition.
- Kohler, E. and Roesler, J. (2006). Accelerated pavement testing of extended life continuously reinforced concrete pavement sections. *FHWA-IL-UI-289*.
- Lee, J. and Fenves, G. (1998). Plastic-damage model for cyclic loading of concrete structures. *Journal of Engineering Mechanics*, 124(8):892–900.
- Lin, S.-T. and Folias, E. S. (1975). On the fracture of highway pavements. *International Journal of Fracture*, 11(1):93–106, 93–106.
- Litwinowicz, A. and Brandon, A. (1994). Dynamic flexure testing for prediction of cement-treated pavement life. *Proceedings - Conference of the Australian Road Research Board*, 17(2):229–247.
- Liu, J.-h. and Wang, D.-y. (2008). Numerical simulation of a crack in the cement stabilized stone using cohesive zone models. In *International Conference on Experimental Mechanics 2008 and Seventh Asian Conference on Experimental Mechanics*, pages 737511–737511. International Society for Optics and Photonics.
- Loof, H. (1965). The theory of the coupled spring foundation as applied to the investigation of structures supported on soil. *HERON*, 13 (3), 1965.
- Losberg, A. (1961). Design methods for structurally reinforced concrete pavements. Bulletin No. 250:305–314.
- Losberg, A. (1978). Pavements and slabs on grade with structurally active reinforcement. In *Journal Proceedings*, volume 75, pages 647–657.
- Lubliner, J., Oliver, J., Oller, S., and Onate, E. (1989). A plastic-damage model for concrete. *International Journal of Solids and Structures*, 25(3):299–326.
- Maekawa, K., Takemura, J., Irawan, P., and Irie, M. (1993). Triaxial elasto-plastic and fracture model for concrete. *Doboku Gakkai Rombun-Hokokushu/Proceedings of the Japan Society of Civil Engineers*, (460 pt 5-18):131–138.

- Mahoney, J., Lary, J. A., Pierce, L. M., Jackson, N. C., and Barenberg, E. (1991). Urban interstate portland cement concrete pavement rehabilitation alternatives for washington state. *Washington State Department of Transportation, Report no. WA-RD*, 202:350.
- Mazars, J. (1986). A description of micro-and macroscale damage of concrete structures. *Engineering Fracture Mechanics*, 25(5):729–737.
- Meda, A. (2003). Design methods for slabs on grade in fiber reinforced concrete. *System-based Vision for Strategic and Creative Design, Vols 1-3*, pages 1413–1418.
- Meda, A., Plizzari, G. A., and Riva, P. (2004). Fracture behavior of sfrc slabs on grade. *Materials and Structures*, 37(270):405–411.
- Meletiou, M. and Knapton, J. (1987). Container terminal pavement management iii. *WWS/WORLD WIDE SHIPPING*, 50(5).
- Meyerhof, G. G. (1963). Some recent research on the bearing capacity of foundations. *Canadian Geotechnical Journal*, 1(1):16–26.
- Miner, A. M. (1945). Cumulative damage in fatigue. *Journal of Applied Mechanics*, 12:A159–A164.
- Moës, N., Dolbow, J., and Belytschko, T. (1999). A finite element method for crack growth without remeshing. *International journal for numerical methods in engineering*, 46(1):131–150.
- Moghadas Nejad, F. and Shadravan, M. (2010). A study on behavior of block pavement using 3d finite element method. *Computational Methods in Civil Engineering*, 1(1):65–71.
- Molenaar, A., Moll, H., and Houben, L. (1984). *Structural model for concrete block pavement*. Number 954.
- Mougaard, J. F., Poulsen, P. N., and Nielsen, L. O. (2010). Modelling concrete structures applying xfem with a mixed mode constitutive model. *Fracture mechanics of concrete and concrete structures: recent advances in fracture mechanics of concrete*, Korea Concrete Institute, Seoul.
- NAASRA (1992). *Pavement design: A guide to the structural design of road pavements*. Austroads, Sidney, Australia.

- Nasser, H. and Chabot, A. (2015). Two-dimensional software for analysing mechanical fields in elastic cracked pavements. *J. Kruis, Y. Tsompanakis, BHV Topping. CC2015 Stirlingshire, UK, Paper*, 214:1–4.
- NCHRP (2003). Guide for mechanistic-empirical design of new and rehabilitated pavement structures: Structural response modeling of rigid pavements - appendix qq. *National Cooperative Highway Research Program, Transportation Research Board, National Research Council, Washington, DC*.
- NCHRP (2004). Guide for mechanistic-empirical design of new and rehabilitated pavement structures: Final report for project 1-37a. *National Cooperative Highway Research Program, Transportation Research Board, National Research Council, Washington, DC*.
- Needleman, A. (1987). A continuum model for void nucleation by inclusion debonding. *Journal of applied mechanics*, 54(3):525–531.
- Nejad, F. M. (2003). Finite element analysis of concrete block paving. In *7th International Conference on Concrete Block Paving*, volume 35.
- Nguyen, G. D. (2005). *A thermodynamic approach to constitutive modelling of concrete using damage mechanics and plasticity theory*. University of Oxford.
- Nguyen, O., Repetto, E., Ortiz, M., and Radovitzky, R. (2001). A cohesive model of fatigue crack growth. *International Journal of Fracture*, 110(4):351–369.
- Nielsen, L. O., Mouggaard, J. F., Jacobsen, J. S., and Poulsen, P. N. (2010). A mixed mode model for fracture in concrete. *Fracture mechanics of concrete and concrete structures: recent advances in fracture mechanics of concrete. Korea Concrete Institute, Seoul*.
- Nishizawa, T. (2003). A tool for structural analysis of block pavements based on 3dfem. In *7th International Conference on Concrete Block Paving*.
- Nishizawa, T., Matsuno, S., and Komura, M. (1984). Analysis of interlocking block pavements by finite element method. In *Proceedings of 2nd international conference on concrete block paving, Delft*, pages 80–85.
- Odemark, N. (1949). Investigations as to the elastic properties of soils and design of pavements according to the theory of elasticity. Technical report.

- Older, C. (1924). Highway research in illinois. *Transactions of the American Society of Civil Engineers*, 88(1):1180–1222.
- Olesen, J. and Poulsen, P. (2013). An embedded crack in a constant strain triangle utilizing extended finite element concepts. *Computers and Structures*, 117:1–9.
- Olesen, J. F. (2001a). Cracks in reinforced frc beams subject to bending and axial load. *Fracture mechanics of concrete structures, vols 1 and 2*, pages 1027–1033.
- Olesen, J. F. (2001b). Fictitious crack propagation in fiber-reinforced concrete beams. *Journal of Engineering Mechanics*, 127(3):272–280.
- Olesen, J. F., Østergaard, L., and Stang, H. (2006). Nonlinear fracture mechanics and plasticity of the split cylinder test. *Materials and structures*, 39(4):421–432.
- Olesen, J. F. and Poulsen, P. N. (2012). Modeling rc beam structures based on cracked hinge model and finite elements. Technical Report SR12-11, Technical University of Denmark, DTU Civil Engineering.
- Oliver, J. (1996). Modelling strong discontinuities in solid mechanics via strain softening constitutive equations. part 1: Fundamentals. *International journal for numerical methods in engineering*, 39(21):3575–3600.
- Ortiz, M. and Pandolfi, A. (1999). Finite-deformation irreversible cohesive elements for three-dimensional crack-propagation analysis. *International Journal for Numerical Methods in Engineering*, 44(9):1267–1282.
- Otte, E. (1978). *A structural design procedure for cement-treated layers in pavements*. PhD thesis, University of Pretoria, South Africa.
- Packard, R. G. (1984). Thickness design for concrete highway and street pavements. *Portland Cement Association*.
- Packard, R. G. and Tayabji, S. D. (1985). New pca thickness design procedure for concrete highway and street pavements. In *Third International Conference on Concrete Pavement Design and Rehabilitation*, number 1 Volume.
- Palmgren, A. (1924). Die lebensdauer von kugellagern. *Zeitschrift des Vereins Deutscher Ingenieure*, 68(14):339–341.

- Pasternak, P. (1954). On a new method of analysis of an elastic foundation by means of two constants [gosudarstvennoe izdatelstvo literaturi po stroitelstvu i arkhitekture]. *Moscow: USSR*.
- Petersson, P.-E. (1981). *Crack growth and development of fracture zones in plain concrete and similar materials*. PhD thesis, Division of Building Materials, Lund Institute of Technolog.
- PIANC (2015). Design and maintenance of container terminal pavements. Technical Report 165, PIANC, Bruxelles, Belgium.
- Plizzari, G., Cangiano, S., and Alleruzzo, S. (1997). The fatigue behaviour of cracked concrete. *Fatigue & Fracture of Engineering Materials & Structures*, 20(8):1195–1206.
- Puzrin, A. (2012). *Constitutive Modelling in Geomechanics*. Springer Berlin Heidelberg.
- Ramsamooj, D. (1993). Fracture of highway and airport pavements. *Engineering Fracture Mechanics*, 44(4):609–626.
- Rao, S. P. (2005). *Characterizing effective built-in curling and its effect on concrete pavement cracking*. PhD thesis, University of Illinois at Urbana-Champaign.
- Rashid, Y. (1968). Ultimate strength analysis of prestressed concrete pressure vessels. *Nuclear engineering and design*, 7(4):334–344.
- Reinhardt, H. W., Cornelissen, H. A., and Hordijk, D. A. (1986). Tensile tests and failure analysis of concrete. *Journal of Structural Engineering*, 112(11):2462–2477.
- Reissner, E. (1958). A note on deflections of plates on a viscoelastic foundation. *Journal of Applied Mechanics*, 25(1):144–145.
- Reissner, E. (1967). Note on the formulation of the problem of the plate on an elastic foundation. *Acta Mechanica*, 4(1):88–91.
- Rhines, W. J. (1969). Elastic-plastic foundation model for punch-shear failure. *Journal of Soil Mechanics & Foundations Div.*
- Rodway, B. and Wardle, L. J. (1998). Layered elastic design of heavy duty and industrial pavements. In *AAPA Pavements Industry Conference, Australia*.

- Roe, K. and Siegmund, T. (2003). An irreversible cohesive zone model for interface fatigue crack growth simulation. *Engineering Fracture Mechanics*, 70(2):209–232.
- Roelfstra, P. and Wittmann, F. H. (1986). Numerical method to link strain softening with failure of concrete. In *Fracture toughness and fracture energy of concrete*, pages 163–175.
- Roesler, J. and Barenberg, E. (1999). Fatigue and static testing of concrete slabs. *Transportation Research Record: Journal of the Transportation Research Board*, (1684):71–80.
- Roesler, J., Littleton, P., Hiller, J., and Long, G. (2004a). Effect of stress state on concrete slab fatigue resistance. *Draft Final Report for Federal Aviation Administration, University of Illinois, Urbana, Illinois*, page 227.
- Roesler, J., Paulino, G. H., Park, K., and Gaedicke, C. (2007). Concrete fracture prediction using bilinear softening. *Cement and Concrete Composites*, 29(4):300–312.
- Roesler, J. R. (1998). *Fatigue of concrete beams and slabs*. PhD thesis, University of Illinois, Urbana, Illinois.
- Roesler, J. R., Cervantes, V. G., and Amirkhanian, A. N. (2012). Accelerated performance testing of concrete pavement with short slabs. *International Journal of Pavement Engineering*, 13(6):494–507.
- Roesler, J. R., Harvey, J. T., Farver, J., et al. (2000). Investigation of design and construction issues for long life concrete pavement strategies. *Final Report, FHWA/CA/OR-2000/04, University of California-Berkeley, Pavement Research Center, Richmond, California*.
- Roesler, J. R., Hiller, J. E., and Littleton, P. C. (2005). Large-scale airfield concrete slab fatigue tests. *Proceedings - 8th International Conference on Concrete Pavements: Innovations for Concrete Pavement: Technology Transfer for the Next Generation*, 3:1247–1268.
- Roesler, J. R., Lange, D. A., Altoubat, S. A., Rieder, K.-A., and Ulreich, G. R. (2004b). Fracture of plain and fiber-reinforced concrete slabs under monotonic loading. *Journal of materials in civil engineering*, 16(5):452–460.
- Roth, S., Hütter, G., and Kuna, M. (2014). Simulation of fatigue crack growth with a cyclic cohesive zone model. *International Journal of Fracture*, 188(1):23–45.

- Rots, J. G. (1988). *Computational modeling of concrete fracture*. PhD thesis, Technische Hogeschool Delft.
- Selvadurai, A. P. (1979). *Elastic analysis of soil-foundation interaction*. Elsevier.
- Shah, S. P. and McGarry, F. J. (1971). Griffith fracture criterion and concrete. *Journal of the Engineering Mechanics Division*, 97(6):1663–1676.
- Shah, S. P., Swartz, S. E., and Ouyang, C. (1995). *Fracture mechanics of concrete: applications of fracture mechanics to concrete, rock and other quasi-brittle materials*. John Wiley & Sons.
- Shahid, M. A. (1997). *Improved cement bound base design for flexible composite pavements*. PhD thesis, University of Nottingham, United Kingdom.
- Shahid, M. A. and Thom, N. H. (1996). Performance of cement bound bases with controlled cracking. In *RILEM Proceedings*, pages 55–64. Chapman & Hall.
- Silfwerbrand, J. (2001). Improvements of the Swedish concrete associations method for design of sfrc slabs on grade. *THE DESIGN OF STEEL FIBRE REINFORCED CONCRETE STRUCTURES*, page 23.
- Silfwerbrand, J. (2005). Design of industrial concrete block pavements. *CBI Rapport*, (1):1–55.
- Silfwerbrand, J., Rossi, P., and Chanvillard, G. (2000). Design of steel fibre reinforced concrete slabs on grade. In *Fifth International RILEM Symposium on Fibre-Reinforced Concrete (FRC)*, pages 305–314. RILEM Publications SARL.
- Slowik, V., Plizzari, G. A., and Saouma, V. E. (1996). Fracture of concrete under variable amplitude fatigue loading. *ACI Materials Journal*, 93:272–283.
- Sorelli, L. G., Meda, A., and Plizzari, G. A. (2006). Steel fiber concrete slabs on ground: a structural matter. *ACI Structural Journal*, 103(4):551.
- Tabatabaie, A. M. and Barenberg, E. J. (1980). Structural analysis of concrete pavement systems. *Transportation Engineering Journal*, 106(5):493–506.
- Terzaghi, K. (1943). Bearing capacity. *Theoretical soil mechanics*, pages 118–143.

- Thøgersen, F., Busch, C., and Henrichsen, A. (2004). Mechanistic design of semi-rigid pavements. *Danish Road Institute. Report*, 138.
- Thompson, M. R. and Barenberg, E. J. (1992). Nchrp report 1-26: Calibrated mechanistic structural analysis procedure for pavements-phase 2. *TRB, National Research Council, Washington, DC*.
- Timoshenko, S., Goodier, J., and Abramson, H. N. (1970). Theory of elasticity. *Journal of Applied Mechanics*, 37:888.
- Ting, E. C. (1973). Unified formulation of two-parameter foundation model. *ZAMM-Journal of Applied Mathematics and Mechanics/Zeitschrift für Angewandte Mathematik und Mechanik*, 53(9):636–637.
- Totsky, O. (1981). Behavior of multi-layered plates on winkler foundation. *Stroitel'naya Mekhanika i Raschet Sooruzhenii*, 6:54–58.
- Toumi, A. and Bascoul, A. (2002). Mode i crack propagation in concrete under fatigue: microscopic observations and modelling. *International journal for numerical and analytical methods in geomechanics*, 26(13):1299–1312.
- Toumi, A., Bascoul, A., and Turatsinze, A. (1998). Crack propagation in concrete subjected to flexuralcyclic loading. *Materials and Structures*, 31(7):451–458.
- Turhan, A. (1992). A consistent vlasov model for analysis of plates on elastic foundations using the finite element method.
- Tvergaard, V. and Hutchinson, J. W. (1992). The relation between crack growth resistance and fracture process parameters in elastic-plastic solids. *Journal of the Mechanics and Physics of Solids*, 40(6):1377–1397.
- Ulfkjær, J. P., Krenk, S., and Brincker, R. (1995). Analytical model for fictitious crack propagation in concrete beams. *Journal of Engineering Mechanics*, 121(1):7–15.
- Vallabhan, C. V. G. and Das, Y. C. (1988). Parametric study of beams on elastic foundations. *Journal of engineering mechanics*, 114(12):2072–2082.
- Vallabhan, C. V. G. and Das, Y. C. (1991). Modified vlasov model for beams on elastic foundations. *Journal of geotechnical engineering*, 117(6):956–966.
- Vesić, A. S. and Saxena, S. K. (1969). Analysis of structural behavior of road test rigid pavements. *Highway Research Record*, (291).

- Vlasov, V. Z. (1966). Beams, plates and shells on elastic foundations. *Israel Program for Scientific Translations, Jerusalem*.
- Vlasov, V. Z. and Leontev, N. (1960). Beams, plates, and shells on an elastic base. *Fizmatgiz, Moscow*.
- Walker, R., Paterson, W., Freeme, C., and Marais, C. (1977). The south african mechanistic pavement design procedure. In *Proceedings of the fourth International Conference on the Structural Design of Asphalt Pavements, University of Michigan, Ann Arbor, Michigan, USA*.
- Walter, R., Østergaard, L., Olesen, J. F., and Stang, H. (2005). Wedge splitting test for a steel-concrete interface. *Engineering Fracture Mechanics*, 72(17):2565–2583.
- Wardle, L., Rickards, I., and Lancaster, J. (2006). Hipave œ a tool to assist in the mechanistic empirical design of heavy duty industrial flexible pavements.
- Westergaard, H. (1926). Stresses in concrete pavements computed by theoretical analysis. *Public roads*.
- Westergaard, H. M. (1948). New formulas for stress in concrete pavements of airfields. *American Society of Civil Engineers Transactions*.
- Winkler, E. (1868). *Die lehre von der elasticitaet und festigkeit*. Verlag Dominicus, Prag.
- Xu, Y. and Yuan, H. (2009). On damage accumulations in the cyclic cohesive zone model for xfem analysis of mixed-mode fatigue crack growth. *COMPUTATIONAL MATERIALS SCIENCE*, 46(3):579–585.
- Yang, B., Mall, S., and Ravi-Chandar, K. (2001). A cohesive zone model for fatigue crack growth in quasibrittle materials. *International Journal of Solids and Structures*, 38(22):3927–3944.
- Yankelevsky, D. Z. and Reinhardt, H. W. (1987). Response of plain concrete to cyclic tension. *Materials Journal*, 84(5):365–373.
- Yeo, R. (2008a). *The development and evaluation of protocols for the laboratory characterisation of cemented materials*. Number AP-T101/08.
- Yeo, R. (2008b). *Fatigue performance of cemented materials under accelerated loading: influence of vertical loading on the performance of unbound and cemented materials*. Number AP-T102/08.

- Yeo, Y. S., Jitsangiam, P., and Nikraz, H. (2012). Mechanistic classification of cement treated base in western australia. *Journal of Civil Engineering and Architecture*, 6(8):1076.
- Zaman, M., Khoury, N., and Solanki, P. (2009). Finite-element modeling of cementitiously stabilized beams using a smeared fracture approach. *International Journal of Geomechanics*, 9(1):34–42.
- Zhang, J., Li, V. C., and Stang, H. (2001). Size effect on fatigue in bending of concrete. *Journal of materials in civil engineering*, 13(6):446–453.
- Zhang, J., Stang, H., and Li, V. C. (1999). Fatigue life prediction of fiber reinforced concrete under flexural load. *International Journal of Fatigue*, 21(10):1033–1049.
- Zhang, J., Stang, H., and Li, V. C. (2000). Experimental study on crack bridging in frc under uniaxial fatigue tension. *Journal of Materials in Civil Engineering*, 12(1):66–73.
- Zhaohua, F. and Cook, R. D. (1983). Beam elements on two-parameter elastic foundations. *Journal of Engineering Mechanics*, 109(6):1390–1402.
- Zokaei-Ashtiani, A., Carrasco, C., and Nazarian, S. (2014). Finite element modeling of slab–foundation interaction on rigid pavement applications. *Computers and Geotechnics*, 62:118–127.
- Zokaei-Ashtiani, A., Tirado, C., Carrasco, C., and Nazarian, S. (2015). Impact of different approaches to modelling rigid pavement base layers on slab curling stresses. *International Journal of Pavement Engineering*, pages 1–9.

*BIBLIOGRAPHY*

*BIBLIOGRAPHY*

**Part II**  
**Appended Papers**



# Paper I

*"3-D cohesive finite element model for application in structural analysis of heavy duty composite pavements"*

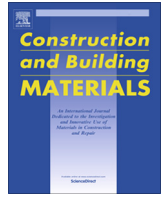
A. Skar & P.N. Poulsen

Published in: *Construction & Building Materials, 2015*



Contents lists available at [ScienceDirect](http://www.sciencedirect.com)

# Construction and Building Materials

journal homepage: [www.elsevier.com/locate/conbuildmat](http://www.elsevier.com/locate/conbuildmat)

## 3-D cohesive finite element model for application in structural analysis of heavy duty composite pavements

Asmus Skar <sup>a,\*</sup>, Peter Noe Poulsen <sup>b</sup><sup>a</sup> COWI A/S, Parallelvej 2, 2800 Kgs. Lyngby, Denmark<sup>b</sup> Technical University of Denmark, Brovej, Building 118, 2800 Kgs. Lyngby, Denmark

### HIGHLIGHTS

- Cohesive models adequately describe the fracture behaviour of cement bound granular mixtures.
- Structural- and local crack response of slabs are highly influenced by the subgrade soil.
- The post-peak response is mainly controlled by slab dimensions and subgrade soil.
- The fracture process is more affected by the fracture energy than the tensile strength.
- Aggregate interlock behaviour has significant influence on the structural response.

### ARTICLE INFO

#### Article history:

Received 4 August 2015

Received in revised form 12 October 2015

Accepted 15 October 2015

#### Keywords:

Cement bound material fracture

Cohesive model

Composite pavements

Pavement analysis

Finite element modelling

Slabs on grade

Aggregate interlock behaviour

Slab soil interaction

### ABSTRACT

The problem of stiffness degradation in composite pavement systems from localised fracture damage in the quasibrittle cement bound granular mixture are today taken into account only by empirical formulas. These formulas deals with a limited number of materials in a restricted range of design options and would yield unrealistic results in ultimate loading conditions. Cohesive modelling is one of the primary methods to handle localised damage in quasi-brittle materials, e.g., concrete, describing the potential crack in a discrete manner. To increase the versatility of existing methods this paper presents a numerical analysis of the fracture behaviour of cement bound granular mixtures in composite concrete block pavement systems applying a cohesive model. The functionality of the proposed model is compared to experimental investigations of beam bending tests. The pavement is modelled as a slab on grade and parameters influencing the response such as geometry, material parameters and loading position are studied and compared to experimental results. It is found that a cohesive model is suitable for the description of the fracture behaviour of cement bound granular mixtures. Moreover, it can be shown that adequately good prediction of the structural response of composite pavements is obtained for monotonic loading without significant computational cost, making the model applicable for engineering design purpose. It is envisaged that the methodology implemented in this study can be extended and thereby contribute to the ongoing development of rational failure criteria that can replace the empirical formulas currently used in pavement engineering.

© 2015 Elsevier Ltd. All rights reserved.

### 1. Introduction

Ports- and industries require special types of pavements to resist the heavy static loads from containers. To reduce the risk of rutting and settlements over time, concrete block pavement systems are typically applied over a stiff cemented base layer, i.e., cement bound granular mixture (CBGM). The structural design of such composite pavements are based on empirical formulas

which converts the response analysis into a measure of performance, commonly referred to as the Mechanistic–Empirical (M–E) method, first introduced in pavement engineering by Kerkhoven and Dormon [1].

Degradation of the cemented base in composite pavements is mainly controlled by initiation and propagation of longitudinal cracks in wheel paths. Moreover, traffic induces further degradation of aggregate interlock joints through shear movement of the cracked edges [2]. Closely spaced transverse cracks in the cemented base have also been reported in post-processing of damaged composite pavements [3,4]. Despite the fact that cement bound

\* Corresponding author.

E-mail address: [asch@cowi.dk](mailto:asch@cowi.dk) (A. Skar).

granular mixtures are quasi-brittle materials, which degradation is controlled by tensile damage of slabs and shear damage of aggregate interlock joints, both highly nonlinear phenomena, elastic calculations are most commonly applied to determine the response [5–11]. The M–E method does not distinguish between crack initiation and crack propagation or elastic and inelastic work, model parameters are simply regression constants without direct physical meaning. This type of model deals with a limited number of materials in a restricted range of design options; each transfer function being restricted by its own design method, typically calibrated for highway traffic and specific local materials- and climatic conditions. Moreover, experimental studies [12] show that such empirically based model yields unrealistic results considering loading regime- or configuration different from typical truck wheel loads, e.g., ultimate loading condition.

In the present study a simple framework for engineering application is sought; creating a rational link between laboratory, design and field applications. For the monotonic load case, considered here, the mechanism of cracks is imagined to occur in a similar fashion to yield line mechanisms considering *Mode I* (opening mode) fracture in the form of a straight separation band where the location is known in advance. In this aspect, the concept of the fictitious crack model [13] stand out as particular attractive; as the model is straightforward in implementation and requires only few model parameters, which can be defined from standardised laboratory tests.

Production of cement bound mixtures from high quality crushed aggregates results in high stiffness and strength properties, i.e., 1/3 of those for normal plain concrete. Not only will such materials exhibit softening behaviour in tension, after the onset of cracking, but also on structural level the composite pavements will often exhibit softening, or so-called snap-back type of load–displacement response, due to the relatively low stiffness of supporting layers. This type of localised fracture behaviour can be described numerically with different classes of constitutive models, e.g., those proposed by Jirasek [14] as; (i) strong discontinuity models, (ii) weak discontinuity models, and (iii) continuum models. The first model a crack as a geometrical discontinuity, whereas the latter two approaches imagine a cracked solid to be a continuum.

The discontinuity models, e.g., the fictitious crack model, embedded elements with strong discontinuities [15] and the extended finite elements [16], incorporates jumps in displacements across a discontinuity surface corresponding to the crack. Models with localisation bands bounded by weak discontinuities can be considered as simple regularizations of models with strong discontinuities, e.g. the smeared crack model [17]. Instead of splitting the constitutive law into elastic and inelastic parts, one could use a law that directly links the stress to the total strain, as is the case for continuum models. Subsequently several models have been developed to describe the complicated fracture process in quasi-brittle materials, e.g., by coupling damage and plasticity [18–20].

Application of modern fracture mechanics to the field of pavement engineering began in the late 1960s and early 1970s, studying mainly asphalt concrete mixtures, adopting the principles of linear elastic fracture mechanics [21–25]. Subsequently, efforts to obtain a better understanding of fracture in asphalt concrete materials primarily followed an experimental approach [26–29]. Jenq and Perng [30] developed a cohesive zone model based on the principles of the fictitious crack model for asphalt mixtures and used this model to simulate low-temperature fracture of asphalt overlay on old concrete pavement structures [31] followed by extensive application- and development of cohesive zone models for simulating fracture in asphalt concrete mixtures [32–39].

Cohesive zone models and the principles of the fictitious crack model has also been extended to more practical problems for concrete pavement structures, following an extensive review of

fracture mechanics applications in pavement engineering [40]. At first, a standalone computer program was coded and applied to simply supported beams [41]. Subsequently, nonlinear spring elements were adopted in commercial software for concrete beams and slabs on grade subjected to mechanical loads [42]. Roesler et al. [43] created user elements based on the fictitious crack model, and implemented them locally in commercial software to simulate crack propagation in concrete beam specimens and in fibre reinforced concrete materials [44,45]. Although these elements were two-dimensional, responses obtained were compared with experimental measurements and adequately good agreement was reported. Subsequently several independent investigations of crack propagation in beams and slabs on grade subjected to mechanical loads was carried out, with some very encouraging results [46–49]. Gaedicke and Roesler [46] found that the linear softening model applied to slabs was able to reasonably predict the flexural load capacity of the experimental slabs while significantly reducing the computation time. Aure and Ioannides [48] found, that for slabs on grade structures, the type of softening curve, cohesive zone width and mesh does not influence the response significantly.

This paper presents a numerical study of a three-layered composite pavement applying a simplified cohesive model in ABAQUS [50], including also the effects from aggregate interlock behaviour. Idealisation is applied, modelling the pavement as a slab on grade structure, neglecting the effect from the concrete block surface, resulting in computationally fast finite element (FE) models suitable for engineering applications. Numerical analysis of experimental results are presented, giving new valuable information on the behaviour of composite pavements which cannot be captured by the M–E method. Parameters influencing the response such as geometry, material parameters and loading position is then studied creating a solid basis for further application of cohesive models in analysis composite pavement systems.

## 2. Methodology

### 2.1. Model idealisations

Analysis of a three-layered composite pavement structure is considered; concrete block pavers (CBP), cement bound granular mixture (CBGM) and subgrade soil. For the fracture process, built-in traction separation based cohesive contact surfaces are inserted along the anticipated fracture plane in the cemented base layer (slab) in the orthogonal directions as per Meda et al. [51]. This is deemed a reasonable model at the edge- and interior of the cemented base layer, since the fracture plane is anticipated in the direction of the maximum stress.

The response of the composite concrete block pavement structure is mainly controlled by the cemented base layer and the subgrade soil. The properties and thickness of the concrete block pavers does hardly influence the overall response and bearing capacity of the pavement structure [52], since the loading from container castings produce a close to rigid body movement of the stiff concrete block pavers over the soft layer of bedding sand, which is unable to absorb any significant bending moments [53].

Thus, for the present study the response from concrete block pavers is simulated using a simplified approach, placing unit displacements over an approximated area, i.e., the area of blocks in contact with the container casting. Four single slabs on grade models is developed for evaluation of interior (full- and simplified model, applying symmetry conditions), edge and corner loading, assuming that the slabs are intact before monotonically loaded. Square slabs of  $2.5 \times 2.5 \text{ m}^2$  to  $4.5 \times 4.5 \text{ m}^2$ , dimensions commonly applied in ports- and industrial pavements, is considered.

**Table 1**  
Geometry, material mixture- and mechanical properties for beams- and slabs used in numerical studies.

	Chapter	Experiments		Sensitivity studies	
		3		4	5
Geometry	Unit	Beam		Sabs on grade	
Length	(m)	0.40	5.00	2.50–4.50	3.00
Width	(m)	0.10	1.25	2.50–4.50	3.00
Thickness	(m)	0.10	0.18	0.15–0.40	0.30
<i>Material properties</i>					
Material type		Siltstone	Gravel	–	–
Maximum stone size, $D_{max}$	(mm)	20	32	–	–
Cement type		GP	CEM I 42,5 R	–	–
Cement content	(%)	4.0	4.4	–	–
Maximum dry density, $MDD$	(kg/m <sup>3</sup> )	2070	2184	–	–
Optimum moisture content, $OMC$	(%)	8.0	5.8	–	–
Curing age	(days)	56	28	–	–
<i>Mechanical- and fracture properties</i>					
Young's modulus, $E$	(MPa)	12,760	12,300	15,000	15,000
Poisson's ratio, $\nu$	(–)	0.20	0.20	0.20	0.20
Tensile strength, $f_t$	(MPa)	1.00	0.96	0.60–1.20	0.80
Compression strength, $f_c$	(MPa)	7.30	6.70	8.00	8.00
Fracture energy, $G_f$	(N/mm)	0.028	0.037	0.018–0.045	0.025

In this study, commercial general purpose FE program ABAQUS/Standard®, version 6.13-1 is employed in the analysis of beams- and slab on grade structures, whose geometry and material properties are shown in Table 1 and Table 2. Foundation material properties are given in Table 3.

**Table 2**  
Aggregate interlock behaviour used in numerical studies.

	Chapter	Experiments		Sensitivity studies	
		3		4	5
Aggregate interlock	Unit	Beam		Sabs on grade	
Initial crack width, $w$	(mm)	–	2.00	–	0.40–2.00
Load Transfer Efficiency, $LTE_\delta$	(%)	–	50	–	50–90
Normal stiffness, $K_{nn}$	(MPa/mm)	–	0.45	–	0.45
Initial tangential stiffness, $K_{tt}$	(MPa/mm)	–	0.65	–	0.65–3.00
Critical shear displacement (slip)	(mm)	–	2.00	–	0.58–2.00

**Table 3**  
Foundation material properties used in numerical studies.

	Chapter	Experiments			Sensitivity studies	
		3			4	5
Material properties	Unit	Beam		Sabs on grade		
Material type		–	Clayey gravel	–	–	
Maximum stone size, $D_{max}$	(mm)	–	80	–	–	
Maximum Dry Density, $MDD$	(kg/m <sup>3</sup> )	–	2034	–	–	
Optimum Moisture Content, $OMC$	(%)	–	7.4	–	–	
Degree of compaction	(%)	–	95–97	–	–	
<i>Mechanical properties</i>						
Young's modulus, $E$	(MPa)	–	'Winkler'	'Elastic'	'Plastic'	–
Modulus of subgrade reaction, $k_0$	(MPa/mm)	–	0.045	350 <sup>a</sup>	350a	–
Poisson's ratio, $\nu$	(–)	–	–	0.35	0.35	–
Cohesion yield stress, $c_y$	(MPa)	–	–	–	0.005	–
Angle of internal friction, $\phi$	(°)	–	–	–	25–35 <sup>b</sup>	–
Layer friction coefficient, $\mu$	(–)	–	–	0–1.0	0–1.0	–

<sup>a</sup> Back-calculated Young's modulus of 313–368 MPa found from plate load test (PLT) measurements [12].

<sup>b</sup> Expected interval of angle of internal friction for 'soil fill' to 'good selected subgrade' [65].

## 2.2. Constitutive laws and materials

### 2.2.1. Cohesive crack and cemented material behaviour

In the present study cement bound granular mixtures with relatively high strength, i.e., a  $C_{8/10}$ -material [54], commonly applied in port- and industry composite pavements, is considered. Such materials have similar characteristics as normal plain concrete, however, whereas concrete are dense mixtures, where aggregates are completely bonded by the cement paste, as shown in Fig. 1 (a). Cement bound granular mixtures are less dense and aggregates are bonded by weaker cement links, as shown in Fig. 1(b), resulting in somewhat lower strength and more brittle behaviour.

Overview of geometry and cement bound granular material mixture properties for beams- and slabs used in the numerical studies are shown in Table 1. Grading curves for materials investigated in numerical analysis of experimental results in Sections 3.1 and 3.2 are shown in Fig. 2.

Liu and Wang [55] applied a cohesive zone model to investigate Mode I crack propagation of cement stabilized crushed stone in the indirect tension test (IDT) following a micro-mechanical approach using embedded elements. Heymsfield et al. [56] developed a damage model for stabilized soil layers subjected to cyclic aircraft

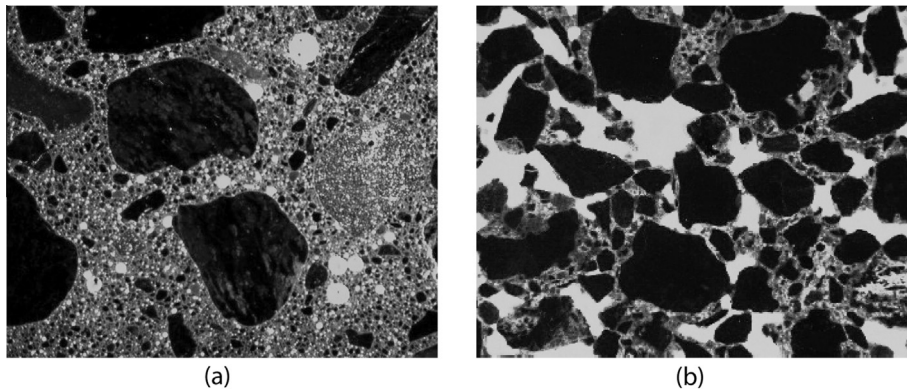


Fig. 1. Thin section of normal concrete (a) and cement bound granular mixture (b), showing how aggregates in the cement bound granular mixture is connected by cement links surrounded by more porous areas with loosely packed sand held by relatively little paste.

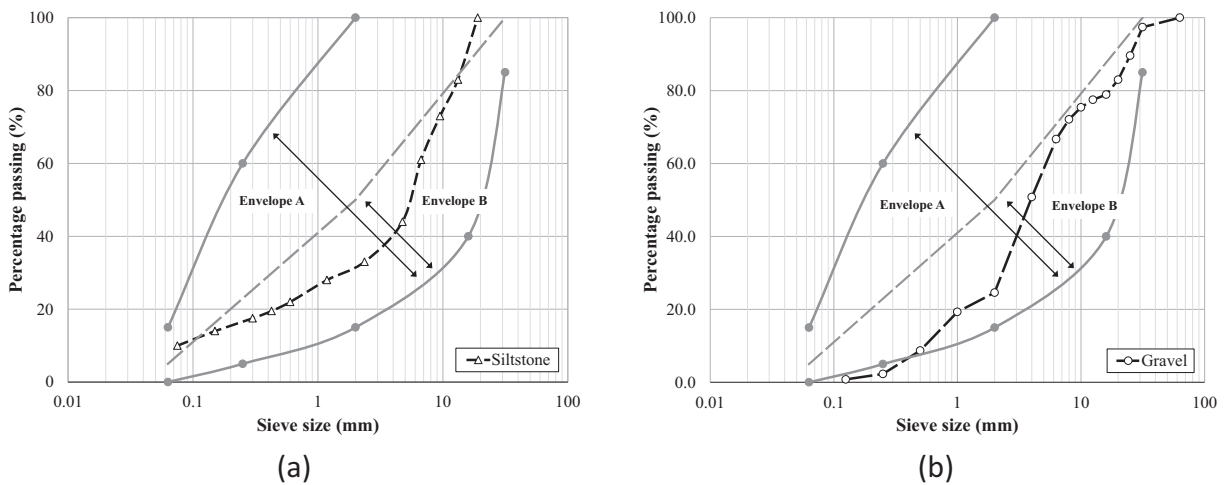


Fig. 2. Grading curves for high quality (envelope 'B') CBGM materials according to [54] (grey) compared to CBGM materials used in experiments of (a) 4-point bending beam- and (b) slabs on grade tests in Section 3.1 and 3.2, respectively.

loading. Zhong et al. [57] developed a unified permanent deformation model to simulate the permanent deformation behaviour of cement bound granular materials in flexible pavements. However, the literature contains little information on the fracture behaviour of cemented base materials with high strength properties for application in realistic composite pavement systems.

In lack of experimental data and based on the findings of other independent researchers, e.g., Gaedicke and Roesler [46] and Aure and Ioannides [48], the fictitious crack model with a simple linear traction–separation law (softening curve), as shown in Fig. 3(c), is chosen for the present study. Moreover, the fracture energy applied in the present study is predicted based on the approach suggested by Hilsdorf and Brameshuber [58], assuming that code

standards for normal concrete also apply to cement bound granular mixtures.

The cohesive contact model in ABAQUS is selected to save computational time; enabling the use of symmetry conditions and application of a coarser mesh for the cohesive zone. Moreover, as shown in Fig. 4, the cohesive contact model in ABAQUS is found to adequately describe the load–displacement response of slabs on grade reported by other independent researchers.

2.2.2. Aggregate interlock behaviour

The mechanics of aggregate interlock between slabs, shown in Fig. 5, is a complex phenomenon that depends on several parameters, including aggregate size and distribution, compressive

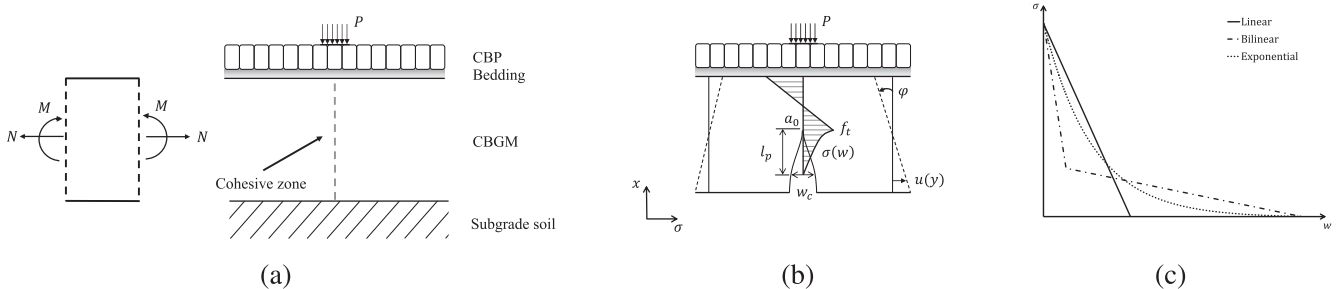


Fig. 3. Sketch of pavement structure (a) the fictitious crack model (b), where  $a_0$  is the crack tip,  $l_p$  is the fracture process zone (FPZ),  $f_t$  is the tensile strength,  $w_c$ , is the stress-free crack opening and  $\sigma(w)$  the cohesive softening law and typical softening curves for concrete (c).

strength, friction between the aggregate particle and the cement paste, crack opening, and crack interface sliding.

According to Bazant and Gambarova [59], the normal and shear stresses at a cracked concrete interface, in a two-dimensional

plane, are functions of the normal and shear displacements of the interface, as follows:

$$t_n = f_n(\delta_n, \delta_t) \tag{1a}$$

$$t_t = f_t(\delta_n, \delta_t) \tag{1b}$$

where  $t_n$  is the normal stress,  $t_t$  is the tangential shear stress,  $\delta_n$  and  $\delta_t$  are the normal and shear displacements respectively, and  $f_n$  and  $f_t$  are functions to be described. Differentiation of Eq. 1a and 1b results in:

$$\begin{Bmatrix} dt_n \\ dt_t \end{Bmatrix} = \begin{bmatrix} \frac{\partial f_n}{\partial \delta_n} & \frac{\partial f_n}{\partial \delta_t} \\ \frac{\partial f_t}{\partial \delta_n} & \frac{\partial f_t}{\partial \delta_t} \end{bmatrix} = \begin{Bmatrix} d\delta_n \\ d\delta_t \end{Bmatrix} = \begin{bmatrix} K_{nn} & K_{nt} \\ K_{tn} & K_{tt} \end{bmatrix} \begin{Bmatrix} d\delta_n \\ d\delta_t \end{Bmatrix} \tag{2}$$

where  $K_{nn} = \partial f_n / \partial \delta_n$ ,  $K_{nt} = \partial f_n / \partial \delta_t$ ,  $K_{tn} = \partial f_t / \partial \delta_n$ ,  $K_{tt} = \partial f_t / \partial \delta_t$ , are crack stiffness coefficients that can be determined once the functions  $f_n$  and  $f_t$  are established. If the variation of functions  $f_n$  and  $f_t$  is nonlinear with respect to  $\delta_n$  and  $\delta_t$ , the crack stiffness coefficients may be sensitive to stress level of the cracked interface, and

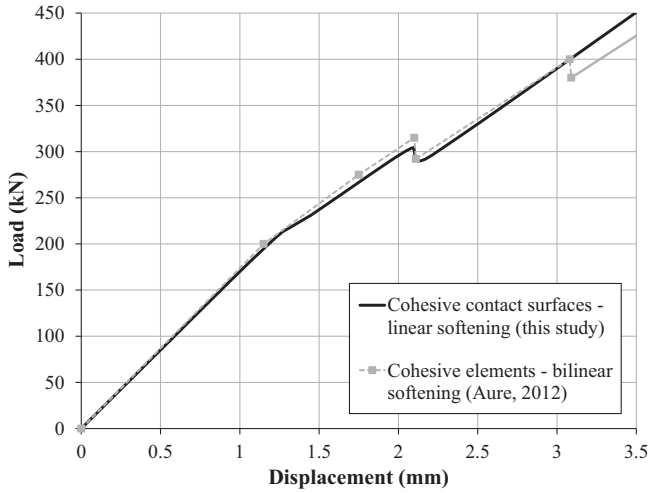


**Fig. 4.** Comparison of load–displacement curves for interior loading of a rectangular concrete slab on grade ( $3 \times 6 \times 0.15 \text{ m}^3$ ), applying different modelling techniques in ABAQUS: cohesive contact surfaces applying a linear softening law and cohesive zone element size ( $h/l$ ) of  $8 \times 15 \text{ mm}^2$  to  $8 \times 65 \text{ mm}^2$  (this study) versus cohesive elements using bilinear softening law and a relatively fine mesh of  $3.5 \times 3.5 \text{ mm}^2$  for the cohesive zone (Aure [48]).

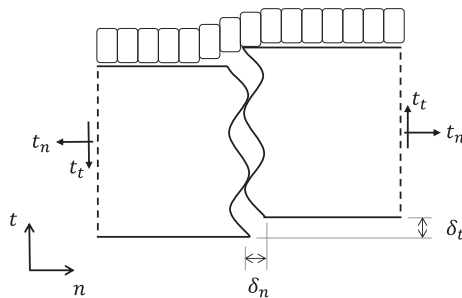


**Fig. 5.** Sketch of the rough crack model [59] within the composite pavement system.

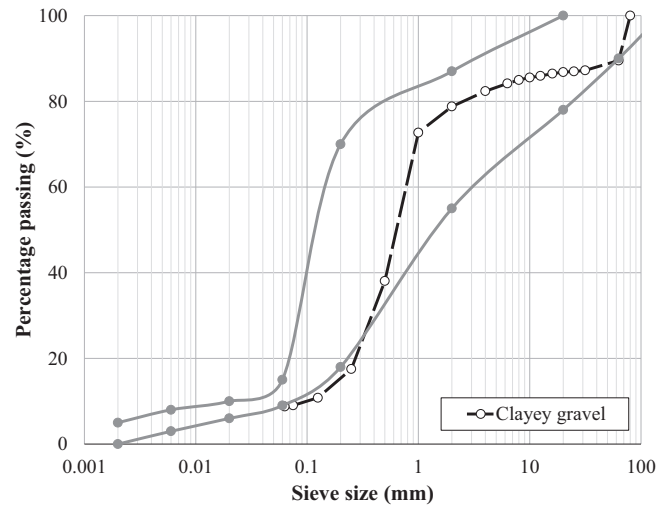
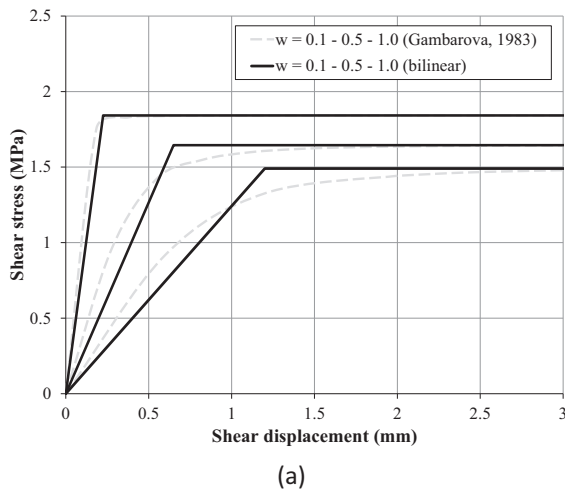


**Fig. 7.** Grading curve for clayey gravel material ('SP-SC') according to [66] (grey) compared to clayey gravel material used in experiments of slabs on grade tests in Section 3.2.

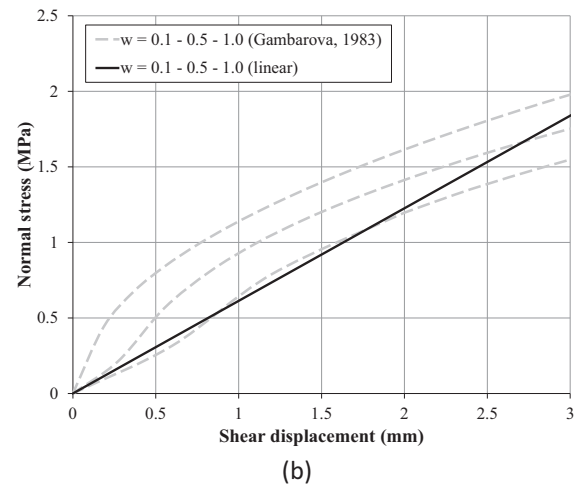


**Fig. 6.** Linear idealisation of the modified rough crack model (Gambarova [60]) shown for a  $C_{8/10}$ -material, maximum aggregate size,  $D_{max}$ , of 32 mm and initial crack width,  $w$ , of 0.1, 0.5 and 1.0 mm.

therefore, will change as the load is applied. This behaviour is identified as nonlinear aggregate interlock mechanism. Several constitutive models for nonlinear aggregate interlock behaviour (crack dilatancy) have been proposed in the literature, e.g., the rough crack model [59,60], the aggregate interlock relation [61], the two-phase model [62] and the contact density model [63].

In lack of adequate experimental data the modified rough crack model [60], incorporating both influence of aggregate size and

compression strength, is used as basis to determine the stiffness coefficients of springs as seen in Fig. 6. Linear normal stiffness with no dependence on initial crack width is assumed. Material parameters for aggregate interlock behaviour used in numerical studies are shown in Table 2.

### 2.2.3. Subgrade material behaviour

In the present study the subgrade has been idealised as linear elastic using independent springs or a so-called Winkler's foundation model [64]. However, to exemplify the deficiencies of this model and to evaluate full bearing capacity of the structure, elastic solid continuum elements, including a Mohr–Coulomb yield criterion [50], is applied in the numerical analysis of experiments in Section 3.2. Overview of subgrade material properties used in the numerical studies are shown in Table 3. Grading curve for the subgrade material investigated in numerical analysis of experimental results in Section 3.2 is shown in Fig. 7.

### 2.3. Solution technique

In materials that exhibit snap-back type of load–displacement curves, *arc-length* based solvers are often recommended. Accordingly ABAQUS implements the so-called modified Riks algorithm [67] used in the present study. Based on preliminary convergence and sensitivity studies solution technique and standard model parameters selected for the present study can be seen in Table 4.

## 3. Comparison with experimental results

### 3.1. Numerical analysis of four point bending tests with cement bound granular mixture

Numerical analysis of four-point bending (FPB) beam tests is carried out to verify the functionality of the cohesive contact model to simulate the fracture behaviour of cement bound granular mixture with crushed quartzite siltstone aggregates. Five CBGM-beams was cut from field slabs and tested under monotonic load, with a distance of 0.10 m between load points, in a comprehensive study of CBGM-materials conducted by Austroads [68]. Geometry and material properties is shown in Table 1.

The beam is modelled with 2-D plain stress elements (CPE4) in ABAQUS. A total of 840 elements are used to represent the elastic material, separated by pre-determined contact surfaces,

**Table 4**  
Solution technique and standard model parameters applied in the present study.

Solver		Model parameters	
Technique	<i>arc-length</i>	Cohesive zone width, $T_0$ (mm)	0.01
Initial increment	0.006	Viscous damping factor, $\mu$ (-)	$1 \times 10^{-5}$
Maximum increment size	0.03	Bulk elements (elastic)	CPE4 (2-D)/C3D8 (3-D)
Minimum increment size	$1 \times 10^{-9}$	Interface elements	SPRING1/elastic foundation

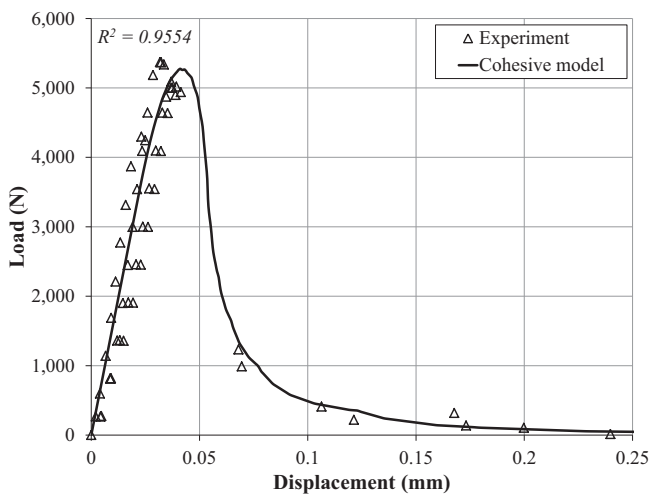


**Fig. 8.** Comparison between experiments, carried out by Austroads [68] and numerical results for CBGM beams.

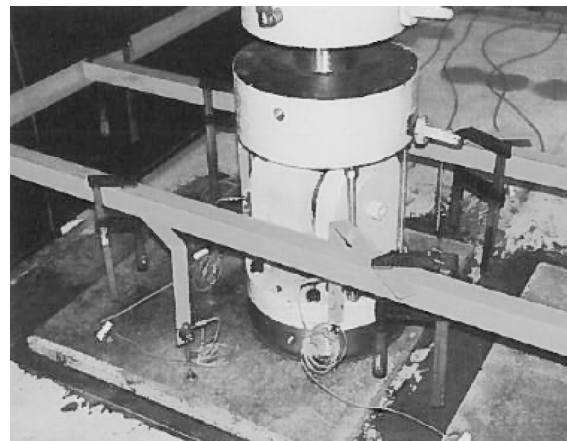
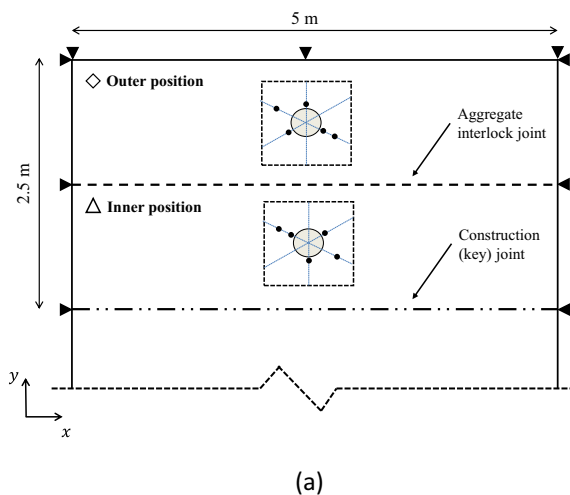


**Fig. 9.** Layout of slabs, showing outer- and inner loading position, supports ( $x$ -axis: concrete wall,  $y$ -axis: steel wall) and the placing of displacement sensors (a) and picture of test set-up (b), showing the load configuration and the displacement sensors placed on top of a 35 mm thin asphalt plate.

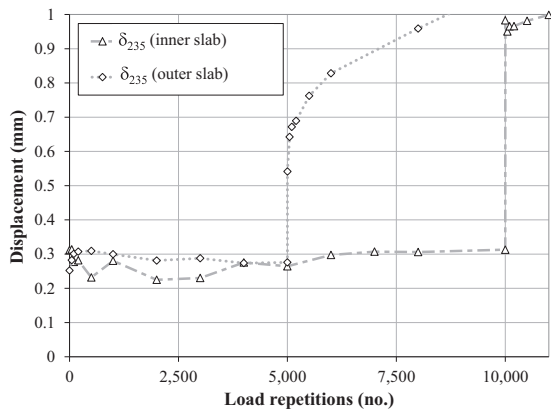
representing the cohesive zone (5 mm size elements), in the vertical plane at the mid-beam position.

From the comparison between experimental and numerical results, shown in Fig. 8, it can be observed that good agreement is obtained applying the cohesive model for simulation of the load–displacement response of the four-point bending beams. Relatively few data-points were obtained on the post-peak failure curve as no horizontal clip-gage control was applied during testing. The results show that a linear softening law is suitable to the description of fracture in cement bound granular mixtures. It is also found that the fracture energy of the cement bound granular

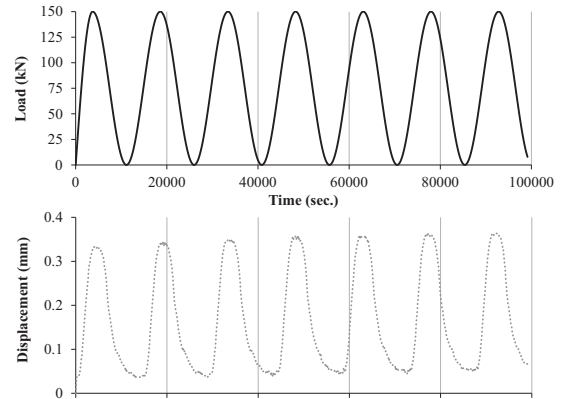
mixture can be predicted without further calibration, based on simple scaling with regard to compressive strength, e.g.,  $G_{F,CBGM} = f_{c,CBGM}/f_{c,PCC} \times G_{F,PCC}$ , or code standards for concrete materials.

### 3.2. Numerical analysis of large scale slab on grade structure

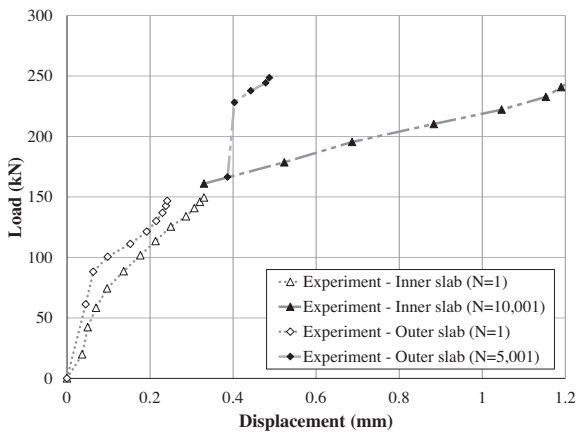
Numerical analysis of cement bound granular mixture slabs, shown in Fig. 9, separated by aggregate interlock-or construction joints, on subgrade soil of 1.0m clayey gravel material, is conducted in order to validate the methodology implemented,



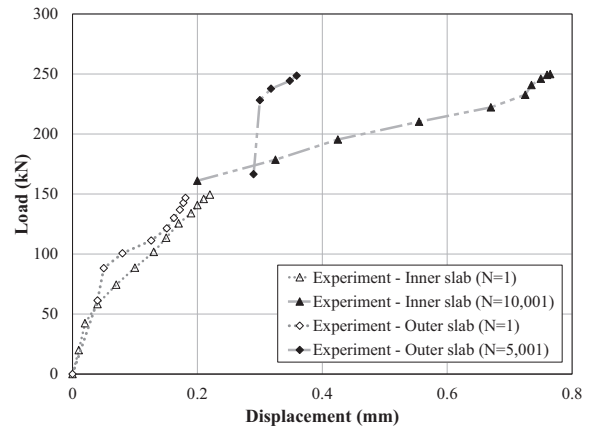
(a)



(b)

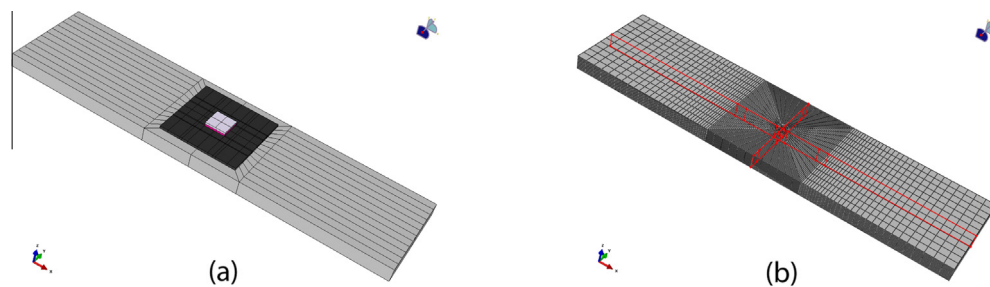


(c)



(d)

**Fig. 10.** Presentation of experimental data: average peak–loads and peak–load displacements measured during experiments at a distance of 235 mm from the load centre (a), example of typical sinusoidal load applied to the pavement (b); first seven load cycles for the inner slab position at a distance of 235 mm from the load centre and experimental load–displacement curves at a distance of 235 mm (c) and 450 mm (d) from load centre.



(a)

(b)

**Fig. 11.** Sketch of FE model (a), showing the load- and rubber plate, asphalt surface, and CBGM slab, and mesh and pre-determined cohesive zone in the slab orthogonal planes (b).

modelling the composite pavement as a slab on grade structure. The pavement was constructed on a concrete floor supported by a steel or concrete wall in the indoor test facility STEND in Poland.

The data was collected during the European Commission thematic network project ECO-serve [12,69,70] and was partly initiated in the attempt to evaluate the before mentioned M–E models.

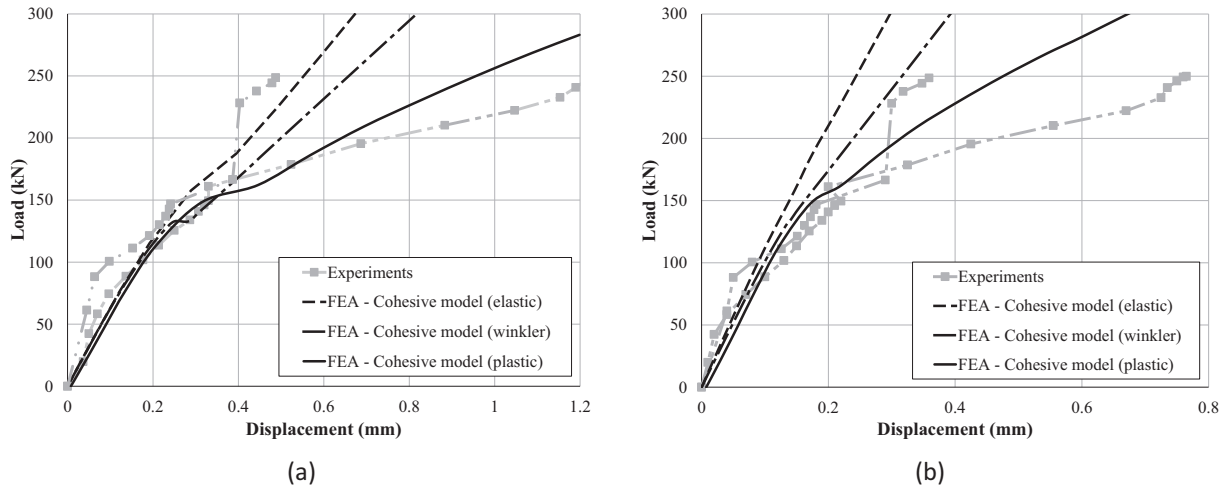


Fig. 12. Comparison between experiment and numerical analysis showing the load–displacement curves obtained at a distance of 235 mm (a) and 450 mm (b) from load centre for the three selected subgrade models ‘Winkler’, ‘Elastic’ and ‘Plastic’ using a angle of internal friction of 30° for the latter model.

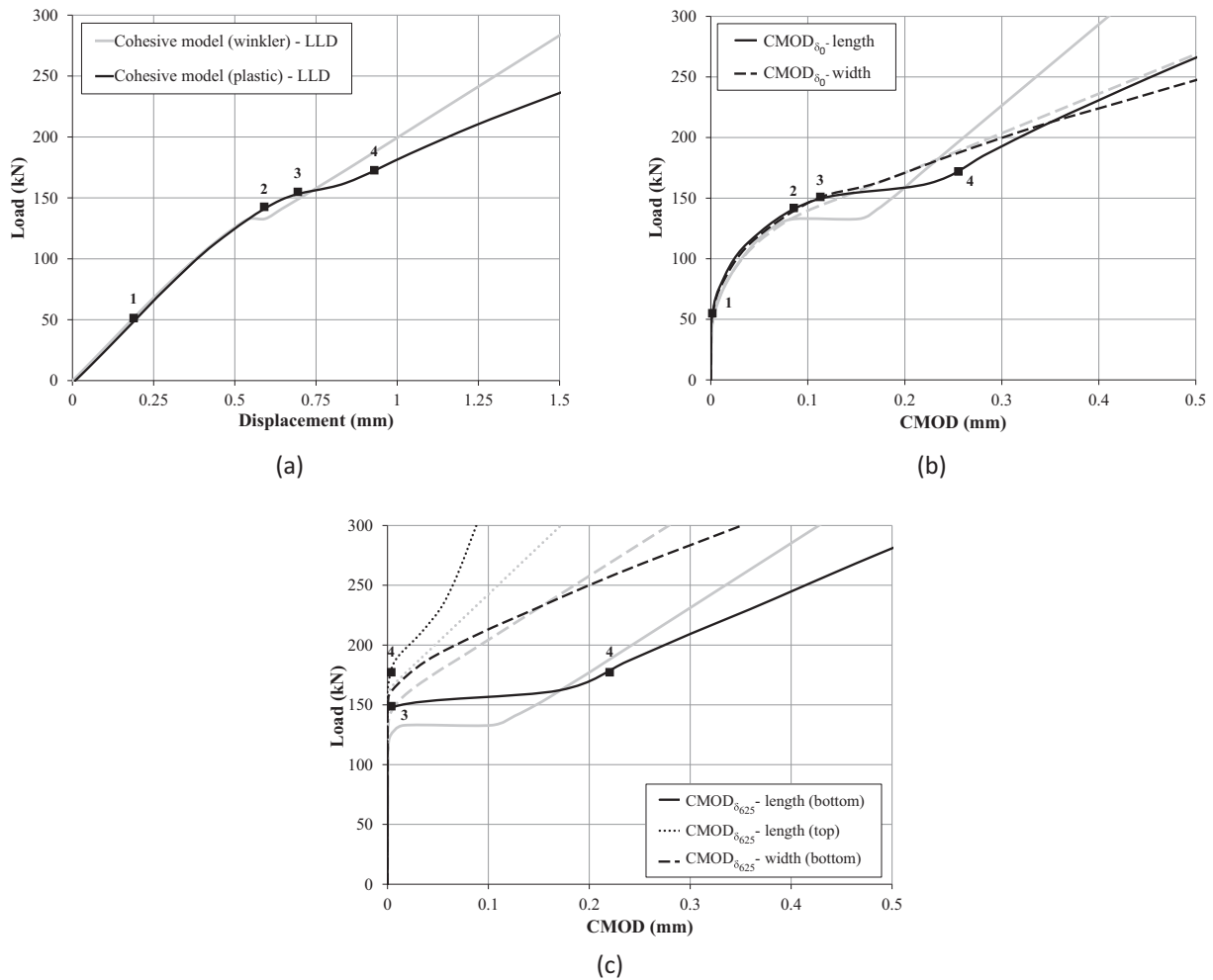


Fig. 13. Presentation of numerical results for the ‘Winkler’ (grey) and ‘Plastic’ (black) subgrade model: load line displacement (LLD) (a), load-CMOD curve for cohesive crack at the bottom of the slab under the load centre (b), and load-CMOD curve for the cohesive crack at the bottom and the top of the slab 625 mm from load centre in the length direction and at the bottom in the width direction.

The success in the application of M–E models was modest at best, as no or little damage was recorded during each load cycle as shown in Fig. 10(a). To reduce the test time, the load was increased from typical equivalent standard axle load (ESAL) of 50–60 kN (per wheel) to 150 kN. However, to record damage development, the load was finally increased to 250 kN, which caused excessive cracking in the cement bound granular mixture and local yielding of the subgrade soil foundation below the plate load, correlating badly with the M–E models calibrated for highway pavement design. The experimental load displacement curves for the the two load series are shown in Fig. 10(c) and (d) for displacements measured at a distance of 235 and 450 mm from the loaded centre, respectively.

From Fig. 10 it can be observed that the load–displacement curves extracted from the two load series, for the inner slab ( $N = 1$  and  $N = 10,001$ ) and the outer slab ( $N = 1$  and  $N = 5001$ ), follow each other closely up to the load level of app. 150 kN. Then, the inner slab shows a pronounced drop in stiffness. Similar drop in stiffness is also indicated for the outer slab, but at a higher load level of app. 225 kN. The most likely explanation for this difference in structural response, can be found in the natural variation in subgrade soil properties and it's shear strength, which is highly influenced by the angle of internal friction, and the different number of load cycles between load steps which can have caused a different

damage state of the subgrade soil, slabs and aggregate interlock joints.

The load, asphalt surface and slab geometry, shown in Fig. 11(a), is modelled with solid 3-D elements (C3D8 and C3D6) in ABAQUS. A total of 51,155 elements are used to represent the elastic material, shown in Fig. 11(b), separated by pre-determined cohesive contact surfaces, representing the cohesive zone (average 10 mm size elements), in the vertical plane in orthogonal directions. The average strength properties of the cemented material were determined from specimens extracted from slabs, shown in Table 1. The cohesive model is evaluated applying three different subgrade models with mechanical material properties as shown in Table 3.

From comparison between numerical and experimental load–displacement curves at a distance of 235 mm and 450 mm from the load centre, shown in Fig. 12(a) and (b), it can be observed that relatively good agreement is obtained between experimental and numerical results up to the peak-load for all three models. The peak-load is app. 157, 133 and 162 kN for the 'Elastic', 'Winkler' and 'Plastic' model, respectively. The experimental result shows a pronounced post-peak decrease in stiffness at a load level of app. 150 kN, probably due to local plastic yielding of the subgrade soil. This behaviour can only be captured by the 'Plastic' model. Moreover, it is found that modelling the subgrade soil with elastic solid continuum elements result in a more realistic prediction of the

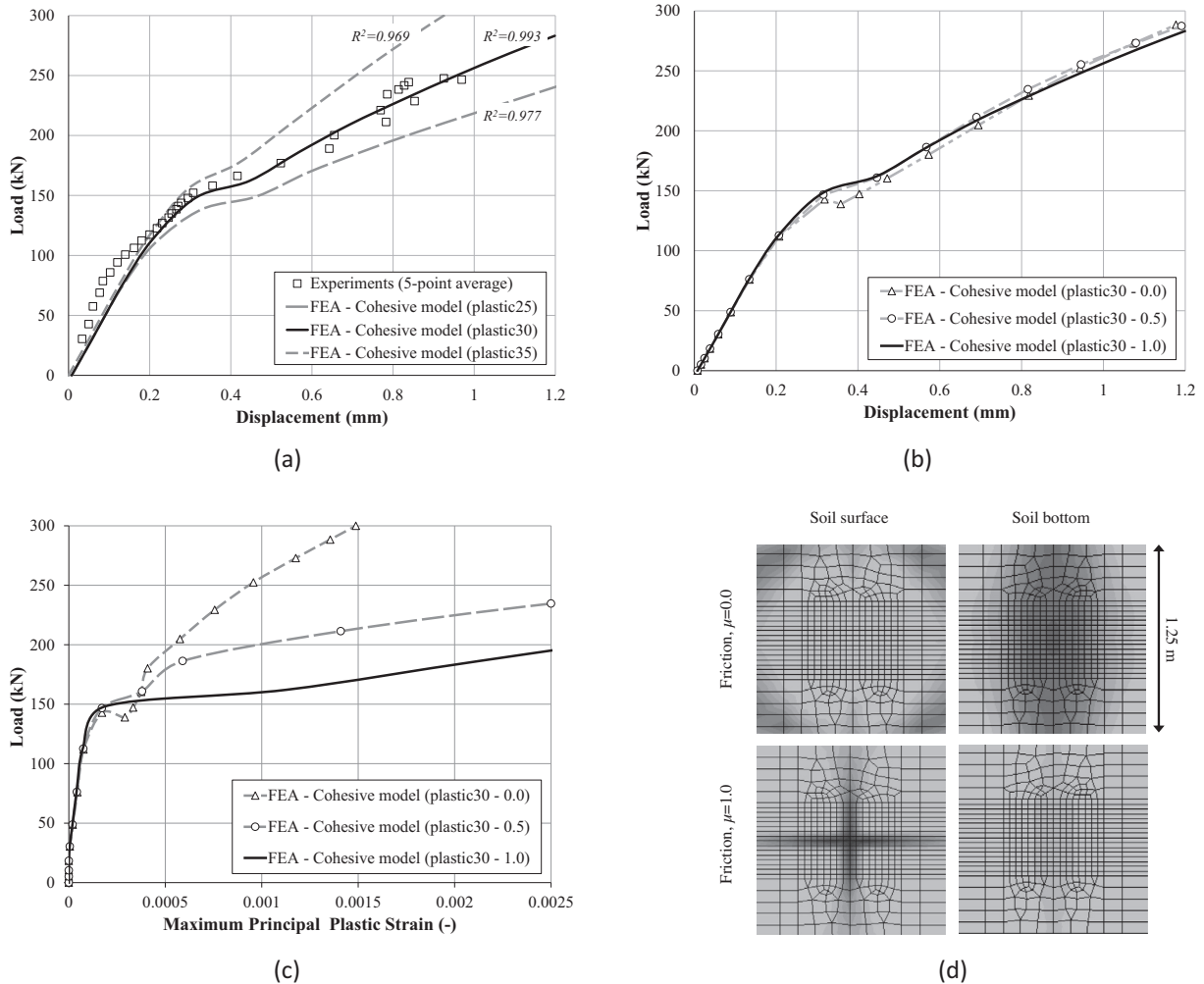


**Fig. 14.** Comparison between averaged experimental- and numerical results for the 'Plastic' model: (a) and (b) influence of angle of internal friction ( $\phi = 25\text{--}35^\circ$ ) and friction coefficient ( $\mu = 0\text{--}1.0$ ) between the cemented slab and subgrade soil layer on the load–displacement curves at a distance of 235 mm from load centre, (c) influence friction coefficient on maximum principal plastic strains and (d) plastic strain distribution in the peak-region at the top and bottom of the subgrade soil layer at the maximum load level of 250 kN.

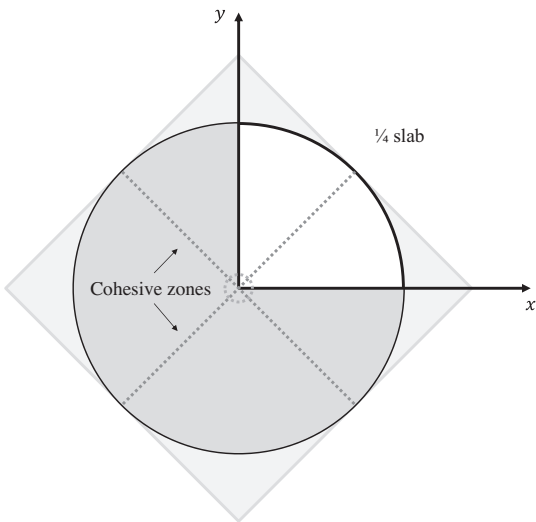
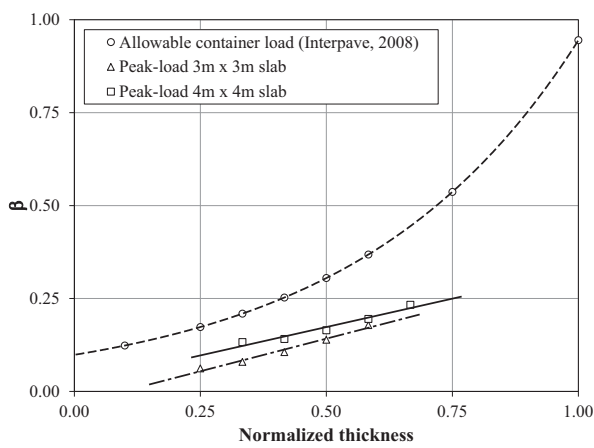


Fig. 15. Sketch of model applied in the sensitivity study.

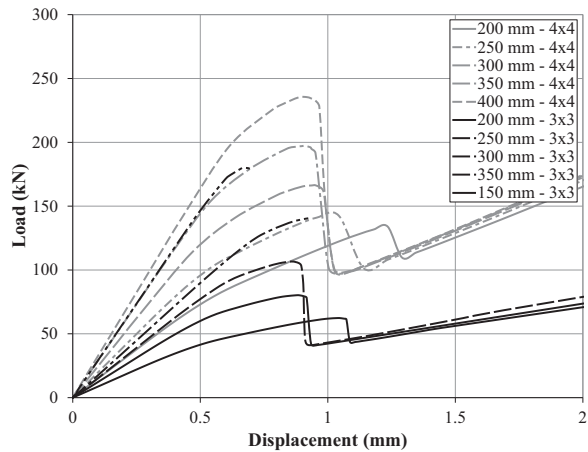
peak-load compared to the ‘Winkler’ model as this model essentially suffers from a complete lack of continuity in the supporting medium, neglecting the shear stiffness of the subgrade soil. The influence of subgrade soil model type on local crack behaviour can be seen in Fig. 13.

From the load versus crack mouth opening displacement (CMOD) curve in Fig. 13, it can be observed that cracks in both directions are initiated at load point 1, damage of the cohesive crack then progress toward the edges of the slab. At load level point 2, nodes at the bottom of the slab in length direction (shortest direction) have exceeded the final (zero traction) displacement. The cohesive zone then progress upwards until the ‘snap’ at load level point 3, resulting in the kink on the load–displacement curve in Fig. 13(a) and (b), whereas the crack in the width remains stable in the width direction as shown in Fig. 13(b) and (c). Unloading on the load–displacement curve is prevented by the high stiffness of the subgrade soil and the geometry of the slab. At load level point 4, all nodes in the length direction have exceeded the final displacement, as shown in 13(c).

The numerical results shown in Fig. 13 can explain some of the observations made during the experimental investigations which

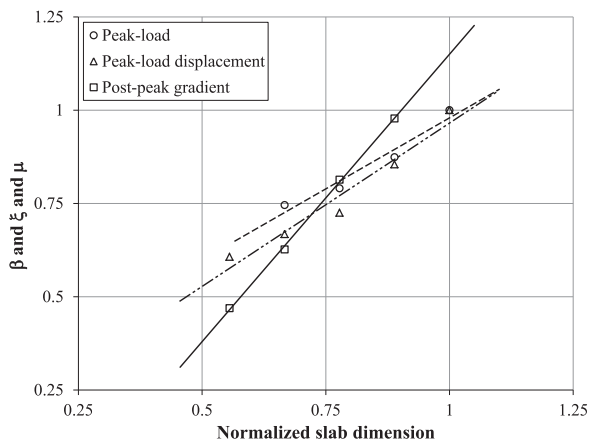


(a)

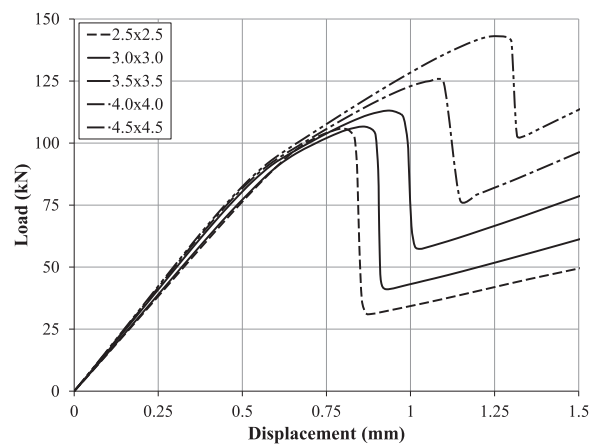


(b)

Fig. 16. Influence of slab thickness varying from 150 to 400 mm keeping length/width constant for a 3 × 3 m<sup>2</sup> slab (black) and 4 × 4 m<sup>2</sup> slab (grey) compared to the Interpave guideline [11]; normalised peak-load ( $\beta$ ) versus normalised thickness curve (a) and load–displacement curves (b).



(a)



(b)

Fig. 17. Influence of slab dimensions from 2.5 × 2.5 m<sup>2</sup> to 4.5 × 4.5 m<sup>2</sup>, keeping thickness constant (250 mm); normalised peak-load ( $\beta$ ), peak-load displacement ( $\xi$ ) and post-peak gradient ( $\mu$ ) versus normalised slab dimension (a) and load–displacement curves (b).

could not be described by the M–E models. The most obvious observation is that the crack along the length (shortest direction) has fully propagated at the applied load of 150 kN (load level point

3), explaining why no damage was recorded during experiments with repeated loads at this load level. Then, the response is controlled by further crack propagation along the width and the

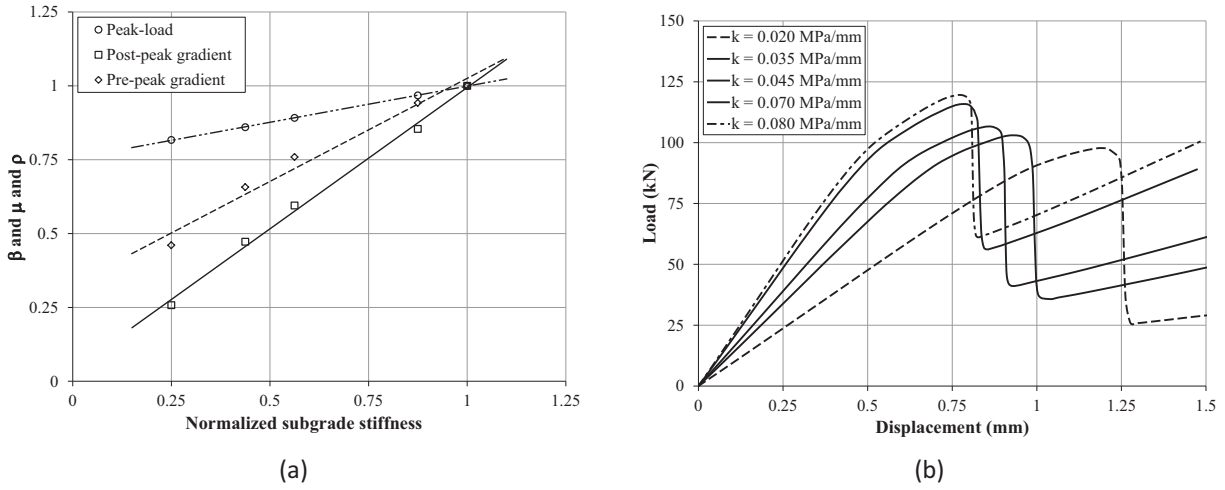


Fig. 18. Influence of subgrade stiffness varying from 0.02 to 0.08 MPa/mm; normalised peak-load ( $\beta$ ), post-peak gradient ( $\mu$ ) and pre-peak gradient ( $\rho$ ) versus normalised subgrade stiffness (a) and load–displacement curves (b).

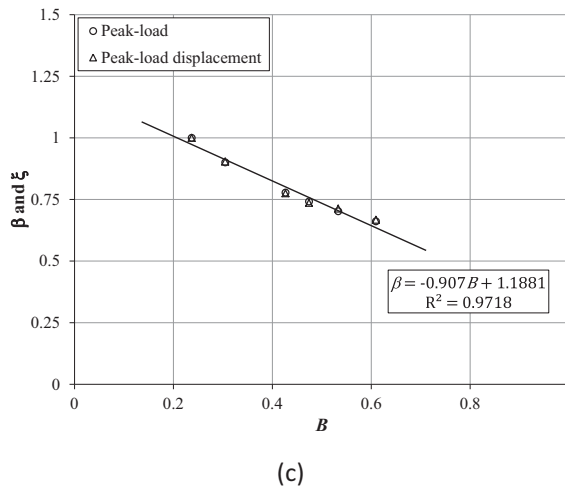
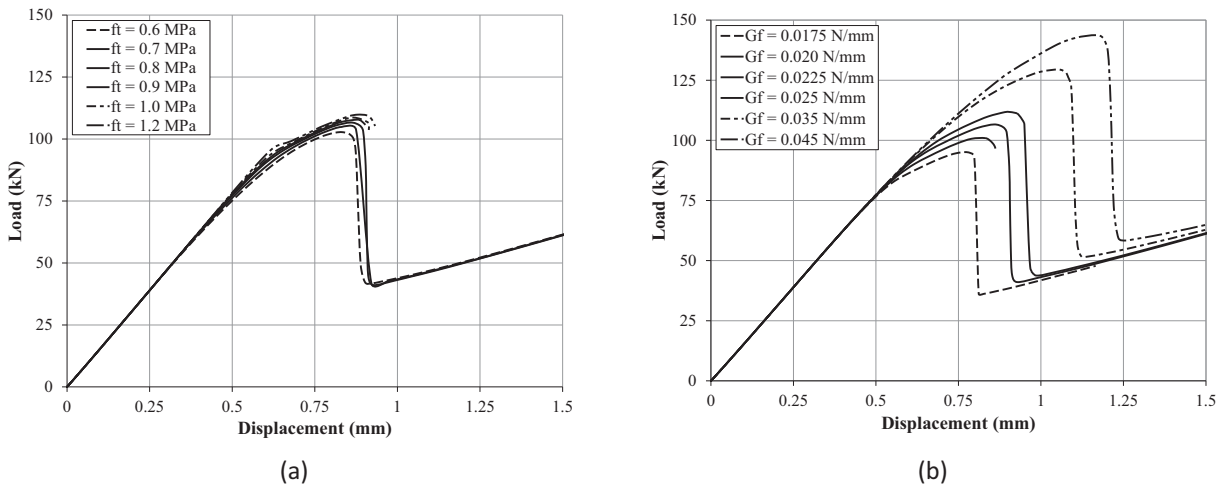


Fig. 19. Influence of fracture energy; load–displacement curve for tensile strength varying from 0.6 to 1.2 MPa keeping fracture energy constant (a), load–displacement curve for fracture energy varying from 0.0175 to 0.045 N/mm keeping tensile strength constant (b) and normalised peak-load ( $\beta$ ) and peak-load displacement ( $\xi$ ) versus the brittleness number ( $B$ ) defined by Bache and Vinding [71] (c).

subgrade soil behaviour. Moreover, it is observed that cracking is initiated at load level 1 of 50 kN, the same load magnitude as a equivalent standard axle loads.

From Fig. 14(a) it is observed that the angle of internal friction has significant influence on the load–displacement response. However, a relatively good fit between averaged experimental- and numerical results can be found for all models in the expected interval. It is also found, that the friction between layers has little influence on the overall structural response, but significant influence on local subgrade soil response, as shown in Fig. 14(b) and (c), respectively. Increasing friction between layers results increasing maximum plastic strains and strain localisation at the subgrade soil surface below the loaded plate. Whereas no friction, gives larger distribution of strains, increasing towards the bottom of the layer as shown in Fig. 14(d).

#### 4. Sensitivity studies

##### 4.1. Model idealisations

To investigate the influences of geometry and important material properties on the model response a sensitivity study is carried out for interior loading of a single slab. The slab geometry is modelled with solid 3-D elements (C3D8I and C3D6) in ABAQUS. Symmetry conditions are applied, modelling one slab crack.

Cohesive zones are inserted with a 45° angle between the symmetry-lines and in an arch close to the centre.

This methodology result in somewhat lower ultimate load bearing capacity of the structure, as a circular disc is considered, with an reduction in area of 20% compared to the 1/4 slab. However, it is found from preliminary analysis that the structure sketched in Fig. 15 adequately predicts the responses of a full slab. The arch cohesive zone is inserted to avoid convergence problems at the boundary. The energy used to create the arch crack is small and can be neglected. The subgrade is idealised as linear elastic.

##### 4.2. Effect of cemented base thickness, slab dimensions and subgrade stiffness

In linear elastic analysis of pavement structures, the layer thickness is increased for increasing load levels, to ensure a relatively constant stress level in the subgrade soil, avoiding any plastic deformation. This approach can be questioned based on the results presented herein; as it is observed in Fig. 16 that the allowable load levels in presently available guidelines [11] is twice the magnitude compared to the peak-loads found in the present study. As expected, the thickness of the cemented base layer has significant influence on the peak-load, but little influence on the post-peak response of the structure. It is also observed that the slab dimensions has influence on the normalised peak-load relationship curve.

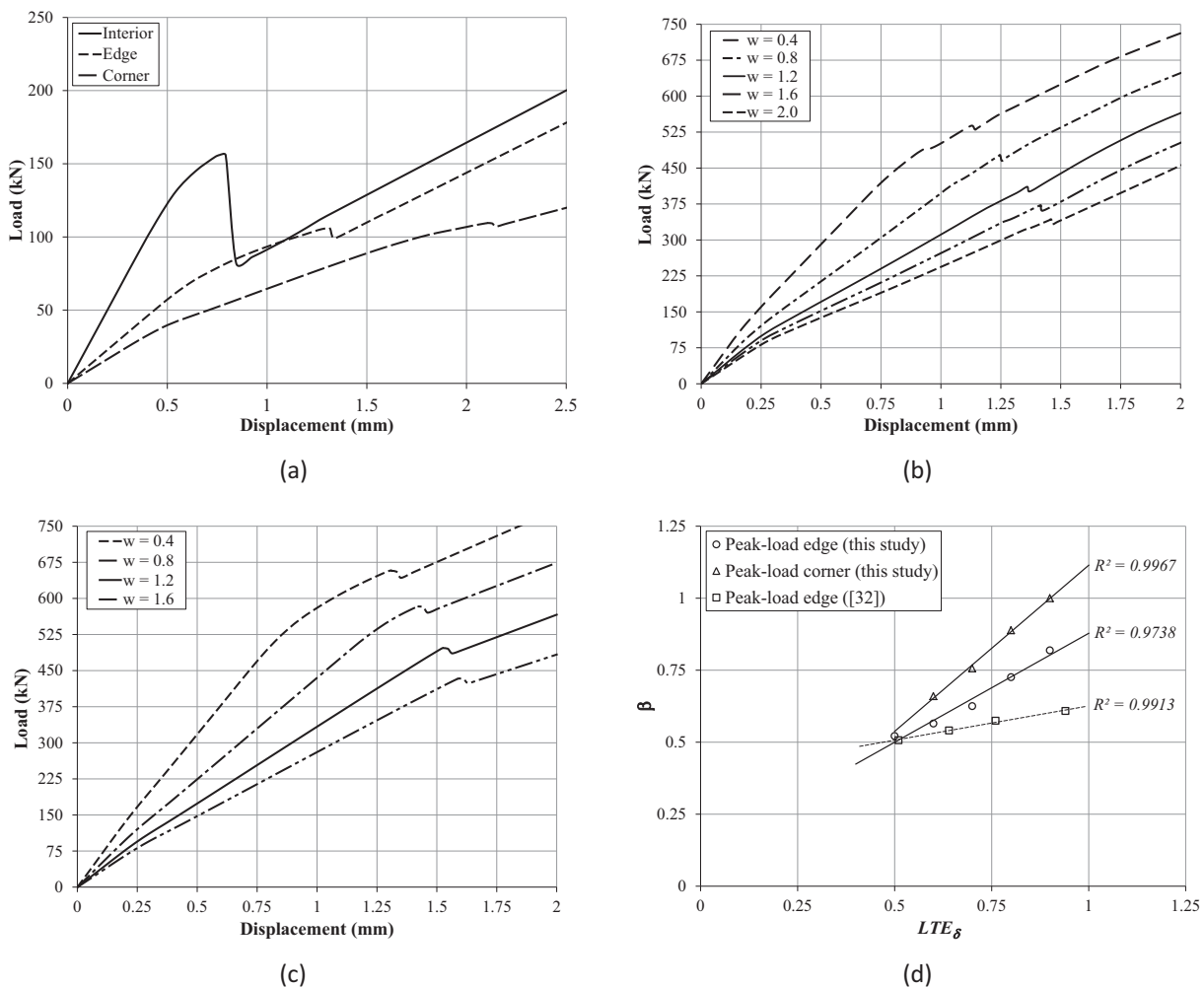


Fig. 20. Evaluation of influence from load position and aggregate interlock joints; load–displacement curve for the three load cases (a), load–displacement curve with variation in initial joint opening for edge loading (b), corner loading (c) and normalised peak-load ( $\beta$ ) versus  $LTE_{\delta}$  (d).

The stiffness- and peak-load of the structure increase with increasing thickness up to unloading. Then the structural response is mainly influenced by the slab dimension, shown in Fig. 17, and the stiffness of the subgrade soil.

It is observed from Fig. 17 that the peak-load and peak-load displacement increases with increasing slab dimensions before unloading occur. It is also found that there is a significant effect from bending; with a steep increasing post-peak stiffness for increasing slab dimensions.

As expected, Fig. 18 shows that increasing stiffness of the subgrade results in increasing peak-load, post-peak and pre-peak stiffness. The difference in peak-load is 20% for the variation in subgrade stiffness evaluated, assuming that slabs is constructed on a 150 mm thick high quality sub-base material over subgrade soil of varying quality (california bearing ratio 5–20).

#### 4.3. Effect of tensile strength and fracture energy

The softening curve depicted in Fig. 3(c) makes it obvious that the two main material parameters influencing the fracture process of the quasi-brittle material is tensile strength and fracture energy. However, as shown in Fig. 14(a), the influence of tensile strength is small, both with regard to peak-load and pre- and post-peak response. This can be explained by the fact that cracking is initiated at a displacement of 0.2 mm. Where after the response is primarily controlled by fracture energy, as shown in Fig. 19(b). It is found, that as the fracture energy decreases the material becomes more brittle. This is shown by plotting the normalised peak-load ( $\beta$ ) and peak-load displacement ( $\xi$ ) against the dimensionless parameter,  $B$ , defined by Bache and Vinding [71] as:

$$B = \frac{h}{l_{ch}} = \frac{f_t h}{EG_F} \quad (3)$$

where  $l_{ch}$  is the characteristic length of the material, first introduced by Hillerborg [72],  $E$  is elastic stiffness, and  $h$  is the slab thickness.

It is also observed from Fig. 19(c) that  $\beta$  is inversely proportional to  $B$ , and that it may be postulated that a unique relationship exists that would allow one to determine the peak load for a particular value of  $B$ , given the corresponding peak load for different brittleness number [48].

### 5. Influence of aggregate interlock behaviour and load position

To extend the analysis to more realistic pavement systems, evaluating the influences from interaction with adjacent slabs and the load position, numerical studies of three full ( $3 \times 3 \times 0.3 \text{ m}^3$ ) slabs on grade structures is carried out. The load position influence is evaluated at the interior, edge and corner of the slab; assuming two orthogonal, one length and one diagonal fracture plane in each case respectively.

The influence of variation in normal- and shear stiffness of joints is evaluated for an initial crack width,  $w$ , of 0.4–2.0 mm, simulated by application of idealised bilinear springs as shown in Table 2. The average strength properties for the cement bound granular mixture selected are shown in Table 1. The subgrade is idealised as linear elastic.

As expected, Fig. 20(a) shows that the load supported by the slab is higher under interior than under edge- and corner loading, with peak loads of 156, 106 and 109 kN respectively, considering no load transfer between adjacent slabs. It is also found that that the post-peak behaviour, in the case of interior- and edge loading, are more or less similar.

The initial crack width has little influence on the peak-load and peak-load displacement for interior load, whereas a pronounced

increase in stiffness and peak-load can be found for edge- and corner load, shown in Fig. 20(b) and (c). Plotting the normalised peak-load ( $\beta$ ) versus  $LTE_\delta$ , assuming that a linear relationship exist between  $w$  and  $LTE_\delta$  [73], it can be found that  $\beta$  decrease linearly with increasing  $w$  as shown in Fig. 20(d). Similar trends has also been reported in numerical studies of slabs on grade by other researchers [74].

### 6. Conclusion

The use of a cohesive model for simulating the fracture in the cement bound granular mixtures in composite block pavement systems has been investigated by studying the main parameters that affect the responses of the pavement structure.

Comparison of numerical and experimental results for four point bending beam tests show that good agreement is obtained with the cohesive model. It is found that the cohesive model adequately describe the structural response of slabs on grade structures and that aggregate interlock behaviour can be realistically incorporated in models by idealised bilinear springs. However, tests results are limited and more testing is necessary to evaluate the fracture behaviour of cement bound granular mixtures, e.g., fracture energy and shear interaction.

Moreover, the numerical analysis of slabs on grade experiments reveal the importance of incorporating realistic subgrade soil behaviour in models. Most importantly, the shear stiffness of the soil and the plastic yield limit, as these two parameters have significantly influence on the prediction of peak-load and post-peak response, respectively.

The influence of slab thickness-and dimensions proved to be important parameters. The peak-load is highly influenced by thickness, whereas slab dimensions proved to be a main controlling parameter of the post-peak response of the structure. Furthermore, it can be concluded that the fracture process is more affected by the fracture energy than the tensile strength.

The peak-loads found in the present study are significantly lower than allowable load levels given in available guidelines for composite block pavements. To extend the analysis to full evaluation of structural bearing capacity, one could include a failure criteria of the subgrade soil as shown in Section 3.2. It would then be feasible with the methodology presented, to evaluate the critical load case, e.g., also including the influence of temperature loads (shrinkage).

The full slab model shows that cracking is initiated at an early stage, and that the structural response is affected by aggregate interlock behaviour. This effect is primarily important to the response of structures subjected edge- and corner loading. Moreover, it is found that the peak-load decrease linearly with increase in initial crack width.

In the present study idealised FE composite block pavement structures is developed with application of a cohesive model to describe the fracture behaviour of the cement bound granular mixture. Computationally fast models are obtained, with a minimum of elements, applying the cohesive contact model in ABAQUS. Furthermore, numerical instabilities are avoided, not compromising the penalty stiffness. It is found that the idealised FE models developed adequately describe the structural response of composite block pavements subjected to heavy static loads, showing their applicability for engineering design purpose. It is envisaged that the methodology implemented can be extended to more complex and realistic problems, e.g., including also a cyclic formulation of the cohesive zone and aggregate interlock behaviour, for development of more rational failure criteria in pavement engineering in the future.

## Acknowledgements

This work was supported by COWIfonden.

The experimental data presented in Fig. 8 was provided by Austroads. The cooperation with Austroads and Dr. Richard Yao is kindly acknowledged.

## References

- [1] R. Kerkhoven, G.M. Dormon, Some Considerations on the California Bearing Ratio Method for the Design of Flexible Pavements, Shell Petroleum Company, 1953.
- [2] M.A. Shahid, N.H. Thom, Performance of cement bound bases with controlled cracking, in: Rilem Proceedings, Chapman & Hall, 1996, pp. 55–64.
- [3] H.L. Theyse, M. De Beer, F.C. Rust, Overview of South African mechanistic pavement design method, *Transp. Res. Rec.* 1539 (1996) 6–17.
- [4] R. Yeo, Fatigue performance of cemented materials under accelerated loading: influence of vertical loading on the performance of unbound and cemented materials, no. AP-T102/08, 2008.
- [5] C. Freeme, J. Maree, A. Viljoen, Mechanistic design of asphalt pavements and verification using the heavy vehicle simulator, National Institute for Transport and Road Research, 1982.
- [6] J.-F. Corté, M.-T. Goux, Design of pavement structures: the French technical guide, *Transp. Res. Rec. J. Transp. Res. Board* 1539 (1) (1996) 116–124.
- [7] G. Jameson, K.G. Sharp, R. Yeo, Cement-treated Crushed Rock Pavement Fatigue Under Accelerated Loading: The Mulgrave (Victoria) ALF Trial, 1989/1991, no. ARR229, 1992.
- [8] F. Thgersen, C. Busch, A. Henriksen, Mechanistic design of semi-rigid pavements, Danish Road Institute. Report 138.
- [9] Austroads, Pavement Design: A Guide to the Structural Design of Road Pavements, Austroads, 2004.
- [10] AASTHO, Mechanistic-empirical design of new and rehabilitated pavement structures. NCHRP 1–37A., *Transp. Res. Board* (2006).
- [11] J. Knapton, The Structural Design of Heavy Duty Pavements for Ports and Other Industries, fourth ed., Interpave, 2008.
- [12] C. Busch, A. Wysokowski, M. Cwiakala, A. Adesiyun, A. Zurawicka, A. Duszynski, L. Korusiewicz, P. Kaszub, A. Nowak, Large scale test of semi rigid pavements at test stand in zmigrod, IBDIM, COWI A/S and ECO-SERVE Thematic Network European Construction in Service of Society Report no. TW 65406/G1RT-CT-2002-05085, 2006.
- [13] A. Hillerborg, M. Modér, P.-E. Petersson, Analysis of crack formation and crack growth in concrete by means of fracture mechanics and finite elements, *Cem. Concr. Res.* 6 (6) (1976) 773–781.
- [14] M. Jirásek, Modeling of localized damage and fracture in quasibrittle materials, in: Continuous and Discontinuous Modelling of Cohesive-Frictional Materials, Springer, 2001, pp. 17–29.
- [15] T. Belytschko, J. Fish, B.E. Engelmann, A finite element with embedded localization zones, *Comput. Methods Appl. Mech. Eng.* 70 (1) (1988) 59–89.
- [16] T. Belytschko, T. Black, Elastic crack growth in finite elements with minimal remeshing, *Int. J. Numer. Methods Eng.* 45 (5) (1999) 601–620.
- [17] Y. Rashid, Ultimate strength analysis of prestressed concrete pressure vessels, *Nucl. Eng. Des.* 7 (4) (1968) 334–344.
- [18] J. Mazars, A description of micro-and macroscale damage of concrete structures, *Eng. Fract. Mech.* 25 (5) (1986) 729–737.
- [19] J. Lubliner, J. Oliver, S. Oller, E. Onate, A plastic-damage model for concrete, *Int. J. Solids Struct.* 25 (3) (1989) 299–326.
- [20] K. Maekawa, J. Takemura, P. Irawan, M. Irie, Triaxial elasto-plastic and fracture model for concrete, *Proc. Japan Soc. Civil Eng.* 460 (5–18) (1993) 131–138.
- [21] F. Moavenzadeh, Asphalt fracture, in: Assoc Asphalt Paving Technol Proc, Association of Asphalt Paving Technologists, 1967.
- [22] A. Bahgat, M. Herrin, Brittle fracture of asphalt mixtures, in: Proceedings of the Association of Asphalt Paving Technologists, vol. 37, Association of Asphalt Paving Technologists, 1968, pp. 32–50.
- [23] K. Majidzadeh, E. Kauffmann, D. Ramsamooj, Application of fracture mechanics in the analysis of pavement fatigue, in: Association of Asphalt Paving Technologists Proc, vol. 40, Association of Asphalt Paving Technologists, 1971.
- [24] D.V. Ramsamooj, K. Majidzadeh, E. Kauffmann, The analysis and design of the flexibility of pavements, Presented at the Third International Conference on the Structural Design of Asphalt Pavements, Sept. 11–15, vol. 1, Grosvenor House, Park Lane, London, England, 1972.
- [25] Y. Salam, C. Monismith, Fracture characteristics of asphalt concrete, *Asphalt Pav. Technol.* 41 (1972) 215–256.
- [26] A. Abdulshafi, K. Majidzadeh, J-integral and cyclic plasticity approach to fatigue and fracture of asphaltic mixtures, *Transp. Res. Rec.* (1034) (1985).
- [27] K.W. Kim, H. El Hussein, Effect of differential thermal contraction on fracture toughness of asphalt materials at low temperatures (with discussion), *J. Assoc. Asphalt Pav. Technol.* 64 (1995).
- [28] M. Jacobs, P. Hopman, A. Molenaar, Application of fracture mechanics principles to analyze cracking in asphalt concrete, *J. Assoc. Asphalt Pav. Technol.* 65 (1996).
- [29] A. Bhurke, E. Shin, L. Drzal, Fracture morphology and fracture toughness measurement of polymer-modified asphalt concrete, *Transp. Res. Rec. J. Transp. Res. Board* 1590 (1997) 23–33.
- [30] Y.-S. Jenq, J.-D. Perng, Analysis of crack propagation in asphalt concrete using cohesive crack model, no. 1317, 1991.
- [31] Y.-S. Jenq, C.-J. Liaw, P. Lieu, Analysis of crack resistance of asphalt concrete overlays – a fracture mechanics approach, *Transp. Res. Rec. J. Transp. Res. Board* 1388, 160–166.
- [32] J.B. Soares, F. Freitas, D.H. Allen, Crack modeling of asphaltic mixtures considering heterogeneity of the material, *Transp. Res. Rec.* 2003 (1832) 113–120.
- [33] G.H. Paulino, S.H. Song, W.G. Buttler, Cohesive zone modeling of fracture in asphalt concrete, in: Proceedings of the 5th International RILEM Conference-Cracking in Pavements: Mitigation, Risk Assessment, and Preservation, Limoges, France, 2004, pp. 63–70.
- [34] M.P. Wagoner, W.G. Buttler, G.H. Paulino, Development of a single-edge notched beam test for asphalt concrete mixtures, *J. Test. Evaluat.* 33 (6) (2005) 452.
- [35] S.H. Song, G.H. Paulino, W.G. Buttler, Simulation of crack propagation in asphalt concrete using an intrinsic cohesive zone model, *J. Eng. Mech.* 132 (11) (2006) 1215–1223.
- [36] J. Baek, I. Al-Qadi, Finite element method modeling of reflective cracking initiation and propagation: Investigation of the effect of steel reinforcement interlayer on retarding reflective cracking in hot-mix asphalt overlay, *Transp. Res. Rec. J. Transp. Res. Board* 2006 (1949) 32–42.
- [37] H. Kim, M.P. Wagoner, W.G. Buttler, Numerical fracture analysis on the specimen size dependency of asphalt concrete using a cohesive softening model, *Constr. Build. Mater.* 23 (5) (2009) 2112–2120.
- [38] L.T. Souza, Y.-R. Kim, F.V. Souza, L.S. Castro, Experimental testing and finite-element modeling to evaluate the effects of aggregate angularity on bituminous mixture performance, *J. Mater. Civil Eng.* 24 (3) (2012) 249–258.
- [39] G. Zeng, X. Yang, A. Yin, F. Bai, G. Zeng, Simulation of damage evolution and crack propagation in three-point bending pre-cracked asphalt mixture beam, *Constr. Build. Mater.* 55 (2014) 323–332, <http://dx.doi.org/10.1016/j.conbuildmat.2014.01.058>.
- [40] A.M. Ioannides, Fracture mechanics in pavement engineering: the specimen-size effect, *Transp. Res. Rec.* 1568 (1997) 10.
- [41] A.M. Ioannides, S. Sengupta, Crack propagation in Portland cement concrete beams: implications for pavement design, *Transp. Res. Rec.* 2003 (1853) 110–120.
- [42] A.M. Ioannides, J. Peng, J.R. Swindler Jr, Abaqus model for PCC slab cracking, *Int. J. Pavement Eng.* 7 (4) (2006) 311–321.
- [43] J. Roesler, G.H. Paulino, K. Park, C. Gaedicke, Concrete fracture prediction using bilinear softening, *Cem. Concr. Compos.* 29 (4) (2007) 300–312, <http://dx.doi.org/10.1016/j.cemconcomp.2006.12.002>.
- [44] F. Evangelista, J. Roesler, G. Paulino, Numerical simulations of fracture resistance of functionally graded concrete materials, *Transp. Res. Rec.* 2113 (2113) (2009) 122–131, <http://dx.doi.org/10.3141/2113-15>.
- [45] K. Park, G.H. Paulino, J. Roesler, Cohesive fracture model for functionally graded fiber reinforced concrete, *Cem. Concr. Res.* 40 (6) (2010) 956–965.
- [46] C. Gaedicke, J. Roesler, Fracture-based method to determine the flexural load capacity of concrete slabs, *FAA COE Rep* (31) (2009).
- [47] C. Gaedicke, J. Roesler, F. Evangelista, Three-dimensional cohesive crack model prediction of the flexural capacity of concrete slabs on soil, *Eng. Fract. Mech.* 94 (2012) 1–12.
- [48] T.W. Aure, A.M. Ioannides, Numerical analysis of fracture process in pavement slabs, *Canad. J. Civil Eng.* 39 (5) (2012) 506–514, <http://dx.doi.org/10.1139/L2012-020>.
- [49] F. Evangelista, J.R. Roesler, S.P. Proença, Three-dimensional cohesive zone model for fracture of cementitious materials based on the thermodynamics of irreversible processes, *Eng. Fract. Mech.* 97 (2013) 261–280.
- [50] ABAQUS, Analysis users manual, Version 6.13-1, Dassault Systems, Providence, RI, 2013.
- [51] A. Meda, G.A. Plizzari, P. Riva, Fracture behavior of SFRC slabs on grade, *Mater. Struct.* 37 (270) (2004) 405–411, <http://dx.doi.org/10.1617/14093>.
- [52] M. Huurman, L.J.M. Houben, A.W.M. Kok, Development of a three-dimensional finite element model for concrete block pavements, in: Proceedings Fourth International Conference on Concrete Block Paving, 1992, pp. 89–98.
- [53] A. Molenaar, H. Moll, L. Houben, Structural model for concrete block pavement, no. 954, 1984.
- [54] British Standards Institution – Hydraulically Bound Mixtures. Specifications. Cement Bound Granular Mixtures, BS EN 14227–1:2013 (2013).
- [55] J.-H. Liu, D.-Y. Wang, Numerical simulation of a crack in the cement stabilized stone using cohesive zone models, in: International Conference on Experimental Mechanics 2008 and Seventh Asian Conference on Experimental Mechanics, International Society for Optics and Photonics, SPIE, 2008, pp. 737511–737511, <http://dx.doi.org/10.1117/12.839044>.
- [56] E. Heymsfield, R.E. Wahl, W. Hodo, Development of a damage model for stabilized soil layers subjected to repetitive aircraft loadings, *Proc. 2006 Airfield Highway Pavement Specialty Conf.* 2006 (2006) 260–271.
- [57] Z. Wu, Z. Zhang, X. Yang, X. Chen, Finite element model for rutting prediction of flexible pavement with cementitiously stabilized base-subbase, *Transp. Res. Rec.* 2226 (2011) 104–110, <http://dx.doi.org/10.3141/2226-11>.
- [58] Brameshuber Hilsdorf, Code-type formulation of fracture mechanics concepts for concrete, *Int. J. Fract.* 51 (1) (1991) 61–72, <http://dx.doi.org/10.1007/BF00020853>.
- [59] Z.P. Bazant, P. Gambarova, Rough cracks in reinforced concrete, *ASCE J Struct Div* 106 (4) (1980) 819–842.
- [60] P. Gambarova, C. Karakoç, A new approach to the analysis of the confinement role in regularly cracked concrete elements, in: Transactions of the 7.

- International Conference on Structural Mechanics in Reactor Technology. Vol. H, 1983.
- [61] J.C. Walraven, H.W. Reinhardt, Theory and experiments on the mechanical behaviour of cracks in plain and reinforced concrete subjected to shear loading, *Heron* 26 (1) (1981).
- [62] J.C. Walraven, Fundamental analysis of aggregate interlock, *J. Struct. Div. ASCE* 107 (11) (1981) 2245–2270.
- [63] B. Li, Contact density model for stress transfer across cracks in concrete, *J. Faculty Eng. Univ. Tokyo* 1 (1989) 9–52.
- [64] E. Winkler, *Die lehre von der elasticitaet und festigkeit*, Verlag von H. Dominicus, Prag, 1868.
- [65] J. Maree, Aspects of the design and behaviour of pavements with granular base layers, Ph.D. thesis, Department of Civil Engineering, University of Pretoria (1982).
- [66] Swiss Association of Road and Traffic Experts – Geotechnical investigations and studies: Geotechnical Soil Parameters, SN 670010b, 1998.
- [67] E. Riks, An incremental approach to the solution of snapping and buckling problems, *Int. J. Solids Struct.* 15 (7) (1979) 529–551.
- [68] R. Yeo, The development and evaluation of protocols for the laboratory characterisation of cemented materials, no. AP-T101/08, 2008.
- [69] C. Busch, A. Adesiyun, Large scale testing of semi rigid pavements, in: Proceedings of the Second International Conference of Transport Research Arena Europe (TRA) 2008, Ljubljana, Slovenia, 2008.
- [70] C. Busch, Incremental-recursive modeling of performance for cement bound base layers, in: Proceedings of the Third International Conference on Accelerated Pavement Testing (APT) 2008, Madrid, Spain, 2008.
- [71] H. Bache, I. Vinding, C.T. Oplysningskontor., CtO., *Beton-teknik. Brudmekanik i design af betonbelægninger*, 1990.
- [72] A. Hillerborg, The theoretical basis of a method to determine the fracture energy  $G_f$  of concrete, *Mater. Struct.* 18 (4) (1985) 291–296.
- [73] W.G. Davids, J.P. Mahoney, Experimental verification of rigid pavement joint load transfer modeling with everFE, *Transp. Res. Rec. J. Transp. Res. Board* 1684 (1) (1999) 81–89.
- [74] T.W. Aure, A.M. Ioannides, Fracture analysis of aggregate interlock jointed slabs-on-grade, *Constr. Build. Mater.* 77 (2015) 340–348, <http://dx.doi.org/10.1016/j.conbuildmat.2014.12.086>.



# Paper II

*”Cohesive cracked-hinge model for simulation of fracture in one-way slabs on grade”*

A. Skar & P.N. Poulsen & J.F. Olesen

Published in: *International Journal of Pavement Engineering, 2017*



## Cohesive cracked-hinge model for simulation of fracture in one-way slabs on grade

Asmus Skar<sup>a</sup> , Peter Noe Poulsen<sup>b</sup> and John Forbes Olesen<sup>b</sup> 

<sup>a</sup>COWI A/S, Lyngby, Denmark; <sup>b</sup>Section for Structural Engineering, Technical University of Denmark, Lyngby, Denmark

### ABSTRACT

Numerical analysis of slab on grade structures subjected to mechanical loads is a complex matter often requiring computationally expensive models. In order to develop a simplified and general concept for non-linear analysis of slab on grade structures, this paper presents a cohesive cracked-hinge model aimed at the analysis of the bending fracture of the cemented material. The model is based on the fracture mechanics concepts of the fictitious crack model with a linear stress–crack opening relationship. Moreover, the paper presents a two-parameter spring foundation model applied to realistically capture the continuity in the supporting medium. The functionality of the proposed model is compared to numerical analysis with application of the more conventional cohesive zone model. The results obtained show that the methodology is a attractive and powerful one well-suited for practical use and further development.

### ARTICLE HISTORY

Received 8 August 2016  
Accepted 24 January 2017

### KEYWORDS

Cohesive crack; non-linear FEM; slab on grade; cemented materials; pavement analysis; two-parameter foundation model

### 1. Introduction

Numerical analysis of fracture in concrete and composite pavement systems, or so-called slab on grade structures, is a highly complex matter. This type of analysis often requires large and computationally expensive models applicable to relatively simple design problems. Moreover, concrete and composite pavement systems typically exhibit softening load–displacement post-peak behaviour in bending on both material and structural levels. This often results in convergence issues and aborted simulations making complex non-linear analysis less attractive for design engineering purposes. In order to create a simple and robust modelling framework for engineering application, this paper presents a non-linear cracked-hinge model based on the fracture mechanics concepts of the fictitious crack model (Hillerborg *et al.* 1976). The hinge model for modelling the crack propagation due to pure bending in a concrete beam without reinforcement was first presented by Ulfkjær *et al.* (1995). This hinge was successfully applied in the modelling of pure concrete beams in three-point bending considering the development of only one crack. Olesen (2001b) expanded the hinge model by applying a bi-linear softening curve to allow for the incorporation of the effects of fibres on concrete fracture. Further, this modified hinge model allowed for the existence of a sectional normal force. This last feature is crucial for the ability of the hinge to model a number of situations such as the wedge splitting test (Walter *et al.* 2005) and the split cylinder test (Olesen *et al.* 2006). Subsequently, this type of semi-analytical hinge models have primarily been applied for analysis of fracture in reinforced concrete beams (Olesen 2001a, Kwak and Kim 2002, 2010, Buratti *et al.* 2011, Carpinteri and Corrado 2011, Castel *et al.* 2011, Visintin *et al.* 2012). Murthy *et al.* (2013) used a hinge model to evaluate bi-linear softening diagrams of plain concrete corresponding to their size-independent fracture energy and Wardeh and Ghorbel (2015) used a hinge model to

study the effect of frost action on fracture properties and strain softening behaviour.

The principles of the fictitious crack model have been extended to practical problems for concrete and composite pavement structures applying cohesive interface elements or contact formulations, with some very encouraging results (Meda *et al.* 2004, Ioannides *et al.* 2006, Gaedicke and Roesler 2009, Aure and Ioannides 2012, 2015, Gaedicke *et al.* 2012, Evangelista *et al.* 2013, Skar and Poulsen 2015). Gaedicke and Roesler (2009) and Gaedicke *et al.* (2012), who published one of the few simulations with experimental results, used the interface element with tabular traction–displacement relation featured by ABAQUS (2013). The authors reported lack of convergence, instability problems, snap-backs and aborted simulations upon local unloading and reloading paths. Aure and Ioannides (2012) presented reduced finite element (FE) models compared to Gaedicke *et al.* and found that for slabs on grade structures, the type of softening curve, cohesive zone width and mesh do not influence the response significantly. Evangelista *et al.* (2013) developed a user-built cohesive element based on a damage mechanics framework resulting in more robust cohesive elements. Skar and Poulsen (2015) used the cohesive surface model in ABAQUS and applied a relatively coarse mesh for the cohesive zone. This resulted in computationally efficient models for analysis of the composite pavement systems studied. However, although there are successful examples of optimisation with regard to model size and robustness, all methods published deal with relatively large FE models compared to the complexity of the pavement system studied.

Another issue is the idealisation of soil foundation properties often applied in analysis of slab on grade structures. The interaction between structure and foundation and soil foundation properties is commonly idealised as independent linear elastic springs or so-called Winklers foundation (Winkler 1868). The

Winkler model is simple and practical to many engineering problems; however, care should be taken in application of such model as it essentially suffers from a complete lack of continuity in the supporting medium. Moreover, another fundamental problem with the use of this model is to determine the stiffness of elastic springs used to replace the soil. The problem becomes twofold since the numerical value of the Winkler stiffness (or modulus of subgrade reaction) not only depends on the nature of the soil foundation, but also on the dimensions of the slab and the loaded area.

Traditionally, the way to overcome the deficiency of Winkler models is to introduce an interaction between the independent springs, e.g. interconnections such as flexural elements, shear layers and deformed, pre-tensioned membranes (Kerr 1964, Hetenyi 1966). This class of mathematical models has another constant parameter which characterises the interaction implied between springs and hence called two-parameter foundation models. However, interpretation of how soil foundation material properties and characteristics are reflected in the various elements in the mechanical foundation models can be difficult; thus, evaluation on a rational, theoretical basis is cumbersome.

The semi-analytical hinge models reported in the literature are effective for studying the behaviour of simple fracture tests or problems where the crack path is known a priori. However, for studying more complex problems, a numerical formulation of the hinge is more convenient. Thus, this study presents a FE cohesive cracked-hinge beam resting on a two-parameter foundation for analysis of fracture in one-way slabs on grade supported by an elastic medium. At the lowest level, we consider a strip of cemented material including a crack and establish a stress–mean strain relationship. At the intermediate level, we consider a hinge element which is a finite part of the beam consisting of layered strips of cemented material, and establish a relationship between generalised sectional forces and strains. At the highest level, we apply the hinge model as a constitutive model in a non-linear beam element as proposed by Olesen and Poulsen (2012).

The effective stiffness concept is applied allowing formation of multiple cracks along the slab axis which is an essential feature of both plain and reinforced concrete slabs before exhibiting localised rotations. The effective stiffness which is a function of the state of deformation is treated as a constitutive relationship. Although the underlying description of the hinge is based on the formation of discrete cracks, the constitutive behaviour of the hinge is smeared (smooth). This particular feature is practical and effective as it requires no a priori knowledge of the crack pattern.

We show how the cracked-hinge model can be extended to pavement applications, implementing a two-parameter foundation model into beam elements. Moreover, a simple method for estimating foundation model parameters is proposed. This part is important because it describes a simplified methodology for simulating fracture in slabs on grade structures linking all necessary analysis steps in a rational and consistent manner.

The objective of the work presented is to develop a general and consistent framework based on a mechanistic approach for design of concrete and composite pavements. In this paper, we focus on establishing a simple model for two-dimensional analysis, assuming a continuum representation of the soil medium.

The general and consistent format selected makes the model suited for further developments, taking into account more complex material behaviour, soil response and cyclic loading conditions Skar *et al.* (2017).

## 2. Methodology

### 2.1. The mechanics of the cracked-hinge model

The basic assumption of the hinge model is the fact that the presence of a crack influences the overall stress and strain field of a structure only locally. The discontinuity created by the crack is expected to vanish outside a certain width. Under constant moment, e.g. between the loaded points in Figure 1(a), the beam sections at the midpoints between the cracks will, due to the periodicity of the cracks, remain plane during deformation of the beam. The width  $s$  between two such sections embracing one crack defines a hinge element, as shown in Figure 1(b). For the beam area outside the loaded points, the moment distribution is no longer constant. Such phenomena can be handled with appropriate numerical tools, i.e. the FE method, as exemplified for a single-beam element in Figure 1(b).

The hinge width  $s$  is a fundamental calibration parameter of the model, and it was suggested in Ulfkjær *et al.* (1995) to use a hinge width half the height of the beam, also adopted in the present study. Thus, the flexural deformation of the beam is concentrated and the propagation of a crack can be modelled as a hinge, whereas the rest of the beam can be treated as elastic bulk material.

The uni-axial tensile behaviour of the concrete is modelled according to the fictitious crack model by Hillerborg *et al.* (1976). The linear elastic pre-crack state is described by the elastic modulus,  $E_c$ . The uni-axial tensile strength is denoted by  $f_t$  and the corresponding strain by  $\varepsilon_{ct}$ . For the fracture analysis of concrete slab on grade pavement structures, the stress–crack opening relationship, or so-called softening law, does not influence the response significantly (Gaedicke and Roesler 2009, Aure and Ioannides 2012). Thus, in the present study, the softening law is given as a linear curve

$$\sigma(w) = f_t + aw \quad (1)$$

where  $a$  is the negative slope on the softening curve and  $w$  is the crack opening. The fracture energy,  $G_F$ , is given by the area under the softening curve, resulting in a final zero-stress crack opening  $w_c = -f_t/a$ .

The hinge model provides the relationship between the state of deformation of the hinge and the sectional forces ( $N$ ,  $M$ ). The state of deformation is described by the mean normal strain of the beam axis and the mean curvature of the hinge,  $(\bar{\varepsilon}_0, \bar{\kappa})$ .

The hinge solution is based on the assumption that the hinge may be seen as consisting of independent infinitesimal layers of cemented material. The tensile behaviour of this layer may be established by considering a strip of material in uni-axial tension as shown in Figure 2(d). The elongation of the strip located at  $y$  can be expressed in terms of the mean normal strain

$$\bar{\varepsilon}(y) = \frac{2u(y)}{s} = \frac{2u_0(y)}{s} + \frac{2\varphi}{s}y \equiv \bar{\varepsilon}_0 + \bar{\kappa}y \quad (2)$$

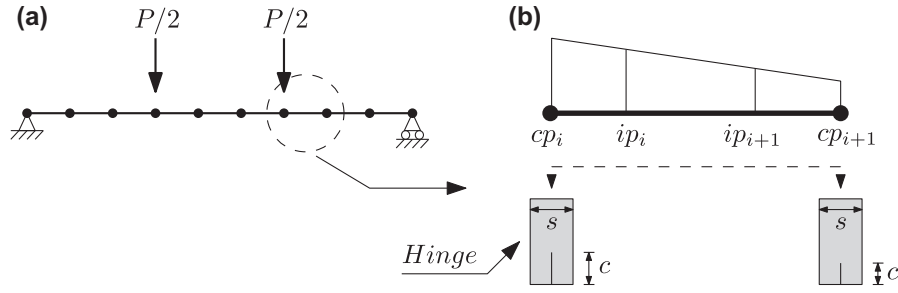


**Figure 1.** Sketch of hinge model implemented in a simply supported beam in four point bending: (a) overview of beam structure, (b) underlying discrete formulation of cracks at constitutive points,  $cp$ , and smeared constitutive behaviour obtained from interpolation between constitutive points at integration points,  $ip$ .

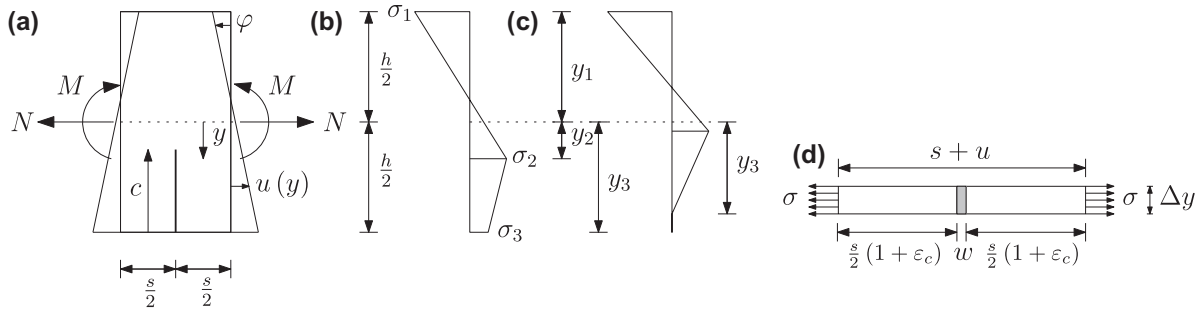


**Figure 2.** Hinge model: (a) beam segment with constant sectional forces and deformation of cracked beam segment, (b) and (c) hinge stress distribution after initiation of cracking at the two different Phases I and II, respectively. The distances  $y_1$  to  $y_3$  are used to perform integration in blocks shown in Appendix 2, (d) material strip in uni-axial tension: loaded state beyond peak load showing crack deformations.

where  $\bar{\varepsilon}_0$  is the mean normal strain at the beam axis, and  $\bar{\kappa}$  the mean curvature of the hinge. Utilising (2), the depth coordinates of characteristic points of the stress distribution at the midsection of the hinge may be determined.

Assume that the hinge has been deformed to a state where a crack has formed and penetrated a distance  $c$  into the hinge. The position of the crack tip is denoted by  $y_2 = h/2 - c$ , and is given as follows

$$\sigma_2 = f_t \Rightarrow (\bar{\varepsilon}_0 + \bar{\kappa}y_2)E_c \Rightarrow y_2 = \frac{\varepsilon_{ct} - \bar{\varepsilon}_0}{\bar{\kappa}} \quad (3)$$

In the cracked state,  $0 < w \leq w_c$  (Phase I), the crack opening and the corresponding stress in the strip is given as

$$\left. \begin{aligned} \sigma_c = \sigma_w \Rightarrow \sigma_c = f_t + aw \\ s + 2u = s(1 + \varepsilon_c) + w \Rightarrow s\bar{\varepsilon}(y) = s\varepsilon_c + w \end{aligned} \right\} \Rightarrow \begin{cases} w^I = s \frac{E_c \bar{\varepsilon}(y) - f_t}{E_c + as} \\ \sigma_3^I = E_c \frac{f_t - as\bar{\varepsilon}(y)}{E_c - as} \end{cases} \quad (4)$$

In the cracked state,  $w_c \leq w$  (Phase II), the crack is stress free, leading to the simple solution for the strip

$$\left. \begin{aligned} w = s(1 + \bar{\varepsilon}(y)) - s \\ \sigma_c = 0 \end{aligned} \right\} \Rightarrow \begin{cases} w^{II} = s\bar{\varepsilon}(y) \\ \sigma_3^{II} = 0 \end{cases} \quad (5)$$

From (4) and (5), the state of stress and crack opening in the cracked part of the hinge can be established. The cohesive stresses extend from  $y = y_2$  to  $y = y_3$ , depicted in Figure 2(b) and (c);  $y_2$  is given by (3) and

$$y_3 = \min \left( \frac{h}{2}, -\frac{1}{\bar{\kappa}} \left( \frac{f_t}{as} + \varepsilon_0 \right) \right) \quad (6)$$

Finally, the sectional forces with respect to  $y = 0$  may then be calculated from integration over the hinge height

$$N(\bar{\varepsilon}_0, \bar{\kappa}) = t \int_{-h/2}^{h/2} \sigma_c dy \quad (7a)$$

$$M(\bar{\varepsilon}_0, \bar{\kappa}) = t \int_{-h/2}^{h/2} \sigma_c y dy \quad (7b)$$

Contribution from a reinforcement bar can be included by adding the term  $A_s \sigma_s$  and  $A_s \sigma_s y_s$ , in (7a) and (7b), respectively. Where  $A_s$  is the area,  $\sigma_s$  is the stress in the steel and  $y_s$  is the position of the rebar.

## 2.2. Foundation model and calibration

### 2.2.1. The mechanics of the two-parameter foundation model

The development of two-parameter models has been approached along two distinct lines. The first type proceeds from the discontinuous Winkler model and eliminates its discontinuous behaviour by providing mechanical interaction between the spring elements by either elastic membranes (Filonenko-Borodich 1940), elastic beams (Hetényi 1946) or elastic layers capable of pure shear deformation (Pasternak 1954,

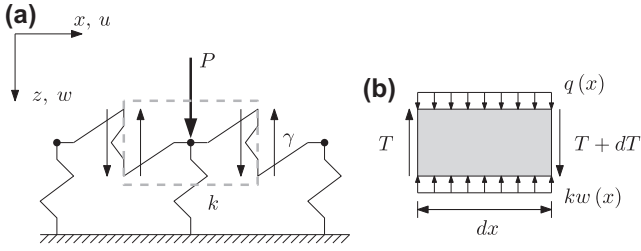


**Figure 3.** Mechanical model of two-parameter spring foundation, where  $k$  is the Winkler stiffness and  $\gamma$  is the second parameter stiffness.

Kerr 1964). The second approach starts from the elastic continuum model and simplifying assumptions with respect to the distribution of displacements and stresses, see e.g. Reissner (1958), Vlasov (1966).

The influence of using two-parameter models in design of rigid pavement slab on grade structures has been studied by e.g. Ioannides *et al.* (1985) and Khazanovich and Ioannides (1993), following implementation of such models in several special purpose FE tools for rigid pavement design (NCHRP 2003). Moreover, two-parameter models have been used to study complex phenomena occurring in rigid pavements, such as slab-curling (Khazanovich and Ioannides 1994, Khazanovich 2003, Zokaei-Ashtiani *et al.* 2015) and layer contact problems (Zokaei-Ashtiani *et al.* 2014). However, the influence of using two-parameter models, or soil idealisation techniques in general, for analysis of slab fracture has drawn little attention.

Several recent efforts have been made to implement mechanical models more sound and logic than the Winkler model. However, no foundation model has yet replaced the Winkler model and achieved a reasonably widespread level of acceptance among design engineers (Horvath 2002, Colasanti and Horvath 2010). In this aspect, the Winkler foundation with shear interaction is mechanically a logical extension of the Winkler model and analytically the next higher approximation (Kerr 1965). This model offers an attractive alternative to the elastic solid continuum by providing a degree of shear interaction between adjacent soil elements while remaining relatively simple to analyse (Ioannides 2006). Moreover, implementation of such a model in commercial FE codes is straightforward using discrete spring elements.

The two-parameter foundation model presented here is composed of coupled spring elements similar to the methodology proposed by (Loof 1965). The coupling between two springs to ground is modelled as second a spring transmitting a shear force  $T$  per unit width, as shown in Figure 3(a). This force is associated with the difference in vertical displacements  $w$  between the springs.

A simple assumption is that the shear force is proportional to the difference in displacements between two consecutive elements and therefore to the first derivative of the displacement, where  $\gamma$  is the second parameter and equivalent to the shear constant  $G_p$  in the Pasternak model. From the equilibrium of an element, shown in Figure 3(b), the differential equation governing the deflections of the soil surface is established as

$$q(x) = kw(x) - \frac{dT}{dx} \Rightarrow q(x) = kw(x) - \gamma \frac{d^2}{dx^2} w(x) \quad (8)$$

where the Winkler stiffness is  $k = k_0 t$ ,  $k_0$  is the modulus of subgrade reaction and  $t$  is the plane strain thickness of the model.

First, the case of a point load  $P$  is investigated, shown in Figure 4(a). Introducing the terms  $\alpha^2 = \gamma/k$  and  $\beta = 1/\alpha$ , the homogeneous solution yields

$$w(x) = C_1 e^{-\beta x} + C_2 e^{\beta x} \quad (9)$$

In the solution for large positive values of  $x$  in (9), the term with the coefficient  $C_1$  represents the decreasing displacement due to the influence of the load. The solution for positive  $x$  can be found, inserting the boundary condition  $w \rightarrow 0$  for  $x \rightarrow \infty$  in (9), i.e.  $w(x \rightarrow \infty) : C_1 e^{-\beta x} \rightarrow 0$  and  $C_2 e^{\beta x} \rightarrow \infty \Rightarrow C_2 = 0$ . The constant  $C_1$  can now be found, assuming that the difference in shear force to the right due to the point load in  $x = 0$  is equal to half the magnitude of the point load, giving the relations:  $\Delta T = P/2$ ,  $\Delta T = \gamma \Delta w' = \Delta T = \gamma w'(0)$  and  $w'(0) = -\beta C_1 e^{-\beta \cdot 0} = -\beta C_1$ . Combining these relations and applying the term  $\alpha^2 = \gamma/k$ , the solution for a point load is given as

$$w_p(x) = \frac{P}{2k\alpha} e^{-\beta x} \quad (10)$$

Using the superposition technique, (10) can be integrated to obtain expressions for the surface displacements for a uniformly distributed load shown in Figure 4(b), given as

$$w_q(x) = \frac{q}{2k} \left[ 2 - e^{-\beta(x+a)} - e^{-\beta(a-x)} \right] \quad \text{for } x \leq |a| \quad (11a)$$

$$w_q(x) = -\frac{q}{2k} \left[ e^{-\beta(x+a)} - e^{-\beta(a-x)} \right] \quad \text{for } x \geq |a| \quad (11b)$$

where  $x \leq |a|$  and  $x \geq |a|$  symbolise if the displacement is calculated inside or outside the loaded area, respectively.

### 2.2.2. Calibration of spring parameters

In order to obtain the necessary foundation model parameters, this study presents a simple methodology, combining the two-parameter model presented in Section 2.2.1, and the elastic continuum theory. The problem of the elastic stress field within a semi-infinite medium loaded by a point load has been solved by Flamant (1892) using Boussinesq's solution (Timoshenko and Goodier 1951). The surface displacement in the vertical direction can be written as

$$w_p(x) = \frac{2P}{\pi E} \ln \left( \frac{d}{|x|} \right) - \frac{(1-\nu)P}{\pi E} \quad (12)$$

where  $P$  is the point load,  $E = \frac{E_s}{(1-\nu_s^2)}$  and  $\nu = \frac{\nu_s}{(1-\nu_s)}$  are the Young's modulus and Poisson's ratio of the soil foundation, respectively,  $|x|$  is the numerical value of  $x$  (distance from the loaded point) and  $d$  is a rigid body constant found from assuming zero vertical displacements at a distance  $x = d$ .

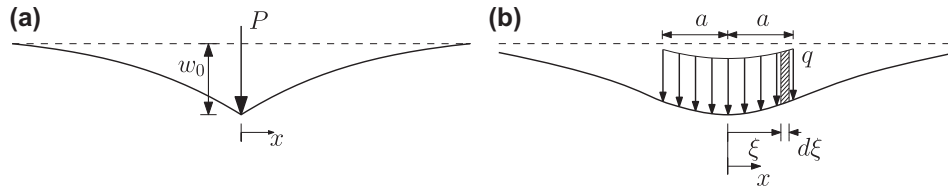


Figure 4. Sketch of elastic isotropic continuum foundation subjected to (a) a point load  $P$  and (b) a distributed load  $q$ .

Using the superposition technique, (12) can be integrated to obtain expressions for the surface displacements for a uniformly distributed load, given as

$$w_q(x) = -\frac{2q}{\pi E} \left[ (x-a) \ln \left( \frac{d}{|a-x|} \right) + (-a-x) \ln \left( \frac{d}{|x+a|} \right) + a(\nu-1) \right] \text{ for } x \leq |a| \quad (13a)$$

$$w_q(x) = -\frac{2q}{\pi E} \left[ (x-a) \ln \left( -\frac{d}{a-x} \right) + (-a-x) \ln \left( \frac{d}{|x+a|} \right) + a(\nu-1) \right] \text{ for } x \geq |a| \quad (13b)$$

where  $x \leq |a|$  and  $x \geq |a|$  symbolise if the displacement is calculated inside or outside the loaded area, respectively.

In the present study, the response of the slab and the influence of model parameters on the crack initiation and propagation are of primary interest. In this aspect, the vertical displacements and the curvature of the foundation are important features due to localisation of cracks and the increasing soil stresses near the crack front during progressive cracking.

In order to realistically capture the response of an elastic continuum, it is here proposed to calibrate the model analytically, combining these measures at different positions below the slab, i.e. the vertical displacement at the centre of the loaded area  $w(0)$ , the vertical displacement at the edge of the loaded area  $w(a)$  and the curvature at the centre of the loaded area  $w''(0)$ . Thus, the continuum model and the two-parameter model yield the exact same result at these positions for each measure. Two-and-two measures are combined, resulting in three different analytical calibration methods. The relevant expressions for the two model types, i.e.  $w(0)$ ,  $w(a)$  and  $w''(0)$ , are given in Appendices A.1 and A.2.

Table 1. Calibrated foundation model parameters  $k$  and  $\gamma$ .

Method	Criteria	$k$ (N/mm <sup>2</sup> )	$\gamma$ (N)	$R^2$ ( $x \leq 10$ m)	$R^2$ ( $x \leq 1.0$ m)
1	$w_0$ & $w_0''$	0.0076	$6.33 \cdot 10^7$	0.976	0.999
2	$w_0$ & $w_a$	0.0104	$3.95 \cdot 10^7$	0.928	1.000
3	$w_0''$ & $w_a$	0.0086	$6.18 \cdot 10^7$	0.978	0.992

The two-parameter model can now be calibrated; first, the theoretical displacements and curvature at the centre and displacements at the edge of the distributed load can be found from (A2a)–(A2c) and inserted in the relevant expressions for the two-parameter model, i.e. (A1a)–(A2c). A simple procedure is adopted here keeping one parameter constant, e.g. for calibration method no. 1, we have  $\gamma \rightarrow \gamma_{w_0} = \gamma_{w_0''}$ . The equation is then solved iteratively for  $k$  until  $k_{w_0} = k_{w_0''}$ .

In order to evaluate the influence of the different calibration methods, a uniformly distributed load over a strip length  $l$  of 2.0 m is applied directly on the soil surface comparing the two-parameter model and the elastic continuum model. Due to symmetry conditions, only half the loaded strip  $a = l/2$  is considered here. The resulting calibrated foundation model parameters can be found in Table 1.

Comparing the surface displacements for the continuum model and the three different two-parameter models, shown in Figure 5(a) and Table 1, it is observed that Calibration Method no. 1 gives a good overall fit. Method no. 2 gives the closest prediction of the surface displacements in the loaded region, i.e.  $x \leq 1.0$  m, whereas method no. 3 yields realistic results far from the loaded region. It is also observed from Figure 5(b) that increasing the load strip length results in a decreased

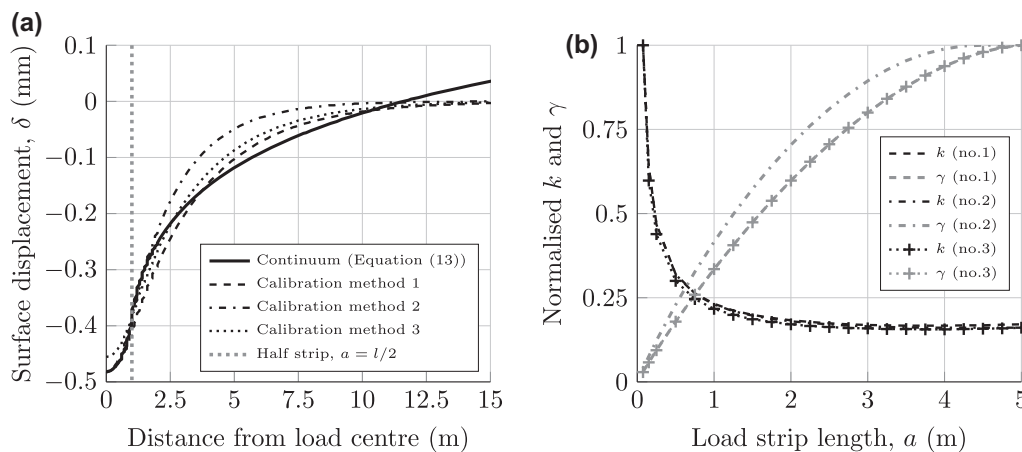
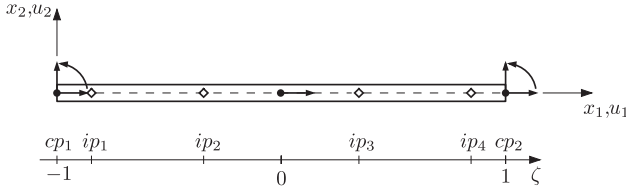


Figure 5. (a) Comparison of analytical and two-parameter foundation model for the three different calibration techniques (b) influence of half load strip length  $a$  on model parameters  $k$  and  $\gamma$  for a distributed load (normalised with respect to maximum value obtained in interval 0–5 m). Uniformly distributed load:  $q = 25,000$  N/m. Soil properties:  $E_s = 100$  MPa,  $\nu_s = 0.35$ ,  $t = 1$  m and  $d = 25$  m.



**Figure 6.** Plane beam element: Constitutive points ( $cp_i$ ) are located at endpoints, integration points ( $ip_i$ ) at Gauss points ( $i = 1, 4$ )  $\pm 0.861136312$  and ( $i = 2, 3$ )  $\pm 0.339981044$  (6th order polynomial function).

$k$ , stabilising at app.  $a = 1 - 2$  m, whereas  $\gamma$  increases with increasing load strip length, stabilising at app.  $a = 4 - 5$  m.

### 2.3. Implementation of hinge and foundation model into beam element

The hinge and two-parameter model are implemented following standard FE beam theory and procedures for building elements with non-linear material behaviour, see e.g. Cook *et al.* (2007). The expressions for the element stiffness matrix and equivalent nodal loads are based on the cubic displacement function and for direct incorporation of the foundation model. Thus, full contact is assumed between the beam and the foundation.

For the present study, a plane three-node beam element is chosen as shown in Figure 6. This element is capable of modelling quadratic variations of the axial displacements and cubic variations of the transverse displacements. The choice of element ensures that both generalised strains are interpolated linearly as opposed to a typical two-node beam element where constant normal strain is assumed.

The vector of generalised displacements of the beam,  $\mathbf{u}$ , holds the axial displacements  $u_1(x_1)$  and the transverse displacements  $u_2(x_2)$ . The interpolation of  $\mathbf{u}$  in the element is given by

$$\mathbf{u} = \begin{bmatrix} u_1 \\ u_2 \end{bmatrix} = \mathbf{N}\mathbf{v} \quad (14)$$

where  $\mathbf{N}$  is the displacement interpolation matrix and  $\mathbf{v}$  is the element dof vector. The interpolation functions are standard polynomial expressions. The vector of generalised strains,  $\boldsymbol{\varepsilon}$ , holds the linearised axial strain  $\varepsilon_0$  and the linearised curvature  $\kappa$ . The interpolation of  $\boldsymbol{\varepsilon}$  in the element is given by

$$\boldsymbol{\varepsilon} = \begin{bmatrix} \varepsilon_0 \\ \kappa \end{bmatrix} = \begin{bmatrix} \frac{du_1}{dx} \\ \frac{d^2u_2}{dx^2} \end{bmatrix} = \mathbf{B}\mathbf{v} \quad (15)$$

where  $\mathbf{B}$  is the strain interpolation matrix. The vector of generalised stresses,  $\boldsymbol{\sigma}$ , holds the sectional normal force  $N$  and the sectional moment  $M$ . In the element,  $\boldsymbol{\sigma}$  may be established applying (7a) and (7b) as

$$\boldsymbol{\sigma} = \boldsymbol{\sigma}(\boldsymbol{\varepsilon}) = \begin{bmatrix} N(\boldsymbol{\varepsilon}) \\ M(\boldsymbol{\varepsilon}) \end{bmatrix} \quad (16)$$

Based on the contribution to the variation in internal work  $\delta\Omega$ , from the beam and the two-parameter foundation, and the potential work of external forces  $\delta W$  from point and surface loads, the principle of virtual work for the system can be established

$$\int_V \delta \boldsymbol{\varepsilon}^T \boldsymbol{\sigma} + \delta \mathbf{u}^T \mathbf{k} \mathbf{u} + \delta \boldsymbol{\theta}^T \gamma \boldsymbol{\theta} dV = \int_S \delta \mathbf{u}^T \mathbf{f} dS + \sum_i \delta \mathbf{u}_i^T p_i \quad (17)$$

where  $V$  is the structural volume,  $S$  is the surface area,  $\delta \mathbf{u}$  and  $\delta \boldsymbol{\theta}$  are the displacement and rotational variations, respectively,  $\mathbf{f}$  is the surface traction vector,  $p_i$  is a concentrated (nodal) load and  $\delta \mathbf{u}_i$  is the associated (nodal) displacement variation. The contribution of the second parameter spring is here given on a general form considering  $\gamma$  as a rotational stiffness.

The beam element and two-parameter foundation contribution to the internal nodal force,  $\mathbf{q}$ , are then given by the expression

$$\mathbf{q} = \int_0^{L_e} \mathbf{B}^T \boldsymbol{\sigma} dx + \int_0^{L_e} \mathbf{N}^T k \mathbf{I} \mathbf{N} \mathbf{v}_e dx + \int_0^{L_e} \mathbf{G}^T \gamma \mathbf{I} \mathbf{G} \mathbf{v}_e dx \quad (18)$$

where  $L_e$  is the length of the element and  $\mathbf{v}_e$  is the global dof element displacements. The matrix  $\mathbf{I} = \begin{bmatrix} 0 & 0 \\ 0 & 1 \end{bmatrix}$  is used to omit axial terms in interpolation matrix  $\mathbf{N}$  and  $\mathbf{G}$ . The latter is given as  $\mathbf{G} = \mathbf{N}'$ .

The beam element and two-parameter foundation contribution to the tangential stiffness matrix,  $\mathbf{k}_t$ , are given by the expression

$$\mathbf{k}_t = \int_0^{L_e} \mathbf{B}^T \mathbf{D}_t \mathbf{B} dx + \int_0^{L_e} \mathbf{N}^T k \mathbf{I} \mathbf{N} dx + \int_0^{L_e} \mathbf{G}^T \gamma \mathbf{I} \mathbf{G} dx \quad (19)$$

The hinge tangent stiffness matrix,  $\mathbf{D}_t$ , is defined through

$$\begin{bmatrix} dN \\ dM \end{bmatrix} = \mathbf{D}_t \begin{bmatrix} d\varepsilon_0 \\ d\kappa \end{bmatrix}, \quad \text{where } \mathbf{D}_t = \begin{bmatrix} \frac{\partial N}{\partial \varepsilon_0} & \frac{\partial N}{\partial \kappa} \\ \frac{\partial M}{\partial \varepsilon_0} & \frac{\partial M}{\partial \kappa} \end{bmatrix} \quad (20)$$

Full derivation of the hinge tangent stiffness matrix,  $\mathbf{D}_t$ , can be found in Appendix 2.

The hinge model is implemented in a user-built FE code using the numerical computing package MATLAB. The functionality of the proposed hinge is tested for a simply supported beam under four point loadings and compared with experimental and numerical studies on cement-bound granular mixtures reported in Yeo (2008) and Skar and Poulsen (2015). Comparison of experimental and numerical results is evaluated in the view of load-displacement and load-crack mouth opening displacement (CMOD) behaviours, shown in Figure 7(a) and (b), respectively. The load-displacement response is given as the displacement under the loaded point, or so-called load line displacement (LLD).

It is observed from Figure 7 that there is good agreement between the proposed hinge model and experimental and numerical results reported in the literature. The difference between numerical models, i.e. the cohesive zone model (CZM) and the cracked-hinge model (FE hinge), is mainly related to the pre-peak behaviour. Whereas the hinge model behaves perfectly elastic up to initiation of cracking (load level of app. 3.5 kN), the CZM incorporates a small error in crack-opening displacements related to the penalty stiffness. This error is best exemplified in Figure 7(b), observing that the crack-opening in the CZM

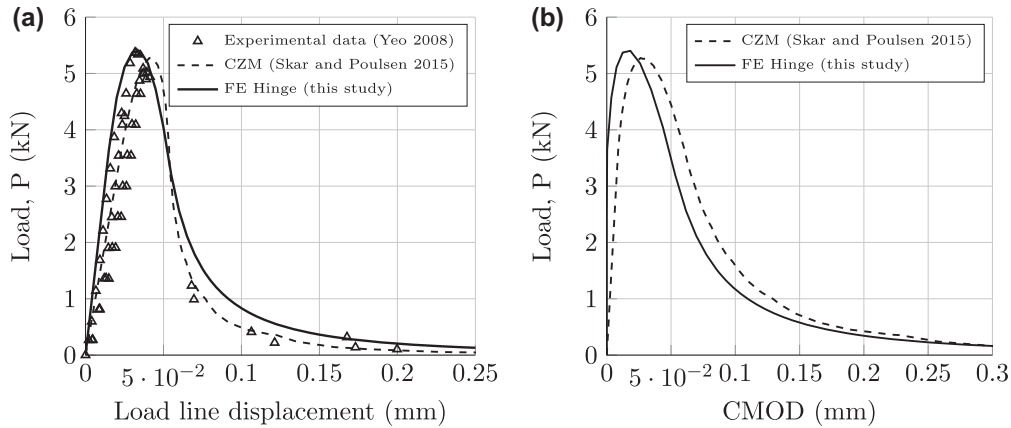


**Figure 7.** Comparison between the proposed hinge and experimental and numerical results reported in Yeo (2008) and Skar and Poulsen (2015), respectively: (a) Load–displacement response (b) numerical Load–CMOD response. Beam geometry ( $L/h/t$ ):  $300 \times 100 \times 100 \text{ mm}^3$ . Element size  $9.375 \text{ mm}$ . Load positions:  $L/3, 2L/3$ . Mechanical properties:  $E_c = 12,760 \text{ MPa}$ ,  $\nu = 0.2$ ,  $f_t = 1.0 \text{ MPa}$ ,  $G_F = 0.028 \text{ N/mm}$ .

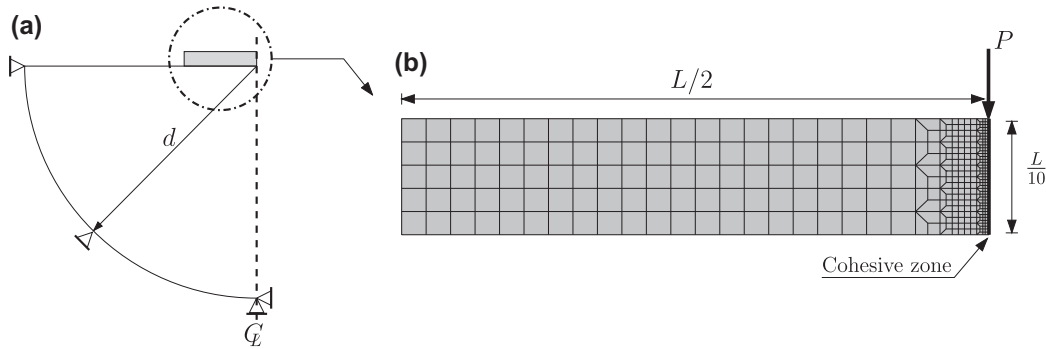


**Figure 8.** (a) Overview of model geometry and boundary conditions for the standard cemented slab on elastic solid foundation in ABAQUS ('CZM slab' model). (b) close-up of the slab region showing the cohesive zone mesh.

**Table 2.** Material properties for single cement-bound granular mixture slab on elastic foundation.

Material	$E_c/E_s$ (MPa)	$\nu$ (-)	$f_t$ (MPa)	$G_F$ (N/mm)	$k$ (N/mm <sup>2</sup> )	$\gamma$ (N)	$d$ (m)
CBGM	15,000	0.20	0.80	0.035	–	–	–
Soil	100	0.35	–	–	0.0076	$6.33 \cdot 10^7$	25

evolves from the beginning of the analysis and thus resulting in a more flexible behaviour of the beam. Increasing penalty stiffness reduces this error; however, very high levels of penalty stiffness result in ill-conditioned stiffness matrix and thus slow convergence and abort simulations. This problem is avoided applying the finite element hinge, resulting in a more robust model and stable simulations.

## 2.4. Continuum model, solution technique and numerical characteristics

### 2.4.1. CZM resting on elastic medium

In order to evaluate the hinge slab model and to investigate the influence of different modelling techniques for slab–soil interaction in concrete and composite pavement systems, a model representing the full continuum model is developed. A simplified two-layer model is considered: a single slab, with standard dimensions ( $L/h$ ) of  $4 \times 0.4 \text{ m}^2$ , constructed over soil

**Table 3.** Solution technique and standard model parameters applied in the present study.

Solver	Model parameters		
Technique	N-R	Cohesive zone width, $T_0$ (mm)	0.01
Initial increment	0.001	Viscous damping parameter, $\mu$ (-)	$1 \times 10^{-5}$
Maximum increment size	0.01	Bulk elements (elastic)	CPE4 (2-D)
Minimum increment size	$1 \times 10^{-9}$	Cohesive zone mesh (mm)	10

foundation with rigid body constraint,  $d = 25 \text{ m}$ , representing the semi-infinite elastic medium, as shown in the sketch in Figure 8(a). The slab is in subsequent sections referred to as the 'CZM slab'.

The CZM slab is modelled with 2D plain strain elements (CPE4) in ABAQUS. A total of 1400 elements are used to represent the elastic material, separated by predetermined contact surfaces, representing the cohesive zone (10 mm size elements), in the vertical plane at the mid-beam position. The subgrade soil is modelled with a total of 6000 elements (CPE4). A close-up of the mesh in the slab region is shown in Figure 8(b) and standard mechanical properties are given in Table 2.

### 2.4.2. Solution technique and numerical characteristics

To increase the efficiency of numerical simulations, a conventional Newton–Raphson (N-R) method is implemented

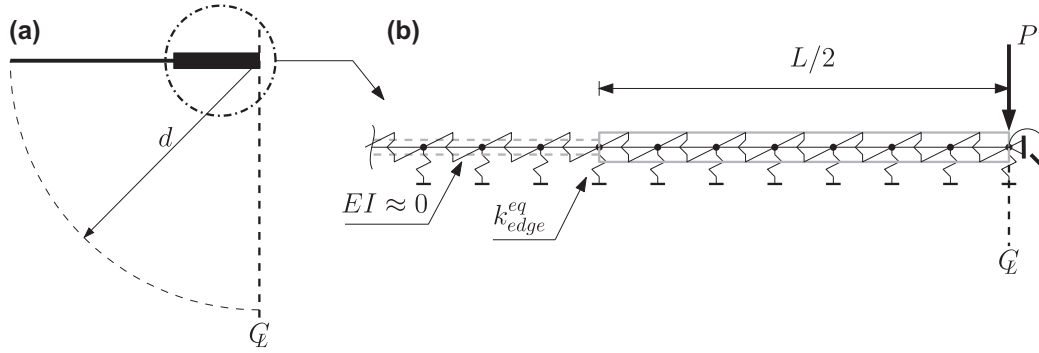


**Figure 9.** (a) Overview of model geometry and boundary conditions for the standard cemented slab on elastic solid foundation in ABAQUS ('CZM slab' model). (b) Model geometry, boundary conditions for the proposed cracked-hinge model resting on two-parameter foundation ('hinge slab' model).

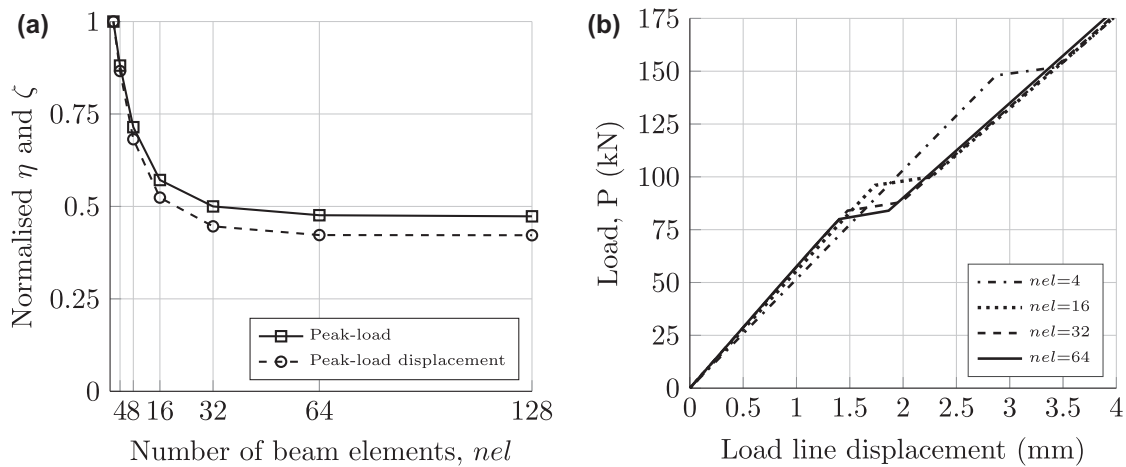


**Figure 10.** Convergence test: (a) Number of beam elements,  $nel$ : 2–128 (element size,  $elsz$ : 0.5–0.015625) vs. the normalised first peak load  $\eta$  and peak load displacements  $\zeta$  applying foundation parameters for calibration method no. 1. (b) Load–displacement response.

extended to handle displacement control, see e.g. Batoz and Dhett (1979). The solver implemented sufficiently describes both pre- and post-peak behaviour, whereas the potential snap-back load–displacement response is ignored.

Similarly the N–R method is selected for the purpose of analysis in ABAQUS. Based on preliminary convergence and sensitivity studies, solution technique and standard model parameters selected for the present study are listed in Table 3.

### 3. Numerical model of a single hinge slab

#### 3.1. Model geometry and analysis results

Consider a single hinge slab, shown in Figure 9, consisting of cement-bound granular mixture with standard dimensions ( $L/h$ ) of  $4 \times 0.4 \text{ m}^2$  supported by a two-parameter foundation, representing the semi-infinite elastic medium, and loaded by a concentrated force at mid-span position. The soil adjacent to the slab can be modelled by extending the beam elements outside the slab to the length  $d$ , assigning a bending stiffness  $EI$  close to zero. Alternatively, an equivalent spring can be implemented at slab ends, representing the soil adjacent to the slab, i.e.  $k_{edge}^{eq} = k \cdot \alpha$ . Standard mechanical properties given in Table 2 are applied.

Convergence test of the model is evaluated plotting the normalised peak load  $\eta$  and peak load displacements  $\zeta$  for different beam mesh densities,  $nel$  : 2 – 128, shown in Figure 10. It is observed that sufficient accuracy can be obtained with 64 elements; however, little is gained by increasing the number of elements from 32 to 64. Element size of 0.1 m ( $nel = 40$ ) is selected in subsequent analysis. Typical load–displacement response is shown in Figure 10(b).

In order to evaluate the fracture behaviour of the hinge slab model, the load–crack mouth opening and load–crack length curve are plotted, shown in Figure 11(a) and (b), respectively. To visualise the influence of the second parameter and to compare the two modelling techniques, the response for both hinge and CZM slab resting on a Winkler foundation is shown for reference. Standard mechanical properties given in Table 2 are applied.

It is observed from Figure 11(a) and (b) that reasonably good agreement between the hinge and CZM slab models can be obtained. Both models reflect the influence of the continuity in the soil comparing the two foundation types. It can also be shown that a closer prediction of the first peak load can be obtained applying an empirical transfer function for converting the elastic soil properties to an apparent Winkler stiffness  $k^*$  (FAA 2009). However, the post-peak response resembles that

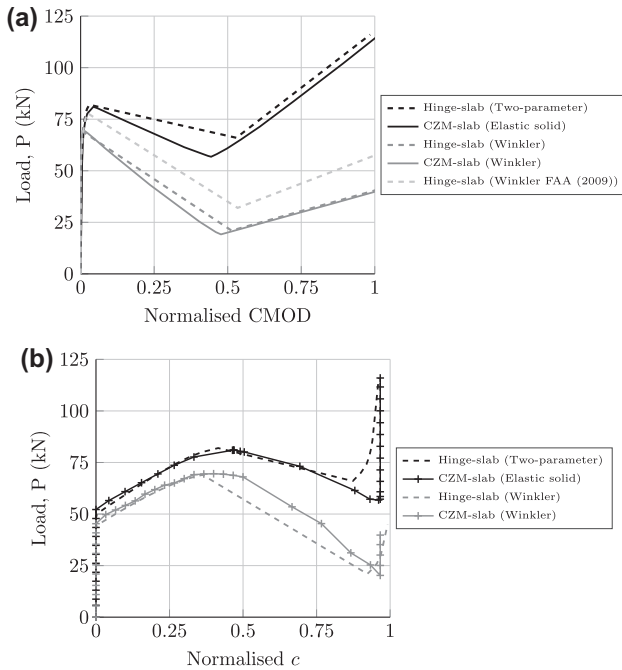


**Figure 11.** Comparing the structural response and fracture behaviour of the hinge slab vs. the CZM slab model in ABAQUS; (a) load-CMOD curve and (b) load-crack length curve, where the crack length in the CZM slab model is taken as the progressive depth of damage initiation in the cohesive zone.

of the analytical Winkler foundation type due to the lack of continuity between springs.

The difference in first peak load and peak load displacement is app.  $\pm 1\%$  for the two model types. The two-parameter slab hinge model slightly overestimates the post-peak residual stiffness compared to the CZM slab model. Close to perfect fit is obtained between the two modelling techniques applying only a Winkler foundation as the supporting medium. It is also observed that the load level at unloading is higher for the hinge slab model compared to the CZM slab model. This tendency is observed for both foundation model types, and can partly be regarded as an effect of the difference in modelling technique. However, this difference is also related to the foundation type and the contact behaviour applied. This will be further discussed in the section below.

### 3.2. Comparison of numerical modelling techniques

A fundamental difference in the methodology between the CZM slab model and the hinge model is that the CZM slab model only considers one discrete crack at mid-span position, whereas the effective stiffness concept adopted in the hinge model allows for multiple cracks along the beam. For the specific case, a cracked zone of app. 1.0 m at the centre of the slab has initiated and opened at first peak load, shown in Figure 12(a). Then, the crack at mid-span progresses rapidly, causing the neighbouring cracks to close.

Moreover, in the hinge model presented, increasing or decreasing the hinge rotation is modelled by the same equilibrium path. Thus, the hinge model does not have a unique unloading branch that models the closure of a previously opened crack.

The cracks outside mid-span position are small ( $<1\%$ ) and do not influence the solution in the specific cases studied here.

A more significant influence on the model response can be found by studying the different soil models. Although the two-parameter model possess some of the characteristic features of continuous elastic solids, it is a simplification which cannot capture all complexities. Special care should be taken when selecting a representative load strip length for calibration of model parameters. This is exemplified plotting the vertical soil pressure below cemented slabs with different slenderness ratios (length/thickness ratio), shown in Figure 13.

The pressure will initially be distributed over the total slab length, as observed from Figure 13. As cracking is initiated and cracks propagate, there will be only minor changes in the overall vertical pressure profile, ignoring minor stress intensities below cracks. After crack propagation to a certain depth, the structure becomes unstable, resulting in unloading on the load-CMOD curve, see Figure 12(b). This further results in a significant change in the vertical soil pressure and stresses localise around the open cracks, in this case at the mid-span position. Moreover, a variation in vertical pressure, and especially the vertical reaction pressure along slab edges comparing different slab sizes, is expected. The soil pressure under short thick slabs will resemble the stress distribution under a stiff plate, whereas the vertical reaction pressure along slab edges for larger size and slender slabs will be small.

In order to capture both pre- and post-peak vertical pressure distributions in the two-parameter model considering typical slab lengths and thicknesses of app. 2.0-5.0 m and 0.15-0.45 m, respectively, a fixed load strip length of 1.0 m is applied for calibration of foundation model parameters and is recommended for the present problem.

The theoretical pressure distribution between the slab and the supporting elastic medium tends towards infinity at the perimeter; this of course, cannot occur in real soils. However, for cohesive soils, the actual stress distribution will resemble the theoretical distribution. For granular soils, stresses at the edges will be small because the bearing capacity at the surface of an unconfined granular material is small. In order to capture this behaviour, the methodology proposed could be extended using a 'Modified Pasternak model' consisting of two layers of vertical springs as proposed by Kerr (1964) allowing the slab to 'sink' into the supporting layer.

## 4. Sensitivity studies

### 4.1. Effect of slab thickness and soil stiffness

In linear elastic analysis of pavement structures, the slab or layer thickness is increased for increasing design loads, to ensure both a relatively constant stress level in the soil foundation, avoiding any plastic deformation. However, as observed in Figure 14, this assumption is only valid as long as cracks are small as the thickness of the cemented slab has significant influence on the peak load, but little influence on the post-peak response of the structure.

The stiffness and peak load of the structure increase with increasing thickness up to unloading. Then, the structural response is mainly influenced by the stiffness of the soil foundation, as shown in Figure 15.

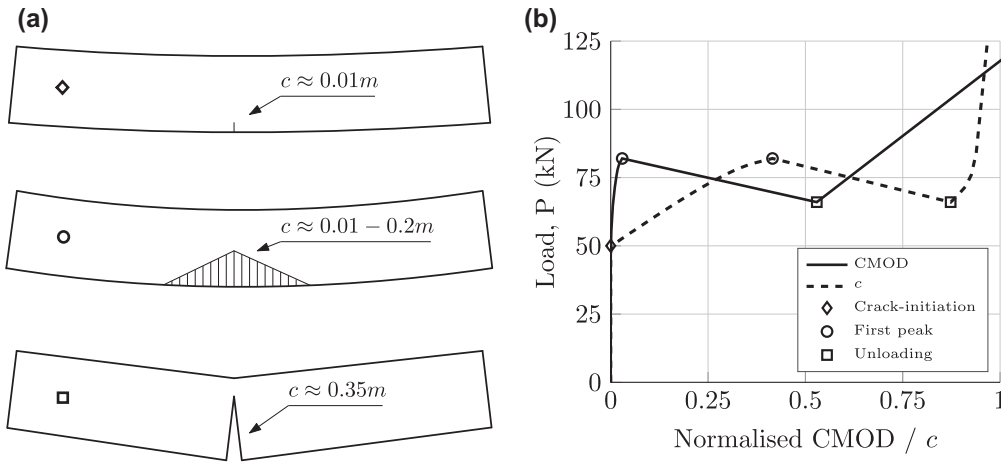


**Figure 12.** Development of crack width in slab for point of interest for the two-parameter model; (a) deformation of slab and crack lengths at points of interest and (b) points of interest plotted on the normalised load–CMOD and load–crack length curve.

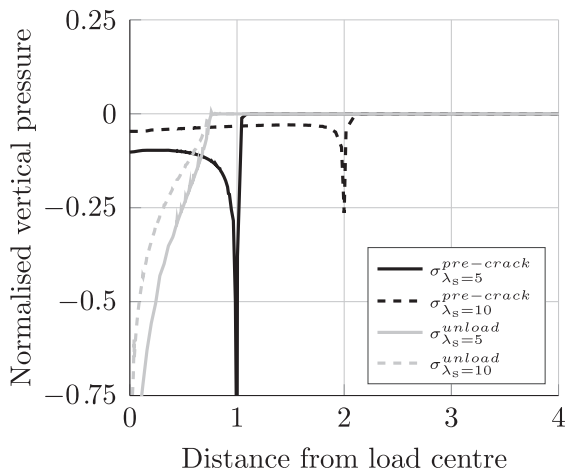


**Figure 13.** Vertical soil pressure of elastic solid under cemented slabs with slenderness ratio  $\lambda_s = 5$  and 10 before and after development of a single open crack below the loaded point, i.e. before ‘first peak’ and after ‘unloading’ in Figure 12(b).

As expected, increasing stiffness of the soil results in increasing peak load and post-peak stiffness, as shown in Figure 15. It can also be concluded that the soil stiffness has a more significant influence on the peak load than the thickness of slabs. The influence of slab size is found to be small as only crack propagation in one direction is considered here.

#### 4.2. Effect of tensile strength and fracture energy

Considering a simple linear softening law, it is obvious that the two main material parameters influencing the fracture process of the quasi-brittle material are the tensile strength and the fracture energy. Both tensile strength and fracture energy influence the peak load and peak load displacement, as shown in Figure 16(a) and (b), respectively.

It should be noted that the influence of tensile strength will be reduced compared to the fracture energy in three-dimensional simulations, as the out-of-plane crack propagation significantly influences the load–displacement response

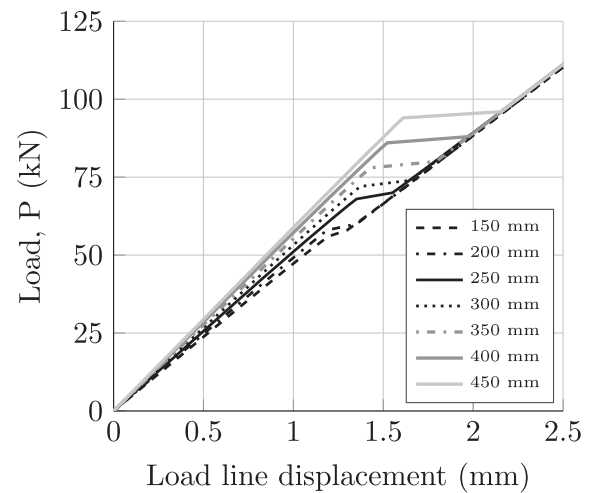


**Figure 14.** Influence of slab thickness on the load–displacement response. Thickness varying from 150 to 450 mm keeping length constant (3 m).

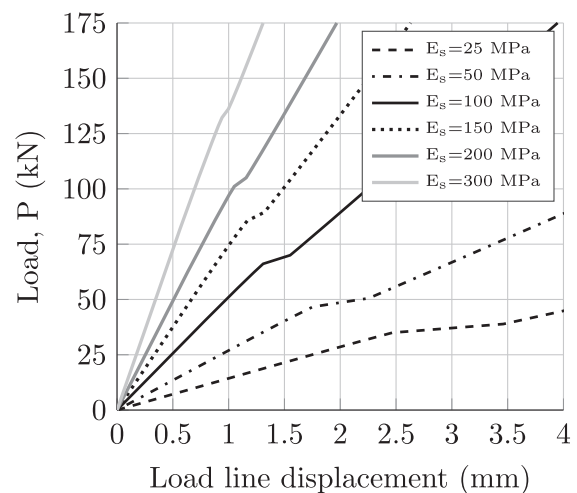


**Figure 15.** Influence of soil stiffness on the load–displacement response. Young’s modulus  $E_s$  varying from 25 to 300 MPa.

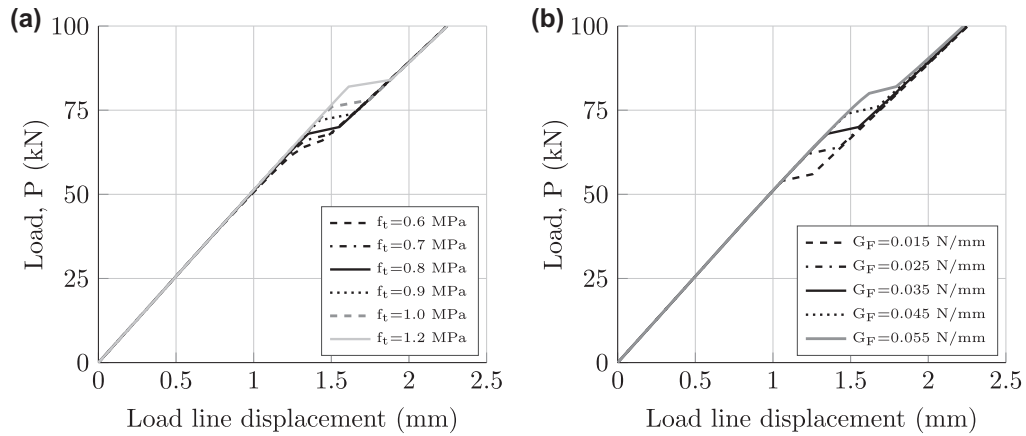


Figure 16. Influence of fracture properties on the load–displacement response: (a) tensile strength  $f_t$  varying from 0.6 to 1.2 MPa and (b) fracture energy  $G_F$  varying from 0.015 N/mm to 0.055 N/mm.

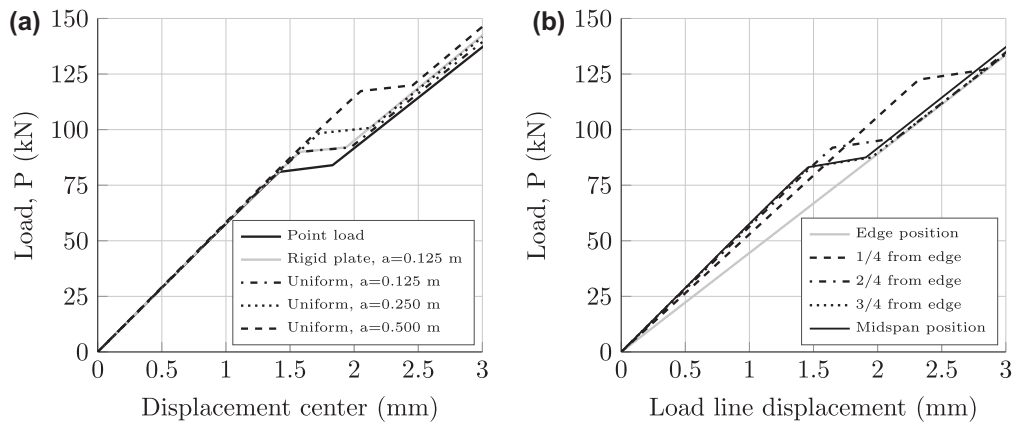


Figure 17. Influence of load configuration and position on load–displacement response: (a) typical load configurations, e.g. rigid and uniformly distributed loads with varying load strip length  $a$  and (b) slab loaded at edge, mid-span and intermediate positions.

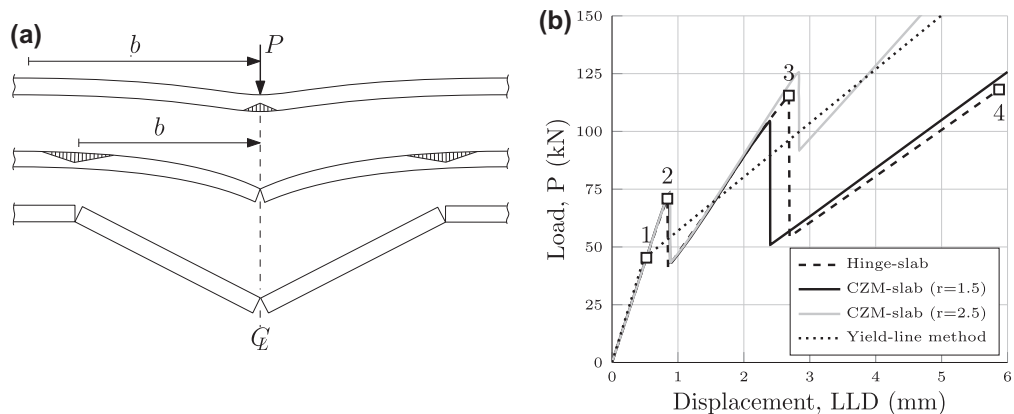
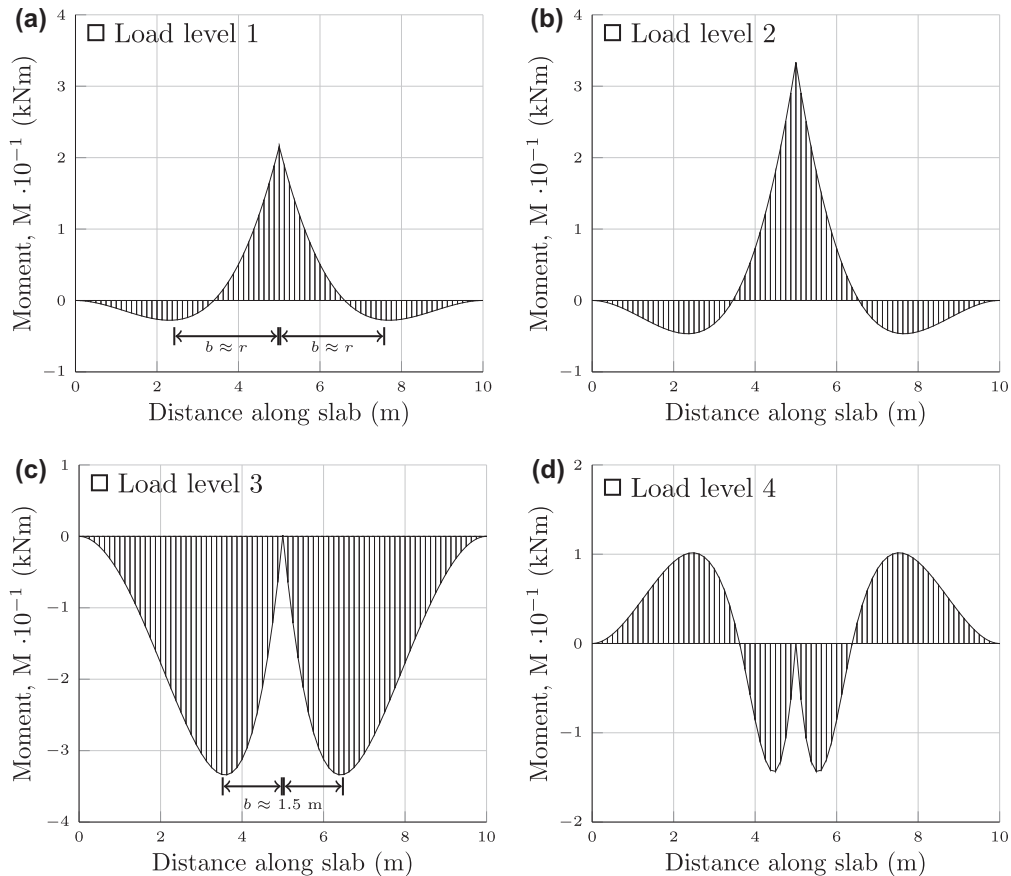


Figure 18. Comparison between modelling techniques for infinite slab: (a) Deformation of the slab during loading: before first peak, after first peak and after second peak. (b) CZM slab (solid line), hinge slab models (dashed line) and the yield-line method (dotted line) reported in Baumann and Weisgerber (1983).



**Figure 19.** Predicting distance between cracks showing the moment in the hinge slab model at four different phases: (a) crack initiation, (b) first peak, (c) second peak and (d) after full crack propagation of top-down cracks, also visualising the distance between cracks equivalent to  $r$  in the yield-line method.

(Gaedicke and Roesler 2009, Aure and Ioannides 2012, Skar and Poulsen 2015).

### 4.3. Effect of load configuration and position

Realistic concrete and composite pavement systems are subjected to different loading conditions. In order to demonstrate the applicability of the proposed method to evaluate different load cases, the load–displacement response for typical load configurations and positions is plotted, shown in Figure 17.

It is observed from Figure 17(a) that increasing load strip length results in increasing peak load, as expected. For the rigid plate load, modelled as two point loads at each end of the loaded strip, one crack develops at each edge. However, for the two-dimensional problem considered here, this has little influence on the structural response compared to a uniformly distributed load. From Figure 17(b), it is observed that the peak load increases for increasing distance from mid-span position, whereas the stiffness decreases. Loading at mid-span and intermediate positions results in one crack opening and progressing after the first peak, whereas no cracks develop in case of edge loading.

## 5. Structural example

In order to demonstrate the applicability of the numerical hinge to predict a realistic crack pattern, an infinite slab ( $h = 0.4$  m)

resting on Winklers foundation ( $k = 0.0233$  MPa/mm) and loaded by a concentrated force at mid-span position is considered. Slab displacements and internal forces decline relatively fast to zero as the distance from the load increases. Accordingly, a finite slab of 10 m ( $nel = 100$ ) may be replacing the infinite beam. Standard material properties for the cemented material given in Table 2 are applied.

The numerical results are compared to the yield-line theory following the methodology proposed by Baumann and Weisgerber (1983). The deformation of the slab during loading, i.e. before first peak, before second peak and after the second peak, is shown in Figure 18(a). Load–displacement curves for the three models are plotted in Figure 18(b).

It is observed from Figure 18(b) that the first peak in the CZM slab model and the hinge slab model is app. 73 and 71 kN, respectively. Moreover, it is observed that the kink point on the yield-line curve is app. 45 kN, complying well with the results reported by Meda (2003). Moreover, it is found that the distance between yield-lines  $r = 2.534$  m in the yield-line method is approximately equal to the distance,  $b$ , from the negative peak moments to the crack at mid-span in the hinge slab model at crack initiation (load level 1), shown in Figure 19(a). Then, according to the CZM slab and hinge slab models, the load continues to increase as the crack propagates before reaching the ultimate moment capacity of app. 33.3 kNm (load level 2), shown in Figure 19(b).

The crack at mid-span then unloads, before the load continues to increase, resulting in two top-down cracks initiating app.  $\pm 1.5$  m from the mid-span position. Then, these cracks grow rapidly to the negative ultimate moment capacity of app.  $-33.3$  kNm (load level 3), shown in Figure 19(c), resulting in the second peak on the load–displacement curve. Finally, the post-peak residual stiffness of the structure is reached (load level 4) with the moment distribution shown in Figure 19(d).

The distance between cohesive zones in the CZM slab model is set to 1.5 m based on simulations with the hinge slab model. This results in a good fit between the two methods as shown in Figure 18 (b). The responses of the two methods are identical up to the second peak of the CZM slab model. Then, the load in the hinge slab model continues to increase due to the stiffness and stress redistribution in the hinge slab. The second peak in the models occurs at app. 105 and 115 kN, respectively. The difference in response between models is small up to first peak as cracks localise to one crack below the loaded point. Then, top-down cracks at a distance  $b$  develop; however, these are smeared over a larger area, resulting in evolving stress redistribution in the slab during crack propagation. This phenomena cannot be captured by the CZM slab model. Thus, a lower second peak load is predicted with the CZM slab model. Increasing the length between cohesive zones in the CZM model would result in increasing second-peak and post-peak stiffness.

The present example highlights the practical use of the model Proposed: the hinge slab being able to predict the stress redistribution and stiffness during crack development. This results in a precise prediction of the crack-opening and the distance between cracks that finally localise and propagate through the thickness of the slab.

## 6. Conclusion

The use of a cohesive cracked-hinge model for simulating the fracture in one-way slab on grade structures has been investigated showing good performance.

Comparing numerical and experimental results for four point bending beam tests show that good agreement is obtained with the hinge model. It is also found that good agreement is obtained for both structural and fracture behaviours of slab on grade structures, comparing the hinge model with the more conventional cohesive zone model. The adaptive hinge proved to adequately predict the distance between cracks compared to the yield-line theory. Moreover, peak loads and structural response comply well with other results reported in the literature. The hinge model has the advantage that it is numerically robust, resulting in fast simulations and few convergence issues.

It can be shown that the two-parameter foundation model and the calibration methodology proposed are efficient tools which realistically capture the response of the elastic medium below the slab. The calibration methodology is consistent and model parameters are determined on a rational basis. Moreover, the foundation model applied is applicable for implementation in commercial codes applying discrete spring elements and/or connectors, making the methodology an attractive alternative for design engineers.

Slab thickness and soil stiffness proved to be important parameters. The peak load is highly influenced by thickness of the

slab, whereas the soil stiffness proved to be a main controlling parameter of both pre- and post-peak response of the structure. Furthermore, it can be concluded that the fracture process is more affected by the fracture energy than by the tensile strength.

The present paper demonstrates the use of a cohesive crack-hinge model resting on a two-parameter foundation to describe the fracture behaviour of cemented slab on grade structures. Although a simplified two-dimensional problem is investigated here, the results obtained are encouraging, showing that the methodology is applicable for practical use. Moreover, a general and consistent format is applied making the methodology well suited for further development.

## Disclosure statement

No potential conflict of interest was reported by the authors.

## Funding

This work was supported by COWIfonden [grant number C-123.03] and Innovation Fund Denmark [grant number 1355-00060].

## ORCID

Asmus Skar  <http://orcid.org/0000-0003-3176-791X>

John Forbes Olesen  <http://orcid.org/0000-0001-6695-7719>

## References

- ABAQUS, 2013. *Analysis user's manual, Version 6.13-1* [online], Available from: <http://www.3ds.com>
- Aure, T.W. and Ioannides, A.M., 2012. Numerical analysis of fracture process in pavement slabs. *Canadian Journal of Civil Engineering*, 39 (5), 506–514.
- Aure, T.W. and Ioannides, A.M., 2015. Fracture analysis of aggregate interlock jointed slabs-on-grade. *Construction and Building Materials*, 77, 340–348.
- Batoz, J.L. and Dhatt, G., 1979. Incremental displacement algorithms for nonlinear problems. *International Journal for Numerical Methods in Engineering*, 14 (8), 1262–1267.
- Baumann, R.A. and Weisgerber, F.E., 1983. Yield-line analysis of slabs-on-grade. *Journal of Structural Engineering*, 109 (7), 1553–1568.
- Buratti, N., Mazzotti, C., and Savoia, M., 2011. Post-cracking behaviour of steel and macro-synthetic fibre-reinforced concretes. *Construction and Building Materials*, 25 (5), 2713–2722.
- Carpinteri, A. and Corrado, M., 2011. Upper and lower bounds for structural design of RC members with ductile response. *Engineering Structures*, 33 (12), 3432–3441.
- Castel, A., Vidal, T., and François, R., 2011. Finite-element modeling to calculate the overall stiffness of cracked reinforced concrete beams. *Journal of Structural Engineering*, 138 (7), 889–898.
- Colasanti, R.J. and Horvath, J.S., 2010. Practical subgrade model for improved soil-structure interaction analysis: software implementation. *Practice Periodical on Structural Design and Construction*, 15 (4), 278–286.
- Cook, R.D., et al., 2007. *Concepts and applications of finite element analysis*. University of Wisconsin, Madison, John Wiley & Sons.
- Evangelista, Francisco J., Roesler, J.R. and Proença, S.P., 2013. Three-dimensional cohesive zone model for fracture of cementitious materials based on the thermodynamics of irreversible processes. *Engineering Fracture Mechanics*, 97, 261–280.
- FAA, 2009. *Advisory Circular (AC) 150/5320-6E* [online], [www.faa.gov](http://www.faa.gov)
- Filonenko-Borodich, M., 1940. Some approximate theories of the elastic foundation. *Uchenyie Zapiski Moskovskogo Gosudarstvennogo Universiteta Mekhanika*, 46, 3–18.

- Flamant, A., 1892. On the distribution of pressures in a transversely loaded rectangular solid. *Comptes Rendus*, 114, 1465–1468.
- Gaedicke, C. and Roesler, J., 2009. *Fracture-based method to determine the flexural load capacity of concrete slabs*. FAA COE Rep., (31).
- Gaedicke, C., Roesler, J., and Evangelista, F., 2012. Three-dimensional cohesive crack model prediction of the flexural capacity of concrete slabs on soil. *Engineering Fracture Mechanics*, 94, 1–12.
- Hetényi, M., 1946. *Beams on elastic foundation: theory with applications in the fields of civil and mechanical engineering*. Ann Arbor, Michigan, University of Michigan.
- Hetenyi, M., 1966. Beams and plates on elastic foundations and related problems. *Applied Mechanics Reviews*, 19 (2), 95–102.
- Hillerborg, A., Modéer, M., and Petersson, P.E., 1976. Analysis of crack formation and crack growth in concrete by means of fracture mechanics and finite elements. *Cement and Concrete Research*, 6 (6), 773–781.
- Horvath, J., 2002. *Soil-structure interaction research project: basic SSI concepts and applications overview*. Bronx, NY: Manhattan College School of Engineering.
- Ioannides, A.M., 2006. Concrete pavement analysis: the first eighty years. *International Journal of Pavement Engineering*, 7 (4), 233–249.
- Ioannides, A.M., Peng, J., and Swindler Jr, J.R., 2006. ABAQUS model for PCC slab cracking. *International Journal of Pavement Engineering*, 7 (4), 311–321.
- Ioannides, A., Thompson, M., and Barenberg, E., 1985. Finite element analysis of slabs-on-grade using a variety of support models. In: *Third International Conference on Concrete Pavement Design and Rehabilitation*, Vol. 1, Urbana, Illinois.
- Kerr, A.D., 1964. Elastic and viscoelastic foundation models. *Journal of Applied Mechanics*, 31 (3), 491–498.
- Kerr, A.D., 1965. A study of a new foundation model. *Acta Mechanica*, 1 (2), 135–147.
- Khazanovich, L., 2003. Finite element analysis of curling of slabs on Pasternak foundation. In: *16th ASCE Engineering Mechanics Conference*, July, University of Washington, Seattle, 16–18.
- Khazanovich, L. and Ioannides, A.M., 1993. Finite element analysis of slabs-on-grade using higher order subgrade soil models. In: *Airport Pavement Innovations Theory to Practice*, 8–10 September 1993, Vicksburg, MS, USA.
- Khazanovich, L. and Ioannides, A.M., 1994. Structural analysis of unbonded concrete overlays under wheel and environmental loads. *Transportation Research Record*, 1449, 174–181.
- Kwak, H.G. and Kim, S.P., 2002. Nonlinear analysis of RC beams based on moment-curvature relation. *Computers & Structures*, 80 (7), 615–628.
- Kwak, H.G. and Kim, S.P., 2010. Simplified monotonic moment-curvature relation considering fixed-end rotation and axial force effect. *Engineering Structures*, 32 (1), 69–79.
- Loof, H., 1965. The theory of the coupled spring foundation as applied to the investigation of structures supported on soil. *HERON*, 13 (3), 29–49.
- Meda, A., 2003. Design methods for slabs on grade in fiber reinforced concrete. In: *System-based Vision for Strategic and Creative Design*, Vols. 1–3, Rome, Italy, 1413–1418.
- Meda, A., Plizzari, G.A., and Riva, P., 2004. Fracture behavior of SFRC slabs on grade. *Materials and Structures*, 37 (270), 405–411.
- Murthy, A.R., et al., 2013. Bilinear tension softening diagrams of concrete mixes corresponding to their size-independent specific fracture energy. *Construction and Building Materials*, 47, 1160–1166.
- NCHRP, 2003. *Guide for mechanistic-empirical design of new and rehabilitated pavement structures: Structural response modeling of rigid pavements – Appendix QQ*. Washington, DC: National Cooperative Highway Research Program, Transportation Research Board, National Research Council.
- Olesen, J.F., 2001a. Cracks in reinforced FRC beams subject to bending and axial load. In: *Fracture mechanics of concrete structures*. Vols. 1 and 2, Cachan, France, 1027–1033.
- Olesen, J.F., 2001b. Fictitious crack propagation in fiber-reinforced concrete beams. *Journal of Engineering Mechanics*, 127 (3), 272–280.
- Olesen, J.F., Østergaard, L., and Stang, H., 2006. Nonlinear fracture mechanics and plasticity of the split cylinder test. *Materials and Structures*, 39 (4), 421–432.
- Olesen, J.F. and Poulsen, P.N., 2012. Modeling RC Beam Structures Based on Cracked Hinge Model and Finite Elements. Technical University of Denmark, DTU Civil Engineering.
- Pasternak, P., 1954. *On a new method of analysis of an elastic foundation by means of two constants* [Gosudarstvennoe Izdatelstvo Literaturi po Stroitelstvu I Arkhitekture]. Moscow: USSR.
- Reissner, E., 1958. A note on deflections of plates on a viscoelastic foundation. *Journal of Applied Mechanics*, 25 (1), 144–145.
- Skar, A. and Poulsen, P.N., 2015. 3-D cohesive finite element model for application in structural analysis of heavy duty composite pavements. *Construction and Building Materials*, 101 (Part 1), 417–431.
- Skar, A., Poulsen, P.N., and Olesen, J.F., 2017. General cracked-hinge model for simulation of low-cycle damage in cemented beams on soil. *Engineering Fracture Mechanics*. doi:10.1016/j.engfracmech.2017.01.016.
- Timoshenko, S., and Goodier, J.N., 1951. *Theory of elasticity*. McGraw-Hill book Company, New York.
- Ulfkjær, J.P., Krenk, S. and Brincker, R., 1995. Analytical model for fictitious crack propagation in concrete beams. *Journal of Engineering Mechanics*, 121 (1), 7–15.
- Visintin, P., et al., 2012. A mechanics solution for hinges in RC beams with multiple cracks. *Engineering Structures*, 36, 61–69.
- Vlasov, V.Z., 1966. *Beams, plates and shells on elastic foundations*. Jerusalem: Israel Program for Scientific Translations.
- Walter, R., et al., 2005. Wedge splitting test for a steel-concrete interface. *Engineering Fracture Mechanics*, 72 (17), 2565–2583.
- Wardeh, G. and Ghorbel, E., 2015. Prediction of fracture parameters and strain-softening behavior of concrete: effect of frost action. *Materials and Structures*, 48 (1–2), 123–138.
- Winkler, E., 1868. *Die lehre von der elasticitaet und festigkeit* [Theory of Elasticity and Strength of Materials]. Prag: Verlag Dominicus.
- Yeo, R., 2008. *The development and evaluation of protocols for the laboratory characterisation of cemented materials*. AP-T101/08.
- Zokaei-Ashtiani, A., Carrasco, C., and Nazarian, S., 2014. Finite element modeling of slab-foundation interaction on rigid pavement applications. *Computers and Geotechnics*, 62, 118–127.
- Zokaei-Ashtiani, A., et al., 2015. Impact of different approaches to modelling rigid pavement base layers on slab curling stresses. *International Journal of Pavement Engineering*, 17 (10), 861–869.

## Appendix 1. Expressions for calibration of two-parameter model

### A.1. Two-parameter model

Expressions for points of interest for the two-parameter model can be found from (11b), i.e.

$$w(0) = \frac{q}{k} [1 - e^{-\beta a}] \quad (\text{A1a})$$

$$w(a) = \frac{q}{2k} [1 - e^{-2\beta a}] \quad (\text{A1b})$$

$$w''(0) = \frac{\beta^2 q}{k} [e^{-\beta a}] \quad (\text{A1c})$$

where  $w(0)$  is the vertical displacement at the centre of the loaded area,  $w(a)$  is the vertical displacement at the edge of the loaded area and  $w''(0)$  is the curvature at the centre of the loaded area.

### A.2. Elastic continuum model

Expressions for points of interest for the continuum model can be found from (13b), i.e.

$$w(0) = \frac{2qa}{\pi E} \left[ 2 \ln \left( \frac{d}{|a|} \right) + (1 - \nu) \right] \quad (\text{A2a})$$

$$w(a) = \frac{2qa}{\pi E} \left[ 2 \ln \left( \frac{d}{|2a|} \right) + (1 - \nu) \right] \quad (\text{A2b})$$

$$w''(0) = -\frac{4q}{\pi E a} \quad (\text{A2c})$$

where  $w(0)$  is the vertical displacement at the centre of the loaded area,  $w(a)$  is the vertical displacement at the edge of the loaded area and  $w''(0)$  is the curvature at the centre of the loaded area.

## Appendix 2. Derivation of hinge tangent stiffness matrix

For the linear elastic Phase 0, the hinge tangent stiffness matrix is given as

$$\mathbf{D}_t^0 = \begin{bmatrix} htE_c & 0 \\ 0 & \frac{1}{12}th^3E_c \end{bmatrix} \quad (\text{B1})$$

The constituents of the hinge tangent stiffness matrix in (20) are obtained from the sectional forces  $N$  and  $M$  in (7a) and (7b), respectively.

Utilising the following relations for the relevant part of the integral corresponding to  $0 < w \leq w_c$  yields

$$\frac{\partial \sigma_c}{\partial \bar{\epsilon}_0} = E_c \frac{as}{E_c + as}, \quad \frac{\partial \sigma_c}{\partial \bar{\kappa}} = E_c \frac{as}{E_c + as} \gamma \quad (\text{B2})$$

Here, the parameters  $\alpha = \frac{as}{E_c + as}$  and  $E_{cc} = E_c \alpha$  are introduced, where the latter represents the reduced stiffness of the cracked part of the hinge. The full hinge tangent stiffness matrix for Phases I and II can then be established

$$\begin{aligned} dN &= t \int_{-h/2}^{h/2-c} E_c (d\bar{\epsilon}_0 + d\bar{\kappa}y) dy + t \int_{h/2-c}^{h/2} E_{cc} (d\bar{\epsilon}_0 + d\bar{\kappa}y) dy \\ &= D_t(1,1) d\bar{\epsilon}_0 + D_t(1,2) d\bar{\kappa} \\ dM &= t \int_{-h/2}^{h/2-c} yE_c (d\bar{\epsilon}_0 + d\bar{\kappa}y) dy + t \int_{h/2-c}^{h/2} yE_{cc} (d\bar{\epsilon}_0 + d\bar{\kappa}y) dy \\ &= D_t(2,1) d\bar{\epsilon}_0 + D_t(2,2) d\bar{\kappa} \end{aligned} \quad (\text{B3})$$

which by solving the integral yields

$$D_t(1,1) = E_c t ((y_2 - y_1) + (y_3 - y_2) \alpha) \quad (\text{B4a})$$

$$D_t(1,2) = E_c t \left( \frac{1}{2} (y_2 - y_1) (y_1 + y_2) + \frac{1}{2} (y_3 - y_2) (y_2 + y_3) \alpha \right) \quad (\text{B4b})$$

$$D_t(2,1) = D_t(1,2) \quad (\text{B4c})$$

$$D_t(2,2) = E_c t \left( \frac{1}{3} (y_2 - y_1) (y_1^2 + y_2^2 + y_1 y_2) \right) \quad (\text{B4d})$$

$$+ \frac{1}{3} (y_3 - y_2) (y_2^2 + y_3^2 + y_2 y_3) \alpha \quad (\text{B4e})$$

$$\mathbf{D}_t^{I,II} = \begin{bmatrix} D_t(1,1) & D_t(1,2) \\ D_t(2,1) & D_t(2,2) \end{bmatrix} \quad (\text{B4f})$$

where  $y_1$ ,  $y_2$  and  $y_3$  are the distances depicted on Figure 2.

Contribution from a reinforcement rebar can alternatively be included in the beam hinge tangent stiffness matrix as

$$\mathbf{D}_t^{I,II} = \begin{bmatrix} D_t(1,1) + E_s A_s & D_t(1,2) + E_s A_s y_s \\ D_t(2,1) + E_s A_s y_s & D_t(2,2) + E_s A_s y_s^2 \end{bmatrix} \quad (\text{B5})$$

where  $A_s$  is the area of the rebar,  $E_s$  the Young's modulus of the steel and  $y_s$  is the position of the rebar.



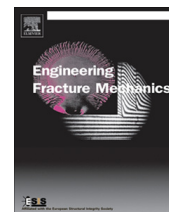
# Paper III

*"General cracked-hinge model for simulation of low-cycle damage in cemented beams on soil"*

A. Skar & P.N. Poulsen & J.F. Olesen

Published in: *Engineering Fracture Mechanics*, 2017





# General cracked-hinge model for simulation of low-cycle damage in cemented beams on soil



Asmus Skar<sup>a,\*</sup>, Peter Noe Poulsen<sup>b</sup>, John Forbes Olesen<sup>b</sup>

<sup>a</sup> COWI A/S, Parallelvej 2, 2800 Kgs. Lyngby, Denmark

<sup>b</sup> Technical University of Denmark, Brovej, Building 118, 2800 Kgs. Lyngby, Denmark

## ARTICLE INFO

### Article history:

Received 2 September 2016

Received in revised form 11 January 2017

Accepted 16 January 2017

Available online 7 February 2017

### Keywords:

Fracture mechanics

Cohesive crack

Non-linear FEM

Low-cyclic fatigue

Cemented materials

Pavement analysis

## ABSTRACT

The need for mechanistic constitutive models to evaluate the complex interaction between concrete crack propagation, geometry and soil foundation in concrete- and composite pavement systems has been recognized. Several models developed are either too complex or designed to solve relatively simple problems, e.g. limited to one type of load configuration or test set-up. In order to develop a general and mechanistic modeling framework for non-linear analysis of low-cycle damage in cemented materials, this paper presents a cracked-hinge model aimed at the analysis of the bending fracture of the cemented material. The model is based on the fracture mechanics concepts of the fictitious crack model. The proposed hinge is described in a general and consistent format, allowing for any type of stress-crack opening relationship and unloading-reloading formulation. The functionality of the proposed hinge model is compared to numerical- and experimental results. The proposed hinge shows good performance and seems promising for the description of low-cycle fracture behavior in cemented materials.

© 2017 Elsevier Ltd. All rights reserved.

## 1. Introduction

Concrete- and composite pavement systems are subjected to cyclic loading from vehicles resulting in initiation of bending cracks in the quasi-brittle cemented material. Subsequently, these cracks propagate leading to failure of the pavement structure. The structural design of such pavements is primarily based on empirical formulas which convert the elastic response analysis into a measure of performance [1–3], referred to as the Mechanistic-Empirical (M-E) method. However, such a method cannot account for significant factors influencing the response, e.g. describing the interaction between loads, material properties, geometry and soil foundation in a unified manner.

The limitations of the M-E method and the growth in computer capabilities have resulted in an increasing development of more rational models for pavement analysis during the past decades. That work began in the early 1990s, studying mainly asphalt concrete mixtures in flexible pavements [4–6], reflective cracking in asphalt overlays [7] and permanent deformation of unbound materials [8–10]. These models are typically based on a mechanistic approach using appropriate numerical tools, e.g. the finite element (FE) method. This allows for geometry, inhomogeneities, anisotropy, and nonlinear material properties of all pavement layers to be considered.

Numerical analysis of crack propagation in concrete- and composite pavement systems have primarily carried out applying cohesive zone modeling [11–15]. Gaedicke and Roesler [16,17] applied a cohesive zone model for studying fracture in

\* Corresponding author.

E-mail address: [asch@cowi.dk](mailto:asch@cowi.dk) (A. Skar).

**Nomenclature**

$a_i$	slope of tangent line segment on softening curve
$a_0$	depth of notch
$b_i$	intersection of the tangent line segment on softening curve and the abscissa
<b>B</b>	strain interpolation matrix
$c_1$	softening curve model parameters
$c_2$	softening curve model parameters
<b>CMOD</b>	measured crack mouth opening displacement
$cp$	constitutive point
$c$	crack-length
$d$	distance from beam face to measurement point
<b>D<sub>t</sub></b>	hinge tangent stiffness matrix
$e_i$	lever arm of hinge fiber
$E_c$	Young's modulus of cemented material
$E_d$	damaged unloading- reloading stiffness of hinge fiber
$f_t$	uni-axial tensile strength of cemented material
$G_F$	fracture energy
$h$	hinge height
$H$	beam height
$ip$	interpolation point
$k_1$	softening curve model parameters
$k_h$	horizontal spring stiffness
<b>K<sub>t</sub></b>	beam element tangent stiffness matrix
$k_v$	vertical spring stiffness
$L$	beam length
$L_e$	beam element length
$M$	moment force
$N$	normal force
<b>N</b>	displacement interpolation matrix
$n$	number of fibers
$P$	load
<b>q</b>	beam element internal nodal force
$s$	hinge width
$t$	hinge thickness
$u$	elongation of hinge fiber
<b>v</b>	element dof vector
$w$	crack-opening
$w_c$	zero-stress displacement
$w_{k_1}$	softening curve model parameters
$\alpha_i$	monotonic damage parameter
$\delta$	total midspan displacement of beam
$\delta^{cr}$	cracking beam midspan deformation of hinge
$\delta_g$	geometrical amplification
$\delta^{el}$	elastic beam midspan deformation of hinge
$\delta_e$	elastic deformation of specimen
$\delta_{COD}$	the opening due to the presence of the crack
$\bar{\epsilon}_0$	mean normal strain at beam axis
$\bar{\epsilon}$	mean normal strain of hinge fiber
$\epsilon_{ct}$	strain at crack initiation
$\bar{\epsilon}^{pl}$	mean plastic strain component
$\bar{\epsilon}^{cr}$	inelastic cracking strain component
$\eta$	tensile cyclic damage parameter
$\bar{\epsilon}_{ult}$	zero-stress strain
$\bar{\epsilon}^{unt}$	strain during unloading- and reloading
$\gamma$	shear coupling spring coefficient
$\bar{\kappa}$	mean curvature of the hinge
$\mu$	normalized moment
$\sigma_u^k$	negative intersecting point on abscissa
$\sigma_{ur}$	normal cohesive stress during unloading- and reloading of hinge fiber

$\sigma$	normal cohesive stress
$\theta$	normalized hinge rotation
$\varphi$	hinge rotation

beams resting on soil. The cohesive zone model stand out as particularly attractive for studying beams- and slabs on grade under monotonic loading, where the fracture plane can be anticipated a priori, i.e. orthogonal cracks in the direction of maximum principal stress. Although the results published show good performance, relatively large finite element models are applied compared to the complexity of the pavement system studied. Moreover, some authors reported lack of convergence, instability problems and aborted simulations [16,13,14].

In order to create a simple and robust modeling framework for engineering application, this paper presents a non-linear hinge model based on the fracture mechanics concepts of the fictitious crack model by Hillerborg et al. [18]. The hinge model for modeling the crack propagation due to pure bending in a concrete beam without reinforcement was first presented by Ulfkjaer et al. [19]. This hinge was successfully applied in the modeling of pure concrete beams in three-point bending considering the development of only one crack. Olesen [20] expanded the hinge model by applying a bi-linear softening curve to allow for the incorporation of the effects of fibers on concrete fracture. Further, this modified hinge model allowed for the existence of a sectional normal force. This last feature is crucial for the ability of the hinge to model a number of situations such as the wedge splitting test [21] and the split cylinder test [22]. Olesen and Poulsen [23] implemented a numerical hinge for investigation of the fracture behavior of reinforced concrete beams applying the effective stiffness concept, allowing for the formation of multiple cracks along the beam axis.

The basic idea of the hinge has also been used for studying cyclic fatigue of plain concrete beams [24–26], as well as reinforced and fiber-reinforced concrete beams [27–30]. Maitra et al. [31] applied the influence method [32] in conjunction with the stress-degradation law proposed by Zhang et al. [25] to simulate fatigue crack length propagation in plain concrete pavements. However, these models suffer from another drawback: they are limited to one type of test or structural problem where the crack path is known a priori.

This paper presents a simple multi-scale damage model for simulation of low-cyclic damage of cemented beam structures. At the lowest level, a fiber of cemented material including a crack is considered, and a stress-mean strain relationship is established. At the intermediate level, a hinge element, which is a finite part of the beam, consisting of fibers in layered strips of cemented material is considered, and a relationship between the generalized sectional forces and strains established. At the highest level, the hinge model is applied as a constitutive model in a non-linear beam element. Although the underlying description of the hinge is based on the formation of discrete cracks, the constitutive behavior of the hinge is smeared (smooth). This particular feature is practical and effective as no a priori knowledge of the crack pattern is required. Moreover, the hinge formulation makes it straightforward to implement different types of stress-crack opening relationships and unloading- reloading schemes.

## 2. The mechanics of the cracked-hinge model

The basic assumption of the hinge model is the fact that the presence of a crack influences the overall stress and strain field of a structure only locally. The discontinuity created by the crack is expected to vanish outside a certain width. Under constant moment, e.g. between the loaded points in Fig. 1(a), the beam sections at the midpoints between the cracks will,

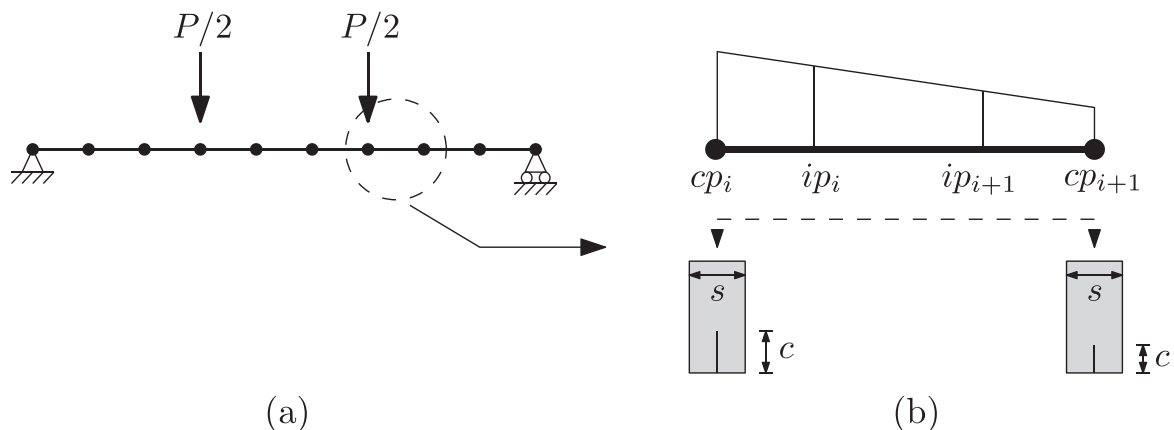


**Fig. 1.** Sketch of hinge model implemented in simply supported beam under four point loading: (a) overview of beam structure and (b) underlying discrete formulation of cracks at constitutive points,  $cp$ , and smeared constitutive behavior obtained from interpolation between constitutive points at integration points,  $ip$ .

due to the periodicity of the cracks, remain plane during deformation of the beam. The width  $s$  between two such sections embracing one crack defines a hinge element, as shown in Fig. 1(b). For the beam area outside the loaded points, the moment distribution is no longer constant. Such phenomena be handled with appropriate numerical tools, i.e., the finite element (FE) method, as exemplified for a single beam element in Fig. 1(b).

The hinge width  $s$  is a fundamental calibration parameter of the model, and it was suggested in [19] to use a hinge width half the height of the beam, also adopted in the present study. Thus, the flexural deformation of the beam is concentrated and the propagation of a crack can be modeled as a hinge whereas the rest of the beam can be treated as elastic bulk material.

The uni-axial tensile behavior of the cemented material is modeled according to the fictitious crack model by Hillerborg et al. [18]. The linear elastic pre-crack state is described by the elastic modulus,  $E_c$ . The uni-axial tensile strength is denoted by  $f_t$  and the corresponding strain by  $\varepsilon_{ct}$ . To make the proposed model as versatile as possible, a multi-linear stress-crack opening relationship, or so-called softening law is selected

$$\sigma(w) = b_i - a_i w \begin{cases} b_1 - a_1 w & 0 \leq w \leq w_1 \\ b_2 - a_2 w & w_1 \leq w \leq w_2 \\ b_3 - a_3 w & w_2 \leq w \leq w_3 \\ \dots & \dots \\ 0 & w_i > w_c \end{cases} \quad (1)$$

where  $w$  is the crack opening,  $w_c$  is the final zero-stress displacement,  $a_i$  is the slope and  $b_i$  the intersection of the tangent line segment and the abscissa for a given point on softening curve as shown in Fig. 2.

The total fracture energy  $G_F$  given by the area under the softening curve is

$$G_F = \int_0^{w_c} \sigma(w)dw = \frac{1}{2} \sum_{i=1}^n [(2b_i - a_i(w_{i-1} + w_i))(w_i - w_{i-1})] \quad (2)$$

where  $n$  is the number of lines on the softening curve.

For the semi-analytical hinge models published in the literature, see e.g. [20,25,33,26], sectional forces are calculated over the full beam-hinge segment (integration in blocks) for a given stress crack-opening relationship. A similar approach was used in the finite element implementation of the cracked-hinge reported by Olesen and Poulsen [23]. This type of model is simple and numerically robust. However, such formulation becomes cumbersome if one wish to study unloading- and reloading of cracks as well as more complex material behavior, e.g. damage and fatigue. Following the basic idea of the 'multilayer model' by Hordijk [24], this study presents a general hinge model consisting of fibers of cemented material shown in Fig. 3.

The tensile behavior of the hinge may be established by considering a fiber of material in uni-axial tension as shown in Fig. 3(c). The elongation of the fiber located at  $y$  can be expressed in terms of the mean normal strain

$$\bar{\varepsilon}(y) = \frac{2u(y)}{s} = \frac{2u_0(y)}{s} + \frac{2\varphi}{s}y \equiv \bar{\varepsilon}_0 + \bar{\kappa}y \quad (3)$$

where  $\bar{\varepsilon}_0$  is the mean normal strain at the beam axis, and  $\bar{\kappa}$  the mean curvature of the hinge. In the cracked state,  $0 < w \leq w_c$ , the crack opening and the corresponding stress in the strip is given as

$$\left. \begin{aligned} \sigma_c = \sigma_w \Rightarrow \sigma_c = b_i + a_i w \\ s + 2u = s(1 + \varepsilon_c) + w \Rightarrow s\bar{\varepsilon}(y) = s\varepsilon_c + w \end{aligned} \right\} \Rightarrow \begin{cases} w_i = s \frac{E_c \bar{\varepsilon}(y) - b_i}{E_c + a_i s} \\ \sigma_i = E_c \frac{b_i - a_i s \bar{\varepsilon}(y)}{E_c - a_i s} \end{cases} \quad (4)$$

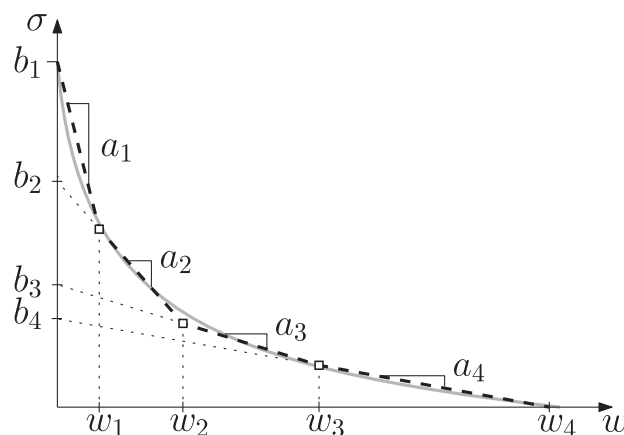
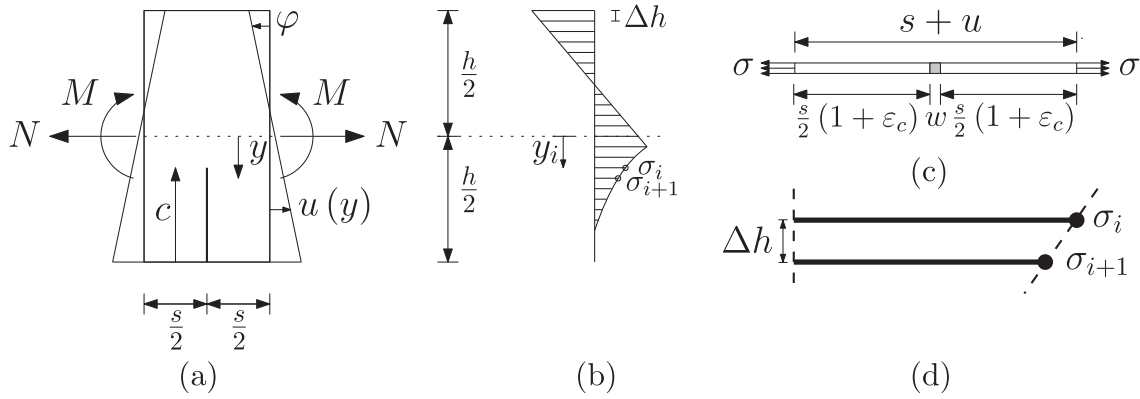


Fig. 2. Definition of parameters  $a_i$ ,  $b_i$  and  $w_i$  for softening law selected: multi-linear idealization (black dashed) of exponential softening curve (gray solid) using four linear line segments.



**Fig. 3.** Fiber hinge model: (a) Beam segment with constant sectional forces and deformation of cracked beam segment. (b) Hinge stress distribution after initiation of cracking showing the individual fibers ( $n = 24$ , whereof 4 stress free). (c) Material fiber in uni-axial tension: loaded state beyond peak-load showing crack deformations. (d) Geometrical definition of one hinge strip (interpolation of stresses between two fibers).

In the cracked state,  $w_c \leq w$ , the crack is stress free, leading to the simple solution for the strip

$$\left. \begin{aligned} w &= s(1 + \bar{\varepsilon}(y)) - s \\ \sigma_c &= 0 \end{aligned} \right\} \Rightarrow \begin{cases} w_i = s\bar{\varepsilon}(y) \\ \sigma_i = 0 \end{cases} \tag{5}$$

The hinge is divided in,  $n + 1$ , number of fibers with the strip height  $\Delta h$  between fibers, shown in Fig. 3(b). The position (top-down) of each fiber with respect to  $y = 0$  can be calculated as  $y_i = -h/2 + \Delta h \cdot (i - 1)$ . The normal force contribution from each strip between two fibers is given by

$$N_i = \frac{1}{2}(\sigma_i + \sigma_{i+1})\Delta ht \tag{6}$$

The eccentricity of the normal force for each strip is found from trapezoidal calculation and is given by

$$e_i = \frac{1}{3} \frac{\sigma_i + 2\sigma_{i+1}}{\sigma_i + \sigma_{i+1}} \Delta h + y_i \tag{7}$$

The moment contribution for each strip then yields

$$M_i = N_i \cdot e_i \tag{8}$$

The sectional forces with respect to  $y = 0$  is then a sum of the contribution from all,  $n$ , strips and may be calculated from

$$N(\bar{\varepsilon}_0, \bar{\kappa}) = t \int_{-h/2}^{h/2} \sigma_c dy = \sum_{i=1}^n N_i \tag{9a}$$

$$M(\bar{\varepsilon}_0, \bar{\kappa}) = t \int_{-h/2}^{h/2} \sigma_c y dy = \sum_{i=1}^n M_i \tag{9b}$$

Convergence of the hinge is evaluated plotting the normalized error in moment  $\beta$  between the original hinge model [19] and the proposed hinge, considering a simple linear softening law for different hinge mesh densities,  $n$ : 2–100, shown in Fig. 4(b). It is observed that sufficient accuracy can be obtained with 30 fibers, however, little is gained by increasing the number of fibers from 10 to 30. Typical moment-curvature response is shown in Fig. 4(a).

In the analysis presented in Fig. 4 the error in normalized moment is taken as the average difference in moment between the analytical hinge model in [19] and the proposed fiber hinge; at peak ( $\kappa = 0.003 \text{ m}^{-1}$ ), on the descending branch ( $\kappa = 0.0065 \text{ m}^{-1}$ ) and at the transition point between softening and stress free bottom fiber ( $\kappa = 0.01 \text{ m}^{-1}$ ).

### 3. Tensile damage model for cemented material

In order to realistically capture the influence from unloading of a previously open crack, as well as the stiffness reduction for structures subjected to repeated loads, a low-cyclic damage plasticity model for the fiber in tension is implemented. A simple format is proposed, defining a fixed negative intersecting point  $\sigma_u^k$  on the abscissa towards which unloading takes place after initiation of cracking. The geometrical meaning of the strain components for the damage-plasticity model are shown in Fig. 5.

From Fig. 5 it is evident that the unloading stiffness and plastic strain component can be defined as

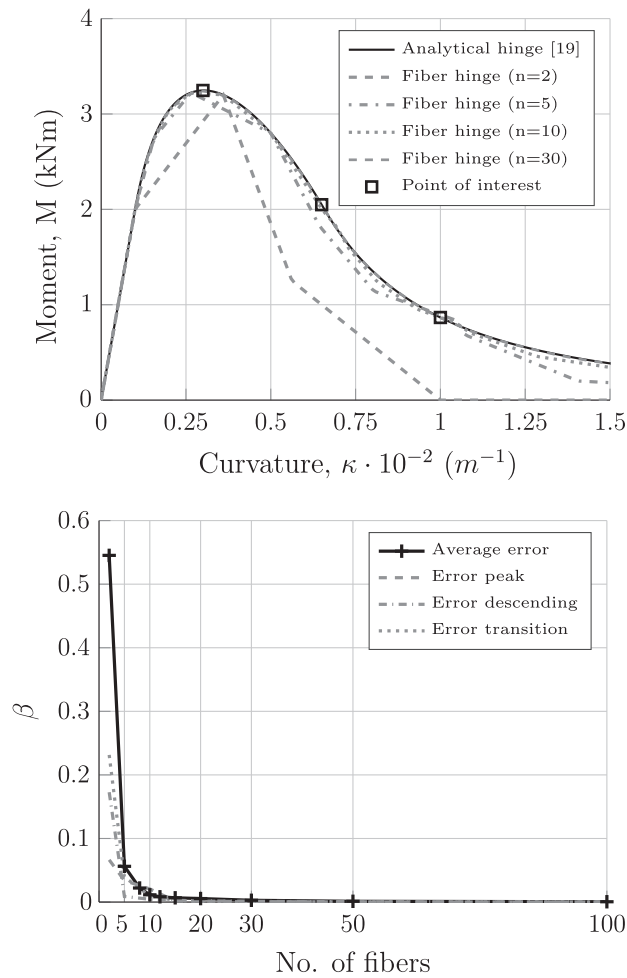


**Fig. 4.** (a) Typical moment-curvature response. (b) Number of hinge fibers,  $n$ : 2–100 (element size,  $elsz$ : 0.01–0.002 m) versus the average normalized difference in moment  $\beta$ . Hinge dimensions ( $h/t$ ):  $0.20 \times 0.10 m^2$ . Material properties:  $E_c = 30$  GPa,  $f_t = 3.5$  MPa  $G_f = 150$  N/m and  $w_c = 0.1$  mm (linear softening).

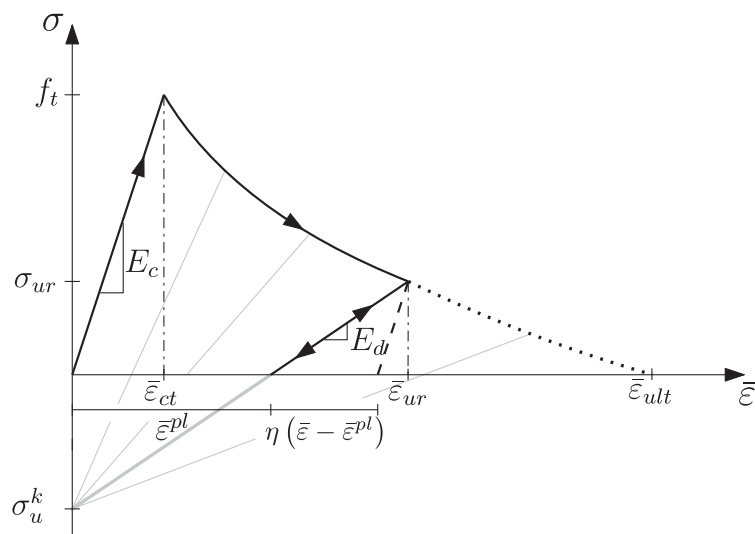


**Fig. 5.** Geometrical meaning of strain components for the damage-plasticity model. The inelastic cracking strain  $\bar{\epsilon}^{cr}$  is composed of the reversible  $\eta(\bar{\epsilon} - \bar{\epsilon}^{pl})$  and irreversible  $\bar{\epsilon}^{pl}$  parts. The dashed line represent elastic unloading with the initial stiffness whereas gray lines represent the reduced stiffness and unloading towards point  $\sigma_u^k$ .

$$E_s^\pm = \frac{\sigma_{ur} - \sigma_u^k}{\bar{\epsilon}_{ur}} \quad (10a)$$

$$\bar{\epsilon}^{pl} = -\frac{\sigma_u^k}{E_s^\pm} \quad (10b)$$

where  $E_s^\pm$  is the unloading- and reloading stiffness and  $\sigma_{ur}$  and  $\bar{\epsilon}_{ur}$  is the maximum cracking stress and strain upon unloading and reloading, respectively. The format above is found to comply well with experimental data for concrete materials as well as more advanced concrete damage plasticity model formats, see e.g. [34–36]. Accordingly, a conventional 1-D damage-plastic stress strain law can be formulated

$$\sigma = (1 - \eta)E_c(\bar{\epsilon} - \bar{\epsilon}^{pl}) \quad (11)$$

where the damage parameter is given as

$$\eta = 1 - \frac{E_s^\pm}{E_c} \quad (12)$$

The crack width  $w$  can be found from

$$w = \begin{cases} s\bar{\epsilon} - s\frac{\sigma_{ur}}{E_c} \Rightarrow s\bar{\epsilon}^{cr} & 0 < w \leq w_c \\ s\bar{\epsilon} & w_c < w \end{cases} \quad (13)$$

where the inelastic strain is given as  $\bar{\epsilon}^{cr} = \bar{\epsilon}^{pl} + \eta(\bar{\epsilon} - \bar{\epsilon}^{pl})$ .

The constitutive behavior of a single hinge-fiber is tested plotting the stress-crack opening curve for one hinge fiber subjected to cyclic loading versus experimental results of plain concrete in uni-axial tension reported in Reinhardt et al. [37], shown in Fig. 6.

It is observed from Fig. 6 that good fit is obtained between the hinge-fiber behavior and experimental results. More detailed studies of the applicability of the semi-analytical cracked-hinge model can be found in [38].

#### 4. Implementation of hinge into beam element

The proposed fiber hinge, in subsequent chapters referred to as the 'FEM hinge', is implemented in a user-built finite element code following standard finite element beam theory and procedures for building elements with non-linear material behavior, see e.g. [39]. The expressions for the element stiffness matrix and equivalent nodal loads is based on the cubic displacement function.

For the present study a plane three-node beam element is chosen as shown in Fig. 7. This element is capable of modelling quadratic variations of the axial displacements and cubic variations of the transverse displacements. The choice of element ensures that both generalized strains are interpolated linearly as opposed to a typical two-node beam element where constant normal strain is assumed.

The vector of generalized strains,  $\boldsymbol{\varepsilon}$ , holds the linearized axial strain  $\epsilon_0$  and the linearized curvature  $\kappa$ . The interpolation of  $\boldsymbol{\varepsilon}$  in the element is given by

$$\boldsymbol{\varepsilon} = \begin{bmatrix} \epsilon_0 \\ \kappa \end{bmatrix} = \begin{bmatrix} \frac{du_1}{dx} \\ \frac{d^2u_2}{dx^2} \end{bmatrix} = \mathbf{B}\boldsymbol{v} \quad (14)$$

where  $\mathbf{B}$  is the strain interpolation matrix. The vector of generalized stresses,  $\boldsymbol{\sigma}$ , holds the sectional normal force  $N$  and the sectional moment  $M$  and may be established applying (9a) and (9b), i.e.  $\boldsymbol{\sigma} = \boldsymbol{\sigma}(\boldsymbol{\varepsilon}) = \begin{bmatrix} N(\boldsymbol{\varepsilon}) \\ M(\boldsymbol{\varepsilon}) \end{bmatrix}$ .

The hinge model presented here first determine the constitutive state and stiffness of each individual fiber. Integration over the strip height between fibers is then performed and the sum of all contributions is included in the tangent stiffness matrix. The hinge tangent stiffness matrix,  $\mathbf{D}_t$  is defined through

$$\begin{bmatrix} dN \\ dM \end{bmatrix} = \mathbf{D}_t \begin{bmatrix} d\bar{\epsilon}_0 \\ d\bar{\kappa} \end{bmatrix}, \quad \mathbf{D}_t = \sum_{i=1}^n \begin{bmatrix} \frac{\partial N_i}{\partial \bar{\epsilon}_0} & \frac{\partial N_i}{\partial \bar{\kappa}} \\ \frac{\partial M_i}{\partial \bar{\epsilon}_0} & \frac{\partial M_i}{\partial \bar{\kappa}} \end{bmatrix} \quad (15)$$

Monotonic loading of the hinge results in constant positive stiffness of fibers in linear elastic state. Fibers in the cracked state along the softening branch and cracked stress-free state result in negative and zero stiffness contributions, respectively. The constituents of (15) are obtained from (9a) and (9b) utilizing the following relations for the relevant part of the integral corresponding to  $0 < w \leq w_c$

$$\frac{\partial \sigma_c}{\partial \bar{\epsilon}_0} = E_c \frac{a_i s}{E_c + a_i s}, \quad \frac{\partial \sigma_c}{\partial \bar{\kappa}} = E_c \frac{a_i s}{E_c + a_i s} y \quad (16)$$

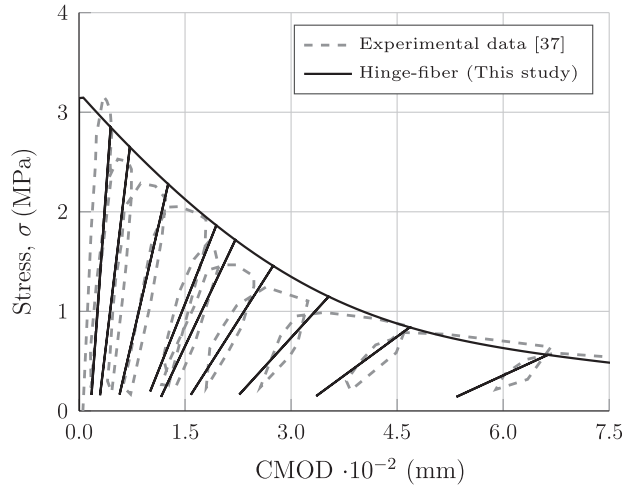


**Fig. 6.** Constitutive behavior of hinge-strip in uni-axial tension; stress-crack opening displacement compared to experimental results reported by Reinhardt et al. [37]. Relevant material parameters are;  $E_c = 39.27$  GPa,  $f_t = 3.2$ ,  $G_F = 99.7$  N/m,  $c_1 = 3, c_2 = 6.93$ ,  $w_c = 5.14G_F/f_t = 0.16$  mm,  $s = 0.25$  m and  $\sigma_u^k = -0.4f_t$  (exponential softening).

Here the parameters  $\alpha_i = \frac{a_i s}{E_c + a_i s}$  and  $E_{cc}^i = E_c \alpha_i$  are introduced, where the latter symbolises the reduced stiffness of the cracked fiber.  $a_i$  is the slope at a given point on the softening curve, see Fig. 2. The stiffness contribution from one fiber in the three different phases; elastic, softening and stress-free is given by (17a)–(17c), respectively

$$\mathbf{D}_t^{el} = \begin{bmatrix} E_c t & E_c t y \\ E_c t y & E_c t y^2 \end{bmatrix} \quad \bar{\varepsilon} \leq \bar{\varepsilon}_{ect} \tag{17a}$$

$$\mathbf{D}_t^{cr} = \begin{bmatrix} E_{cc} t & E_{cc} t y \\ E_{cc} t y & E_{cc} t y^2 \end{bmatrix} \quad \bar{\varepsilon}_{ect} < \bar{\varepsilon} \leq \bar{\varepsilon}_{ult} \tag{17b}$$

$$\mathbf{D}_t^0 = \begin{bmatrix} 0 & 0 \\ 0 & 0 \end{bmatrix} \quad \bar{\varepsilon} > \bar{\varepsilon}_{ult} \tag{17c}$$

In the case of unloading- and reloading, a fiber in linear elastic state will not change whereas a fiber along the softening branch change from a negative to a positive stiffness contribution. Moreover, the tensile damage parameter is introduced, i.e.

$$\mathbf{D}_t^u = (1 - \eta)\mathbf{D}_t^{el} \quad \text{for } \bar{\varepsilon}_{ct} < \bar{\varepsilon}^{unl} < \bar{\varepsilon}_{ult} \tag{18}$$

The full tangent stiffness matrix for loading, unloading and reloading can now be established by interpolation between each fiber and integration over the strip height as given in Appendix A.1. The internal nodal force and the contribution from the beam-element to the tangential stiffness matrix can then be found from standard finite element beam theory.

The implemented hinge is validated by plotting the moment-curvature behavior for a single FEM hinge versus the analytical hinge. It can be observed from Fig. 8 that exact fit is obtained between the FEM hinge and analytical model considering two types of unloading schemes. Fast convergence, within 1–2 iterations, is obtained for this simple model applying a fixed increment of  $\Delta\theta = 0.225 \text{ mm}^{-1}$ . The two transition points between the phases; elastic-softening (crack initiation) and softening-stress free (bottom fiber stress free) are shown for reference.

## 5. Structural examples

### 5.1. Finite element model

The performance of the proposed hinge model is further evaluated by structural analysis of two fracture tests on plain concrete. First, a conventional notched beam under three point loading is considered, shown in Fig. 9(a). Second, a notched

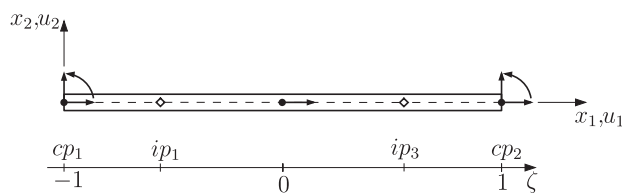


**Fig. 7.** Plane beam element: Constitutive points ( $cp_i$ ) are located at endpoints, integration points ( $ip_i$ ) at Gauss points  $\pm\sqrt{1/3}$ .

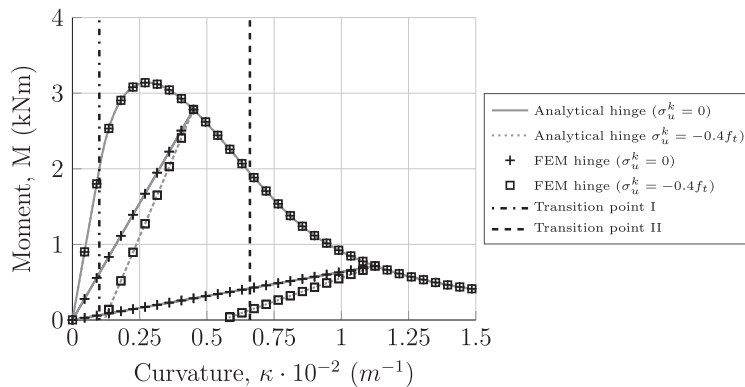


Fig. 8. Implementation of hinge into beam element: comparison between analytical and finite element hinge model. Hinge dimensions (h/t):  $0.20 \times 0.10 \text{ m}^2$ . Material properties:  $E_c = 30 \text{ GPa}$ ,  $f_t = 3.5 \text{ MPa}$ ,  $G_F = 150 \text{ N/m}$  and  $w_c = 0.1 \text{ mm}$  (linear softening).

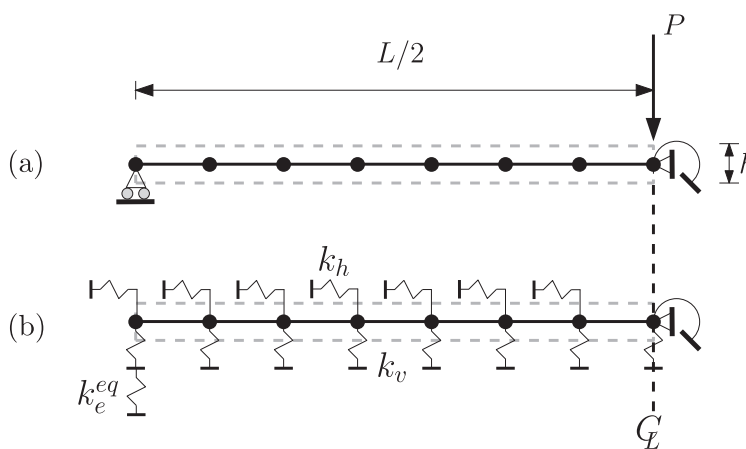


Fig. 9. Model geometry and boundary conditions of finite element model used in the present study: (a) simply supported beam and (b) soil supported beam.

Table 1  
Geometry and mechanical properties for beams used in numerical studies.

	Unit	Three-point	Soil
<i>Geometry</i>			
Length, $L$	(m)	0.60	0.80
Height, $H$	(m)	0.15	0.15
Thickness, $t$	(m)	0.08	0.08
Notch depth, $a_0$	(m)	0.05	0.05
<i>Mechanical- and fracture properties</i>			
Young's modulus, $E$	(MPa)	32,040	32,040
Poisson's ratio, $\nu$	(-)	0.15	0.15
Tensile strength, $f_t$	(MPa)	4.15	4.15
Fracture energy, $G_F$	(N/mm)	0.164	0.164
<i>Soil properties</i>			
Vertical spring, $k_v$	(MPa/mm)	-	0.1560
Horizontal spring, $k_h$	(MPa/mm)	-	0.0156
<i>Cohesive model parameters</i>			
Softening type	(-)	Bilinear	Bilinear
Stress ratio at kink point, $k_1$	(-)	0.25	0.25
Displacement at kink point, $w_{k_1}$	(mm)	0.0204	0.0204
Final zero displacement, $w_c$	(mm)	0.234	0.234
<i>Hinge model and numerical parameters</i>			
Number of fibers, $n$	(-)	30	30
Number of elements, $nel$	(-)	8	10
Unloading point, $\sigma_u^k$	(MPa)	$-0.4f_t$	$-0.4f_t$
Increment size, $\Delta\delta_c$	(mm)	$1 \cdot 10^{-2}$	$1 \cdot 10^{-2}$
Error tolerance, $\epsilon$	(-)	$1 \cdot 10^{-4}$	$1 \cdot 10^{-4}$

beam resting on clay soil subjected to a concentrated load at midspan position is considered, shown in Fig. 9(b). Beam geometry, material properties and model parameters used in the analysis are given in Table 1. Overview of model geometry and boundary conditions is shown in Fig. 1.

To simulate the softening response of beam structures and to compare experimental- and numerical unloading and reloading curves, a conventional Newton-Raphson (N-R) solver is implemented with direct displacement control, see e.g. [40]. In the present study the energy norm ratio  $\delta E_1/\Delta E_0$  is applied as a measure in the convergence criterion.

### 5.2. Three-point beam

Convergence of the FEM hinge model is evaluated plotting the load displacement behavior of a three point-beam, see Fig. 9(a), for different beam mesh densities,  $nel$ : 2–14, shown in Fig. 10. It is observed that sufficient accuracy for peak-load and peak-load displacement can be obtained with only 2 elements. However, on the softening branch, a minimum of 8 elements are needed to resemble the softening response of the analytical model. To obtain satisfactory convergence a minimum of 10 elements are needed, resulting in an element size of 0.06 m, selected in subsequent analysis. In the analytical model, implementing the hinge into an elastic beam as suggested by Olesen [20], only one hinge is considered. This explains the slightly stiffer behavior compared to the finite element hinge.

The functionality of the proposed numerical hinge to simulate the low-cycle fracture behavior of a three-point beam is demonstrated by plotting the load-crack mouth opening displacement versus experimental and numerical results reported in [16], see Fig. 11(a) and (b), respectively.

It is observed from the load-CMOD curve in Fig. 11(a) that there is good agreement between the FEM hinge model and the experimental results. The hinge model resemble both pre-peak, softening and unloading- reloading response adequately well. The difference in peak-load and peak-load displacement is app. 10% and 5% respectively, which is within the expected scatter. It is also found that the monotonic behavior of the proposed hinge comply well with finite element simulations using a discrete cohesive zone model and the commercial computer package ABAQUS reported in [16], see Fig. 11(b).

The difference between the FEM hinge and the cohesive zone model is mainly related to the pre-peak behavior. Whereas the hinge model behaves perfectly elastic up to initiation of cracking, the cohesive zone model incorporates a small error in crack-opening displacements related to the penalty stiffness. Increasing penalty stiffness reduce this error, however, very high levels of penalty stiffness result in ill-conditioned stiffness matrix and thus slow convergence and aborted simulations. This problem is avoided applying the proposed hinge, resulting in a more robust model and stable simulations.

### 5.3. Beam resting on soil foundation

The beam resting on soil foundation is modeled using a simple spring soil model suggested by Gaedicke and Roesler [16]. The idealized spring foundation model consists of independent vertical springs with a spring stiffness coefficient,  $k_v$ , similar to a conventional Winkler model. The constitutive behavior of the vertical spring is modified to allow for separation between the beam and soil, i.e. for positive vertical displacements (tensionless spring). Moreover, the horizontal spring is implemented in the model, representing the frictional contact between soil and beam structure. The horizontal spring is modeled with a stiffness of  $k_h = k_v/10$  and a constant slip limit of  $u_h = 0.5$  mm. A schematic overview of the spring constitutive behavior is shown in Fig. 12. Implementation of the Winkler foundation model into beam elements is described in Appendix A.2.

The functionality of the proposed numerical hinge to simulate the low-cyclic fracture behavior of a beam resting on soil is demonstrated by plotting the load-crack mouth opening displacement versus experimental- and numerical results reported in [16], see Fig. 13(a) and (b), respectively.

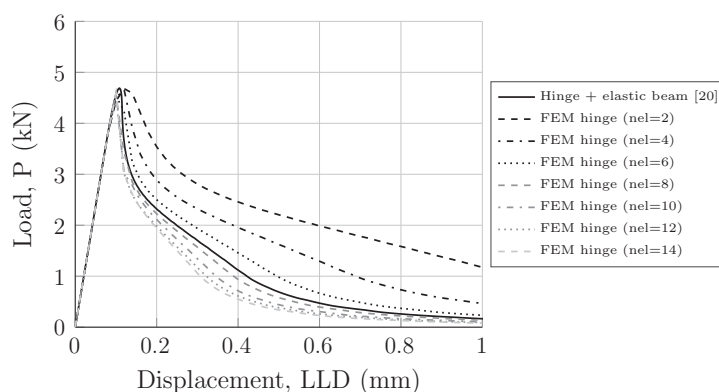
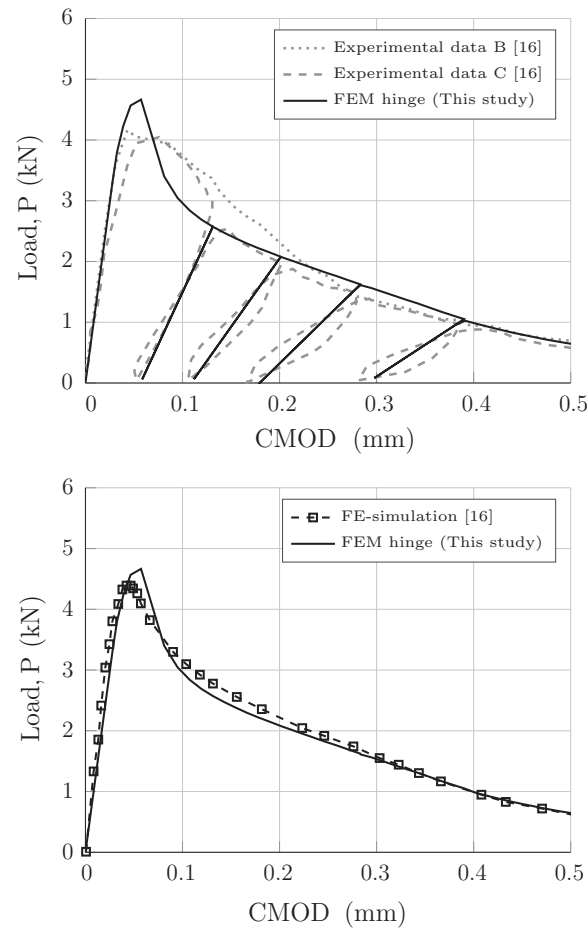
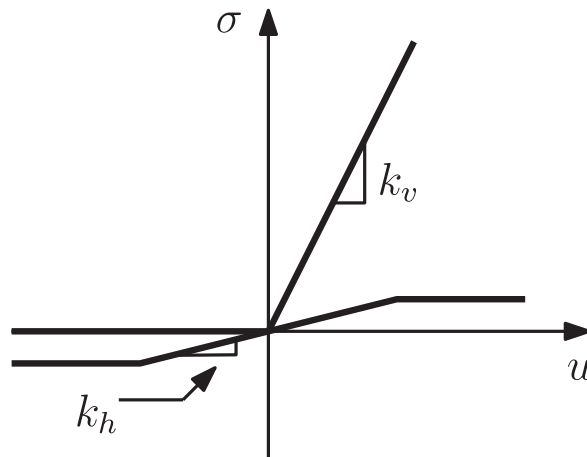


Fig. 10. Convergence test of simply supported showing typical load line displacement (LLD) response for different mesh densities  $nel$ : 2–14 of the FEM hinge compared to the analytical model considering one crack only.



**Fig. 11.** Load-crack mouth opening displacement response of a three-point beam: (a) FEM hinge versus experimental curves plotting 4 of 19 load cycles carried out in experiment. (b) FEM hinge and analytical hinge versus a discrete cohesive zone model.



**Fig. 12.** Constitutive behavior of Winkler spring foundation applied in [16].

It is observed from the load-CMOD curve in Fig. 13(a) that the FEM hinge model captures the overall characteristic response of the beam on soil on the descending branch. However, the peak-load and load level in general, as well as the peak-displacement is overestimated. The difference in peak-load varies between 15 and 50% compared to experimental curves. Similar trend is also found in numerical analysis reported in [16]. Thus, the FEM hinge comply well with the numerical results applying a discrete cohesive zone model as shown in Fig. 13(b). In the example presented, the convergence rate is relatively fast, and below 10 iterations, during unloading and reloading. The convergence rate during monotonic post-peak loading is somewhat slower. This is can be explained by the sudden change in stiffness at peak and at the point where the reloading curve enters the monotonic curve.

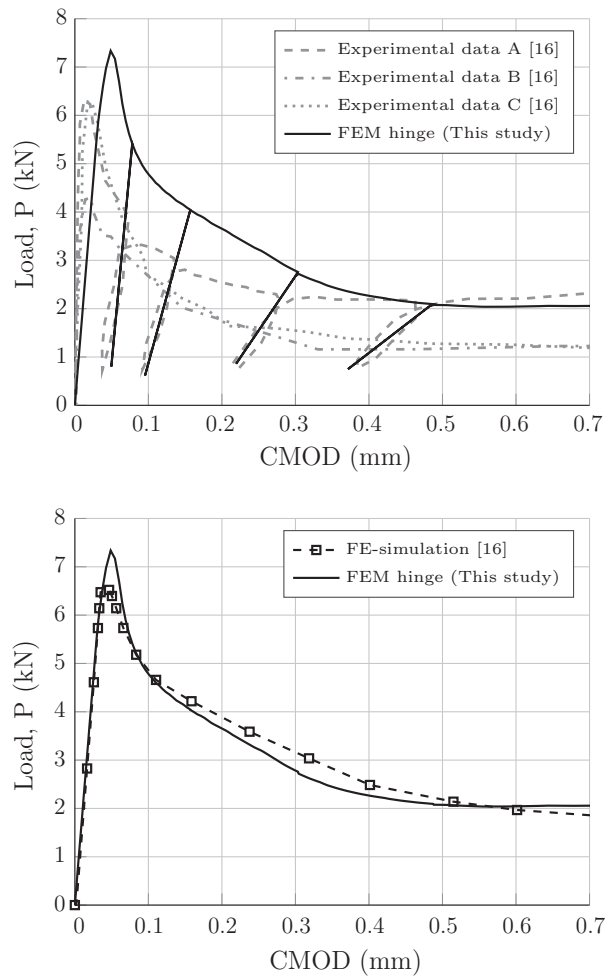


**Fig. 13.** Load-crack mouth opening displacement response of beam on soil: (a) FEM hinge versus experimental curves plotting 4 of 18 load cycles carried out in experiment. (b) FEM hinge versus a discrete cohesive zone model.

The difference between experimental and numerical results indicate that the soil model applied in simulations does not reflect the stress distribution below the beam and/or other boundary conditions in the test set-up very well. The stiff pre-peak response and lower peak load in experiments indicate that the continuity and shear stiffness of the soil influence the response significantly. For cohesive soils, considered here, this influence will theoretically result in a large vertical reaction pressure along beam edges.

In order to obtain a more realistic response of the soil a generalized two-parameter spring model, see e.g. [41,38], is implemented in beam elements as shown in Appendix A.2. The two-parameter model introduce an interaction between independent springs through a shear coupling spring,  $\gamma$ . A simple approach is applied here to demonstrate the applicability of the two-parameter model keeping the Winkler stiffness constant and then adjusting the second parameter to match the

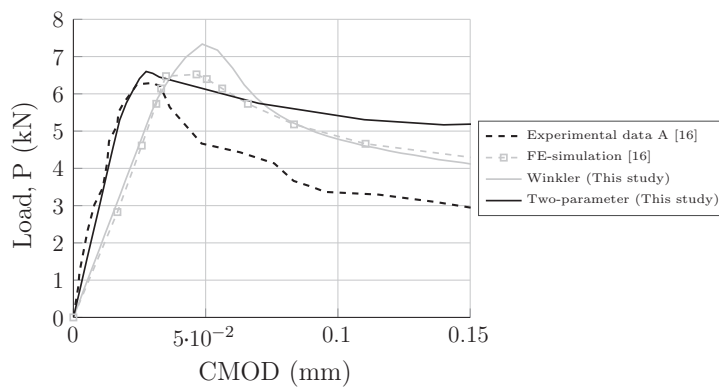


**Fig. 14.** Comparison between experimental results (gray dashed), numerical results applying a Winkler model (black solid) and numerical results applying a calibrated two-parameter model (gray solid): Load-crack mouth opening displacement response of three point beam on soil.

pre-peak behavior of experimental beams, resulting in  $\gamma = 1.75 \cdot 10^6$  N. The soil adjacent to the beam is modeled using an additional spring force, i.e.,  $k_e^{eq} = k_v \sqrt{\gamma/k_v}$ .

It is observed from Fig. 14 that the peak-load and peak-load displacement can be predicted adequately well applying a two-parameter model. However, on the post-peak branch, the continuity created by the second parameter spring, result in a high residual stiffness of the structure. At this stage the shallow clay soil layer is likely to exhibit severe plastic yielding due to the stress concentration at the crack front. To obtain a realistic response for the total load-CMOD curve, it would be necessary apply more advanced foundation models, e.g. by extending the two-parameter to account for plastic yielding.

## 6. Conclusion

The use of a cohesive cracked-hinge model for simulating low-cyclic damage of cemented beam structures has been investigated showing good performance. Implementation of the hinge into a beam element is relatively straightforward and the contribution to the tangent stiffness matrix from each fiber is established following a general format, creating a versatile tool, allowing for different types of softening laws and damage formats.

The analytical hinge model developed shows satisfying performance compared to integration over the full hinge segment. Good fit is obtained using a relatively coarse discretisation of 10–30 fibers. Moreover, it is found that the analytical damage-plasticity format implemented sufficiently captures the response of experimental cyclic uni-axial tensile tests.

The results obtained show that the proposed numerical hinge model adequately describe the cyclic response of a plain concrete beam under three point loading. It is also found that the proposed hinge comply well with other numerical results published in the literature, applying a cohesive zone model using the same cohesive model parameters.

Simulation of beams resting on soil foundation show that the hinge model captures the main structural response of experimental beams. The hinge model resting on Winkler foundation does not describe the pre-peak behavior observed in experiments adequately well, indicating that the soil model and the boundary conditions applied does not comply with the test set-up. This highlights the influence from soil-structure interaction on the structural response of beams on soil. To overcome the deficiency of the Winkler model, an interaction between independent springs is introduced, using a two-parameter spring model, showing good performance.

The present paper demonstrates the implementation and application of a general cohesive crack-hinge model to describe the fracture behavior of cemented beam structures. The results obtained is encouraging and show that the methodology is well suited for practical use.

## Acknowledgements

This work was supported by COWIfonden.

## Appendix A

### A.1. Derivation of hinge tangent stiffness matrix

Interpolation between hinge fibers and integration over the strip height is given as

$$\begin{aligned}
 dN_i &= t \int_{y_i}^{y_{i+1}} \frac{1}{2} (D_i(1, 1) + D_{i+1}(1, 1)) dy + \int_{y_i}^{y_{i+1}} \frac{1}{2} (D_i(1, 2) + D_{i+1}(1, 2)) dy \\
 &= \frac{1}{2} (D_i(1, 1) + D_{i+1}(1, 1)) (y_{i+1} - y_i) \\
 &\quad + \frac{1}{2} (D_i(1, 2) + D_{i+1}(1, 2)) (y_{i+1} - y_i) \frac{1}{2} (y_i + y_{i+1}) \\
 &= D_i(1, 1) d\bar{\epsilon}_0 + D_i(1, 2) d\bar{\kappa} \\
 &= \frac{\partial N_i}{\partial \bar{\epsilon}_0} + \frac{\partial N_i}{\partial \bar{\kappa}}
 \end{aligned} \tag{A.1a}$$

$$\begin{aligned}
 dM_i &= t \int_{y_i}^{y_{i+1}} \frac{1}{2} (D_i(2, 1) + D_{i+1}(2, 1)) dy + \int_{y_i}^{y_{i+1}} \frac{1}{2} (D_i(2, 2) + D_{i+1}(2, 2)) dy \\
 &= \frac{1}{2} (D_i(2, 1) + D_{i+1}(2, 1)) (y_{i+1} - y_i) \frac{1}{2} (y_i + y_{i+1}) \\
 &\quad + \frac{1}{2} (D_i(2, 2) + D_{i+1}(2, 2)) (y_{i+1} - y_i) \frac{1}{3} (y_i^2 + y_{i+1}^2 + y_i y_{i+1}) \\
 &= D_i(2, 1) d\bar{\epsilon}_0 + D_i(2, 2) d\bar{\kappa} \\
 &= \frac{\partial M_i}{\partial \bar{\epsilon}_0} + \frac{\partial M_i}{\partial \bar{\kappa}}
 \end{aligned} \tag{A.1b}$$

where  $y_i$  and  $y_{i+1}$  are the position of each fiber depicted on Fig. 3. The sum of all contributions is included in the tangent stiffness matrix similar to (15), i.e.

$$\mathbf{D}_t = \sum_{i=1}^n \begin{bmatrix} \frac{\partial N_i}{\partial \bar{e}_0} & \frac{\partial N_i}{\partial \bar{\kappa}} \\ \frac{\partial M_i}{\partial \bar{e}_0} & \frac{\partial M_i}{\partial \bar{\kappa}} \end{bmatrix} \quad (\text{A.2})$$

## A.2. Implementation of foundation models

Based on the contribution to the variation in internal work  $\delta\Omega$ , from the beam and the two-parameter foundation, and the potential work of external forces  $\delta W$  from point- and surface loads, the principle of virtual work for the system can be established

$$\int_V \delta \boldsymbol{\varepsilon}^T \boldsymbol{\sigma} + \delta \mathbf{u}^T \mathbf{k} \mathbf{u} + \delta \theta^T \gamma \theta dV = \int_S \delta \mathbf{u}^T \mathbf{f} dS + \sum_i \delta \mathbf{u}_i^T p_i \quad (\text{A.3})$$

where  $V$  is the structural volume,  $S$  is the surface area,  $\delta \mathbf{u}$  and  $\delta \theta$  is the displacement and rotational variations, respectively,  $\mathbf{f}$  is the surface traction vector,  $p_i$  is a concentrated (nodal) load and  $\delta \mathbf{u}_i$  is the associated (nodal) displacement variation. The contribution of the second parameter spring is here given on a general form considering  $\gamma$  as a rotational stiffness. In case of a Winkler foundation type this latter term is omitted.

The beam-element and two-parameter foundation contribution to the internal nodal force,  $\mathbf{q}$ , is then given by the expression

$$\mathbf{q} = \int_0^{L_e} \mathbf{B}^T \boldsymbol{\sigma} dx + \int_0^{L_e} \mathbf{N}^T \begin{bmatrix} k_h & 0 \\ 0 & k_v \end{bmatrix} \mathbf{N} \mathbf{v}_e dx + \int_0^{L_e} \mathbf{G}^T \gamma \mathbf{I} \mathbf{G} \mathbf{v}_e dx \quad (\text{A.4})$$

where  $L_e$  is the length of the element,  $\mathbf{v}_e$  is the global dof element displacements,  $\mathbf{B}$  is the strain interpolation matrix and  $\mathbf{N}$  is the displacement interpolation matrix.

The beam-element and two-parameter foundation contribution to the tangential stiffness matrix,  $\mathbf{k}_t$ , is given by the expression

$$\mathbf{k}_t = \int_0^{L_e} \mathbf{B}^T \mathbf{D}_t \mathbf{B} dx + \int_0^{L_e} \mathbf{N}^T \begin{bmatrix} k_h & 0 \\ 0 & k_v \end{bmatrix} \mathbf{N} dx + \int_0^{L_e} \mathbf{G}^T \gamma \mathbf{I} \mathbf{G} dx \quad (\text{A.5})$$

The matrix  $\mathbf{I} = \begin{bmatrix} 0 & 0 \\ 0 & 1 \end{bmatrix}$  is used to omit the axial terms in the second parameter interpolation matrix  $\mathbf{G}$ . Where  $\mathbf{G}$  is given as  $\mathbf{G} = \mathbf{N}'$ .

## References

- [1] Packard RG. Thickness design for concrete highway and street pavements. Portland Cement Association.
- [2] NCHRP. Guide for mechanistic-empirical design of new and rehabilitated pavement structures: final report for project 1-37a. National Cooperative Highway Research Program, Transportation Research Board, National Research Council, Washington, DC.
- [3] Knapton J. The structural design of heavy duty pavements for ports and other industries. Interpave, 4th ed. December 2008.
- [4] Jenq Y-S, Perng J-D. Analysis of crack propagation in asphalt concrete using cohesive crack model. *Transp Res Rec: J Transp Res Board* 1991(1317):90–9.
- [5] Scarpas A, Al-Khoury R, Van Gurp C, Erkens S. Finite element simulation of damage development in asphalt concrete pavements. *Proc Int Conf Asphalt Pavements* 1997;1:673–92.
- [6] Desai CS. Unified DSC constitutive model for pavement materials with numerical implementation. *Int J Geomech* 2007;7(2):83–101. [http://dx.doi.org/10.1061/\(ASCE\)1532-3641\(2007\)7:2\(83\)](http://dx.doi.org/10.1061/(ASCE)1532-3641(2007)7:2(83)).
- [7] Baek J, Al-Qadi I. Finite element method modeling of reflective cracking initiation and propagation: investigation of the effect of steel reinforcement interlayer on retarding reflective cracking in hot-mix asphalt overlay. *Transp Res Rec: J Transp Res Board* 2006(1949):32–42.
- [8] Bonaquist R, Witczak M. A comprehensive constitutive model for granular materials in flexible pavement structures. *Proc Int Conf Asphalt Pavements* 1997;1:783–802.
- [9] Habiballah T, Chazallon C. An elastoplastic model based on the shakedown concept for flexible pavements unbound granular materials. *Int J Numer Anal Methods Geomech* 2005;29(6):577–96.
- [10] Cortes DD, Shin H, Santamarina JC. Numerical simulation of inverted pavement systems. *J Transp Eng-ASCE* 2012;138(12):1507–19. [http://dx.doi.org/10.1061/\(ASCE\)1093-5436\(2012\)138:12\(1507\)](http://dx.doi.org/10.1061/(ASCE)1093-5436(2012)138:12(1507)).
- [11] Meda A, Plizzari GA, Riva P. Fracture behavior of SFRC slabs on grade. *Mater Struct* 2004;37(270):405–11. <http://dx.doi.org/10.1617/14093>.
- [12] Ioannides AM, Peng J, Swindler Jr JR. Abaqus model for PCC slab cracking. *Int J Pavement Eng* 2006;7(4):311–21.
- [13] Gaedicke C, Roesler J, Evangelista F. Three-dimensional cohesive crack model prediction of the flexural capacity of concrete slabs on soil. *Eng Fract Mech* 2012;94:1–12.
- [14] Evangelista J, Francisco, Roesler JR, Proena SP. Three-dimensional cohesive zone model for fracture of cementitious materials based on the thermodynamics of irreversible processes. *Eng Fract Mech* 2013;97:261–80.
- [15] Skar A, Poulsen PN. 3-d cohesive finite element model for application in structural analysis of heavy duty composite pavements. *Constr Build Mater* 2015;101(Part 1):417–31. <http://dx.doi.org/10.1016/j.conbuildmat.2015.10.052>.
- [16] Gaedicke C, Roesler J. Fracture-based method to determine the flexural load capacity of concrete slabs. *FAA COE Rep* (31).
- [17] Gaedicke C, Roesler J. Fracture-based method to determine flexural capacity of concrete beams on soil. *Road Mater Pavement Des* 2010;11(2):361–85.
- [18] Hillerborg A, Modéer M, Petersson P-E. Analysis of crack formation and crack growth in concrete by means of fracture mechanics and finite elements. *Cem Concr Res* 1976;6(6):773–81.
- [19] Ulfkjær JP, Krenk S, Brincker R. Analytical model for fictitious crack propagation in concrete beams. *J Eng Mech* 1995;121(1):7–15.

- [20] Olesen JF. Fictitious crack propagation in fiber-reinforced concrete beams. *J Eng Mech* 2001;127(3):272–80. [http://dx.doi.org/10.1061/\(ASCE\)0733-9399\(2001\)127:3\(272\)](http://dx.doi.org/10.1061/(ASCE)0733-9399(2001)127:3(272)).
- [21] Walter R, Østergaard L, Olesen JF, Stang H. Wedge splitting test for a steel–concrete interface. *Eng Fract Mech* 2005;72(17):2565–83.
- [22] Olesen JF, Østergaard L, Stang H. Nonlinear fracture mechanics and plasticity of the split cylinder test. *Mater Struct* 2006;39(4):421–32.
- [23] Olesen JF, Poulsen PN. Modeling RC beam structures based on cracked hinge model and finite elements. Tech. Rep. SR12-11, Technical University of Denmark, DTU Civil Engineering; 2012.
- [24] Hordijk D. Tensile and tensile fatigue behaviour of concrete; experiments, modelling and analyses. *Heron* 1992;37(1):1–79.
- [25] Zhang J, Li VC, Stang H. Size effect on fatigue in bending of concrete. *J Mater Civ Eng* 2001;13(6):446–53.
- [26] Brake NA, Chatti K. Prediction of size effect and non-linear crack growth in plain concrete under fatigue loading. *Eng Fract Mech* 2013;109:169–85.
- [27] Carpinteri A. Energy dissipation in RC beams under cyclic loadings. *Eng Fract Mech* 1991;39(2):177–84.
- [28] Zhang J, Stang H, Li VC. Fatigue life prediction of fiber reinforced concrete under flexural load. *Int J Fatigue* 1999;21(10):1033–49.
- [29] Carpinteri A, Spagnoli A, Vantadori S. A fracture mechanics model for a composite beam with multiple reinforcements under cyclic bending. *Int J Solids Struct* 2004;41(20):5499–515.
- [30] Carpinteri A, Spagnoli A, Vantadori S. An elastic–plastic crack bridging model for brittle-matrix fibrous composite beams under cyclic loading. *Int J Solids Struct* 2006;43(16):4917–36.
- [31] Maitra SR, Reddy KS, Ramachandra LS. Numerical investigation of fatigue characteristics of concrete pavement. *Int J Solids Fract* 2014;189(2):181–93. <http://dx.doi.org/10.1007/s10704-014-9969-x>.
- [32] Planas J, Elices M. Nonlinear fracture of cohesive materials. In: Current trends in concrete fracture research. Springer; 1991. p. 139–57.
- [33] Iyengar KSR, Raviraj S, Jayaram T. Analysis of crack propagation in strain-softening beams. *Eng Fract Mech* 2002;69(6):761–78.
- [34] Maekawa K, Takemura J, Irawan P, Irie M. Triaxial elasto-plastic and fracture model for concrete. *Doboku Gakkai Rombun-Hokokushu/proceedings of the Japan society of civil engineers* 1993(460 pt 5–18):131–8.
- [35] Lee J, Fenves G. Plastic-damage model for cyclic loading of concrete structures. *J Eng Mech* 1998;124(8):892–900.
- [36] Grassl P, Xenos D, Nyström U, Rempling R, Gylltoft K. Cdpm2: a damage-plasticity approach to modelling the failure of concrete. *Int J Solids Struct* 2013;50(24):3805–16.
- [37] Reinhardt HW, Cornelissen HA, Hordijk DA. Tensile tests and failure analysis of concrete. *J Struct Eng* 1986;112(11):2462–77.
- [38] Skar A. Deterioration models for cement bound materials in structural design and evaluation of heavy duty pavements [PhD thesis]. Technical University of Denmark; October 2016.
- [39] Cook RD et al. Concepts and applications of finite element analysis. John Wiley & Sons; 2007.
- [40] Batoz J-L, Dhatt G. Incremental displacement algorithms for nonlinear problems. *Int J Numer Methods Eng* 1979;14(8):1262–7.
- [41] Zhaohua F, Cook RD. Beam elements on two-parameter elastic foundations. *J Eng Mech* 1983;109(6):1390–402.



Cemented materials in heavy duty pavement systems are subjected to complex loading conditions which cannot be treated by existing analytical-empirical methods. For description of the fracture behavior of the cemented material, this thesis presents a general mechanistic framework for engineering applications.

The models presented includes the most significant parameters that influences the structural response, i.e. soil-structure interaction and cyclic damage of the cemented material. The obtained results shows that the methodology is attractive and well-suited for further developments and practical use, enabling a full mechanistic analysis of concrete and composite pavement structures, something which is not possible today.

**DTU Civil Engineering**  
Technical University of Denmark

Brovej, Bygning 118  
2800 Kongens Lyngby

[www.byg.dtu.dk](http://www.byg.dtu.dk)

ISBN 9788778779991  
ISSN 1601-2917